

# Concentration Polarisation Minimisation in Membrane Channels through Electro-osmotic Mixing

Liang Yong Yeow

A thesis in fulfilment of the requirements for the degree of  
Doctor of Philosophy



**UNSW**  
AUSTRALIA

School of Chemical Engineering

Faculty of Engineering

September 2015

PLEASE TYPE

THE UNIVERSITY OF NEW SOUTH WALES  
Thesis/Dissertation Sheet

Surname or Family name: Liang

First name: Yong Yeow

Other name/s:

Abbreviation for degree as given in the University calendar: PhD

School: School of Chemical Engineering

Faculty: Faculty of Engineering

Title: Concentration Polarisation Minimisation in Membrane Channels through Electro-osmotic Mixing

Abstract 350 words maximum: (PLEASE TYPE)

Reverse osmosis (RO) promises to play an increasingly crucial role in water supply, especially via desalination. One of the major problems faced by RO technology is the decline in membrane performance due to concentration polarisation (CP) and fouling. CP increases the osmotic pressure gradient across the membrane, hence reducing the net driving pressure gradient. Moreover, CP increases the probability of fouling.

An electro-osmosis technique is proposed in this thesis which has the potential to reduce CP because it induces the movement of fluid in the vicinity of membrane, thus improving mixing within the boundary layer and enhancing mass transfer. Computational Fluid Dynamics (CFD) is used to simulate steady and unsteady electro-osmotic flow (EOF) in 2D unobstructed and obstructed channels.

First, a mathematical simplification of EOF is developed that reduces the required computational load while retaining the model's accuracy and physical meaning. It is shown that EOF can be mimicked using a slip velocity. The results from CFD are found to be in good agreement both with published data and with more rigorous simulation approaches.

For steady EOF in unobstructed channels, the spatial variation in slip velocity is found to be the driver for mass transfer enhancement. For uniform-unsteady EOF in unobstructed channels, a sinusoidal time-varying electro-osmotic slip velocity has negligible effect on the time-averaged hydrodynamics and mass transfer, because the effect is nullified within the time oscillation period. Nevertheless, there are still benefits for using unsteady EOF for fouling reduction/prevention, as increases in slip velocity frequency and amplitude increase the maximum wall stress which is a proxy for fouling reduction.

For unsteady EOF in spacer-filled channels, the simulation results show that an oscillating slip velocity has the potential to induce vortex shedding. This occurs when a resonant slip velocity frequency is used for Reynolds numbers near the transition from steady to unsteady flow.

Declaration relating to disposition of project thesis/dissertation

I hereby grant to the University of New South Wales or its agents the right to archive and to make available my thesis or dissertation in whole or in part in the University libraries in all forms of media, now or here after known, subject to the provisions of the Copyright Act 1968. I retain all property rights, such as patent rights. I also retain the right to use in future works (such as articles or books) all or part of this thesis or dissertation.

I also authorise University Microfilms to use the 350 word abstract of my thesis in Dissertation Abstracts International (this is applicable to doctoral theses only).



Signature



Witness

7/1/2016

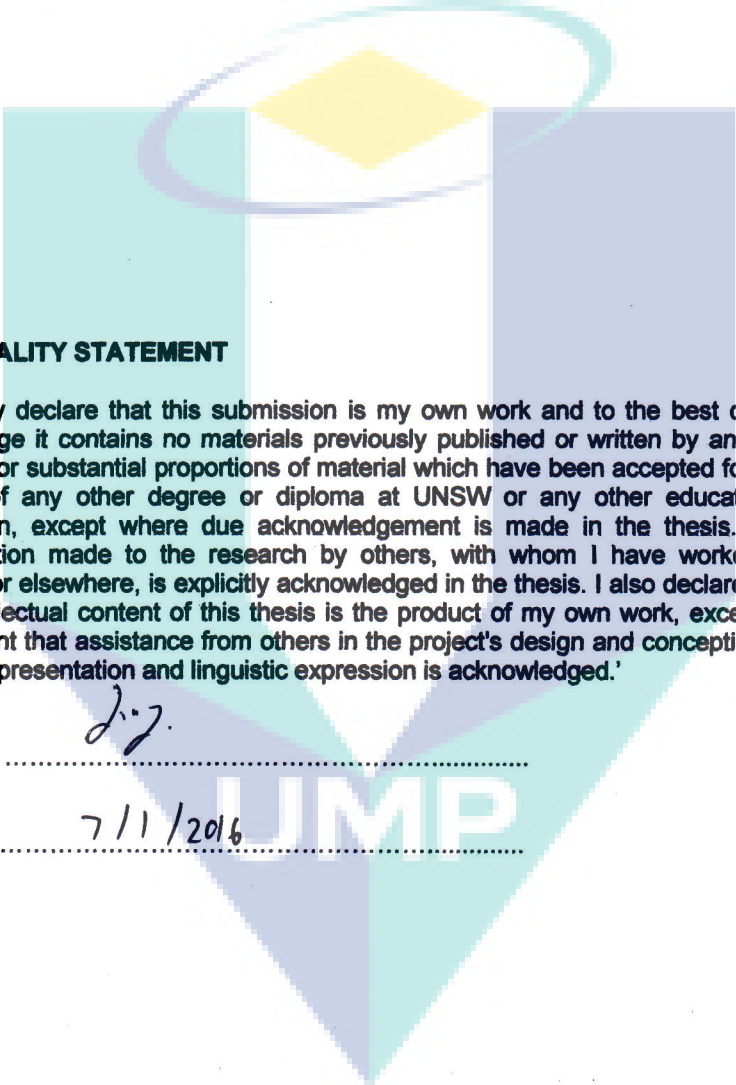
Date

The University recognises that there may be exceptional circumstances requiring restrictions on copying or conditions on use. Requests for restriction for a period of up to 2 years must be made in writing. Requests for a longer period of restriction may be considered in exceptional circumstances and require the approval of the Dean of Graduate Research.

FOR OFFICE USE ONLY

Date of completion of requirements for Award:

THIS SHEET IS TO BE GLUED TO THE INSIDE FRONT COVER OF THE THESIS

The background of the page features a large, semi-transparent watermark of the UNSW logo. The logo consists of a central white diamond shape, a yellow diamond above it, and a teal oval encircling the yellow diamond. Below these elements are two vertical bars, one teal on the left and one purple on the right. At the bottom, the letters 'UNSW' are written in a large, light blue font.

**ORIGINALITY STATEMENT**

'I hereby declare that this submission is my own work and to the best of my knowledge it contains no materials previously published or written by another person, or substantial proportions of material which have been accepted for the award of any other degree or diploma at UNSW or any other educational institution, except where due acknowledgement is made in the thesis. Any contribution made to the research by others, with whom I have worked at UNSW or elsewhere, is explicitly acknowledged in the thesis. I also declare that the intellectual content of this thesis is the product of my own work, except to the extent that assistance from others in the project's design and conception or in style, presentation and linguistic expression is acknowledged.'

Signed ..... *J.J.* .....

Date ..... *7/11/2016* .....

**COPYRIGHT STATEMENT**

'I hereby grant the University of New South Wales or its agents the right to archive and to make available my thesis or dissertation in whole or part in the University libraries in all forms of media, now or here after known, subject to the provisions of the Copyright Act 1968. I retain all proprietary rights, such as patent rights. I also retain the right to use in future works (such as articles or books) all or part of this thesis or dissertation.

I also authorise University Microfilms to use the 350 word abstract of my thesis in Dissertation Abstract International (this is applicable to doctoral theses only).

I have either used no substantial portions of copyright material in my thesis or I have obtained permission to use copyright material; where permission has not been granted I have applied/will apply for a partial restriction of the digital copy of my thesis or dissertation.'

Signed ..... 217.

Date ..... 7/1/2016

**AUTHENTICITY STATEMENT**

'I certify that the Library deposit digital copy is a direct equivalent of the final officially approved version of my thesis. No emendation of content has occurred and if there are any minor variations in formatting, they are the result of the conversion to digital format.'

Signed ..... 217.

Date ..... 7/1/2016



## Abstract

Reverse osmosis (RO) promises to play an increasingly crucial role in water supply, especially via desalination. One of the major problems faced by RO technology is the decline in membrane performance due to concentration polarisation (CP) and fouling. CP increases the osmotic pressure gradient across the membrane, hence reducing the net driving pressure gradient. Moreover, CP increases the probability of fouling.

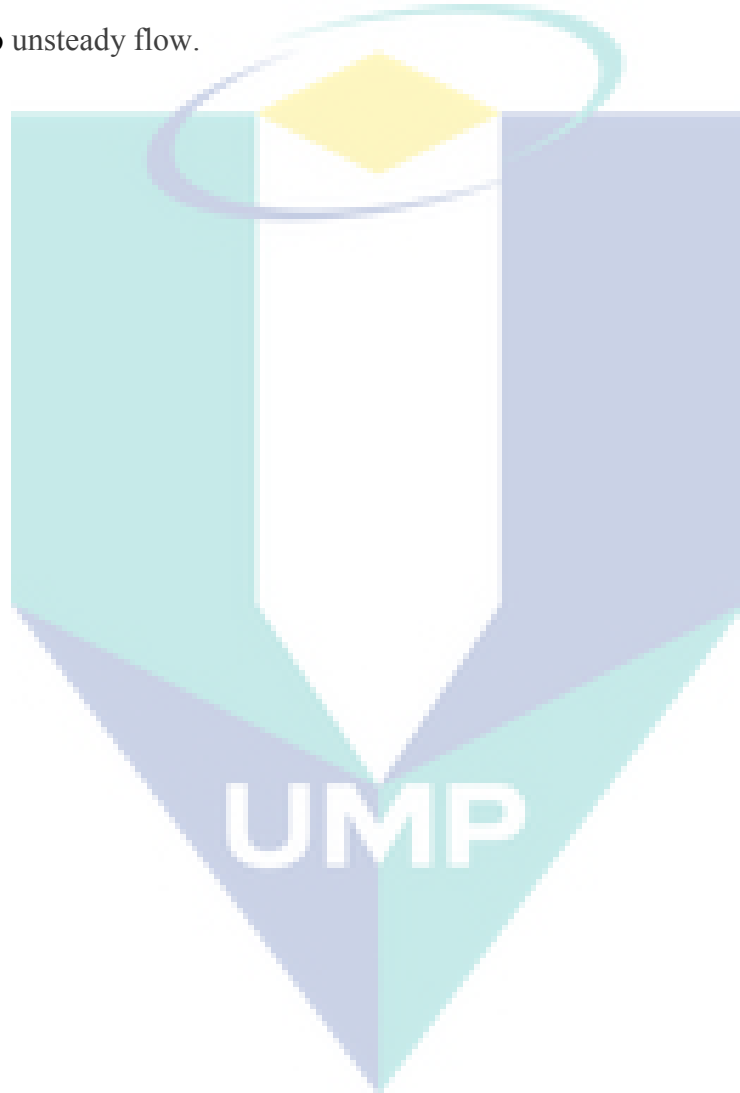
An electro-osmosis technique is proposed in this thesis which has the potential to reduce CP because it induces the movement of fluid in the vicinity of membrane, thus improving mixing within the boundary layer and enhancing mass transfer. Computational Fluid Dynamics (CFD) is used to simulate steady and unsteady electro-osmotic flow (EOF) in 2D unobstructed and obstructed channels.

First, a mathematical simplification of EOF is developed that reduces the required computational load while retaining the model's accuracy and physical meaning. It is shown that EOF can be mimicked using a slip velocity. The results from CFD are found to be in good agreement both with published data and with more rigorous simulation approaches.

For steady EOF in unobstructed channels, the spatial variation in slip velocity is found to be the driver for mass transfer enhancement. For uniform-unsteady EOF in unobstructed channels, a sinusoidal time-varying electro-osmotic slip velocity has negligible effect on the time-averaged hydrodynamics and mass transfer, because the effect is nullified within the time oscillation period. Nevertheless, there are still benefits for using unsteady EOF for fouling reduction/prevention, as increases in slip velocity

frequency and amplitude increase the maximum wall stress which is a proxy for fouling reduction.

For unsteady EOF in spacer-filled channels, the simulation results show that an oscillating slip velocity has the potential to induce vortex shedding. This occurs when a resonant slip velocity frequency is used for Reynolds numbers near the transition from steady to unsteady flow.



## Acknowledgements

I would like to thank the many people who made this thesis possible. First and foremost, I would like to express my sincerest gratitude to my Ph.D supervisor, Professor Dianne Wiley. With her encouragement, her enthusiasm and her great efforts to explain knowledge simply and clearly, she helped me to make research fun for me.

I am particularly thankful to my co-supervisor, Dr Gustavo Fimbres Weihs for his support and knowledge with the CFD simulation in membrane system. Although he is far away in Mexico, he has provided me with much needed advice and suggestions in my research.

I would like to acknowledge funding provided by the Australian Research Council through the Discovery Projects funding scheme (Project no. DP110101643). I would like to thank the Ministry of Higher Education of Malaysia and Universiti Malaysia Pahang (UMP) for scholarship funding. I also would like to thank Professor Jie Bao for supporting my travel expenses to local and international conferences.

Thanks to Peter, Minh, Margaret, Pesila, Ridwan, Denny, Javan, Ao, Zikai, Zakieh, Anggit, Michael, Winnie, Yuchen, Ruigang, Qingyang, Chee Keong, Chaoxu and Yifeng for making the group friendly and fun place to work.

I wish to thank my parents for their love and support throughout my life, without whom I would never have been able to achieve so much. Lastly, thanks to my wife, Woan Shyen for her patience and moral support she has given me over the years.

## Dedication

To Woan Shyen,  
my amazing wife,  
whose sacrificial care for me made it possible for me to complete this thesis.

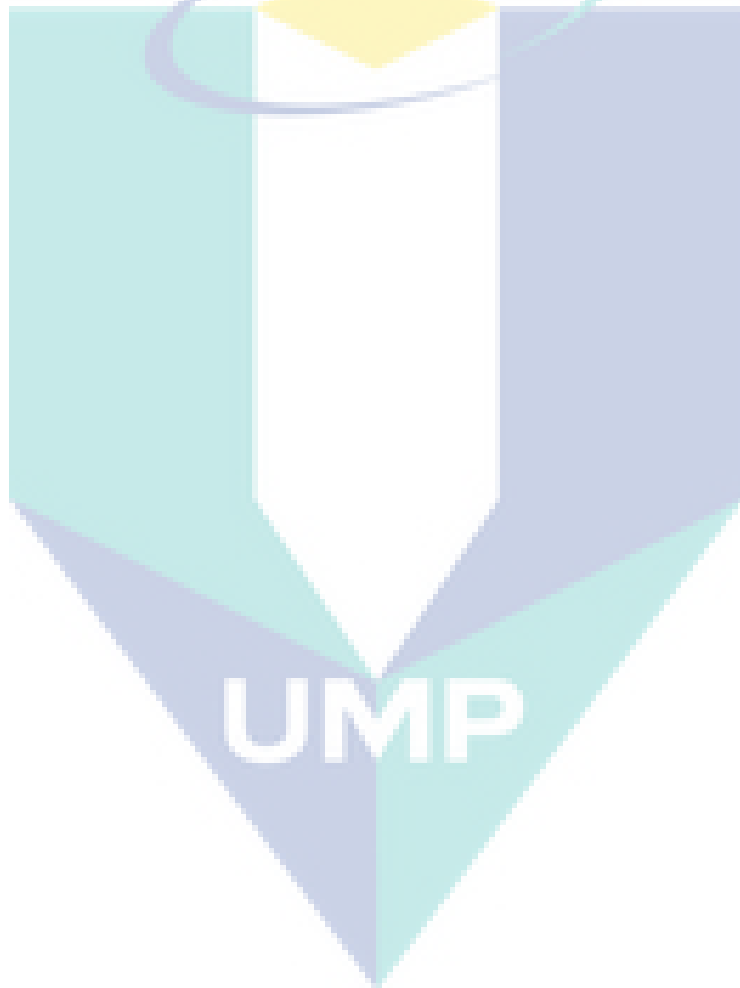


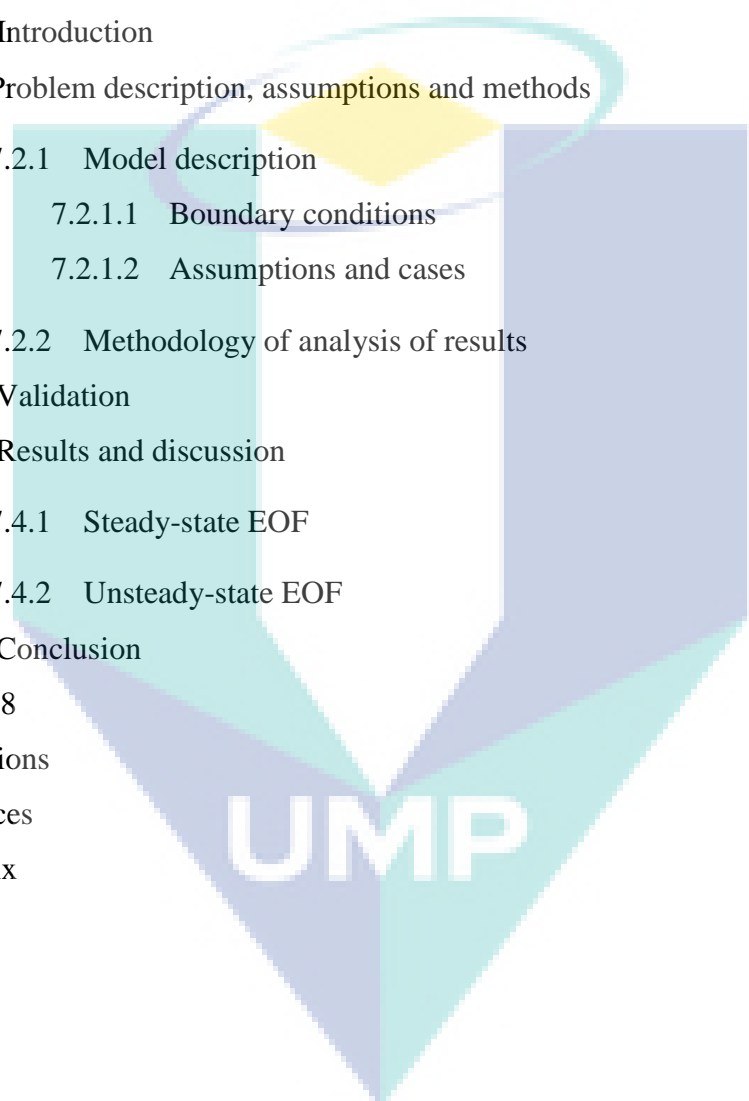
# Table of Contents

Abstract	i
Acknowledgements	iii
Dedication	iv
Table of Contents	v
Nomenclature	ix
List of Publications	xv
Chapter 1	1
Introduction	1
Chapter 2	7
Literature Review	7
2.1 Methods to address concentration polarisation and fouling	7
2.1.1 Boundary layer (velocity) control	8
2.1.2 Membrane modification and materials	9
2.1.3 Spacer-filled channels	10
2.1.4 Electrokinetic phenomena	12
2.2 Electric field effects in membrane processes	13
2.2.1 Electrofiltration and its principles	13
2.2.1.1 Pulsed electric field	14
2.2.1.2 Drawbacks of electrofiltration	16
2.2.2 Electrodialysis and its principles	16
2.2.3 Basic concepts of electro-osmosis	19
2.2.4 Gap analysis for electro-osmosis	22
2.3 CFD modelling	23
2.3.1 CFD modelling of membrane system	23
2.3.2 Modelling of electro-osmosis in other systems	27
2.3.3 Gap analysis for CFD analysis	30
2.4 Flow and its effect on mixing and mass transfer	31

2.4.1	Laminar and turbulence	31
2.4.2	Mass transfer enhancement from mixing	32
2.4.3	Effect of slip velocity on hydrodynamics in obstruction-filled channel	33
2.4.4	Gap analysis for flow analysis	36
Chapter 3		38
Methodology		38
3.1	Basic principles of CFD	38
3.2	Model geometry	40
3.3	Boundary conditions	43
3.4	Methodology for analysis of results	46
3.4.1	Steady EOF	48
3.4.2	Unsteady EOF	50
3.5	Verification and Validation	54
Chapter 4		56
Approximation for modelling electro-osmotic mixing in the boundary layer of membrane systems		56
4.1	Introduction	56
4.2	Charged density (CD) approach vs Helmholtz-Smoluchowski (HS) approach	57
4.3	Problem descriptions, assumptions and methods	58
4.3.1	Model description	60
4.4	Results and discussion	62
4.4.1	Mesh independence study	62
4.4.2	Uniform electric field	62
4.4.3	Non-uniform electric field	65
4.4.3.1	Relative magnitude of convective and viscous terms	65
4.4.3.2	Velocity profile analysis	68
4.4.4	Velocity field analysis	69
4.4.5	Mixing index	71
4.5	Conclusions	75
Chapter 5		78

CFD modelling of electro-osmotic mass transfer enhancement on the feed side of a membrane	78
5.1 Introduction	78
5.2 Problem description, assumptions and methods	79
5.2.1 Model description	79
5.2.1.1 Boundary conditions	80
5.2.1.2 Assumptions and cases	81
5.3 Uniform forced-slip results	83
5.3.1 Validation	83
5.3.2 Hydrodynamics	84
5.3.3 Concentration polarisation	87
5.4 Non-uniform forced slip results	89
5.4.1 Hydrodynamics and mass transfer	89
5.4.2 Concentration polarisation reduction mechanism	92
5.5 Effect of membrane properties and bulk flow conditions	93
5.5.1 Effect of membrane properties	93
5.5.1.1 Effect of membrane permeability	93
5.5.1.2 Effect of intrinsic solute rejection	97
5.6 Effect of bulk flow conditions	98
5.7 Conclusions	101
Chapter 6	104
CFD modelling of unsteady-state electro-osmotic permeate flux enhancement in spiral-wound reverse osmosis membrane systems	104
6.1 Introduction	104
6.2 Problem description, assumptions and methods	104
6.2.1 Model description	104
6.2.1.1 Boundary conditions	105
6.2.1.2 Assumption and cases	106
6.2.2 Methodology of analysis of results	108
6.3 Validation	109
6.4 Results and discussion	111

6.4.1	Unsteady EOF	111
6.4.2	Comparison of results for different cases	121
6.5	Conclusions	123
Chapter 7		125
CFD modelling of electro-osmotic permeate flux enhancement in spacer-filled membrane channels		125
7.1	Introduction	125
7.2	Problem description, assumptions and methods	126
7.2.1	Model description	126
7.2.1.1	Boundary conditions	128
7.2.1.2	Assumptions and cases	128
7.2.2	Methodology of analysis of results	129
7.3	Validation	130
7.4	Results and discussion	131
7.4.1	Steady-state EOF	131
7.4.2	Unsteady-state EOF	134
7.5	Conclusion	143
Chapter 8		144
Conclusions		144
References		153
Appendix		162



## Nomenclature

Symbol	Description	Units
$C_1, C_2$	Convective terms	$\text{kg m}^{-2} \text{s}^{-2}$
$D_1, D_2$	Viscous terms	$\text{kg m}^{-2} \text{s}^{-2}$
$D$	Solute diffusivity	$\text{m}^2 \text{s}^{-1}$
$d_f$	Filament diameter	m
$d_h$	Hydraulic diameter	m
$e$	Charge of an electron	C
$e_{GCI}$	Relative error due to discretisation grid	
$\vec{E}$	Electric field vector	$\text{V m}^{-1}$
$E_x$	Electric field component in the $x$ -direction	$\text{V m}^{-1}$
$E_y$	Electric field component in the $y$ -direction	$\text{V m}^{-1}$
$f_{glob}$	Global friction factor	
$F_{pl}$	Dimensionless peak frequency from frequency response	
$F_{peak}$	Dimensionless peak frequency	
$f_s$	Frequency of oscillation of slip velocity	$\text{s}^{-1}$
$F_s$	Dimensionless frequency of oscillation of slip velocity	
$f$	Friction factor	m
$\mathbb{F}_{coarse}$	Integral function for coarse grid	
$\mathbb{F}_{fine}$	Integral function for fine grid	
$g$	Gravitational acceleration	$\text{m s}^{-2}$
$h_{ch}$	Height of channel	m
$h_m$	Membrane thickness	m

$J$	Permeate flux	$\text{kg m}^{-2} \text{s}^{-1}$
$J_{an}^{mig}$	Flux of anions	$\text{kg m}^{-2} \text{s}^{-1}$
$J_{ca}^{mig}$	Flux of cations	$\text{kg m}^{-2} \text{s}^{-1}$
$J_{pure} = \rho L_p \Delta p_{tm}$	Permeate flux through membrane for a pure water system	$\text{kg m}^{-2} \text{s}^{-1}$
$k_B$	Boltzmann constant	$\text{kg m}^2 \text{s}^{-2}$
$k_{mt} = \frac{-D}{\omega_w - \omega_{b0}} \left( \frac{\partial \omega}{\partial y} \right)_w$	Mass transfer coefficient	$\text{m s}^{-1}$
$k$	Turbulent kinetic energy equivalent	$\text{m}^2 \text{s}^{-2}$
$k_y$	Turbulent kinetic energy equivalent in the y-direction	$\text{m}^2 \text{s}^{-2}$
$K_y$	Dimensionless turbulent kinetic energy equivalent in the y-direction	
$l_m$	Mesh length	$\text{m}$
$L$	Channel length	$\text{m}$
$L_e$	Distance between electrodes	$\text{m}$
$L_{in}$	Entrance length	$\text{m}$
$L_m$	Membrane length	$\text{m}$
$L_{out}$	Exit length	$\text{m}$
$L_p$	Membrane permeability	$\text{m s}^{-1} \text{Pa}^{-1}$
$L_{total}$	Total channel length	$\text{m}$
$M$	Mixing index	$\text{m}^3 \text{s}^{-2}$
$M_{loc}$	Local mixing index	$\text{s}^{-2}$
$M_{vol}$	Volumetric mixing index	$\text{s}^{-2}$
$N_{coarse}$	Number of elements for coarse grid	
$N_{fine}$	Number of elements for fine grid	
$n_o$	Ion concentration in the bulk solution	$\text{ions m}^{-3}$

$P$	Pressure	Pa
$\Delta P$	Pressure difference	Pa
$\Delta p_{tm}$	Inlet transmembrane pressure	Pa
$q$	Charge	C
$r_e$	Electrode radius	m
$\mathbb{R}$	Refinement ratio	
$R$	Membrane intrinsic rejection	
$Re = \frac{\rho u_{eff} d_h}{\mu}$	Hydraulic Reynolds number	
$S$	Surface area	m <sup>2</sup>
$Sc = \frac{\mu}{\rho D}$	Schmidt number	
$Sh = \frac{k_{mt} d_h}{D}$	Sherwood number	
$t$	Time	s
$U$	Dimensionless local velocity in the $x$ -direction	
$u$	Local velocity in the $x$ -direction	m s <sup>-1</sup>
$u_{eff} = \frac{u_{b0}}{\varepsilon}$	Effective velocity	m s <sup>-1</sup>
$u_f$	Fully developed velocity	m s <sup>-1</sup>
$u_p$	Perturbation velocity in the $x$ direction	m s <sup>-1</sup>
$u_{p,error}$	Perturbation velocity error	
$u_{pf}$	Fully developed perturbation velocity	m s <sup>-1</sup>
$\bar{u}_p$	Cross sectional area average of $u_p$	m s <sup>-1</sup>
$U_p$	Dimensionless perturbation velocity in the $x$ direction	m s <sup>-1</sup>
$U_s$	Dimensionless slip velocity	

$U_{s,A}$	Dimensionless slip velocity amplitude	
$u_s$	Slip velocity	$\text{m s}^{-1}$
$u_{s,A}$	Oscillation amplitude of slip velocity	$\text{m s}^{-1}$
$U_{us}$	Unsteady slip velocity	$\text{m s}^{-1}$
$U_{s,RMS}$	Root mean square (RMS) of the time-dependent slip velocity over one sinusoidal cycle	$\text{m s}^{-1}$
$v$	Local velocity in the $y$ -direction	$\text{m s}^{-1}$
$\vec{v}$	Velocity vector	$\text{m s}^{-1}$
$\vec{v}_f$	Fully developed velocity vector	$\text{m s}^{-1}$
$\vec{v}_p$	Perturbation velocity vector	$\text{m s}^{-1}$
$v_p$	Perturbation velocity in the $y$ direction	$\text{m s}^{-1}$
$V$	Potential difference between electrodes	V
$X$	Dimensionless distance in direction parallel to membrane surface	
$x$	Distance in direction parallel to membrane surface	m
$x_{e1}$	First electrode location	m
$x_{e2}$	Second electrode location	m
$Y$	Dimensionless distance from membrane surface, in direction normal to the surface	
$y$	Distance from membrane surface, in direction normal to the surface	m
$z$	Valence or charge of ionic component	
<b>Greek symbol</b>	<b>Description</b>	<b>Units</b>
$\lambda$	Charge per unit length along electrode	$\text{C m}^{-1}$
$\lambda_D$	Debye length	m

$\gamma = \frac{\omega_w}{\omega_{b0}}$	Concentration polarisation index (modulus)	
$\mu$	Viscosity	$\text{kg m}^{-1} \text{s}^{-1}$
$\pi$	Osmotic pressure	Pa
$\rho$	Fluid density	$\text{kg m}^{-3}$
$\rho_e$	Charge density	$\text{C m}^{-3}$
$\sigma$	Reflection coefficient	
$\varphi$	Osmotic pressure coefficient	Pa
$\zeta$	Zeta potential	V
$\tau$	Wall shear stress	Pa
$\delta = \frac{\omega_w - \omega_{b0}}{-\left(\frac{\partial \omega}{\partial y}\right)_w}$	Boundary layer thickness	m
$\delta_{st}$	Stokes penetration depth	m
$\omega$	Solute mass fraction	
$\omega_p = (1 - R)\omega_w$	Solute mass fraction on the permeate side of membrane surface	
$\varepsilon$	Porosity	
$\varepsilon_e$	Permittivity	$\text{F m}^{-1}$
$\eta$	Number of dimensions in flow field	
$\phi$	Potential due to the wall charge	V
$\psi$	Potential due to the external electric field	V
$\Omega$	Volume of fluid region for volumetric mixing index calculation	$\text{m}^3$
$\Phi$	Local mass transfer enhancement factor	
$\tilde{\Phi}$	Global mass transfer enhancement factor	

<b>Subscript</b>	<b>Description</b>
<i>avg</i>	Average
<i>b0</i>	Value at inlet bulk conditions
<i>EO</i>	Value under electro-osmosis
<i>NS</i>	Value without electro-osmosis (no-slip)
<i>p</i>	Value for the permeate
<i>pure</i>	Value for pure water
<i>w</i>	Value on feed side membrane surface (wall)

<b>Variables</b>	<b>Description</b>
$\bar{\phi}$	Area averaged value
$\hat{\phi}$	Maximum value
$\ddot{\phi}$	Time-averaged value
$\phi_A$	Oscillation amplitude

UMP

## List of Publications

### Journal Papers:

**Y.Y. Liang**, G.A. Fimbres Weihs, D.E. Wiley, Approximation for modelling electro-osmotic mixing in the boundary layer of membrane systems, *Journal of Membrane Science*, 450 (2014) 18-27.

**Y.Y. Liang**, M.B. Chapman, G.A. Fimbres Weihs, D.E. Wiley, CFD modelling of electro-osmotic permeate flux enhancement on the feed side of a membrane module, *Journal Membrane Science*, 470 (2014) 378-388.

### Conference Presentations:

**Y.Y. Liang**, G.A. Fimbres Weihs, D.E. Wiley, CFD Modelling of Electro-Osmotic Mass Transfer Enhancement in Membrane System. 8th International Membrane Science & Technology Conference, Melbourne (2013).

**Y.Y. Liang**, G.A. Fimbres Weihs, D.E. Wiley, CFD Modelling of Electro-Osmotic Mass Transfer Enhancement in Spacer-Filled Membrane Channel, The 10<sup>th</sup> International Congress on Membranes and Membrane Processes, Suzhou, China (2014).

D.E. Wiley, **Y.Y. Liang**, G.A. Fimbres Weihs. CFD of Membrane Separation Processes. 2nd International Conference on Desalination using Membrane Technology, Singapore (2015).

### Papers under review:

**Y.Y. Liang**, G.A. Fimbres Weihs, D.E. Wiley, CFD modelling of unsteady-state electro-osmotic permeate flux enhancement in membrane system (under review).

**Y.Y. Liang**, G.A. Fimbres Weihs, D.E. Wiley, CFD modelling of electro-osmotic permeate flux enhancement in spacer-filled membrane channels (under review).

# Chapter 1

## Introduction

To date, water scarcity is being recognized as one of the greatest threats to human activity. With increased global water scarcity, membrane treatment technologies are becoming increasingly important as the most efficient technologies for purification and filtration needs.

Membrane technology covers the engineering processes that utilise synthetic membranes to separate the components of a mixture. Membrane separation processes can be categorized according to the driving forces applied, namely

1. pressure-driven (e.g. microfiltration (MF), ultrafiltration (UF), nanofiltration and reverse osmosis (RO) or hyperfiltration),
2. concentration-gradient driven (e.g. dialysis)
3. temperature-driven (e.g. membrane distillation)
4. electrical-potential driven processes (e.g. electrodialysis).

The most common types membrane processes used in the industry are pressure-driven processes. These membrane processes differ in the particle sizes that can be separated. In microfiltration (MF), particle diameter sizes between 0.1 to 10  $\mu\text{m}$  are separated from a solvent based on a sieving effect. Typical hydrostatic pressure differences (the driving force) in MF range from 0.05 to 0.2 MPa. Ultrafiltration membranes, separate macromolecules or submicrometer particles, and the applied hydrostatic pressures lie in between 0.1 to 5 MPa. In nanofiltration and reverse osmosis (RO) processes, the membrane separates macromolecules and low molecular mass

compounds (e.g. sodium chloride) and ions from the solvent; hydrostatic pressures are typically in the range of 1 to 10 MPa [1].

Hollow fibre and spiral wound membrane modules are the most common commercial membrane modules utilised. The latter dominate for RO and NF due to their good balance between ease of operation, fouling control, permeation rate and packing density [2]. For this reason, they are the focus of this research.

According to Cummings [3], the global market for membrane processes is predicted to reach \$8.1 billion by 2018, driven mainly by RO. This is because RO continues to play a crucial role in water supply given the increasing scarcity of fresh water caused by climate change and human population growth. In response to this, there have been significant gains in RO efficiency [4]. For example, the application of nanotechnology [5, 6] and biotechnology [7, 8] to membrane fabrication has resulted in membranes that exhibit water permeability several orders of magnitude higher than conventional polymeric membranes. There has also been a significant reduction in energy usage, such that current energy usage is only about 20 % of the usage for early RO desalination plants [9]. A recent study by Cohen-Tanugi et al. [10] shows that a membrane with 3× higher membrane permeability shows a reduction in the number of pressure vessels and the capital investment requirements by 44-63 %. In 2005, the total costs (capital and operating cost) for producing water from seawater were less than \$0.7/m<sup>3</sup> [11]. This compares with a cost of \$1.57 to \$3.55/m<sup>3</sup> in 1988 [12].

Although current membranes offer higher permeabilities (flux) than older RO membranes, the benefit of increased flux is limited by concentration polarisation and fouling [4]. Concentration polarisation (CP) occurs when, because of solute rejection, the convective mass transfer of solutes towards the membrane is initially faster than back-diffusion to the bulk. Concentration polarisation leads to an increase of the local

pressure and may lead to precipitation and fouling [13-16]. Fouling increases the operating cost of a treatment plant by reducing the life span of membranes. It can also lead to frequent cleaning necessitating membrane module replacement [17].

Approaches for minimising the effects of concentration polarisation on membrane performance can be categorised into four groups –

1. boundary layer (or velocity) control,
2. eddy inducers/generators/promoters,
3. membrane material and/or surface modification, and
4. external (electrical or magnetic) fields.

Of these, approaches 1–3 only reduce but never mitigate the membrane/solute interaction. On the other hand, external fields (approach 4) can potentially lift the solute from the membrane surface, leading to its subsequent removal due to convection by the bulk flow [17]. The external field approach can be implemented independently of the velocity field and membrane materials. Importantly, this approach does not intrinsically require eddy promoters inside the membrane channel in order to reduce concentration polarisation.

The application of an external electric field near a solid/liquid interface may result in the motion of liquid with respect to an adjacent charged surface. These associated effects are known as electrokinetic phenomena [18]. Electro-osmosis is an electrokinetic phenomenon where the bulk fluid moves relative to a charged surface due to an external electric field. It should be noted that electro-osmosis can only occur if there are charged species in the fluid that can respond to the electric field [17]. Thus, this approach is ideal for desalination and reverse osmosis (RO) water treatment because they involve salts and other charged species. As charge separation generally occurs at a solid-fluid interface (such as a membrane surface), a thin layer that contains

a net electric charge is formed near the wall. This layer is known as the electric double layer [19]. The thickness of the electric double layer can be characterized by the Debye length ( $\lambda_D$ ) which is the distance from the surface to the region where the electric potential is  $\exp(-1)$  or 37 % of the maximum (zeta potential,  $\zeta$ ) [20]. Electro-osmotic flow induced near a membrane surface could potentially disrupt the boundary layer, enhance mass transfer and, therefore, reduce the extent of concentration polarisation and increase permeate flux in membrane separation operations.

Recently, there have been an increasing number of publications that utilise CFD as a tool for aiding with the understanding of hydrodynamics and mass transfer in membrane processes [21-30]. This reflects the potential of CFD as a valuable tool to improve the performance of membrane processes. Therefore, this thesis uses a Computational Fluid Dynamics (CFD) model to simulate the effect of electro-osmotic instabilities on the hydrodynamics in a rectangular membrane channel, similar to those found in SWM modules.

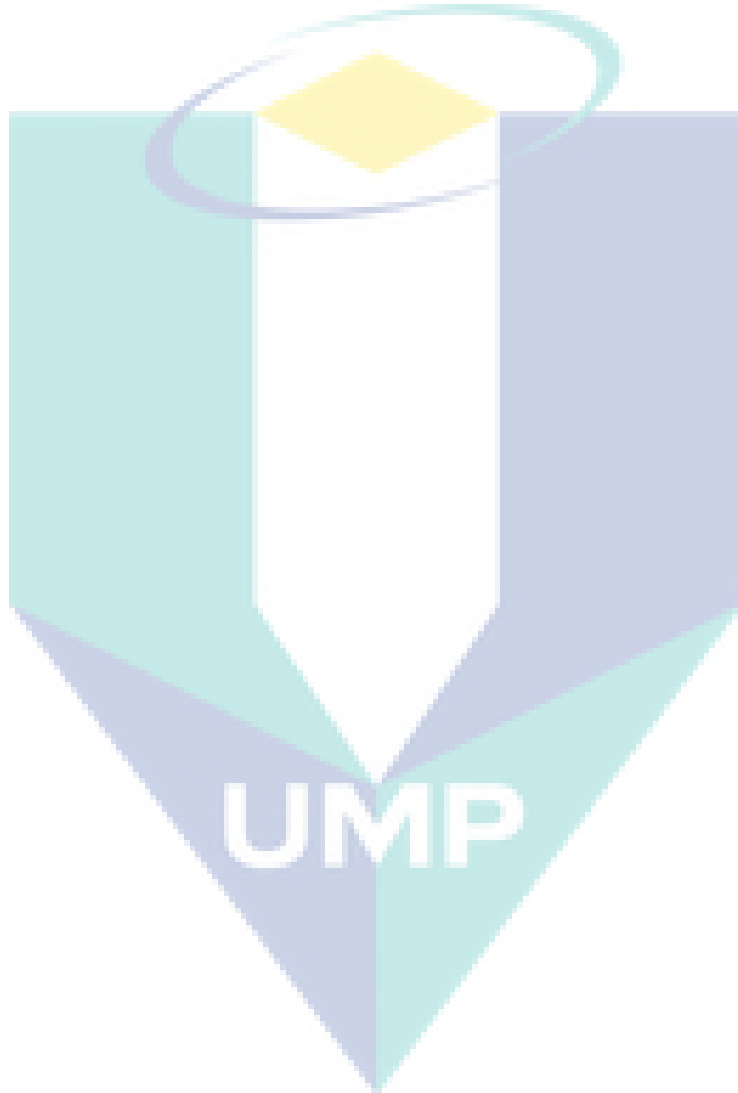
The primary objective of this thesis is to use CFD to investigate the potential for reduction of solute concentration at the membrane surface using electro-osmosis in membrane systems. The specific aims of this thesis are:

- To demonstrate the reliability and accuracy of the Helmholtz-Smoluchowski (HS) approximation in membrane channels
- To understand the mechanisms that lead to electro-osmotic mass transfer enhancement in steady-state
- To investigate time-varying electro-osmotic flow (EOF) on the maximum shear stress and time-averaged permeate flux
- To examine the combined effects of integrating the electro-osmotic mixing and spacer design approaches for mass transfer enhancement

In keeping with these aims, the structure of thesis is organised as follows:

- Chapter 2 reviews previous studies which focus on improving membrane separation. Particular emphasis is given to approaches induce eddies and apply external electric fields (e.g. electro-osmosis).
- Chapter 3 explains the methodology used throughout this thesis. It provides information about the common simulation methodology and methods used to analyse the results in each of the other chapters. Methods unique to each particular chapter can be found in the relevant chapter.
- In Chapter 4, the suitability and applicability of the HS approach for simulating electro-osmotic effects on the velocity profile in membrane channels are investigated. This chapter is based on the journal article of the same name published in the Journal of Membrane Science in 2014 as shown in the list of publications.
- Chapter 5 focuses on understanding the mechanisms that lead to electro-osmotic mass transfer enhancement in steady-state. It is based on the journal article of the same name published in the Journal of Membrane Science in 2014 as shown in the list of publications.
- Chapter 6 investigates the temporal variations in slip velocity, especially since pulsatile flow has the potential to enhance wall stress and slow or eliminate the onset of particle fouling. This chapter is based on the paper under review for publication in Chemical Engineering Science.
- In Chapter 7, the interactions between electro-osmotic mixing and the mixing caused by feed channel spacers on mass transfer enhancement is examined. This chapter is based on the paper under review for publication in the Journal of Membrane Science.

- Final conclusions of this thesis are included in Chapter 8.
- The Appendix contains a list of the CFD videos of vortex shedding related to Figure 7.8 and Figure 7.9 on the disc provided with the thesis.
- The provided disc contains the CFD videos as well as an electronic pdf version of the thesis from which figures in the thesis can be viewed in detail.



## Chapter 2

### Literature Review

The focus of this thesis is on minimising concentration polarisation and/or fouling. This chapter reviews the main approaches used for reducing concentration polarisation or fouling, with the focus on eddy inducer and external field (electro-osmosis) approaches. This chapter also reviews the current state of the art of the use of computational fluid dynamics (CFD) in membrane process analysis. An overview of the basic knowledge on the onset of turbulence and the effect of external forces on the hydrodynamics in spacer-filled channels is also provided in this chapter.

#### 2.1 Methods to address concentration polarisation and fouling

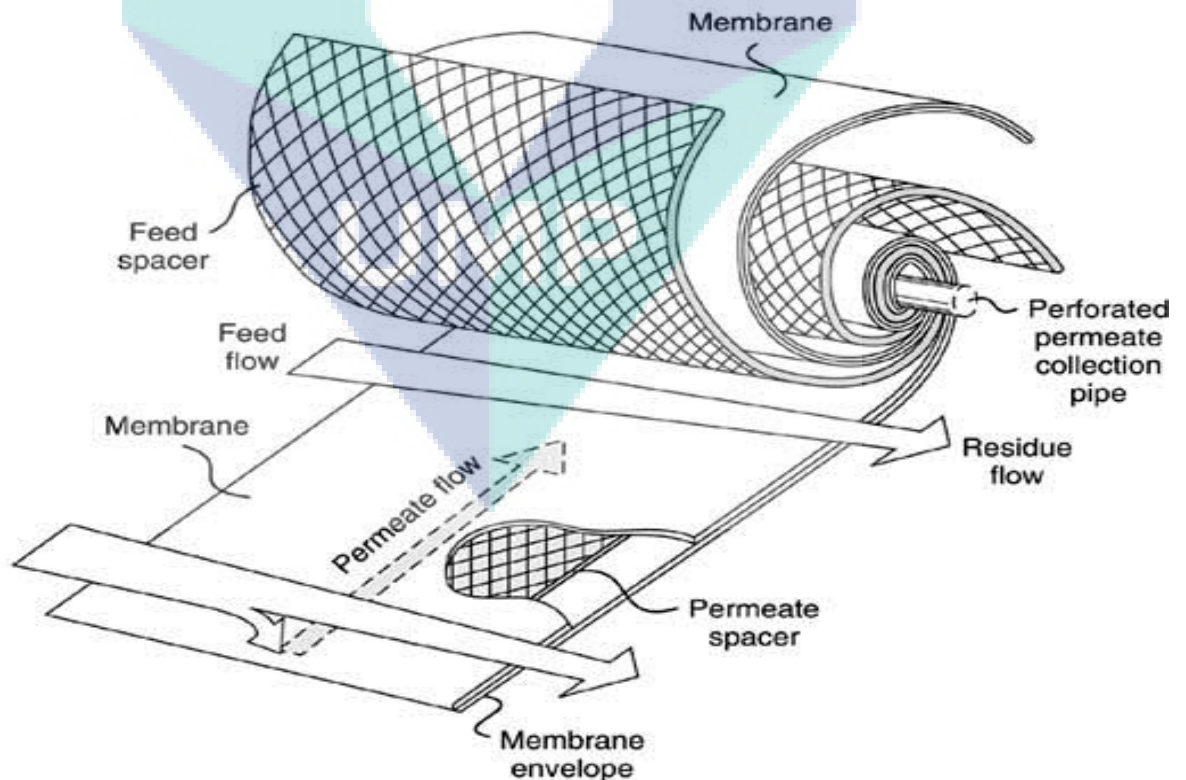


Figure 2.1: Schematic of a typical spiral wound membrane module (as in Baker [31]).

Spiral wound membrane (SWM) modules are widely used in the membrane industry from reverse osmosis (RO) to ultrafiltration (UF) due to their high membrane area to volume ratio [2]. These types of modules are the focus in this research. Figure 2.1 illustrates a schematic SWM module, which is comprised of a series of flat sheets of membrane and spacers rolled up around a central collection pipe.

A major issue associated with these membrane operations is concentration polarisation. Concentration polarisation reduces membrane performance through an increase of the osmotic pressure at the membrane surface, thus increasing the pressure driving force required. Another adverse effect of concentration polarisation is that it promotes membrane fouling. The fouling phenomenon results in greater resistance to solvent flux, which further deteriorates membrane performance.

Numerous methods have been proposed to minimise concentration polarisation and fouling, such as boundary layer control, eddy inducers/promoters, membrane material modifications and external fields. The first two approaches mainly focus on concentration polarisation issues while the latter two focus on fouling mitigation [17]. All of these approaches aim to disturb the boundary layer and increase the shear rate at the membrane surface, leading to an increase in the back-transport of particles and solute away from the membrane and potentially hindering the onset of fouling [32]. An overview to these approaches is provided in sections 2.1.1 to 2.1.4.

### **2.1.1 Boundary layer (velocity) control**

One of the most direct ways to enhance mixing in the vicinity of a membrane is to increase the velocity of the fluid that is flowing past the membrane surface. The thickness of the boundary layer over a flat plate can be estimated by the Blasius solution [33], which gives:

$$\delta_{vel} \sim \left(\frac{\nu x}{u}\right)^{0.5} \quad (2.1)$$

Equation (2.1) implies that for constant fluid properties,  $\nu$ , and at a specific location,  $x$ , the primary reason for a decrease in the thickness of the hydrodynamic boundary layer (or flow resistance) is an increase in flow velocity,  $u$ . Because of this, cross-flow or tangential fluid flow is widely used in membrane separation process to improve mixing. Boundary layer control has the potential to minimise membrane fouling by continuously lifting the fouling material from the membrane surface into the bulk flow [17]. Boundary layer control, however, is insufficient to overcome fouling because the turbulence that can be obtained inside the membrane module is limited by the energy consumption of the pumps required to generate high feed fluid velocities [17]. Boundary layer control therefore has to be combined with other approaches, i.e., spacer, membrane modification and materials and/or electrokinetic approaches, in order to manage/minimize concentration polarisation and fouling.

### **2.1.2 Membrane modification and materials**

The membrane material properties can be modified to reduce foulant-membrane interactions and minimise fouling [17]. Membrane materials have to be modified such that there is a balance with other competing effects such as product stability, chemical resistance, product quality and cost of manufacturing [17]. This means that the development of an anti-fouling membrane is a non-trivial task.

Specifically, it is the skin layer (the top layer) of the membrane surface that plays a key role in fouling reduction [34]. Despite the reductions, fouling is not completely eliminated. Moreover, the effect of modified membranes on fouling seems only noticeable when the solution is dilute [34]. In order to maximize the effectiveness of the modified membrane, other supporting approaches, such as membrane cleaning, are deemed necessary [31].

### 2.1.3 Spacer-filled channels

Membrane spacers are made from plastic netting and are used to separate the membrane leaves, hence providing a passage for the fluid to flow. These spacers are flow obstructions, and are often referred to as “eddy promoters” because inserting them in membrane channels promotes greater mixing between the bulk flow and boundary layer [35]. SWM modules are tightly wrapped, hence they cannot be disassembled easily for mechanical cleaning. Fouling control in a SWM module therefore can only be addressed by hydrodynamics, pre-treatment of feed and operational control/chemical cleaning [36]. In terms of hydrodynamics, the feed spacers can be oriented such that high cross flow velocities or secondary flow patterns, i.e. vortices (Figure 2.2), can be developed in order to generate higher scouring forces along the membrane surface to enhance back-mixing from the membrane surface to the bulk of the feed flow [35]. However, there are several negative effects associated with the presence of spacers in membrane modules; for example, (a) they create areas of stagnant flow and entrapment sites where fouling material can accumulate [37], and (b) they increase pumping energy requirements due to pressure loss [38]. It is generally agreed that concentration polarisation and pressure drop are significantly affected by the spacer geometry [39] (i.e. spacer thickness, porosity, orientation, hydraulic diameter, flow attack angle, distance between spacers) and materials [40, 41].

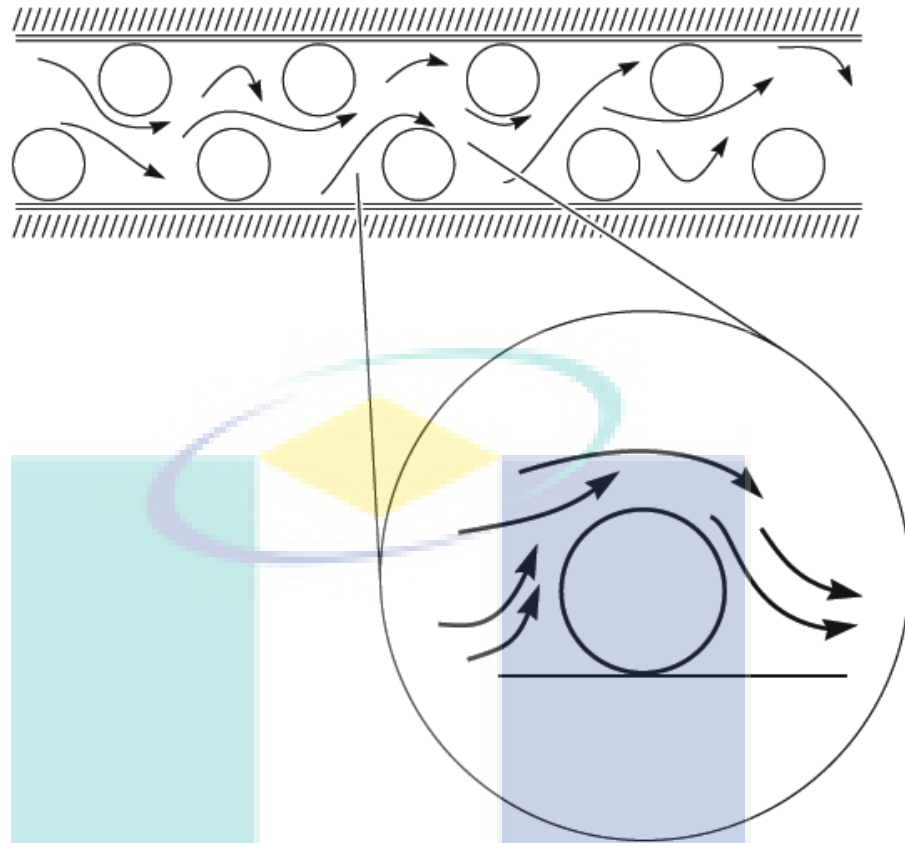


Figure 2.2: Unsteady laminar oscillating patterns or vortices in membrane (as in Baker [31]).

Vrouwenvelder et al. [25] highlighted that fouling on the feed spacer has a great effect on feed channel pressure drop increase and therefore overall performance decline than fouling on the membrane surface. Later work by Suwarno et al. [42], suggests that the relative effect of membrane fouling versus spacer fouling depends on the operating conditions. This emphasizes that spacer design must be considered when managing/addressing membrane fouling [43]. Furthermore, it is extremely difficult for the membrane to act as an anti-fouling layer if the spacer design is not taken into consideration [43]. This is because the effectiveness of membrane surface modifications in fouling reduction is reduced once a fouling layer is formed on the membrane surface [34].

Despite prior research, it is not yet possible to eliminate concentration polarisation and fouling through spacer design. This prompts the need for more studies on membrane spacer design and hydrodynamics effect.

#### 2.1.4 Electrokinetic phenomena

The application of an external electric field near a liquid/solid interface may result in the motion of liquid with respect to the adjacent charged surface. These associated effects are known as electrokinetic phenomena. Electrokinetic phenomena are one of the most common non-mechanical methods for mixing in microfluidic systems. Electrokinetic flow of fluid relative to a charged surface is known as electroosmotic motion, while the electrokinetic motion of a dispersed particle relative to a fluid is known as electrophoretic motion [19]. The application of electric fields to membrane processes began with the work of Bechhold [44] who introduced an electric field as the driving force in an ultrafiltration processes. There are two important membrane processes which rely on electrokinetic phenomena, namely electrofiltration and electrodialysis. The main features of these two processes are summarized in Table 2.1.

Table 2.1: Comparison of main features between electrofiltration and electrodialysis

	<b>Electrofiltration [45]</b>	<b>Electrodialysis [46]</b>
Flux enhancement mechanism	Drives the charged molecules away from the membrane surface and therefore minimises concentration polarisation layer	Electroconvection (discussed in detail in section 2.2.2)
Membrane	Non ion-exchange	Ion-exchange
Driving force	Pressure and electric field	Electric field only

## 2.2 Electric field effects in membrane processes

### 2.2.1 Electrofiltration and its principles

In general, electrofiltration particularly due to electrophoresis, is an efficient method to minimise gel layer formation on membrane surface which hence enhance filtration flux [47]. The schematic diagram of electrofiltration when an electric field is applied across the membrane is shown in Figure 2.3.

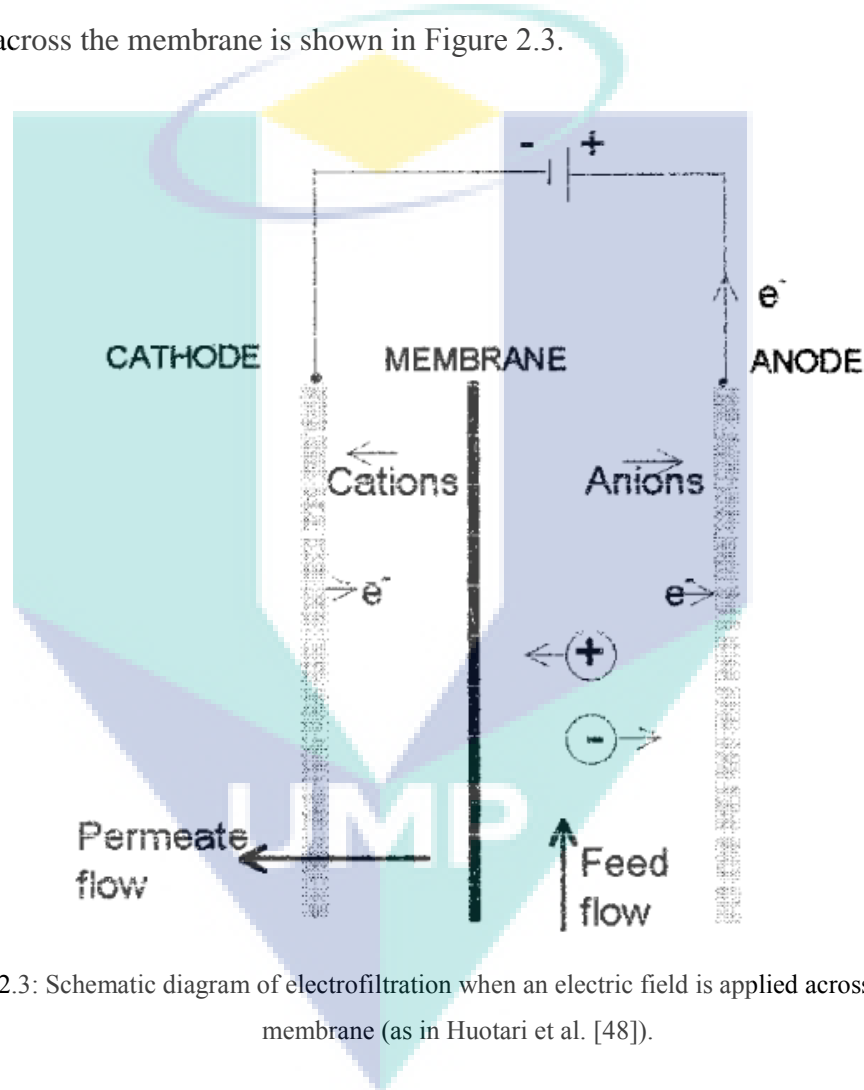


Figure 2.3: Schematic diagram of electrofiltration when an electric field is applied across a flat sheet membrane (as in Huotari et al. [48]).

The main mechanism of electrofiltration is related to the force balance on the charged particle as illustrated in Figure 2.4 [45]. Assuming the particles are not able to pass through the membrane, deposition of particle occurs when the drag force due to permeate flux exceeds the sum of the lift force due to cross flow and the back diffusion away from the membrane due to the concentration gradient. The electric field drives the

charged molecules away from the membrane surface and therefore minimizes the concentration polarisation layer [45].

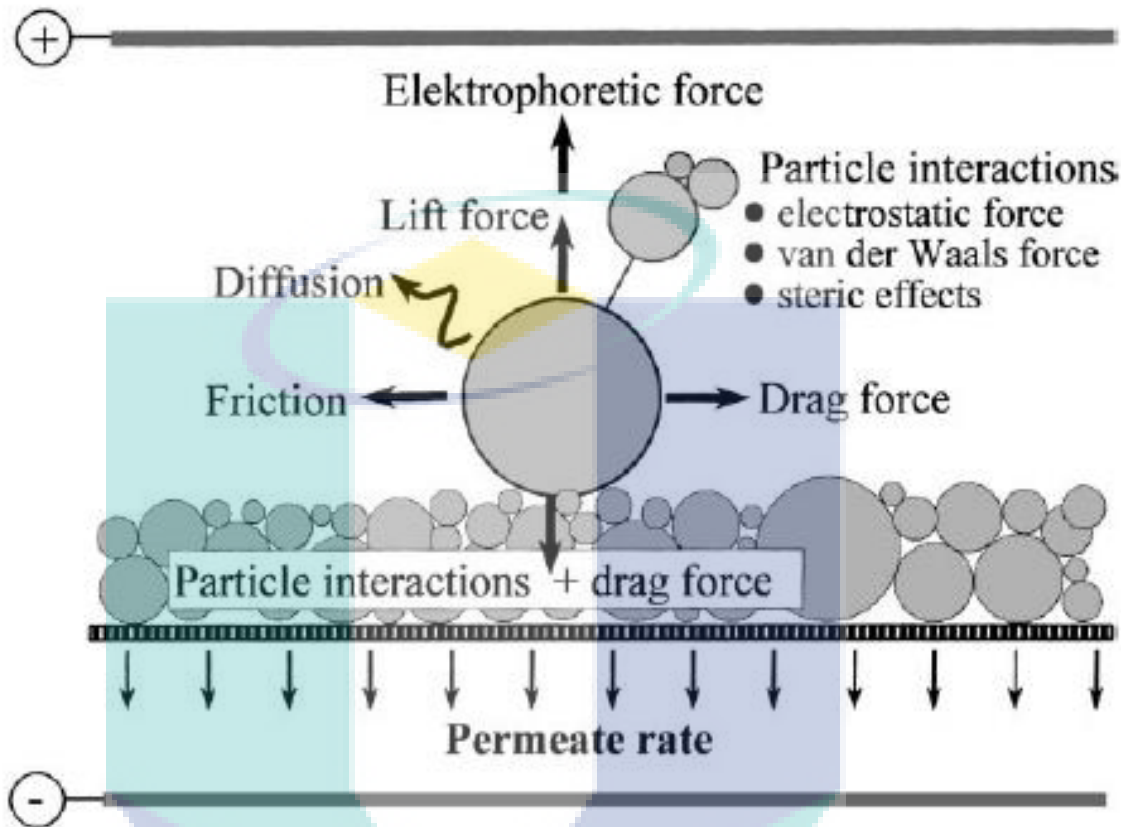


Figure 2.4: Force balance of a particle in filtration process (as in Weigert et al. [45]).

### 2.2.1.1 Pulsed electric field

One of the important decisions when applying an electric field in a membrane system is the choice of electric field mode to be used. There are two types of electric field modes available, namely constant and time-varying electric fields. The continuous application of an electric field typically requires an electric field strength greater than  $10 \text{ kWh m}^{-3}$  permeate, which is at least 5 times greater than the typical pumping energy for microfiltration [48]. For the purpose of reducing the power consumption, pulsed electric fields have been studied.

The pulsed electric field approach requires significantly less energy consumption than required by the continuous electric field application. Wakeman and

Sabri [49] compared the effect of constant and pulsed electric field application on crossflow microfiltration processes. They found that constant electric field results in a more effective utilisation of energy compared to the pulsed electric field. A normalized power factor (NPF) was employed to compare the efficiency of the electrically enhanced electric field microfiltration to the traditional microfiltration. Their research highlighted that a desirable membrane performance is achieved in the case that NPF is below 1, at which the permeate flow rate is greater than the energy consumption.  $NPF < 1$  indicates a better utilization of energy relative to the conventional cross flow without the electric field.

Pulsed electric field can also be combined with other approaches, e.g. obstructions (spacers). Jurado and Bellhouse [101] found that a combination of electrophoresis and obstruction-induced vortex mixing can significantly improve permeate flux in ultrafiltration. The spacers performed two functions: 1) to act as the electrode to produce electric field 2) to produce a standing vortex wave. This suggests that mass transfer enhancement can potentially be realized through the interaction between a pulsed electric field and obstructions.

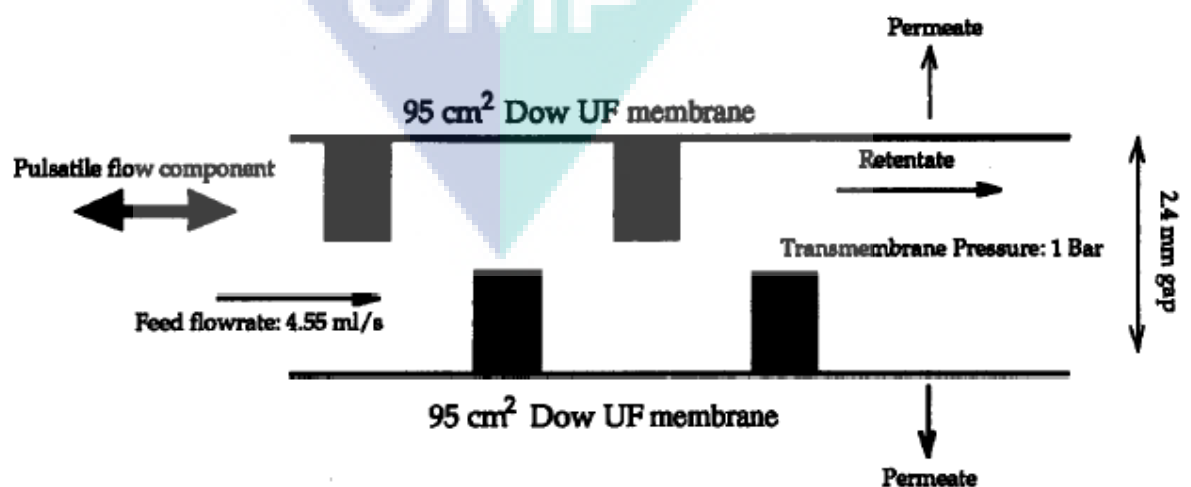


Figure 2.5: Combination of electrophoresis and obstruction-induced vortex mixing (as in Jurado and Bellhouse [50]).

### 2.2.1.2 Drawbacks of electrofiltration

Electrically enhanced pressure driven processes are not commonly used in industry, although some large scale applications have been reported [51]. Jagannadh and Muralihadra in their review about 20 years ago highlighted that one of the major restrictions in the commercial use of electric field enhanced technologies is the lack of proper corrosion-resistant and inexpensive electrode materials [17]. Although platinum dissolves less, it is still too expensive for practical applications. Kondoh and Hiraoka [52] developed an inexpensive carbon electrode for commercial electro-osmotic dewatering which dissolves at a rate less than 0.005 g/Ah. Electrodes made of iridium oxide coated on a metal carrier such as titanium are popular, due to its high corrosion resistant properties [51].

Another potential side effect of the electrokinetic phenomena is that it can result in internal heating (Joule heating) which leads to an increase and non-uniformity in the liquid temperature. The disadvantage of a temperature increase is that it decreases the electrokinetic separation efficiency in a system.

### 2.2.2 Electrodialysis and its principles

Electro-osmotic phenomena have many applications for ion-exchange membranes [53]. Ion-exchange membranes are used in electrodialysis, an electrochemical separation process in which electrical potential differences are employed for separating ionic species. As mentioned in Chapter 1, the driving force across the membrane for RO/NF/UF is the pressure. Meanwhile, for electrodialysis, the driving force for ion transport is the applied electric potential between the anode and cathode [53]. Figure 2.6 illustrates the concentration polarisation at a positively charged nanochannel interface when an electric field is applied across the membrane. A concentration gradient is formed at either side of the nanochannel as cations ( $J_{ca}^{mig}$ ) and

anions ( $J_{an}^{mig}$ ) are moving (migrating) in the opposite direction in the diffusion boundary layer (DBL).

The mechanism for mixing in an electro dialysis membrane channel is known as electroconvection. Two types of electroconvection have been identified: the equilibrium (classical electro-osmosis) and non-equilibrium (electro-osmosis of second kind). The latter occurs when tangential and normal electric fields are applied. This leads to a non-equilibrium double layer that destroys the DBL, thus overcoming diffusion limitations at the interface and resulting in overlimited currents through the nanochannel [46]. The significance of electro-osmosis of second kind phenomena is that its velocity can be much larger than those observed for the classical electro-osmosis case [46, 54], which is preferable to enhance mixing at the membrane interface.

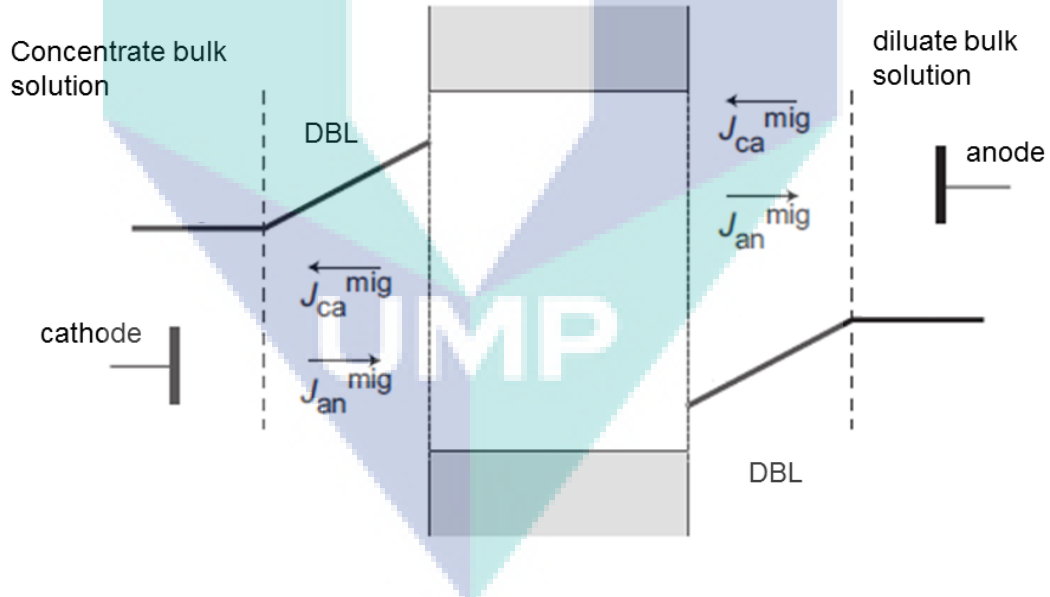


Figure 2.6: Schematic of concentration polarisation at a nanochannel interface (adapted from Schoch et al. [46]).

The voltage-current curve (Figure 2.7) is an important element of charge transfer across ion exchange membranes for electro dialysis, and is closely related with concentration polarisation. There are three distinguishable regions in the voltage-current curve, namely the ohmic current region I, the limiting current region II and the

overlimiting current region III. In region I, when concentration polarisation is low, as voltage increases current also increases. Concentration polarisation causes precipitation of salt at the membrane surface which results in an increase in electrical resistance. When the salt concentration becomes too high on the cathodic side, the salt concentration on the anodic side is reduced to zero. No ions are available to carry the electric current. Therefore, a limiting current region is observed in region II.

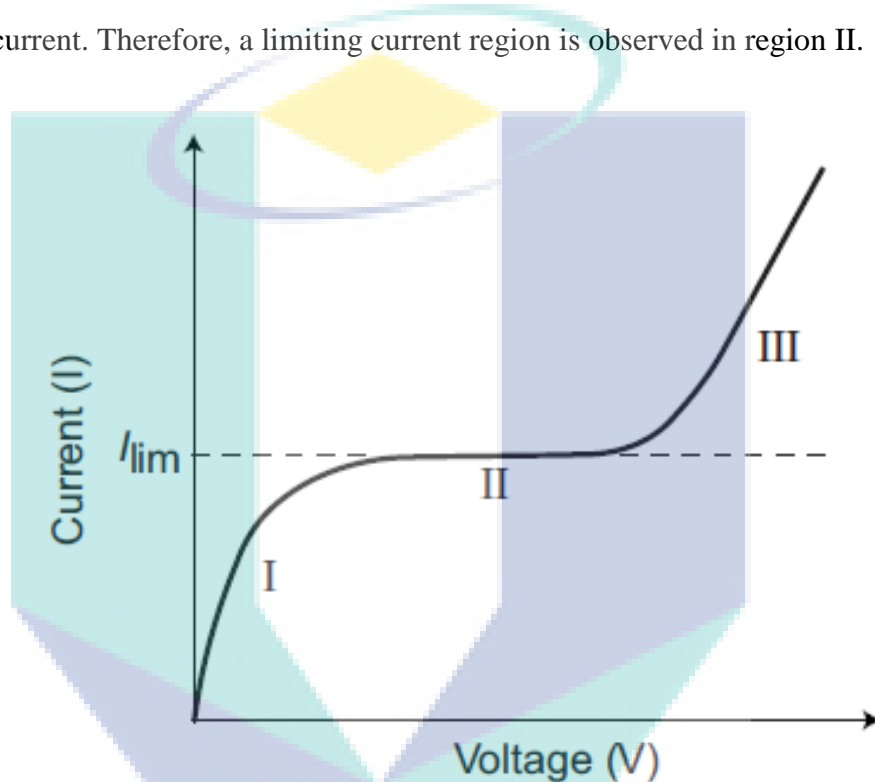


Figure 2.7: Typical voltage-current curve of a cation-exchange membrane (as in Schoch et al. [46]).

In region III (overlimiting current), an inflexion of the voltage-current current at the plateau occurs as voltage increases. The physical phenomenon for the onset of the overlimiting current region has been thoroughly investigated by Rubinstein et al. [55-59]. The transition from region II to III is accompanied by a threshold appearance of a low-frequency excess electric noise [60]. It has been shown that the overlimiting current phenomena is not related to water splitting [61]. Later, Rubinstein et al. [55] in their experimental studies showed that the overlimiting behavior is related to the flow instabilities in the form of vortical flow. The presence of vortical flow has the potential

to promote mixing instabilities in the concentration polarisation region near the permselective membrane, which ultimately enhances wall shear and slows the onset of membrane fouling.

Depending on the membrane properties, the hydrodynamic behaviour near the membrane wall may differ. For example, for a membrane with a surface charge, flow instabilities (vortical flow) can be induced when an electric field is applied across the membrane [55]. This underlines the potential for using an electric field as an alternative to using spacers to induce vortical flow.

### 2.2.3 Basic concepts of electro-osmosis

The flow of fluid induced by electro-osmosis is illustrated in Figure 2.8. The presence of co-ions (similarly charged ions) and counter-ions (oppositely charged ions) results in attraction and repulsion of ions in the vicinity of a charged surface. These phenomena, coupled with the random thermal motion of the ions, create an electric double layer (EDL). In order to neutralise the surface charge, an excess of counter-ions compared to co-ions accumulates near the charged surface, such that electroneutrality is not maintained within the EDL. The inner most part of the EDL (adjacent to the surface) is known as the Stern layer (SL), while the outer layer (away from the surface) is known as the diffuse layer (DL). Figure 2.9 illustrates the structure of the EDL. The electro-osmotic slip velocity is the velocity applied at the outer edge of the EDL; that is, it goes from  $u_s$  at the edge of the EDL to zero at the wall.[19].

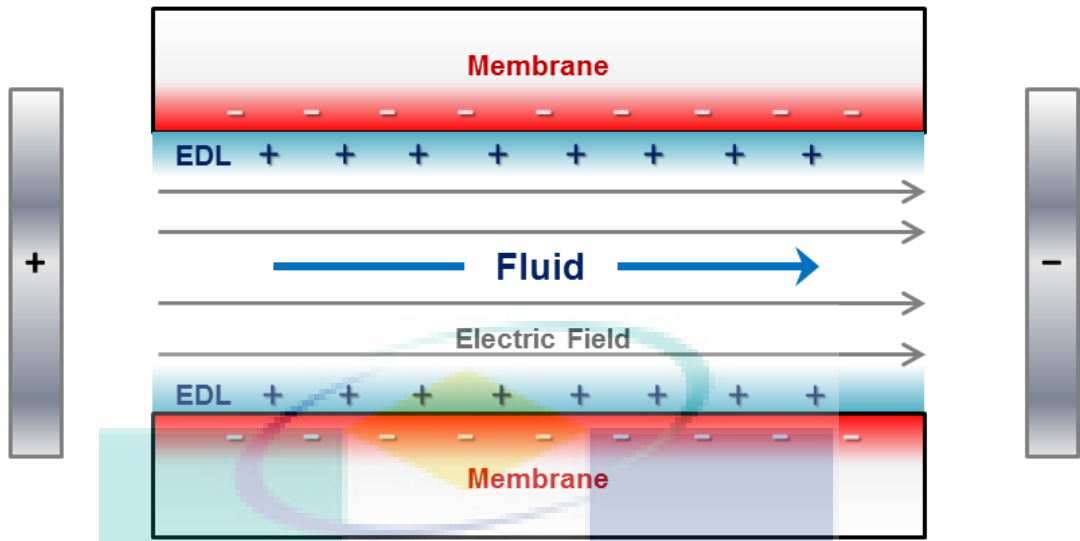


Figure 2.8: Schematic representation of the electro-osmosis phenomenon.

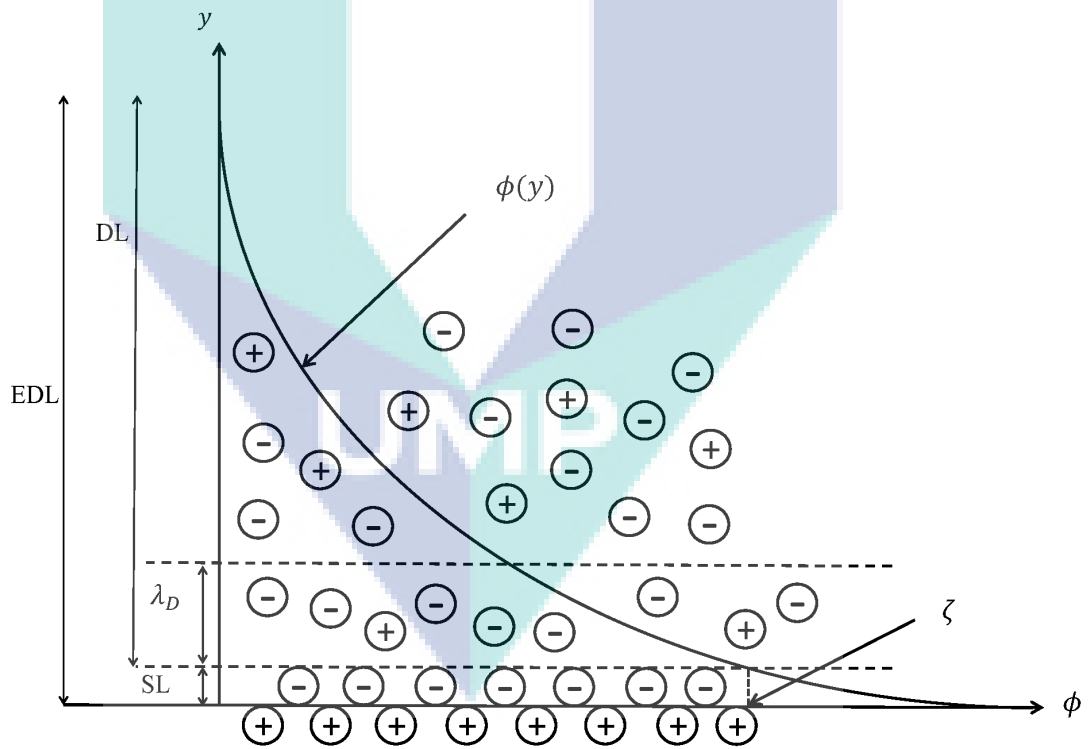


Figure 2.9: Schematic of the electric double layer structure, illustrating the dependence of electric potential ( $\phi$ ) on the distance from the surface ( $y$ ), and indicating the relative sizes of the electric double layer (EDL), Stern layer (SL), diffuse layer (DL) and Debye length ( $\lambda_D$ ).

Poisson's equation for electrostatics relates the spatial variation in the electric potential and the charge density, and is expressed in the following manner [18]:

$$\nabla^2 \phi = \frac{-\rho_e}{\varepsilon} \quad (2.2)$$

where  $\phi$  is the potential due to the double layer,  $\rho_e$  is the electric charge density and  $\varepsilon$  is the permittivity of the fluid. The electric charge density,  $\rho_e$ , can be expressed in terms of a Boltzmann distribution as follows [19]:

$$\rho_e = -2zen_o \sinh\left(\frac{ze\phi}{k_B T}\right) \quad (2.3)$$

where  $n_o$  is the ion concentration in the solution,  $z$  is the ionic valence,  $e$  is the charge of an electron,  $k_B$  is the Boltzmann constant and  $T$  is the temperature.

The system of equations (2.2) and (2.3) can be linearised using the approximation  $\sinh(a) \approx a$  for  $\phi \ll \frac{k_B T}{e}$  (or 26 mV at room temperature) [19, 54]. Assuming the electric potential is constant along the  $x$  direction, equations (2.2) and (2.3) can then be reduced to the following equation:

$$\phi = \zeta \exp\left(\frac{-y}{\lambda_D}\right) \quad (2.4)$$

The CD solution in (2.4) used in this chapter is the analytical solution of the 1D case of equations (2.2) and (2.3), which gives an expression for the charge density in terms of normal distance from the wall.

For a symmetric monovalent electrolyte (such as NaCl), the Debye length can be calculated as [62]:

$$\lambda_D = \sqrt{\frac{\varepsilon k_B T}{2e^2 n_o}} \quad (2.5)$$

Electro-osmotic effects can be introduced to the momentum transport equation in the form of an external force, to yield:

$$\rho \left( \frac{\partial \vec{v}}{\partial t} + \vec{v} \cdot \nabla \vec{v} \right) = -\nabla P + \mu \nabla^2 \vec{v} + \rho_e \vec{E} + \rho g \quad (2.6)$$

where  $P$ ,  $\vec{v}$ ,  $\mu$ ,  $\vec{E}$ ,  $\rho$  and  $g$  are the pressure, velocity, viscosity, electric field, density and gravitational acceleration respectively. For detailed descriptions of the electro-osmosis phenomenon, the reader may refer to the respective pertinent literature [19, 54].

The electric field,  $\vec{E}$ , can be expressed as follows:

$$\vec{E} = -\nabla(\phi + \psi) \quad (2.7)$$

where  $\psi$  is the potential due to the external electric field [20, 63].

Equation (2.6) can be reduced to the HS equation by assuming time-invariance, negligible pressure gradient and gravitational force, and one-dimensional uniform electric field along the flat surface [19]:

$$u_s = -\frac{\varepsilon_e \zeta E_x}{\mu} \quad (2.8)$$

The HS approximation described by equation (2.8) can be used as a slip velocity boundary condition applied at the outer edge of the diffuse double layer [19]. This equation implies that the electro-osmotic flow velocity is proportional to the applied electric field. Therefore, this approach can be referred to as “linear electro-osmosis” [54]. The main advantage of using the HS equation is that the calculation of the flow field is greatly simplified, without the need to solve Poisson’s equation [64], or the need to resolve the charge density or external forces in the momentum transport equation.

#### 2.2.4 Gap analysis for electro-osmosis

The studies for electrofiltration and electrodialysis presented in sections 2.2.1 and 2.2.2 suggest that electrokinetic phenomena have the potential to disrupt a boundary layer. This is important, since boundary layer disruption is generally known to have potential to enhance mixing, and therefore enhance mass transfer. Current electrode configurations for electrofiltration and electrodialysis studies focus on applying the electric field across the membrane (Figure 2.10a) Use of an electrode configuration that

is parallel to the membrane (Figure 2.10b) has not yet been investigated. Boundary layer disruption should happen whether the electric field is perpendicular or parallel to the membrane surface. In addition, use of an electrode configuration adjacent to the membrane surface to enhance mixing has not yet been investigated. There are also no studies that involve the combination of electro-osmotic mixing and spacers. These options are the focus of this thesis.

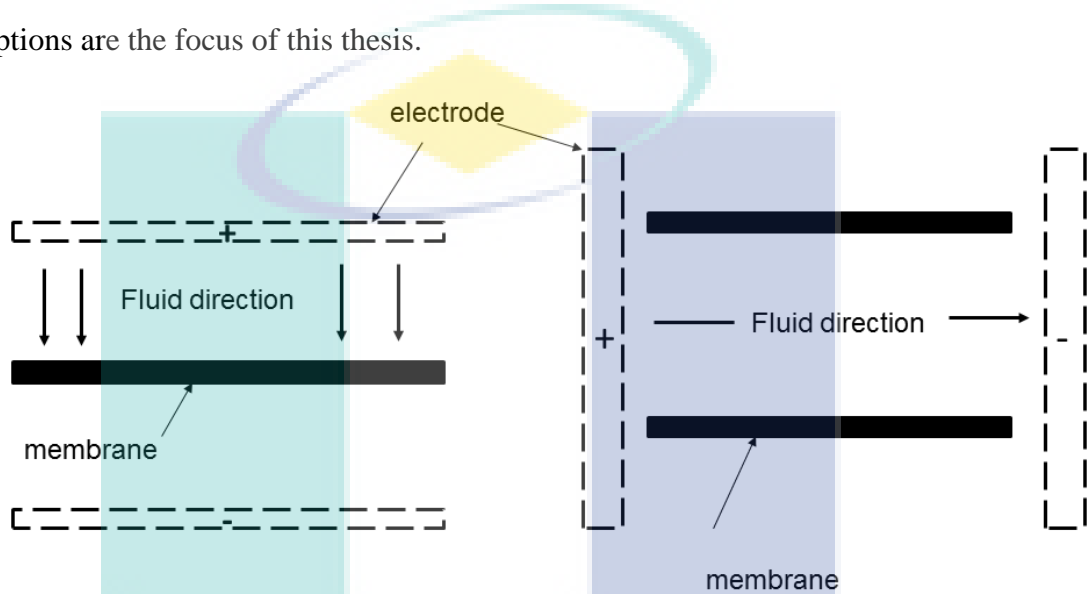


Figure 2.10: Electrode configuration perpendicular (a) and parallel (b) to membrane surface.

## 2.3 CFD modelling

### 2.3.1 CFD modelling of membrane system

Fluid mechanics is the study of forces acting upon a fluid and can be categorised into fluid statics, the study of fluids at rest; fluid kinematics, the study of fluids in motion; and fluid dynamics, the study of the effect of forces on fluid motion. Fluid mechanics/ fluid dynamics is an extensive research field for modelling hydrodynamics and mass transfer in membrane systems [65]. In physics, the Navier-Stokes equations are used to describe the motion of fluid. In the past decades, 2D analytical/semi-analytical solutions for the Navier-Stokes equations have been proposed for the hydrodynamics and mass transfer in unobstructed membrane channels under different conditions such as variable permeation [15, 66], variable solute rejection [15], wall slip

[67] and under the effect of gravity [68]. However, these analytical solutions are only applicable under steady-state or constant permeation flux. In reality, the flow inside membrane channels is inherently unsteady, with non-uniform permeation flux along the membrane, and 3D in nature [35]. Hence, the interaction between fluid dynamics and concentration polarisation is complex. Computational fluid dynamics (CFD) techniques have been used since the 1990s [69] to solve the fluid dynamics and mass transport equations [2]. CFD models have improved the understanding of hydrodynamics and mass transfer in membrane processes [21-23]. CFD is capable of providing large amounts of data at any point in a membrane channel, which can be used to assess the performance of the membrane unit without altering or changing the flow.

CFD studies have shown that the flow inside a membrane channel is greatly influenced by spacer geometry [35]. At low Reynolds numbers, the velocity is steady and not time-dependent, while above a certain critical Reynolds number, the flow becomes oscillating and eventually vortex shedding occurs [70]. Mass transfer is greatly enhanced by the unsteady effects, particularly vortex shedding, and this is related to boundary layer renewal [23]. For example, Fimbres-Weihs and Wiley [23] found that the exponent for the Reynolds number dependence on the Sherwood number increases from 0.605 in steady-state to 0.92 in unsteady-state for a zigzag spacer.

CFD is increasingly being used as an analysis tool to provide insights into the flow behaviour without the need to construct membranes or spacers [35]. CFD has been used to investigate different membrane spacer geometries in order to optimise mass transfer enhancement while minimising pressure loss [29, 43, 71-75].

The question of validation of CFD predictions by experimental data is a crucial one. Particle image velocimetry (PIV), which can provide information about complex fluid flow fields, has proven to be applicable for membrane systems [76] with low

Reynolds numbers (usually much less than 100) [77]. However, PIV is significantly limited for visualising higher flow rates and velocity gradients such as those found in the very thin boundary layer of the order of 1 % to 10 % of membrane channel height [23]. This is mainly because of the video framing rate and poor video resolution of PIV under these conditions [78].

The literature on CFD modelling of SWM modules is rather extensive. Cao et al. [79] and Wiley et al. [80, 81] pioneered the use of CFD to model hydrodynamics and concentration polarisation in membrane systems. Several reviews on the use of CFD for analysing membrane systems have been published [2, 35, 65]. Schwinge et al. [2] emphasized that CFD techniques must be used with great care especially when considering complex processes such as CP and solute rejection. Ghidossi et al. [65] concluded that CFD can be used to describe and optimize the complex hydrodynamics for membrane systems with pulsatile flow and gas sparging, spacers, Dean and Taylor vortices. Fimbres-Weihs and Wiley [35] evaluated the use of 3D CFD simulation for understanding of flow inside membrane channels. Their review concluded that 3D simulations would require significant more computational resources than those required for 2D in terms of memory and computing time.

While there are several reviews of CFD modelling in membrane systems, the reviews have usually considered only flow and mass transfer and not fouling. Only recently, efforts have been made to develop numerical models to test various hypotheses on the mechanisms of formation of fouling layers and their effect on membrane system performance. A summary of these contributions is presented in Table 2.2.

Table 2.2: Summary of major recent contributions to simulation of fouling of membrane systems using CFD.

Fouling type	Fouling mechanism	2D/3D	Fouling model input	Fouling model output	Effects analysed	Reference
Biofouling	Biomass reaction and accumulation	3D	Inlet concentration of substrate and tracer solute	Biomass concentration	The effect of feed channel pressure drop, liquid velocity distribution and residence time distribution on biofilm accumulation	[25, 82]
Biofouling	Biomass reaction and accumulation	3D	Inlet concentration of substrate	Biomass concentration	Effect of flow velocity, biomass location and feed spacer geometries on pressure drop	[83]
Biofouling	Biomass reaction and accumulation	2D, 3D	Inlet concentration of substrate	Biomass concentration	Effect of biomass on permeability	[84]
Biofouling	Biomass reaction and accumulation	3D	Inlet concentration of substrate	Biomass concentration	Effect of biofilm on flux, pressure drop, solute passage	[85]
Biofouling	Biomass reaction and accumulation	3D	Inlet concentration of substrate	Biomass concentration	Effect of biofilm cohesive strength on pressure drop	[86]
Scaling	Crystal nucleation and growth	3D	Super-saturation ratio	Diameter of particle	Effect of degree of scaling on permeability	[87]
Biofouling and scaling	Biomass reaction and accumulation, crystal nucleation and growth	2D	Degree of saturation	Diameter of particle	Effect of biofilm on gypsum precipitation	[88]
Scaling	Crystal nucleation and growth	2D	Degree of saturation	Diameter of particle	Effect of thermodynamic and kinetic on gypsum precipitation	[89]

Scaling	Crystal nucleation and growth	2D	Super-saturation ratio initial nuclei concentration	Diameter of particle	Effect of shear stress on modes of particle formulation (i.e. mean field and particle scale model)	[90]
---------	-------------------------------	----	---	----------------------	--	------

It can be seen in Table 2.2 that most studies have focussed on biofouling and scaling but not on other fouling types, i.e. particulates and organic fouling. For fouling reduction, various studies [25, 82, 83, 85, 86, 88] have shown that an increase in shear stress induces a decrease in cake layer thickness.

Davis and Leighton [91] showed that high amplitude shear oscillation is better than shear alone in terms of concentration polarisation minimisation. During high shear periods, less build-up of particles and solutes occurs on the membrane surface, because of shear-induced diffusion and increased mass transfer [91]. In addition, shear forces have the potential to reduce biofilm layer accumulation on the membrane wall, thus improving the long term stability of permeation [92]. Existing methods to enhance wall shear include mechanical mixing [93], low frequency ultrasound [94] and rotating/vibrating membranes [95]. Given that there are no published CFD modelling studies of electro-osmosis for membrane systems, this section reviews CFD studies of electro-osmosis in micro-channels, which are geometries slightly related to membrane system.

### 2.3.2 Modelling of electro-osmosis in other systems

In micro-channels, electro-osmosis is used to perturb the flow by flow pulsation. CFD studies are generally used to assist the understanding of electro-osmotic flow inside microchannels. Suh [96] presented a 2D simulation of the effect of electro-osmosis in an empty channel. Figure 2.11 shows the velocity vector plot when electrodes are placed on the top and bottom of the channel wall respectively. It can be

seen in this figure that recirculation flow occurs due to the transverse flow (perpendicular to the channel length) caused by EOF. Similar results were obtained by Rawool and Mitra [20] who simulated the electro-osmotic flow in a 3D serpentine channel.

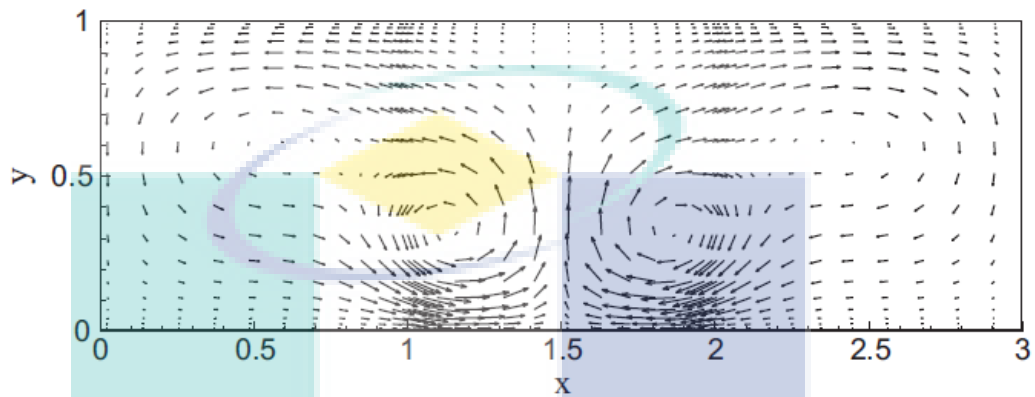


Figure 2.11: Velocity vectors of 2D CFD study (as in Suh [96]).

Song et al. [97] presented results from numerical and experimental studies of electro-osmotic flow inside a microchannel with low frequency oscillations in transverse electro-osmotic flow. The transverse electro-osmotic flow results in stretching and folding of the fluid. The flow geometry is shown in Figure 2.12. They obtained good agreement between the CFD and experimental data approaches (Figure 2.13). They also found that the mixing performance was increased when the applied electric potential increased or the flow rate of the fluid decreased.

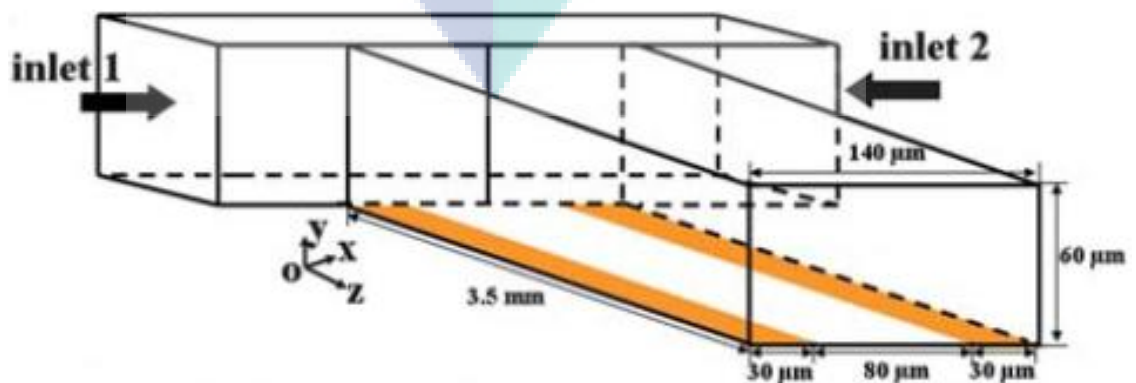


Figure 2.12: 3D model with a pair of parallel electrodes placed at the bottom of channel (as in Song et al. [97]).

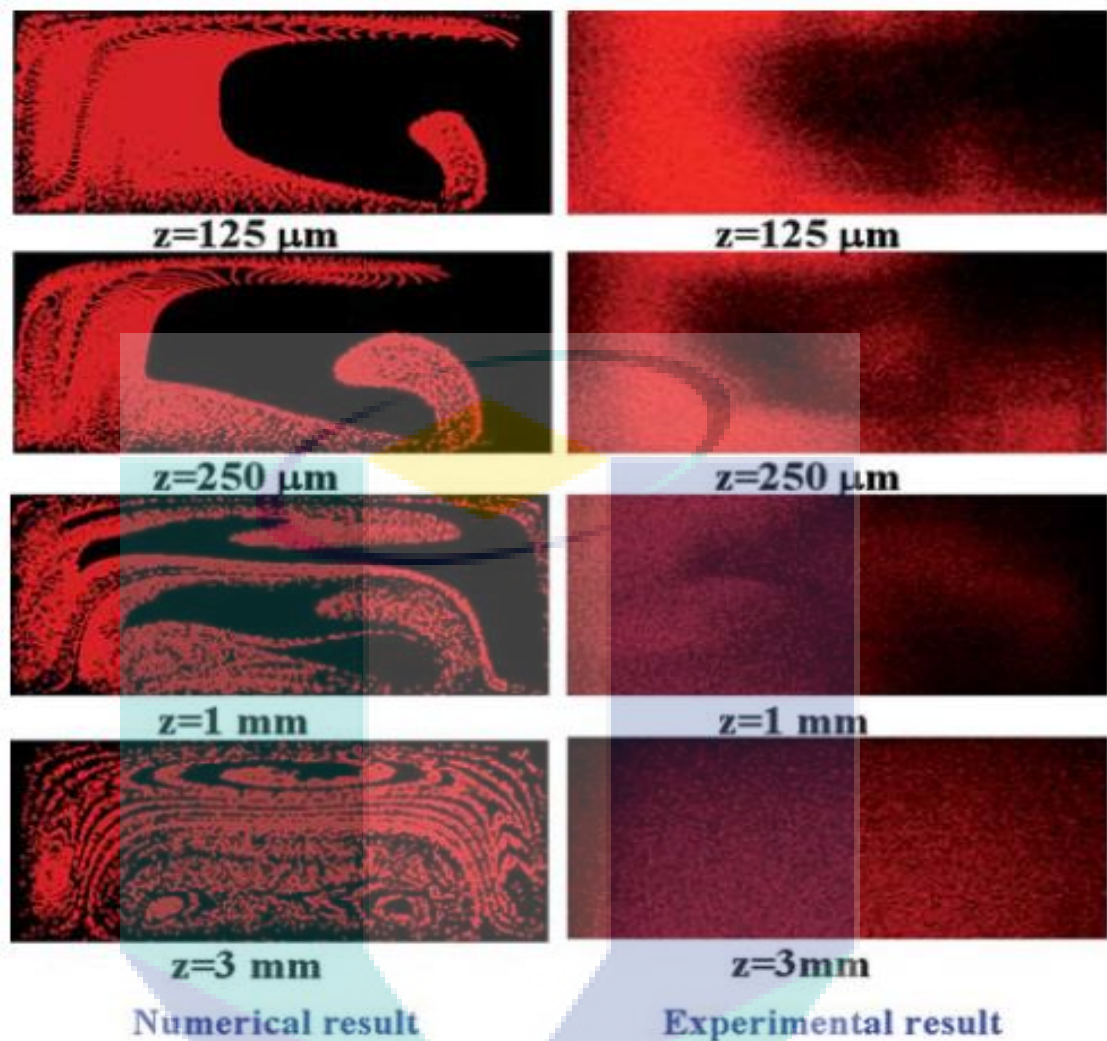


Figure 2.13: Comparison of cross-section images between numerical and experimental studies at different location (as in Song et al. [97]).

CFD has also been used [98, 99] to describe the effect of electro-osmosis on both hydrodynamics and mass transfer behaviour in microchannels. Tang et al. [98] found that an increase in electro-osmosis due to the Joule heating effect caused the sample species to transport faster than in the case without the Joule effect. Zeng et al. [99] compared the deviation between the constant axial concentration gradient from an analytical solution with the varying axial concentration gradient from a numerical solution in a microchannel. They obtained about 25 % deviation that increased significantly down the channel. This highlights the importance of modelling any varying

axial concentration gradient, as the solute concentration gradient in the  $y$ -direction is an important parameter in estimating the mass transfer coefficient in membrane systems.

A dynamic simulation of electro-osmotic flow in an empty microchannel was undertaken by Marcos et al. [100]. An analytical solution for the electrical potential distribution was obtained by solving the linearised Poisson-Boltzmann equation under the Debye-Hückel approximation. They identified that there is a similarity between the slip velocity approximation and the analytical scheme for velocity solutions in the bulk flow region, but they observed a discrepancy for the velocity solutions adjacent to the wall. The agreement between the slip velocity approximation and the analytical scheme increased as the ratio of the Debye layer to the channel height decreased. This means that the slip velocity approximation is an appropriate boundary condition for modelling electro-osmosis [100, 101] when the Debye layer is very thin compared to the channel height.

### **2.3.3 Gap analysis for CFD analysis**

While it has been shown that a slip velocity model is an appropriate boundary condition approximation for modelling electro-osmosis in microchannels [100], the suitability of the slip velocity model for flow caused by a 2D electric field remains unclear. This is of particular interest for modelling electro-osmosis in membrane channels. This is because the HS approximation only takes into account the component of the electric field that is tangential to the charged surface and not the normal component. Although there have been a number of CFD studies [20, 96, 97, 100-102] of the effect of electro-osmosis on hydrodynamics in microchannels, only a handful of studies have considered the effect of electro-osmosis on mass transfer [98, 99] and no study of the effect of electro-osmosis on fouling has been reported. This means that there is an opportunity to build on existing CFD studies in empty (unobstructed) and

spacer-filled (obstructed) membrane channels and include the effect of electro-osmotic slip velocity on mass transfer and fouling. CFD can also be used to generate data required to propose an indicator for mass transfer enhancement due to electro-osmosis.

## 2.4 Flow and its effect on mixing and mass transfer

### 2.4.1 Laminar and turbulence

Understanding of the differences between laminar and turbulent flow is important because they affect mixing and hence mass transfer. Figure 2.14 depicts a situation where turbulent flow occurs when the height of the channel is large enough, as opposed to no turbulence for a smaller channel height. Reynolds [103], in 1883, was among the first researchers to experimentally investigate turbulent flow. When flow is laminar, the coloured fluid elements flow in smooth inside the channel without any breaks. As the flow becomes turbulent, the streamlines break up and the coloured fluid elements inside the channel become randomly distributed [103].



Figure 2.14: Flow patterns for two different channel heights (as in Schlichting et al. [104]).

Turbulent flow results in transverse mixing, which is superimposed on the main flow within the channel. The turbulent flow is unsteady while the laminar flow can be steady or unsteady. The presence of recirculation regions alone does not necessarily indicate turbulent flow. This is because eddies or recirculation regions can occur in both laminar and turbulent flow. The main feature distinguishing laminar unsteady and turbulence is that the unsteadiness associated with turbulence is chaotic, while the unsteadiness for laminar flow is periodic or quasi-periodic. The presence of time-varying eddies and recirculation regions in laminar unsteady and turbulent flow have the potential to reduce concentration polarisation through boundary layer renewal. Because membranes are typically operated in the laminar regime, unsteady laminar flow is the focus of this thesis. The effect of periodic and time-varying eddies and recirculation regions produced by an external force in spacer-filled channel is discussed in the section 2.4.3.

#### **2.4.2 Mass transfer enhancement from mixing**

According to Bird et al. [105], an increase in fluid flow velocity results in a decrease in the boundary layer thickness because of the higher wall shear and mixing. The main drawback of higher wall shear and mixing is an increase in pressure loss, which leads to higher pumping energy for membrane operations. The pressure loss is even higher for turbulent flow, where it is proportional to the square of flow rate as opposed to the first power of the flow for laminar flow [106]. Because of this, laminar and unsteady laminar flows are usually preferred in membrane operations.

A number of studies have evaluated [21-23, 107] mixing enhancement in membranes, especially in spacer-filled channels. At low Reynolds number, the flow is steady while beyond a certain Reynolds number, the spacer perturbs the flow such that vortex shedding occurs in the laminar flow regime. Alexiadis et al. [70] developed a

correlation that describes the critical Reynolds number at which good mixing can be obtained without excessive pressure drop for cavity and zig-zag spacers. It should be noted that the critical Reynolds number proposed by Alexiadis et al. [70] does not explicitly evaluate mass transfer. Rather, fluid mixing was used as a “proxy” for reduction in concentration polarisation, which should ultimately increase permeate flux. In keeping with the definition, the term “proxy” is used in this thesis when a variable is used as a substitute for another desired variable that cannot be measured directly.

### **2.4.3 Effect of slip velocity on hydrodynamics in obstruction-filled channel**

Although there have been numerous studies of different spacer geometries [35], only a handful of researchers have combined the use of spacers with other techniques to enhance mixing such as, electrokinetic methods [50]. Electro-osmotic flow disturbances studied in this thesis can be considered be equivalent to a slip velocity, as discussed in section 2.2.3. This section, therefore, provides a brief review of mixing enhancement that might be achieved with a combination of slip velocity and spacers.

Membrane spacers can be considered as analogous to a bluff body from the fluid mechanics perspective. It is therefore worthwhile to investigate the flow past a bluff body in the vicinity of a slip/stationary wall. Although there have been numerous studies of bluff body obstructions [108], only a handful of researchers have studied the effect of slip velocity on flow in the vicinity of a bluff body [108-111].

The flow past a bluff body in the presence of a stationary or slip wall affects the onset of turbulence and vortex shedding. Arnal et al. [108] found that the presence of a no-slip wall has a greater effect in stabilising the flow than a slip wall. They also concluded that the spatial boundary condition and the geometry of the bluff body have a stronger effect on vortex shedding and on the type of wake observed, than the effect of the bulk Reynolds number. These findings are shown schematically in Figure 2.15,

which depicts the flow profile past a square cross-section body under different conditions: (a) flow past a square body in free-stream, (b) flow past a square body on a stationary wall, (c) flow past a square body on a slip wall. For case (a) (Figure 2.15), vortex shedding occurs behind the body. For case (b), the presence of a no-slip wall stabilizes the flow when the square body is located at the wall [108]. For case (c), the presence of a slip wall results in periodic vortex shedding when the wall slips at the same speed as the free-stream velocity [108].

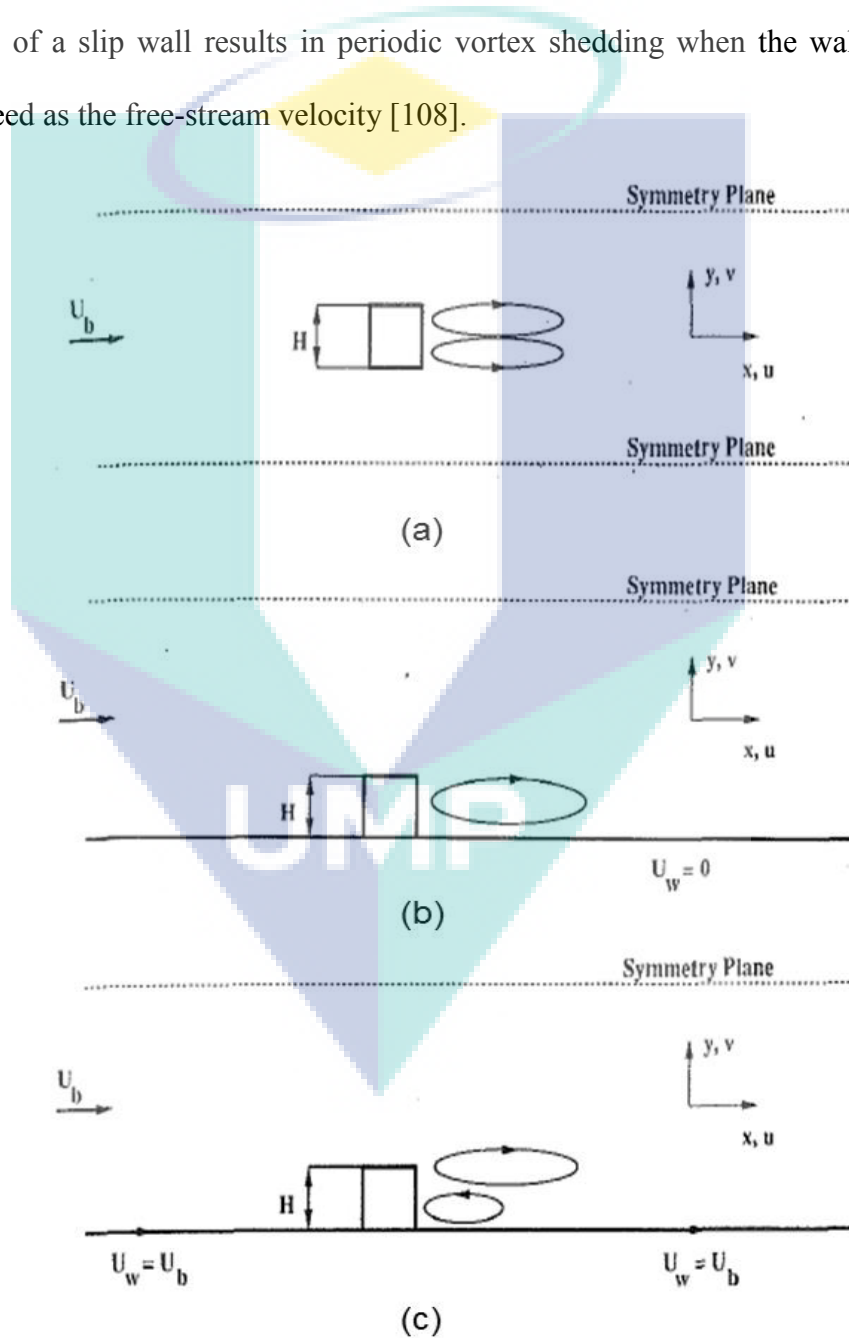


Figure 2.15: Schematic flow diagram showing (a) square in freestream (b) square on a stationary wall (c) square on a slip wall (as in Arnal et al. [108]).

The influence of a slip wall on vortex shedding when the bluff body (spacer) is away from the wall is important. Such a situation can occur in membrane channels when multi-layer spacer geometry designs are considered [38]. Kumarasamy and Barlow [109] studied the flow over a half cylinder close to a slip wall. They solved the flow by the Reynolds-averaged Navier-Stokes (RANS) method and compared the results to the stationary case. They found that the trajectory of the vortices behind the cylinders changes under the influence of a slip wall. A similar study was performed by Bhattacharyya and Maiti [110], who investigated the effect of the ratio of the gap height,  $G$  (the distance from the wall to the bottom side of the square body) to the square body diameter,  $D$  (Figure 2.16) on vortex shedding. They found that vortex shedding still occurs for bluff bodies under the influence of a slip velocity, even at the very small gap ratio of  $G/D = 0.1$  for Reynolds numbers up to 1000. In contrast, for the analogous case of flow past a bluff body with a stationary wall with the same gap ratio conditions, vortex shedding is suppressed.

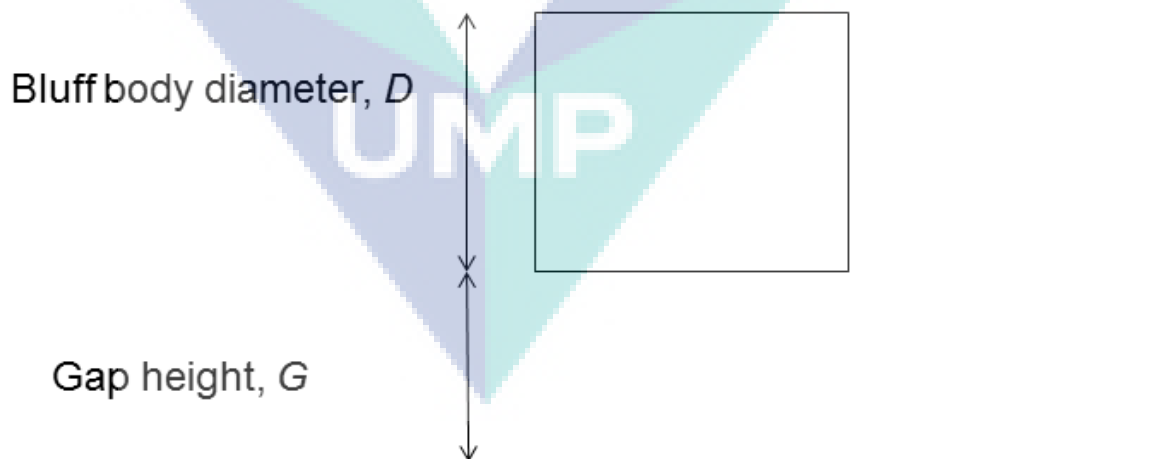


Figure 2.16: Schematic flow diagram showing ratio of gap height,  $G$  to bluff body diameter,  $D$ .

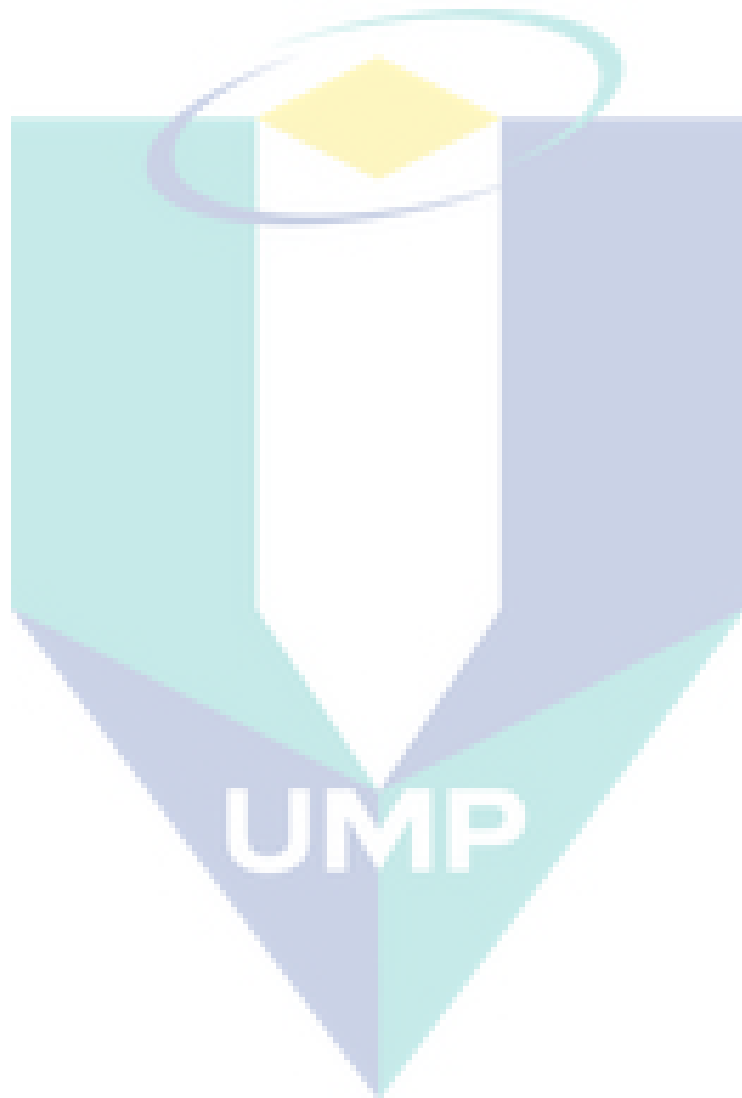
The effect of the variation in ratio of obstruction to channel height (gap ratio,  $G/D$ ) on the shedding Strouhal number ( $f_{vs}u_{\infty}/d_f$ ) when a slip velocity is applied was studied in detail by Huang and Sung [111]. Their study focused on the flow past a

circular cylinder close to a moving wall for a gap ratio  $G/D > 1$  and a free-stream cylinder Reynolds number ( $Re_{cyl} = \rho u_{\infty} d / \mu$ ) less than 600. They defined a critical gap ratio  $(G/D)_C$  as the value for which vortex shedding diminishes. As the gap distance between the cylinder and the wall decreases (at  $Re_{cyl} = 500$ ), the Strouhal number increases from about 0.225 to 0.24 due to the acceleration in the flow through the gap. However, if the gap height is further reduced, there is a rapid decrease in Strouhal number from about 0.24 to 0.19 due to the wall stabilising effects. When  $(G/D)$  is less than  $(G/D)_C$ , the Strouhal number decreases at a lower rate, because the pattern of the vortex shedding changes. They found that vortex shedding still occurs at a small gap ratio,  $G/D = 0.1$  for  $Re_{cyl} \geq 300$ , which is similar to the gap ratio value found by Bhattacharyya and Maiti [110] for  $Re_{cyl} \leq 1000$ . These results indicate that there is a gap height ratio that maximises the Strouhal number, i.e. the frequency of vortex shedding ( $f_{vs}$ ), when a slip velocity is applied. Although a higher vortex shedding frequency has the potential to increase mass transfer, the benefits of vortex shedding for improving mass transfer cannot be exploited if the vortex is being shed solely within the bulk flow region, rather than near the wall region.

#### 2.4.4 Gap analysis for flow analysis

Periodic unsteady flow, which is the focus of this thesis, has the potential to reduce concentration polarisation because it is related to boundary layer renewal. Slip velocity has the potential to induce vortex shedding. It may be possible that the interactions between electro-osmotic mixing and the mixing caused by feed channel spacers could cause greater mass transfer enhancement than spacers alone. This is because electro-osmotic perturbations have the potential to decrease the Reynolds number at which unsteady flow and vortex shedding occur. The studies from section 2.4.3 only focus on steady-state slip velocity and the effect of time-varying slip velocity

on recirculation in an obstruction-filled channel has not yet been explored. Therefore, this thesis focuses on the effect of time-varying slip velocity on mass transfer enhancement in spacer-filled channel.



## Chapter 3

### Methodology

This chapter presents the basic principles of Computational Fluid Dynamics (CFD), which is the main technique used for modelling the hydrodynamics and mass transfer in membrane processes in this thesis. In addition, the model geometry, boundary conditions and methodology for the analysis of results are presented in this chapter. The validation studies for hydrodynamics and/or mass transfer are shown in Chapters 5, 6 and 7 respectively.

#### 3.1 Basic principles of CFD

Viscous fluid flow is governed by the basic principles of mass continuity and momentum, as described by the Navier-Stokes equations (3.1) and (3.2):

$$\nabla \cdot \vec{v} = 0 \quad (3.1)$$

$$\rho \left( \frac{\partial \vec{v}}{\partial t} + \vec{v} \cdot \nabla \vec{v} \right) = -\nabla p + \mu \nabla^2 \vec{v} \quad (3.2)$$

The species transport is given by [105]:

$$\rho \left( \frac{\partial \omega_i}{\partial t} + \vec{v} \cdot \nabla \omega_i \right) = \nabla \cdot (\rho D_{im} \nabla \omega_i) + S_i \quad (3.3)$$

The complexity of most membrane systems usually means it is not possible to obtain an analytical solution to these equations. Therefore, in order to solve the partial differentiation governing the fluid and mass flow, an appropriate numerical differentiation scheme must be adopted. There are three types of commonly used methods: finite differentiation methods, finite element methods and finite volume methods (FVM). Detailed discussion of these methods can be found elsewhere [112].

The main characteristics of these methods are outlined in Table 3.1. Out of these methods, most commercial CFD codes (including ANSYS CFX) adopt a FVM method because it facilitates the use of unstructured meshes and is more flexible in its formulation than using either the finite difference or the finite element methods [113].

Table 3.1: Summary of finite discretisation methods [112].

Methods	Formulation	Mesh
Finite differentiation method	Easy to formulate	Accommodation of complex geometry is less straight forward
Finite element method	Requires mathematical rigor	Easy accommodation of complex geometries
Finite volume method	Can be formulated using either finite differentiation or element method	Easy accommodation of complex geometries

Several assumptions can be made to relax the CFD model for the systems modelled in this thesis [35]. Preliminary work [81, 114] has shown that density variation or gravity has little effect on the hydrodynamics and mass transfer solutions. Therefore, constant density and negligible effect of gravity can be assumed. Constant fluid properties (i.e. viscosity) and Newtonian fluid are assumed to further simplify the complex numerical problem. The flow is simulated as two-dimensional (2D) because of its lower computational demand [21, 22, 38, 81] than three-dimensional case.

In spiral wound modules (SWM), the flow is usually operated below the transition to the turbulent flow regime because of the high pumping cost [31]. Although unsteady flow is usually observed in SWM, the time variation of the velocity field is laminar periodic and is not turbulent. Therefore, it is possible to solve the partial differentiation equations in SWM using direct numerical simulation (DNS) without the need to use turbulence models, i.e. Reynolds Averaging Simulation (RANS) [113].

### 3.2 Model geometry

The key assumptions (boundary condition, geometry, electric field variation, mass transfer) used in subsequent chapters are summarized in Table 3.2.

Table 3.2: Type of models used in subsequent chapters.

Chapter	Include mass transfer and permeation	Geometry	Electric field variation
Chapter 4	No	Unobstructed channel	Uniform and non-uniform steady
Chapter 5	Yes	Unobstructed channel	Uniform and non-uniform steady
Chapter 6	Yes	Unobstructed channel	Uniform unsteady-state
Chapter 7	Yes	Spacer-filled channel	Uniform steady and unsteady-state

As shown in Figure 3.1, two types of electric field case studies are considered in this thesis, namely uniform and non-uniform electric fields. For the uniform electric field, the electrode geometry consists of the placement of two flat-plate electrodes at each end of the channel and perpendicular to the bulk flow direction, which leads to a spatially uniform slip velocity because the electric field is constant along the length of

the membrane wall. For the non-uniform electric field case, an electrical potential difference is assumed between an electrode pair. Specific cases for the location of the electrodes and the model parameters used for the non-uniform electric field simulation study are shown in Chapters 4, 5, 6 and 7 respectively.

Gauss's law is used to deduce the electric field equations. It can be expressed in its integral form as follows:

$$\oint_S \vec{E} \cdot d\vec{S} = \frac{q}{\epsilon} \quad (3.4)$$

For a cylindrical electrode of infinite length, the magnitude of the electric field is therefore given by:

$$|E| = \frac{\lambda}{2\pi\epsilon r_e} \quad (3.5)$$

The direction of the electric field is determined by the charge of the electrode. It is perpendicular to the electrode and points towards the electrode axis if its charge is negative, and away if its charge is positive. Assuming the charge of the electrodes is located on their surface, the potential difference between adjacent electrodes can be determined by the line integral of the electric field from the surface of one electrode to the surface of the other electrode along the plane of the electrode axes [115]:

$$V = \int_L \vec{E} \cdot d\vec{l} \quad (3.6)$$

An infinitely long cylindrical electrode pair of opposite but equal charge per unit length ( $\lambda$ ), placed parallel and below the membrane surface (as seen in Figure 3.1c or d), in the direction perpendicular to the bulk flow is modelled. The electric field equations for this configuration are obtained by summing the contribution of each electrode to the field using equation (3.5) in Cartesian coordinates. The charge per unit length is then obtained by solving equation (3.6) for the potential difference ( $V_{12}$ ). This yields the following mathematical formulation for the non-uniform electric field:

$$E_x = \frac{V_{12}}{2 \ln\left(\frac{x_{e2} - x_{e1} - r_e}{r_e}\right)} \left( \frac{x - x_{e1}}{(r_e + h_m + y)^2 + (x - x_{e1})^2} - \frac{x - x_{e2}}{(r_e + h_m + y)^2 + (x - x_{e2})^2} \right) \quad (3.7)$$

$$E_y = \frac{V_{12}(r_e + h_m + y)}{2 \ln\left(\frac{x_{e2} - x_{e1} - r_e}{r_e}\right)} \left( \frac{1}{(r_e + h_m + y)^2 + (x - x_{e1})^2} - \frac{1}{(r_e + h_m + y)^2 + (x - x_{e2})^2} \right) \quad (3.8)$$

where  $V_{12}$  is the potential difference between first and second electrode, and  $y$  is the distance normal to the membrane surface. It is important to note that, although for this case it is possible to obtain an analytical expression for the electric field, in the general case of arbitrary electrode geometry and position, the electric field must be obtained numerically [116].

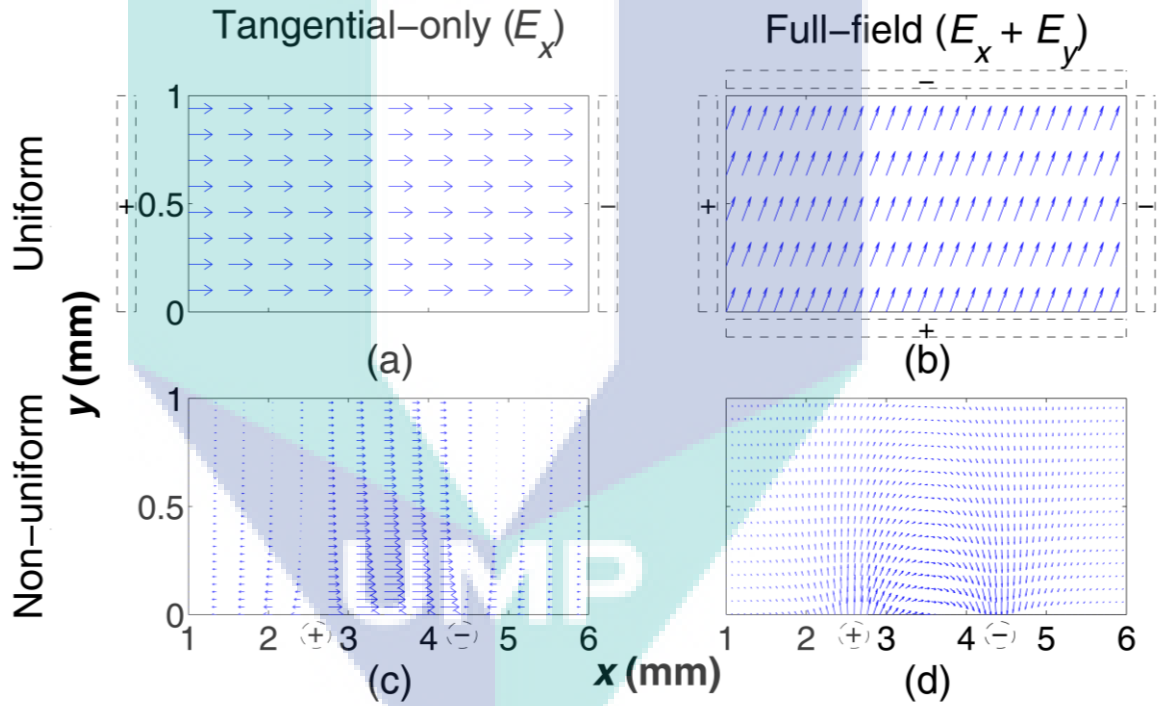


Figure 3.1: Vector plots of the electric fields used for the case studies. Electric fields (a) and (b) are uniform, whereas fields (c) and (d) are non-uniform. Electric fields (a) and (c) only include the field component tangential to the membrane surface ( $E_x$ ), whereas fields (b) and (d) include both the tangential and normal components ( $E_x + E_y$ ).

Figure 3.1 depicts the vector fields for the uniform and non-uniform electric field case studies. It shows two sub-cases for each electric field case, one that includes both the  $E_x$  and  $E_y$  components of the electric field (full-field), and one that only includes the  $E_x$  component (tangential-only). These sub-cases are used to assess the effect of the normal electric field component on the electro-osmotic destabilisation of the flow.

### 3.3 Boundary conditions

One of the main topics of discussion when modelling fluid dynamics using CFD is the choice of boundary conditions. It is important to use boundary conditions appropriately and also to understand their role in the CFD numerical algorithm. Proper selection of boundary condition can help simplify the flow problem and make the calculation of the numerical solution more efficient [35]. Among the most common boundary conditions used are inlet, outlet, opening, wall and symmetry conditions. In addition, in this thesis a permeable wall boundary condition is used for the membrane surface. In Chapters 5 and 6 only the bottom wall is permeable, whereas for Chapter 7 both top and bottom wall are permeable. The location of the boundary conditions and their mathematical description used in this thesis are summarised in Table 3.3.

Table 3.3: Boundary condition location and mathematical description.

Boundary location	Boundary condition	Mathematical description
Inlet	Specified velocity ( $\vec{v}_{in}$ ) and concentration ( $\omega_{i,in}$ ) profiles	$\vec{v} = \vec{v}_{in}(x, y, z)$ $\omega_i = \omega_{i,in}(x, y, z)$
Outlet	Specified average static pressure, constant concentration gradient	$\frac{1}{A_{out}} \int_{S_{out}} p dA = p_{out}$ $\frac{\partial \omega_i}{\partial L} = 0$

Opening	Specified average static pressure. Calculated concentration for flow out of domain, specified for flow into domain	$\frac{1}{A_{out}} \int_{S_{out}} p dA = p_{out}$ $(\omega_i)_{inflow} = \omega_{i,in}$
Impermeable wall	No-slip wall, no mass transfer	$\vec{v} = 0$ $\frac{\partial \omega_i}{\partial n} = 0$
Permeable wall (membrane)	Mass transfer	Equation 3.13
Slip wall (membrane)	Slip wall, no mass transfer	$u_s = -\frac{\varepsilon_e \zeta E_x}{\mu}$
Symmetry Plane	Velocity perpendicular to plane ( $v_n$ ) set to zero. Velocity and concentration gradients perpendicular to plane set to zero.	$v_n = 0$ $\frac{\partial \vec{v}}{\partial n} = 0$ $\frac{\partial \omega_i}{\partial n} = 0$

As shown in Table 3.3, a permeable wall condition is used to model the membrane surface in this thesis. However, two types of boundary conditions are commonly used for modelling mass transfer to/from a membrane surface, namely the dissolving or impermeable wall (IW) and the permeable wall (PW) models [35]. The IW model treats the wall as a non-slip boundary condition and specifies a constant wall concentration or diffusive mass flux [35]. This means that when using the IW model, there is only a weak coupling between concentration polarisation and the velocity profile in the feed channel due to variations in density or other fluid properties with concentration. If constant properties are assumed, then the concentration and velocity

profiles are uncoupled, and mass transfer does not affect the hydrodynamics in the boundary layer.

On the other hand, the PW model involves coupling between the concentration polarisation and permeate flux, and is more computationally intensive than the IW model [117]. Consequently, concentration polarisation and permeate flux are more difficult to analyse separately in this case. Nonetheless, by taking into account the suction of fluid normal to (i.e. towards) the membrane surface, the PW model gives a more realistic prediction of the effect of permeation on the hydrodynamics within the boundary layer [35]. In addition, the PW model also accounts for membrane properties (intrinsic permeability and rejection) in the permeate flux calculation. Therefore, the PW model is used in this thesis.

The local permeate mass flux ( $J$ ) in the membrane region is calculated using the approach of Kedem and Katchalsky [118], mathematically expressed as:

$$J = \rho L_p (\Delta p_{tm} - \sigma \Delta \pi_{tm}) \quad (3.9)$$

where  $L_p$  is the membrane permeability,  $\Delta p_{tm}$  is the transmembrane pressure,  $\sigma$  is the reflection coefficient and  $\Delta \pi_{tm}$  is the transmembrane osmotic pressure difference. The transmembrane osmotic pressure difference is approximated using a linear relationship between concentration and osmotic pressure [119]:

$$\Delta \pi_{tm} = \varphi (\omega_w - \omega_p) \quad (3.10)$$

where  $\varphi$  is the osmotic pressure coefficient,  $\omega_w$  is the solute mass fraction at the feed-side of the membrane wall, and  $\omega_p$  is the corresponding permeate solute mass fraction. The solute mass fraction on the permeate side can be related to the feed side mass fraction through the intrinsic rejection of the membrane:

$$\omega_p = (1 - R)\omega_w \quad (3.11)$$

where  $R$  is intrinsic rejection of the solute for the chosen membrane. Using equations (3.9) and (3.10), the velocity component normal to the wall can then be calculated as [35]:

$$v_w = -\frac{J}{\rho} = -L_p(\Delta p_{tm} - \sigma\phi R\omega_w) \quad (3.12)$$

The solute mass fraction at the membrane surface is determined by the CFD software, using the Neumann boundary condition for the solute mass balance at the membrane surface [35]:

$$\left(\frac{\partial\omega}{\partial y}\right)_w = -\frac{J}{\rho D}(\omega_w - \omega_p) \quad (3.13)$$

### 3.4 Methodology for analysis of results

The mass fraction boundary condition at the membrane stipulates an equilibrium between the net flux of solute to the membrane surface,  $J(\omega_w - \omega_p)$ , and the back-diffusion of solute away from the membrane towards the bulk,  $\rho D(\partial\omega/\partial y)_w$ . The level of mixing can be quantified through the mass transfer coefficient, which relates the back-diffusive flux to the concentration difference between the bulk and the membrane surface:

$$k_{mt} = \frac{-D}{\omega_w - \omega_{b0}} \left(\frac{\partial\omega}{\partial y}\right)_w \quad (3.14)$$

The bulk concentration of solute along the channel remains almost constant ( $\approx\omega_{b0}$ ) because the amount of fluid extracted is very small (at least 3 orders of magnitude lower) relative to the feed rate [35]. Moreover, the ratio of local wall concentration to inlet concentration is an accepted definition of concentration polarisation, as the inlet concentration is easier to measure [120]. The inlet concentration therefore is used in equation 3.14 instead of the local cross sectional average.

In addition, for a steady-state system the concentration boundary layer thickness can be defined as follows:

$$\delta = \frac{\omega_w - \omega_{b0}}{-\left(\frac{\partial \omega}{\partial y}\right)_w} \quad (3.15)$$

Combining equations (3.14) and (3.15), the mass transfer coefficient can also be interpreted as the ratio of diffusivity to boundary layer thickness:

$$k_{mt} = \frac{D}{\delta} \quad (3.16)$$

A number of dimensionless variables are used in this thesis. The channel height is used as the length scale for the dimensionless distances ( $X = x/h_{ch}$ ,  $Y = y/h_{ch}$  with  $X = 0$  at the membrane region inlet and  $Y = 0$  at the membrane surface), the frequency of slip velocity is used as time scale for dimensionless time ( $T = t f_s$ ) and the inlet bulk velocity ( $u_{b0}$ ) is used as the velocity scale for dimensionless velocities ( $U_p = u_p/u_{b0}$ ,  $U_{s,A} = u_{s,A}/u_{b0}$ ,  $U_s = u_s/u_{b0}$ ). The slip velocity frequency ( $f_s$ ) can be made dimensionless using the height of the channel and effective velocity as  $F_s = f_s h_{ch}/u_{eff}$ .

The feed mass fraction is used as the concentration scale. Then, the dimensionless concentration at the membrane surface can be interpreted as a concentration polarisation index (or modulus), defined as the ratio of membrane surface concentration to feed concentration [31]:

$$\gamma = \frac{\omega_w}{\omega_{b0}} \quad (3.17)$$

The scale for permeate flux is the flux through the membrane for a pure water system ( $\omega_{b0} = 0$ ), that is:

$$J_{pure} = \rho L_p \Delta p_{tm} \quad (3.18)$$

Using this scale, the dimensionless flux is defined as the ratio of local flux to pure water flux. Making use of equations (3.12) and (3.17), it can be seen that the

dimensionless local permeate flux along the membrane channel only depends on the local concentration polarisation modulus ( $\gamma$ ):

$$\frac{J}{J_{pure}} = 1 - \left( \frac{\sigma \phi R \omega_{b0}}{\Delta p_{tm}} \right) \gamma \quad (3.19)$$

Furthermore, combining equations (3.11), (3.13), (3.14) and (3.17), an equilibrium relationship between concentration polarisation, flux, rejection and the mass transfer coefficient is obtained:

$$\frac{\rho k_{mt}}{JR} \left( 1 - \frac{1}{\gamma} \right) = 1 \quad (3.20)$$

Thus, equation (3.20) shows that the primary effect of an increase in flux is an increase in the mass transfer coefficient and therefore, according to equation (3.16), a decrease in the boundary layer thickness. Similarly, an increase in mass transfer coefficient (increased mixing) leads to a higher flux and/or lower concentration polarisation, as shown by equation (3.20). However, as flux and concentration polarisation are also inter-related through equation (3.19), they form a complex system in which the hydrodynamics play a key role in determining their values at steady-state.

### 3.4.1 Steady EOF

The section discusses the methodology for analysis of results of the effect of steady EOF used in Chapters 5 and 7. The different measures used in this thesis for analysing membrane system membrane performance due to EOF are summarised in Table 3.4.

Pressure drop and energy consumption are quantified through the friction factor. The friction factor is calculated in terms of the wall stress and pressure drop [121]:

$$\bar{f} = \frac{\bar{\tau}}{\frac{1}{2} \rho u_b^2} = \frac{d_h \Delta P}{2 \rho u_b^2 L} \quad (3.21)$$

where

$$\tau = \frac{\mu}{L} \int_0^L \left( \frac{\partial u}{\partial y} \right)_w dx \quad (3.22)$$

The effect of electro-osmosis on the local Fanning friction factor ( $f$ ) is analysed through the relative change between the cases with electro-osmosis ( $EO$ ) and the cases without electro-osmosis (no-slip,  $NS$ ), at the same Reynolds number. The change is calculated as follows:

$$\Delta f = \frac{f_{EO} - f_{NS}}{f_{NS}} \quad (3.23)$$

The same analysis is carried out for the effect on the global (area-averaged) friction factor ( $\bar{f}$ ), which is defined as the area-averaged Fanning friction factor over the membrane section under consideration. The relative change in global friction factor is therefore expressed as:

$$\Delta \bar{f} = \frac{\bar{f}_{EO} - \bar{f}_{NS}}{\bar{f}_{NS}} \quad (3.24)$$

where  $\bar{f}_{EO}$  refers to the value with electro-osmosis and  $\bar{f}_{NS}$  to the value without electro-osmosis.

To quantify membrane performance, the area-averaged permeate flux is used:

$$\frac{\bar{J}}{J_{pure}} = 1 - \left( \frac{\sigma \phi R \omega_{b0}}{\Delta p_{tm}} \right) \bar{\gamma} \quad (3.25)$$

The effectiveness of electro-osmosis for enhancing mass transfer and improving permeate flux is quantified by:

$$\Phi = 1 - \frac{\gamma_{EO}}{\gamma_{NS}} \quad (3.26)$$

where  $\Phi$  is the relative change in the concentration polarisation index. Substituting equation (3.19) into equation (3.26) yields the following relationship between  $\Phi$ , the pure water flux ( $J_{pure}$ ), the flux under no-slip ( $J_{NS}$ ) and the electro-osmotic enhanced flux ( $J_{EO}$ ):

$$\Phi = \frac{J_{EO} - J_{NS}}{J_{pure} - J_{NS}} \quad (3.27)$$

From equation (3.27),  $\Phi$  can be interpreted as a measure of how close the enhanced flux,  $J_{EO}$ , is to the maximum possible flux,  $J_{pure}$ . Hence,  $\Phi$  can be thought of as a “mass transfer enhancement” factor. The value of  $\Phi$  is zero when  $\gamma_{EO} = \gamma_{NS}$  and  $J_{EO} = J_{NS}$  (no improvement in permeate flux is observed). A negative value of  $\Phi$  represents the case where electro-osmosis causes a decline in mass transfer, thus  $\gamma_{EO} > \gamma_{NS}$  and  $J_{EO} < J_{NS}$ . The theoretical limit to the maximum value of  $\Phi$  can be obtained from equation (3.26) when the system is fully mixed, so that the wall concentration is equal to the feed concentration ( $\omega_w = \omega_{b0}$ ), leading to the absence of concentration polarisation ( $\gamma_{EO} = 1$ ) and:

$$\Phi_{max} = 1 - \frac{1}{\gamma_{NS}} \quad (3.28)$$

The value of  $\Phi_{max}$  is larger for larger values of  $\gamma_{NS}$ , and is reduced to zero when the no-slip system is fully mixed ( $\gamma_{NS} = 1$ ). This suggests that electro-osmosis has more potential to enhance flux for cases that are less mixed and concentration is more polarised. Moreover,  $\Phi_{max}$  quantifies how far the system is from the “fully mixed” state, so  $\Phi_{max}$  can also be interpreted as the mixing potential.

The global mass transfer enhancement ( $\tilde{\Phi}$ ) can be expressed in terms of the area-averaged fluxes or concentration polarisation:

$$\tilde{\Phi} = 1 - \frac{\bar{\gamma}_{EO}}{\bar{\gamma}_{NS}} = \frac{\bar{J}_{EO} - \bar{J}_{NS}}{\bar{J}_{pure} - \bar{J}_{NS}} \quad (3.29)$$

### 3.4.2 Unsteady EOF

This section discusses the methodology for analysis of results of the effect of unsteady EOF used in Chapters 6 and 7. For all transient simulations, the initial state ( $t = 0$ ) is a steady-state solution under similar conditions, but with a steady or absent perturbation. The local and global variables under consideration are recorded once the time-averaged variables have converged. Three characteristics of spatially local

variables are measured: time-averaged value ( $\bar{\phi}$ ), maximum value ( $\hat{\phi}$ ) and oscillation amplitude ( $\phi_A$ ). Further, a global variable ( $\bar{\phi}$ ) is defined as the area average of the local variable, given by:

$$\bar{\phi} = \frac{1}{L} \int_L \phi dx \quad (3.30)$$

In terms of membrane performance, the time-averaged permeate flux is used such that:

$$\frac{\bar{j}}{j_{pure}} = 1 - \left( \frac{\sigma \phi R \omega_{b0}}{\Delta p_{tm}} \right) \bar{\gamma} \quad (3.31)$$

During pulsatile flow [122-124], a high-amplitude shear may lead to a reduced fouling layer. Maximum wall shear is therefore used as proxy measure for long term fouling reduction [125], given by:

$$\bar{\tau} = \mu \frac{d\bar{u}}{dy} \quad (3.32)$$

The effect of electro-osmosis on the maximum shear stress ( $\bar{\tau}$ ) can be analysed through the relative change in maximum friction factor between the cases with electro-osmosis and the cases without electro-osmosis (no-slip,  $NS$ ). This is because as can be seen in equations (3.21-3.22) that friction factor is proportional to shear stress and shear rate under a constant viscosity and bulk flow rate. This change is calculated as follows:

$$\Delta \bar{f} = \frac{\bar{f}_S - \bar{f}_{NS}}{\bar{f}_{NS}} \quad (3.33)$$

Time-averaged pressured drop is used as a measure for energy consumption in this thesis. Equation (3.21) can be rearranged to give a time-averaged pressure drop:

$$\Delta \bar{P} = \frac{4\bar{\tau}L}{d_h} \quad (3.34)$$

The effectiveness of electro-osmosis for enhancing time-averaged mass transfer and improving permeate flux can be quantified by [126]:

$$\widetilde{\Phi} = 1 - \frac{\bar{\gamma}_{EO}}{\bar{\gamma}_{NS}} \quad (3.35)$$

where

$$\bar{\gamma} = \frac{\bar{\omega}_w}{\omega_{bo}} \quad (3.36)$$

In turbulent flow, the flow is unsteady and the unsteadiness can be quantified by turbulent kinetic energy ( $k$ ). Turbulent kinetic energy is used to characterise the kinetic energy of eddies in turbulent flow and is defined as the mean kinetic energy per unit mass of the transient components. The turbulent kinetic energy is also a measure of the amplitude of the output and can be used to identify the resonant frequency at which the amplitude ratio is at a relative maximum. Turbulent kinetic energy can be characterised by the root mean square (RMS) velocity fluctuation.

Unsteady (transient) flow can also develop during laminar flow in an obstructed membrane channel. However, for transient flow, there are no variables available in the literature to conveniently and simply characterise the kinetic energy related to eddies. Therefore, in this thesis, a variable equivalent to the turbulent kinetic energy is used as a proxy indicator for mixing and mass transfer enhancement even though the flow is not technically turbulent. For clarity, this variable is referred to as “turbulent kinetic energy equivalent” in this thesis, because it is a widely recognised name in the literature [113]. The validity of this approach is discussed further in Chapter 7.

The turbulent kinetic energy equivalent in the  $y$ -direction ( $k_y$ ) is used in this thesis due to the significance of  $v$ -velocity in terms of vortex shedding and mass transfer enhancement. It is evaluated as follows:

$$k_y = \frac{1}{2} \left[ \left( \frac{1}{t_2 - t_1} \right) \int_{t_1}^{t_2} (v')^2 dt \right] \quad (3.37)$$

where

$$v' = v - \bar{v} \quad (3.38)$$

and  $\bar{v}$  is the time-averaged  $v$ -velocity at the same location as  $v'$  and  $v$ .

The turbulent kinetic energy equivalent ( $k_y$ ) can be made dimensionless using the hydraulic diameter ( $d_h$ ) and kinematic viscosity ( $\nu$ ) as

$$K_y = k_y d_h^2 / \nu^2 \quad (3.39)$$

In terms of energy losses, comparison at the same pumping power under different flow conditions can be made using Power number, given by [35].

$$Pn = Re^3 \bar{f} \quad (3.40)$$

The recovery rate is defined as the ratio of the product water flow rate ( $Q_p = L_m J w_{ch}$ ) to feed water flow rate ( $Q_{in} = \rho u_{avg} h_{ch} w_{ch}$ ) [31]:

$$Recovery\ rate = \frac{L_m \bar{J}}{\rho u_{avg} h_{ch}} \quad (3.41)$$

Table 3.4: Measures for membrane system performance due to EOF.

Chapter	Effect	Symbol	Global/Local	Equation
5	Change in friction factor	$\Delta f$	Local	3.23
		$\Delta \bar{f}$	Global	3.24
	Change in concentration polarisation index	$\Phi$	Local	3.26
		$\bar{\Phi}$	Global	3.29
	Flux	$J/J_{pure}$	Local	3.19
		$\bar{J}/J_{pure}$	Global	3.25
6	Change in maximum friction factor (as shear stress)	$\Delta \bar{f}$	Global	3.33
	Time-averaged concentration	$\bar{y}$	Global	3.36

	polarisation			
	Time-averaged flux	$\bar{J}/J_{pure}$	Global	3.31
	Time-averaged pressure drop	$\Delta\bar{P}$	Global	3.34
7	Change in concentration	$\Phi$	Local	3.26
	polarisation index	$\bar{\tau}$ $\bar{\Phi}$	Global	3.35
	Time-averaged flux	$\bar{J}/J_{pure}$	Global	3.31
	Maximum wall stress	$\bar{\tau}$	Global	3.32
	Turbulent kinetic energy equivalent	$K_y$	Global	3.39
	Pumping power	$Pn$	Global	3.40
	Recovery rate	-	Global	3.41

### 3.5 Verification and Validation

Oberkampf and Trucano [127] explain that verification and validation is of paramount importance to ensure accuracy and reliability in computational fluid dynamics (CFD) simulation. Verification is performed by comparing the computational solution against analytical and/or proven numerical solutions while validation is performed by comparing the computational solution against experimental data. Common sources of error encountered in CFD are: inadequate spatial discretisation convergence, inadequate temporal discretisation convergence, inadequate convergence of the iterative procedure, computer round-off and computer programming errors [127].

Inadequate spatial discretisation convergence errors can be mitigated by including additional grid points. Inadequate temporal discretisation convergence can be minimised by decreasing the time step size in unsteady simulations. Inadequate convergence of the iterative procedure can be reduced by minimising the iteration residual. Computer round-off error can be minimised by implementing double precision for real numbers [35].

The Grid Convergence Index (GCI) is a useful tool to assess the errors associated with the grid [128]. The refinement ratio,  $\mathbb{R}$  and relative error,  $e_{GCI}$  can be expressed as following [35]:

$$\mathbb{R} = \frac{N_{fine}}{N_{coarse}} \quad (3.42)$$

$$e_{GCI} = \frac{F_{coarse} - F_{fine}}{F_{fine}} \quad (3.43)$$

where  $N_{fine}$  is the number of elements for fine grid,  $N_{coarse}$  is the number of elements for coarse grid,  $F_{coarse}$  is the is the integral function for course grid and  $F_{fine}$  is the integral function for fine grid.

The GCI equations for fine and coarse grids then can be expressed as follows [35]:

$$GCI_{fine} = \frac{3|e_{GCI}|}{\mathbb{R}^{\eta-1}} \quad (3.44)$$

$$GCI_{coarse} = \frac{3|e_{GCI}|\mathbb{R}^{\eta}}{\mathbb{R}^{\eta-1}} \quad (3.45)$$

where  $\eta$  is the number of dimensions used. An acceptable error value for  $GCI_{fine}$  lies within 5 to 10 % [35]. The validation steps in this thesis are performed by comparing the computational solution in the 2D model against available analytical solutions.

## Chapter 4

# Approximation for modelling electro-osmotic mixing in the boundary layer of membrane systems

### 4.1 Introduction

One of the major limitations for the numerical simulation of electro-osmosis is the high computational effort required to solve the Poisson and Navier–Stokes equations at the scale of the Debye length ( $\sim 10^{-9}$  m) when considering the dimensions of a typical membrane channel ( $\sim 10^{-3}$  m). Large velocity gradients near the wall require a very fine mesh in that region in order to capture the velocity profiles [63, 64]. One possible way to address the large computational requirements of numerical simulation is the adoption of the Helmholtz–Smoluchowski (HS) velocity equation, which is an artificial slip velocity implemented on a charged surface to simulate the effect of electro-osmosis on the velocity profile in a channel [19].

In this chapter, a two-dimensional (2D) electric field is assumed to generate flow perturbations due to electro-osmotic effects, with the potential to enhance mixing within the concentration polarisation layer and lift the solute concentration from the membrane surface. Given that the HS approximation only takes into account the component of the electric field that is tangential to the charged membrane surface, it is unclear whether this approximation is appropriate for modelling electro-osmotic effects in membrane channels caused by 2D electrical fields. Moreover, the HS approximation implies that pressure gradients are negligible [19]. This means that the HS approximation shows no dependence on cross-flow velocity other than the flow velocity induced by the electric

field. The applicability of the HS approximation for a system with cross-flow velocity is therefore unclear.

This chapter compares the results from steady-state numerical simulations using the Helmholtz–Smoluchowski (HS) approximation of electro-osmosis against a more rigorous charge density (CD) solution in order to determine the reliability and accuracy of the HS approximation in membrane channels. The effect of cross-flow velocity on the accuracy and reliability of the HS approximation is therefore investigated. The effect of cross-flow velocity on the perturbation velocity flow regime and mixing are also assessed.

#### 4.2 Charged density (CD) approach vs Helmholtz-Smoluchowski (HS) approach

Table 4.1: Summary of the differences between the CD approach and the HS approach.

Description	CD solution (ideal electro-osmosis)	HS approximation (linear electro-osmosis)	Significance and source of difference
Electric double layer	Resolves the velocity distribution within the EDL [64].	Assumes the EDL length scale is much smaller than the channel length scale. Applies a “slip velocity” at the outer edge of the EDL [19].	CD solution requires higher computational effort. HS approximation, is simple and easily incorporated into CFD code [19].
Charge distribution	The charge distribution near the wall is governed by zeta potential and external electric field, and assumes a Boltzmann distribution [63].	Is not calculated directly. Slip velocity equation assumes a 1D integration of charge distribution.	Because HS approximation assumes EDL is much smaller than the channel, if this is not correct then slip velocity is applied at an incorrect location.
External electric field	Incorporated in the momentum transport equation as a force acting on the fluid due to charge separation.	Only tangential component included in slip velocity equation. Normal component is neglected.	It is unclear whether the normal component has a significant effect on the electro-osmotic effect for typical membrane channels.

Table 4.1 summarises the differences between the CD solution (ideal electro-osmosis) and the HS approximation (linear electro-osmosis). Given the relatively small size of the EDL compared to a typical membrane channel, the HS slip velocity in Table 3.3 is applied at the wall surface ( $y = 0$ ). However, because the wall surface is modelled as non-slip (zero velocity) in the CD approach [19], this means that there cannot be a perfect agreement between the two approaches for modelling electro-osmosis. This chapter therefore investigates the suitability and applicability of the HS approach for simulating electro-osmotic effects on the velocity profile in membrane channels.

### **4.3 Problem descriptions, assumptions and methods**

The commercial CFD code ANSYS CFX-13.0 is used to solve the continuity and momentum equations [105] in a membrane channel. For the CD solution, the charge distribution in the channel is governed by the wall zeta potential and the external electric field. If the Debye length is sufficiently small and the charge at the walls is not large, the charge distribution is mostly determined by the zeta potential rather than by the external electric field [63]. The charge distribution adjacent to the channel wall therefore can be calculated independently of the external electric field.

The CD solution is used as a benchmark for validation of the HS approximation. For the sake of simplicity, the zeta potential is assumed to be constant along the membrane surface. Hence, the one-dimensional (1D) potential due to the wall charge can be used. The charge distribution will not be influenced by fluid flow if the fluid velocity is small or the inertial terms in the momentum equation are not dominant [63]. The validation of this latter assumption is discussed in section 4.4.3.1.

Two types of electric field case studies are considered in this chapter, namely uniform and non-uniform electric fields. For uniform electric field simulations, periodic momentum boundary conditions are used in ANSYS CFX to model the repeating flow

pattern over the fluid domain length [35]. For the case of a non-uniform electric field, the electric field is assumed to be generated by a pair of electrodes placed perpendicular to the bulk flow and parallel to the membrane surface, on the permeate side. The model geometry is described in section 4.3.1.

In this chapter, the difference between the calculated local velocity field and the velocity field for fully developed flow without electro-osmosis at the same Reynolds number is referred to as the “perturbation velocity” due to the electro-osmotic effect ( $\vec{v}_p = \vec{v} - \vec{v}_f$ ). Therefore, the perturbation velocity is an indication of the changes in the flow induced by the electro-osmotic effect. It is expected that flow perturbations due to electro-osmotic effect will disturb the developing boundary layer, thus leading to an increase in the mass transfer coefficient, a reduction in concentration polarisation and ultimately higher permeate flux than in the case without electro-osmotic perturbations. However, calculation of mass transfer effects and flux enhancement are not considered in this chapter. Rather, this chapter seeks to establish the applicability of the HS approximation as an essential first step for establishing a suitable CFD model of flow and mass transfer in a membrane system with electro-osmotic flows.

The  $x$ -component perturbation velocity ( $u_p$ ) is calculated as the difference between the local velocity in the  $x$  direction ( $u$ ) and the fully developed velocity ( $u_f$ ).

$$u_p = u - u_f \quad (4.1)$$

where

$$u_f = 6u_{avg} \frac{y}{h_{ch}} \left(1 - \frac{y}{h_{ch}}\right) \quad (4.2)$$

The  $y$ -component of the perturbation velocity ( $v_p$ ) is equal to the calculated local velocity in the  $y$ -direction ( $v$ ) because the fully-developed velocity profile is parallel to the  $x$ -axis. In this chapter, the relationships between cross-flow velocity, perturbation velocity and mixing index are assessed.

### 4.3.1 Model description

For the uniform electric field case, the channel length and height used are 7 mm and 1 mm respectively. The terms  $E_x$  and  $E_y$  used in this chapter refer respectively to the electric field components tangential and normal to the membrane surface. Constant values of 10 000 V/m for  $E_x$  and  $E_y$  and a range of Reynolds number of 100–2 000 are used for the uniform electric field case study. The Reynolds number upper limit of 2 000 is chosen in order to avoid any unsteady effects related to the transition into turbulent flow [35].

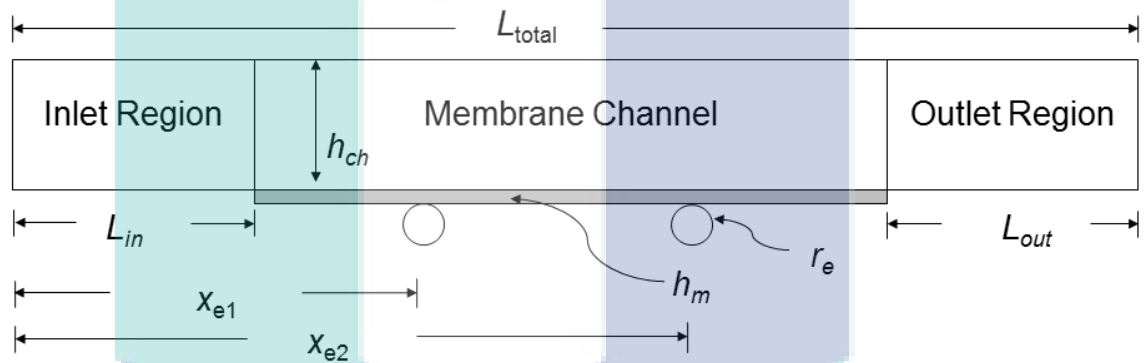


Figure 4.1: Non-uniform electric field model geometry.

For the non-uniform electric field case, an electrical potential difference of 1 000 V is assumed between an electrode pair. A range of Reynolds numbers from 0 to 2 000 are used for the non-uniform electric field case study. The location of the electrodes and the model geometry used are shown in Figure 4.1. Entrance and exit regions with a length of 1 mm are included at each end of the channel in order to ensure that the inlet and outlet boundary conditions do not affect the flow solution in the membrane section. The parameters used for the non-uniform electric field simulation study are shown in Table 4.2.

Table 4.2: Parameters used for non-uniform electric field case study.

Parameter	Value
$h_{ch}$	1 mm
$h_m$	0.25 mm
$L_{in}$	1 mm
$L_{out}$	1 mm
$L_{total}$	7 mm
$x_{e1}$	2.65 mm
$x_{e2}$	4.35 mm
$r_e$	0.1 mm
$V_{12}$	1 000 V

Table 4.3: Summary of equations and assumptions for the different simulation approaches.

Assumption	CD approach	HS approach
<b>Momentum equation</b>	$\rho \left( \frac{\partial \vec{v}}{\partial t} + \vec{v} \cdot \nabla \vec{v} \right) = -\nabla P + \mu \nabla^2 \vec{v} + \rho_e \vec{E}$	$\rho \left( \frac{\partial \vec{v}}{\partial t} + \vec{v} \cdot \nabla \vec{v} \right) = -\nabla P + \mu \nabla^2 \vec{v}$
<b>Charge density</b>	$\rho_e = -2zen_o \sinh \left( \frac{ze\phi}{k_B T} \right)$	N/A
<b>Internal potential</b>	$\phi = \zeta \exp \left( \frac{-y}{\lambda_D} \right)$	N/A
<b>Debye length</b>	$\lambda_D = \sqrt{\frac{\epsilon k_B T}{2e^2 n_o}}$	N/A
<b>Boundary condition at membrane wall surface</b>	$u = 0$ $v = 0$	$u_s = -\frac{\epsilon \zeta E_x}{\mu}$ $v = 0$
<b>Uniform electric field</b>	$E_x = 10\,000$ V/m $E_y = 10\,000$ V/m (full-field only)	$E_x = 10\,000$ V/m
<b>Non-uniform electric field</b>	$E_x$ given by equation (3.7) $E_y$ given by equation (3.8) (full-field only)	$E_x$ given by equation (3.7)

The set of equations and assumptions used for the CD solution and HS approximation approaches are summarised in Table 4.3.

#### 4.4 Results and discussion

##### 4.4.1 Mesh independence study

In order to validate and verify the CFD hydrodynamic results, global friction factor ( $f_{glob}$ ) and perturbation velocity errors are calculated for a Reynolds number ( $Re$ ) of 280. The global friction factor [105] is a function of pressure drop across the channel.

$$f_{glob} = \frac{d_h}{2\rho u_{avg}^2} \frac{\Delta P}{L} \quad (4.3)$$

where  $u_{avg}$  is the inlet velocity,  $d_h$  is the hydraulic diameter,  $\Delta P$  is the inlet-outlet pressure difference and  $L$  is the channel length.

The  $u_p$  area-weighted error ( $u_{p,error}$ ) is used for determining grid independence and is defined by equation (4.4):

$$u_{p,error} = \frac{\int_0^{h_{ch}} (u_{p2} - u_{p1})^2 dy}{\int_0^{h_{ch}} (u_{p2} - \bar{u}_{p2})^2 dy} \quad (4.4)$$

where  $u_{p1}$  is the  $x$ -component perturbation velocity of the system being tested,  $u_{p2}$  is the  $x$ -component perturbation velocity benchmark used for validation of the system being tested and  $\bar{u}_{p2}$  is given by:

$$\bar{u}_{p2} = \frac{1}{h_{ch}} \int_0^{h_{ch}} u_{p2} dy \quad (4.5)$$

Under the conditions of a non-uniform electric field, it was found that meshes with just over 0.3 million elements had a Grid Convergence Index (GCI) [35] for the fine mesh below 1 % for friction factor and below 0.5 % for  $u_{p,error}$ .

##### 4.4.2 Uniform electric field

Analytical solutions for the unidirectional (fully-developed) velocity profile ( $u_f$ ) can be obtained for the cases with and without slip velocity. The difference between these profiles yields the “fully-developed” perturbation velocity profile:

$$u_{pf} = \left(1 - \frac{y}{h_{ch}}\right) u_s \left(1 - \frac{3y}{h_{ch}}\right) \quad (4.6)$$

The CFD simulation results for the HS approximation can be validated against equation (4.6) by means of the  $u_{p,error}$  calculated using equation (4.4). For the range of Reynolds numbers simulated, the maximum  $u_{p,error}$  between the numerical data and the analytical solution is below 0.02 %.

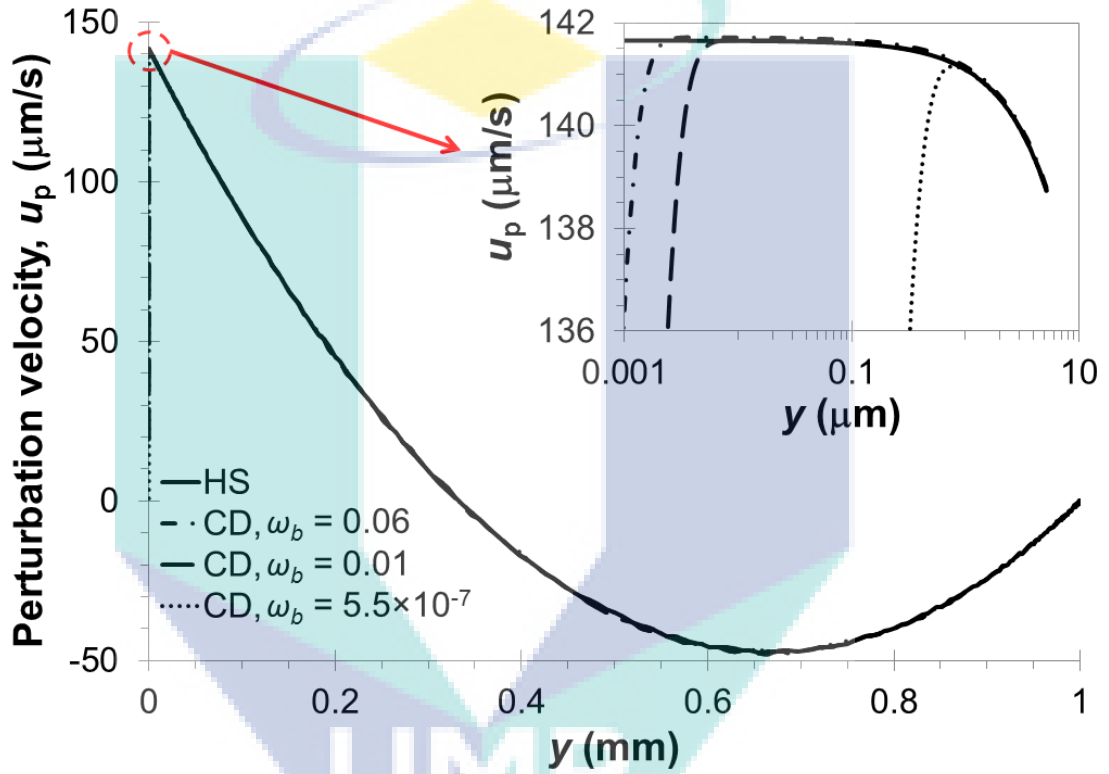


Figure 4.2: Comparison of  $u_p$  profile of HS approximation and the CD solution at different bulk solute mass fraction.

In order to evaluate the effect of solute concentration on the perturbation velocity profile ( $u_p$ ), Figure 4.2 compares  $u_p$  profiles at different bulk solute concentrations ( $\omega_b$ ) for the full-field CD solution against those obtained using the HS approximation for a uniform electric field. A range of bulk salt fractions from  $5.5 \times 10^{-7}$  (corresponding to a Debye length of 100 nm) to 0.06 are considered. It should be noted that for the range of Reynolds numbers analysed in this study, the perturbation velocity profile is independent of the Reynolds number. From Figure 4.2, it can be seen that the

agreement between the CD solution and the HS approximation improves as the solute concentration increases. This is because the increase in solute concentration results in a thinner Debye layer.

Figure 4.3 depicts the maximum  $u_{p,error}$  for the range of Reynolds numbers simulated (100 to 2 000). The error is calculated between the HS approximation and the CD solution using equation (4.4) at different solute concentration values. From Figure 4.3, it can be seen that the error for the HS approximation against the CD solution with a tangential-only electric field ( $E_x$ ) is very similar to the error against the full electric field (including both  $E_x$  and  $E_y$ ). This suggests that the effect of the electric field component normal to the membrane surface ( $E_y$ ) is negligible for the case of a uniform electric field. In addition, the value of  $u_{p,error}$  between the CD solution and the HS approximation is below 0.001 % for a bulk solute mass fraction of 0.001 or higher. Given that sea water salt concentration is around 3 % while brackish water salinity is of the order of 0.1 % [129], this suggests that the HS approximation is suitable for modelling electro-osmotic effects in RO systems for both sea water and brackish water under the conditions of a uniform electric field and cross-flow. In addition, this also suggests that the CD solution is independent of the bulk solute concentration when a high bulk solute concentration ( $\geq 0.001$ ) is used.

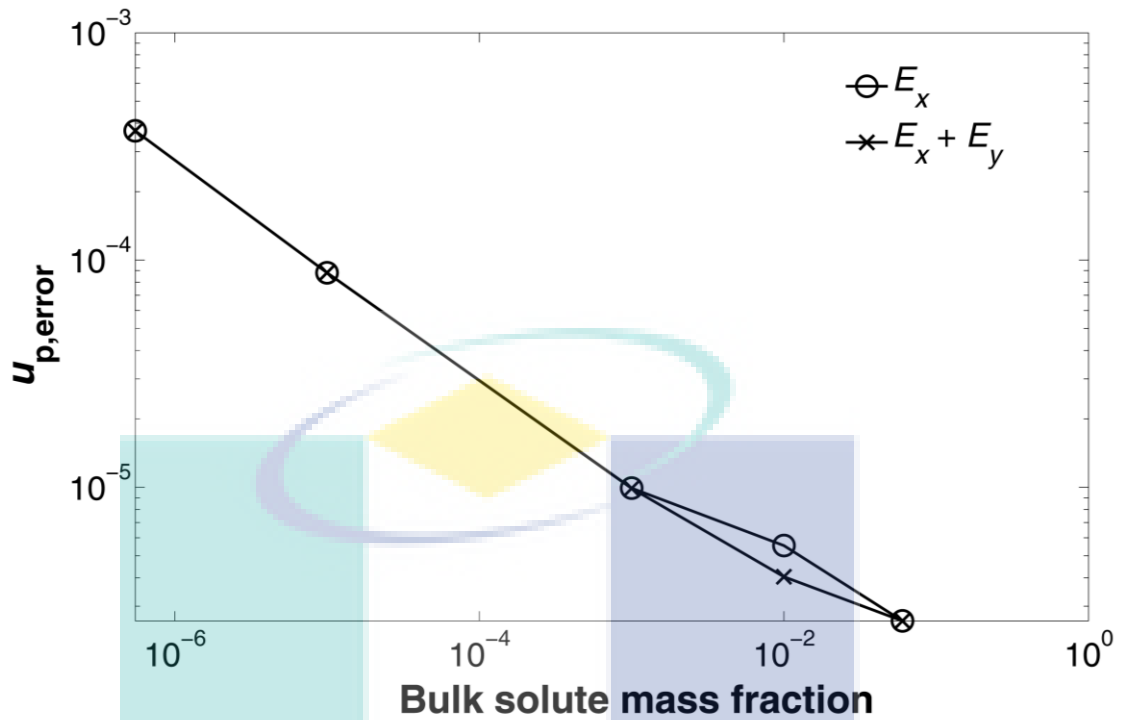


Figure 4.3: Comparison of  $u_{p,error}$  between the HS approximation and the CD solution at different bulk solute mass fraction values.

### 4.4.3 Non-uniform electric field

#### 4.4.3.1 Relative magnitude of convective and viscous terms

In section 4.3, it was assumed that the contributions to the electric potential due to the surface potential (zeta potential,  $\zeta$ ) and the potential due to the external electric field can be decoupled in the CD solution if the convective term in the momentum equation is not dominant. This implies that the charge density ( $\rho_e$ ) profile given by equation (2.3) is not affected by the electric potential due to the external electric field ( $\psi$ ). The reason for this decoupling is related to the effect of the external field on the fluid flow. The CD solution assumes an electric potential profile given by equation (2.4), in which the charge density is balanced by the internal electric field ( $-\nabla\phi$ ). The  $\rho_e$  profile may be altered due to charge convection, a phenomenon related to fluid velocity within the double layer and controlled by the external electric field. If this velocity is small, such that the convective term in the momentum equation does not

dominate, it is expected that charge redistribution due to the external electric field will be minimal and its effect on the charge density and the internal potential can be safely neglected [130]. This section investigates the validity of this assumption for the CD solution.

In order to investigate the relative importance of the convective term, the magnitudes of the convective terms are compared to those of the viscous terms in the momentum equation. The convective terms are given by equations (4.7) and (4.8) while the viscous terms are given by equations (4.9) and (4.10) respectively.

$$C_1 = \rho \left( u \frac{\partial u}{\partial x} + v \frac{\partial u}{\partial y} \right) \quad (4.7)$$

$$C_2 = \rho \left( u \frac{\partial v}{\partial x} + v \frac{\partial v}{\partial y} \right) \quad (4.8)$$

$$D_1 = \mu \left( \frac{\partial^2 u}{\partial x^2} + \frac{\partial^2 u}{\partial y^2} \right) \quad (4.9)$$

$$D_2 = \mu \left( \frac{\partial^2 v}{\partial x^2} + \frac{\partial^2 v}{\partial y^2} \right) \quad (4.10)$$

A bulk solute mass fraction of 0.06 and a range of Reynolds numbers from 100 to 2 000 are used in these comparisons. The full-field non-uniform electric field is used (see Figure 3.1), given by equations (3.7) and (3.8), under the conditions summarised in Table 4.2. The associated Debye length is  $3 \times 10^{-10}$  m for a solute mass fraction of 0.06. The magnitudes of the convective and viscous terms are taken at a distance of one Debye length from the membrane surface, as the net charge distribution is usually governed by the EDL [64].

An *a priori* validation of the insignificance of the inertia term is performed at the Debye length location, assuming  $u \approx u_s$  and  $v \approx -\lambda_D \frac{\partial u_s}{\partial x}$ . This analysis reveals that for  $Re = 2\,000$ , the  $D_1/C_1$  ratio ranges from 200 to over  $10^{16}$ , and the  $D_2/C_2$  ratio ranges from 150 to over  $10^9$ . Moreover, the maximum value of  $u_s$  is approximately 0.5 % of the

bulk flow velocity. This data supports the assumption that the viscous term, and not the convective term, is dominant within the double layer.

In terms of *a posteriori* validation, Figure 4.4 depicts simulation results for the magnitude of  $D_1/C_1$  and  $D_2/C_2$  within the EDL at different Reynolds number. The results show that the minimum and maximum values for the ratio of  $D_1/C_1$  are  $1 \times 10^8$  and  $2 \times 10^{14}$  respectively whereas for the ratio of  $D_2/C_2$  these values are  $1 \times 10^8$  and  $5 \times 10^{16}$  respectively. Given that the viscous terms are over seven orders of magnitude larger than the convective terms, this suggests that the convective terms in the momentum equation are negligible within the EDL. Therefore, the assumption of internal and external potential decoupling is suitable for these cases, both from an *a priori* and an *a posteriori* perspective.

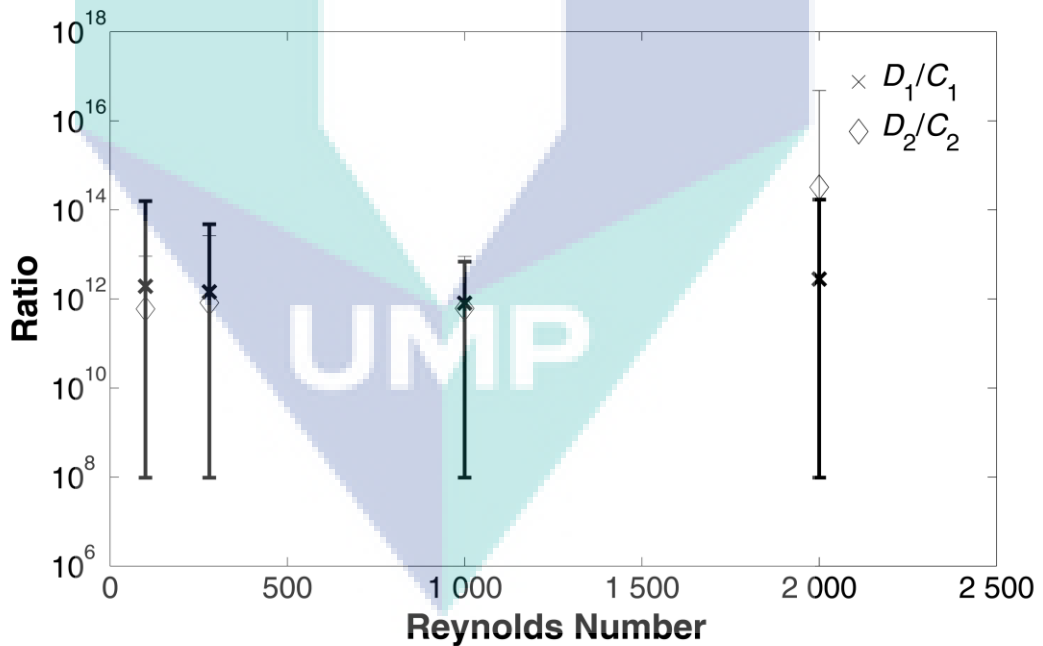


Figure 4.4: Variation of the ratios of  $D_1/C_1$  and  $D_2/C_2$  in the EDL at different Reynolds numbers.

#### 4.4.3.2 Velocity profile analysis

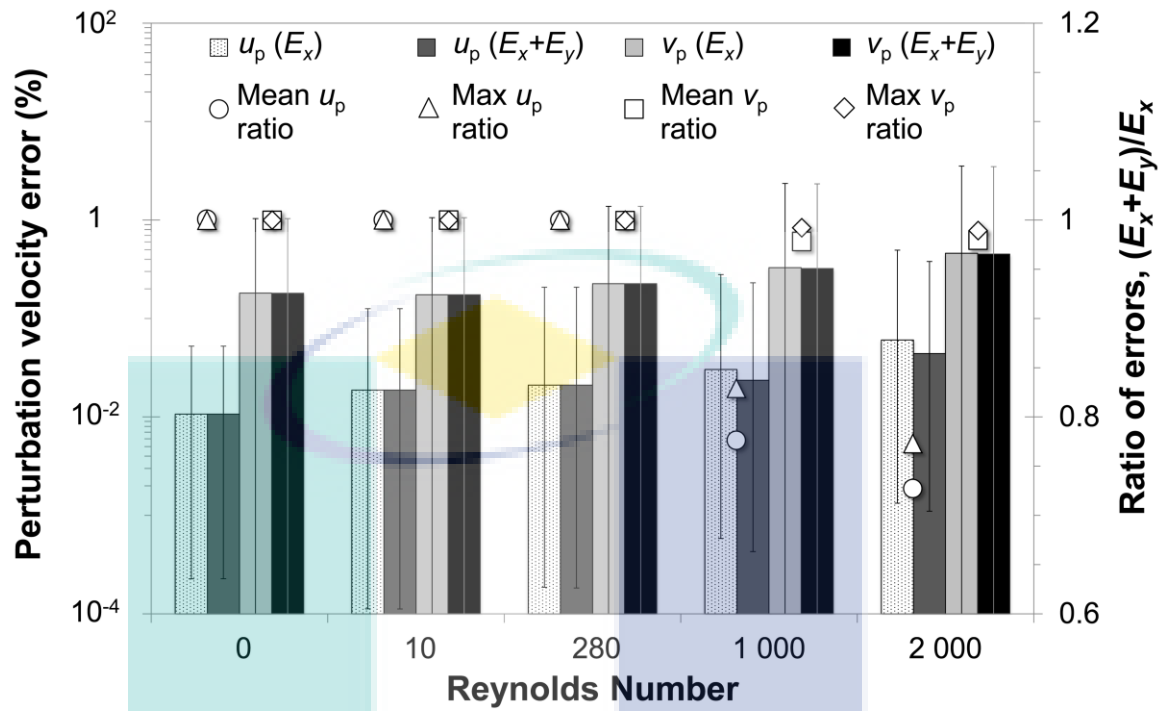


Figure 4.5: Deviation in  $u_p$  and  $v_p$  between the CD solution and the HS approximation at different Reynolds numbers.

Figure 4.5 depicts the difference in perturbation velocity profiles ( $u_p$  and  $v_p$ ) between the HS approximation and the CD solution at different Reynolds numbers. The deviations between the CD solution and the HS approximation are calculated using equation (4.4) under a non-uniform electric field given by equations (3.7) and (3.8) and the conditions summarised in Table 4.2. A range of Reynolds numbers from 0 to 2000 is analysed. From Figure 4.5, it can be observed that the maximum  $u_p$  and  $v_p$  errors are below 0.5 % and 4 % respectively. This shows that the perturbation velocity obtained using the HS approximation is in good agreement with the values obtained using the CD solution for the range of conditions evaluated. Moreover, Figure 4.5 also shows that the mean and max  $u_p$  ratios are below 1 for Reynolds numbers above 1000, which shows that the  $u_p$  results using the HS approach are in better agreement with the full-field than with the tangential-only electric field CD approach.

Figure 4.5 also reveals that almost identical maximum  $u_p$  and  $v_p$  errors are observed regardless of whether the normal component of the electrical field ( $E_y$ ) is included in the simulations. The relative increase in error observed at higher Reynolds numbers is related to the increase in numerical round-off error. This suggests that, as was the case for the uniform electric field, the effect of the normal component of the electric field is also negligible for the non-uniform electric field case. Therefore, it can be concluded that the HS approximation is valid for the Reynolds numbers and concentrations typically encountered in RO operations.

#### 4.4.4 Velocity field analysis

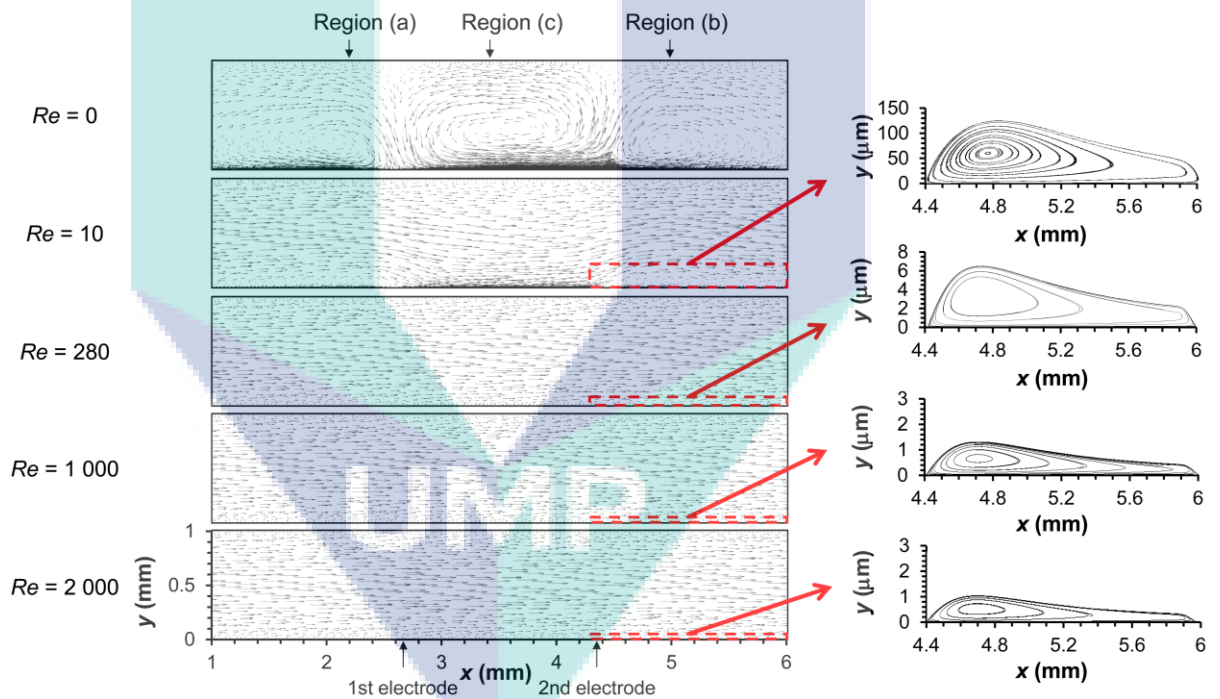


Figure 4.6: Effect of Reynolds number on velocity vector field and recirculation streamlines in region (b), using the HS approximation. Velocity vectors are scaled locally for every subfigure.

Recirculation regions in membrane channels have been identified as one of the main mass transfer enhancement mechanisms [23, 131-133]. Hence, this section discusses the flow patterns for the non-uniform electric field case. Figure 4.6 shows the velocity ( $\vec{v}$ ) vector field and streamlines downstream of the second electrode (region b) for solutions using the HS approximation and Reynolds numbers in the range of 0 to

2 000. Each subfigure in Figure 4.6 has the same geometry for each Reynolds number shown. At  $Re = 0$ , three main recirculation regions are observed on the bottom half of the channel: (a) upstream and (b) downstream of the electrodes, and (c) in the region between the two electrodes. Boundary layer reattachment and separation points are located upstream and downstream of both electrodes. These locations correspond to the points where suction and ejection of fluid to and from the boundary layer occur due to the electro-osmotic flow effect.

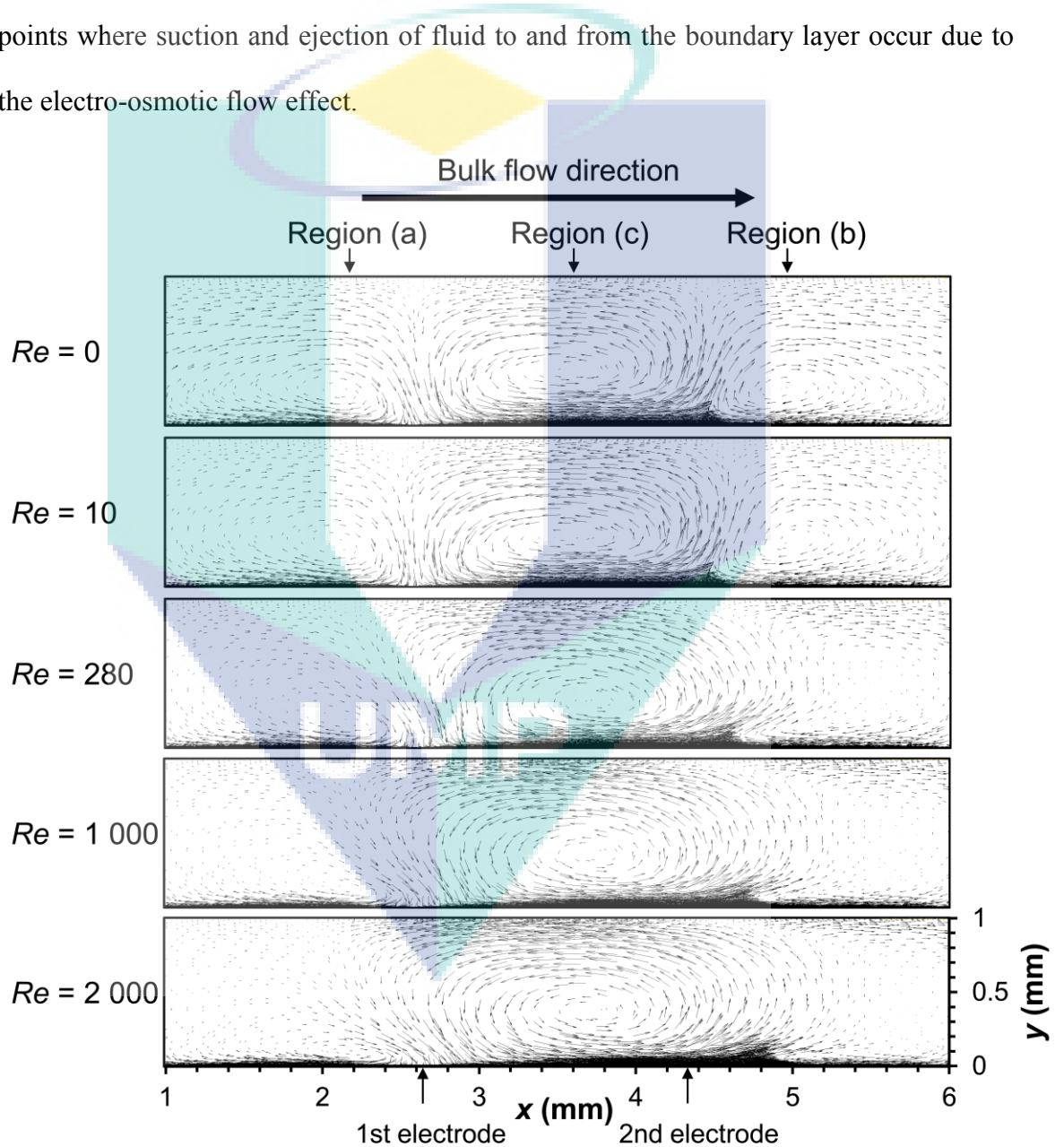


Figure 4.7: Effect of Reynolds number on perturbation velocity vector fields using the HS approximation.

As the Reynolds number increases, the velocity field in Figure 4.6 approaches the fully-developed velocity field described by equation (4.2), and recirculation region (c) disappears. This is expected, as the maximum slip velocity is at least one order of magnitude smaller than the bulk flow velocity for Reynolds numbers above 280. Nevertheless, thin recirculation regions are still present at higher Reynolds numbers, just upstream of the first electrode (region a) and just downstream of the second electrode (region b), where the slip velocity value is negative. This can be seen from the streamline plots in Figure 4.6 which show that, for larger Reynolds numbers, recirculation regions (a) and (b) become thinner and are confined to a narrow region the vicinity of membrane surface.

Figure 4.7 shows the effect of Reynolds number on the perturbation velocity vector field. In Figure 4.7, arrows pointing in the direction of the bulk flow mean that the fluid is flowing faster than for the case without electro-osmosis disturbance. Conversely, arrows pointing opposite the bulk flow represent regions where the fluid is flowing slower than without electro-osmosis. Larger Reynolds numbers cause the perturbation velocity field to become skewed in the direction of the bulk fluid flow. In addition, the region of higher perturbation velocity becomes thinner, which in turn affects mass transfer enhancement. This is because momentum convection increases at higher Reynolds numbers and the velocity perturbation does not penetrate as far into the bulk of the channel. This also suggests that the distribution of mixing is more localised within the concentration polarisation region as the Reynolds number increases.

#### **4.4.5 Mixing index**

Ouyang et al. [134, 135] define a mixing index as a measure of mixing enhancement based on the amount of fluid stretching and folding. This mixing index is

defined using the perturbation velocity due to the electro-osmotic flow effect, and is expressed as follows for 2D flow:

$$M = \int_{\Omega} \left( \frac{\partial u_p}{\partial x} \right)^2 + \left( \frac{\partial u_p}{\partial y} \right)^2 + \left( \frac{\partial v_p}{\partial x} \right)^2 + \left( \frac{\partial v_p}{\partial y} \right)^2 d\Omega \quad (4.11)$$

where  $\Omega$  is the volume of the fluid region considered. In this chapter, we define a volumetric mixing index by dividing the mixing index by the volume of the region investigated:

$$M_{\text{vol}} = \frac{M}{\Omega} \quad (4.12)$$

Figure 4.8 depicts the calculated volumetric mixing index ( $M_{\text{vol}}$ ) values for regions extending from the membrane surface to channel heights of 50  $\mu\text{m}$ , 100  $\mu\text{m}$  and 1 mm (the whole channel) respectively. It can be seen that the volumetric mixing index becomes larger as smaller fluid regions closer to the membrane surface are considered. This is expected, as most of the velocity perturbation is located near the membrane surface, as seen in Figure 4.7. In addition, it can also be seen that the volumetric mixing index increases with Reynolds number. It is interesting to note that when the Reynolds number is varied from 1 to 2 000, the volumetric mixing index for the channel height of 50  $\mu\text{m}$  is nearly quadrupled whereas the index for the whole membrane channel (1 mm height) is only approximately doubled. This suggests that a larger proportion of the mixing occurs near the membrane wall.

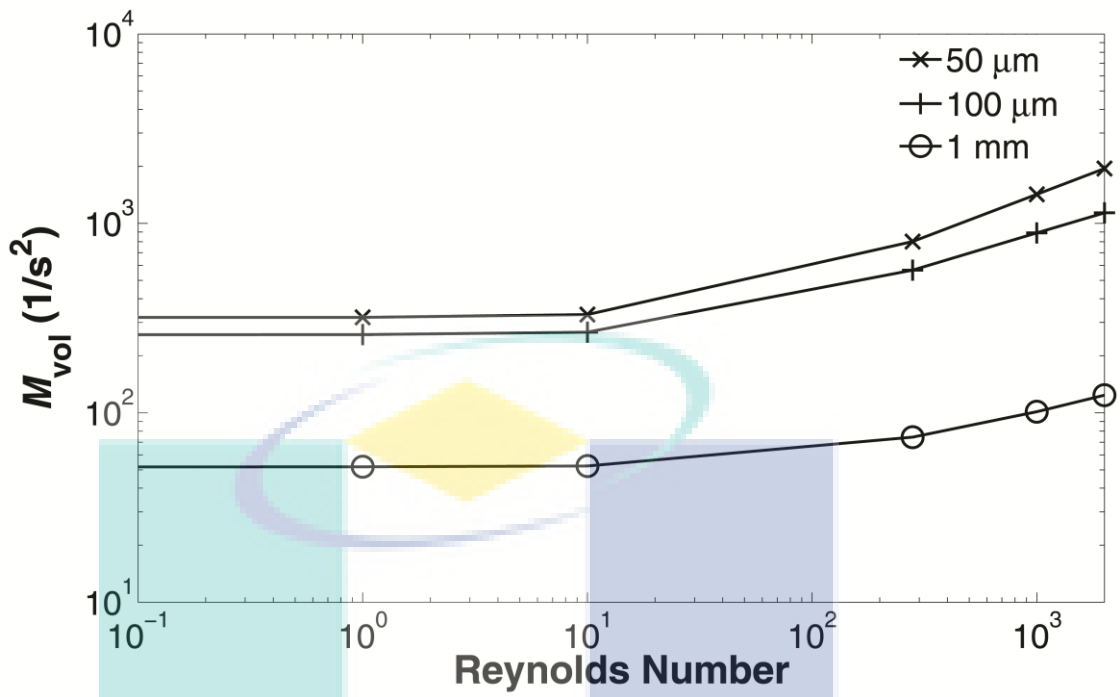


Figure 4.8: Dependence of the volumetric mixing index ( $M_{vol}$ ) on Reynolds number for different channel regions.

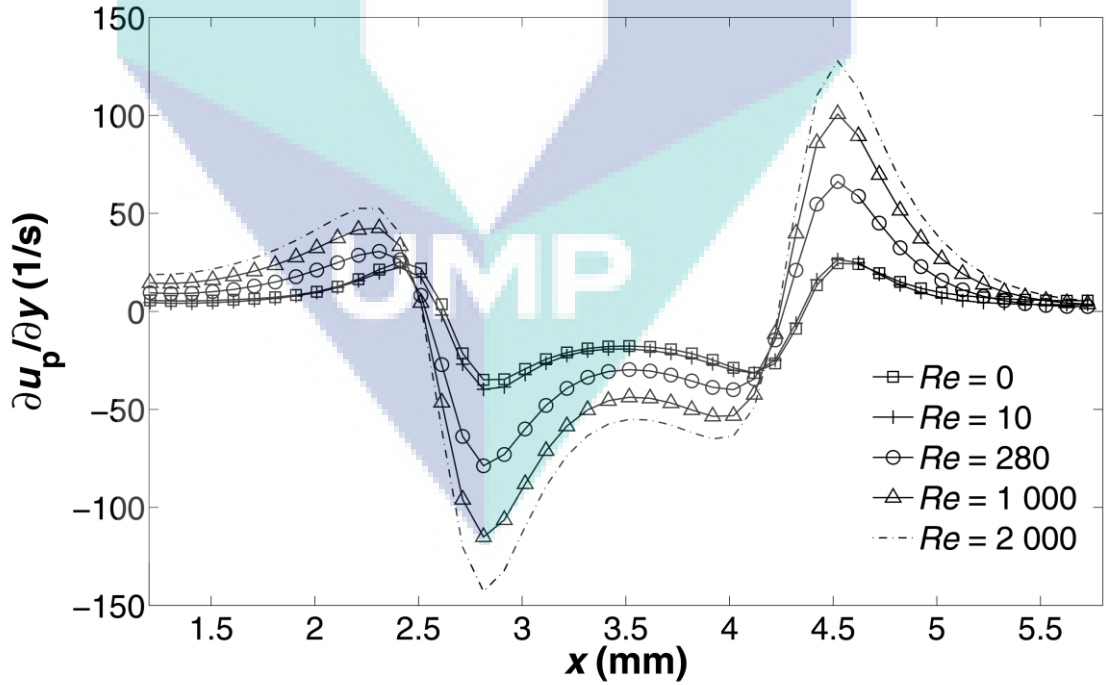


Figure 4.9: Perturbation velocity gradient ( $\partial u_p / \partial y$ ) at the membrane surface along the length of the membrane channel.

Equation (4.13) shows that the volumetric mixing index for 2D flow is a function of the four components of the velocity gradient tensor. At the membrane surface, for the system with negligible or almost zero permeation,  $v_p$  is zero and therefore  $\partial v_p / \partial x$  is also zero. The gradient components  $\partial u_p / \partial x$  and  $\partial v_p / \partial y$ , on the other hand, are related through the continuity equation. Moreover, the values of  $\partial u_p / \partial x$  (and hence  $\partial v_p / \partial y$ ) along the membrane surface are determined by the slip velocity profile and are not influenced by the cross-flow velocity. Thus, the only volumetric mixing index term affected by the cross-flow velocity is  $\partial u_p / \partial y$ , which is related to wall shear. Figure 4.9 shows the value of  $\partial u_p / \partial y$  at different locations along the membrane surface for different Reynolds numbers. It can be seen that increases in Reynolds number lead to the increases in the magnitude of  $\partial u_p / \partial y$ .

Based on the definition of the volumetric mixing index in equations (4.11) and (4.12), a local mixing index ( $M_{loc}$ ) is defined as follows:

$$M_{loc} = \left(\frac{\partial u_p}{\partial x}\right)^2 + \left(\frac{\partial u_p}{\partial y}\right)^2 + \left(\frac{\partial v_p}{\partial x}\right)^2 + \left(\frac{\partial v_p}{\partial y}\right)^2 \quad (4.13)$$

Figure 4.10 depicts contour plots of the local mixing index for different Reynolds numbers. It can be seen that (as was the case with the perturbation velocity plots) as the Reynolds number increases the region with a higher level of mixing is skewed in the direction of the bulk flow. This agrees with the trends observed in Figure 4.8 and Figure 4.9, where higher Reynolds numbers lead to increased mixing within the boundary layer, and therefore a higher magnitude of  $\partial u_p / \partial y$ . Here, it should be noted that the mixing index only depends on the perturbation velocity and therefore does not account for mixing effects related to changes in Reynolds number. Hence, any changes to the mixing index with Reynolds number are related to the convection of the perturbation velocity.

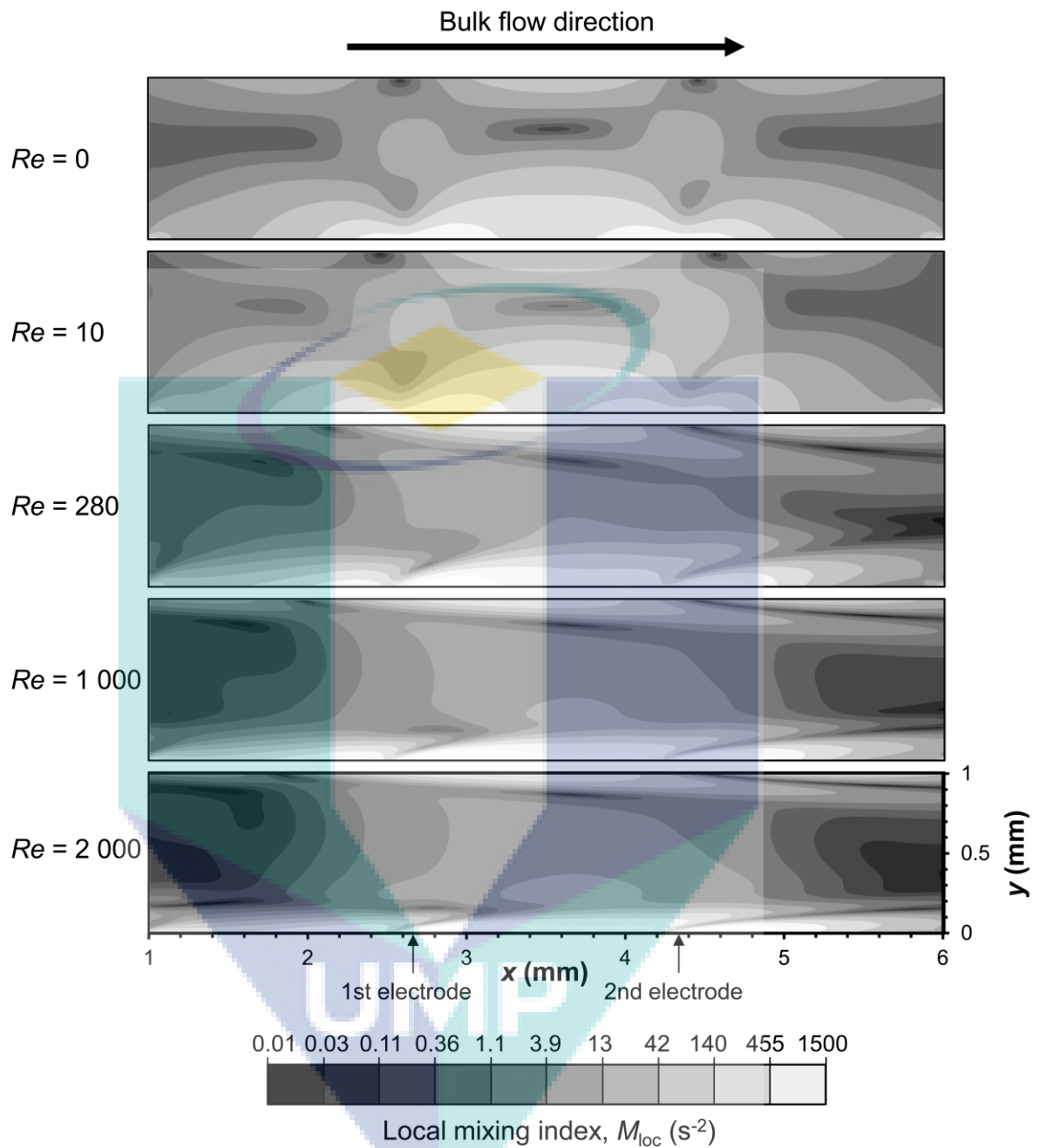


Figure 4.10: Local mixing contour plot. The contours are depicted using a logarithmic scale.

#### 4.5 Conclusions

A comparative study between the CD solution and the HS approximation was performed for uniform and non-uniform electric fields in 2D membrane channels with electro-osmotic flow. For the case with a uniform electric field, it was found that there is better agreement between these two methods as the solute concentration is increased.

This is because an increase in bulk solute concentration reduces the size of the Debye layer. Conversely, low solute concentrations (below 10 ppm) result in higher error, which renders the Helmholtz–Smoluchowski approximation an inaccurate representation of electro-osmotic phenomena in RO membrane channels with low solute concentrations. Therefore the HS approximation is only valid for higher solute mass fractions (0.001 or higher), which are typical salt concentrations near the membrane surface for RO systems.

The comparison between these two methods was also carried out for cases with a non-uniform electric field. In order to ensure the decoupling of electric potential due to wall surface charges and due to the external electric field, the convective terms were compared to the viscous terms in the momentum equation. It was found that the viscous terms are dominant within the electric double layer, and therefore the Debye length is sufficiently small such that the electric potential can be decoupled into potential due to the wall surface charge and potential due to the external electric field. The non-uniform electric field case study shows that the effect of the electric field normal to the membrane surface is negligible for both perturbation velocity components ( $u_p$  and  $v_p$ ). Overall, the HS approximation is in good agreement with the CD solution for both cases excluding and including the normal electric field component.

This chapter also investigated the effect of cross-flow velocity on the validity of the HS approximation against the CD solution. It was found that the maximum perturbation velocity error is below 4 %, which suggests that the HS approximation is valid for the typical flow conditions encountered in real world SWM modules for RO. This means that the HS approximation can be utilised to calculate the velocity profiles for 2D electric field cases without the need to solve Poisson’s equation at the scale of the Debye length ( $\sim 10^{-9}$  m).

The effect of Reynolds number on the perturbation velocity profile and volumetric mixing index was also assessed. Increases in Reynolds number skew the perturbation velocity in the bulk fluid direction and cause an increase in the volumetric mixing index. A higher level of increase of volumetric mixing index near the surface of the channel than for the whole channel is expected because electro-osmotic mixing is highest closer to the wall. Although the mixing index is an indirect method of estimating mass-transfer enhancement, it is an indicator that can be used to gain insights into the effects of electro-osmotic instabilities and cross-flow on mixing in the boundary layer. The results presented in this chapter also suggest that combination of cross-flow and other mass-transfer enhancement techniques are possible means for achieving mass-transfer enhancement within the boundary layer of membrane systems.

The work presented in this chapter is the first step towards modelling the complex process of mass transfer enhancement through electro-osmosis. As such, it is a simplification of the “complete” problem. Further research is required to evaluate the extent of permeate flux improvement due to electro-osmotic flow and will be the subject of Chapter 5-7.

## Chapter 5

### CFD modelling of electro-osmotic mass transfer enhancement on the feed side of a membrane

#### 5.1 Introduction

The effect of a slip velocity on mass transfer and pressure drop has been the focus of a few studies in the context of ultrafiltration (UF) processes [136]. This is because the porosity of UF membranes leads to a slip velocity at the membrane surface. Beavers et al. [137] found excellent agreement between experimental data and the analytical solution of the Navier–Stokes equations for a 2D unobstructed empty channel under the influence of a slip velocity. Singh and Laurence [67] developed a perturbation solution for the velocity profiles in a 2D unobstructed empty channel subject to permeation from both walls. The perturbation solution was then used to obtain numerical solutions for the mass transport equation. They found that an increase in slip velocity results in decreased friction factor and increased mass transfer. In addition, they observed that the slip velocity induced mass transfer enhancement is greater in the region closer to the membrane entrance, and for solutes with lower diffusivity. Despite these findings, the effect of slip velocity on mass transfer has not been studied in the context of RO.

While there are some recent studies on the use of electro-osmosis for mixing [135, 138], none of them have focused on the reduction of concentration polarisation and fouling at the surface of a membrane. Although previous studies have simulated the effect of electro-osmosis on the hydrodynamics [135, 139], they have not incorporated

mass transfer or the effect of electro-osmosis on permeate flux. Moreover, CFD membrane studies in the literature have mainly focused on the optimisation of spacer geometry and configuration for SWM applications [25, 35, 43, 82, 83, 140, 141], or other physical approaches for mass transfer enhancement [124, 142, 143], and have not considered the effect of electro-osmosis.

This chapter therefore uses CFD to investigate the role of electro-osmosis in enhancing mixing at the membrane surface. For this purpose, electrodes are assumed to be located in the vicinity of the membrane surface, on the permeate side, so that the electric field is localised within the feed-side boundary layer. The effect of this electric field in terms of boundary layer disruption and consequent increase in mass transfer and permeate flux are then analysed. This chapter extends our previous work [139], focusing on understanding the mechanisms that lead to electro-osmotic mass transfer enhancement in steady-state alone. It analyses the effect of membrane properties and bulk flow conditions under constant transmembrane pressure, in order to identify the conditions under which electro-osmosis is effective for enhancing mass transfer and permeate flux. Consideration of unsteady effects such as caused by the presence of spacers is beyond the scope of this chapter and is investigated in Chapter 7.

## **5.2 Problem description, assumptions and methods**

### **5.2.1 Model description**

CFD ANSYS CFX-13.0 is used to solve the steady-state continuity, momentum and mass transfer equations. The channel geometry used is depicted in Figure 5.1. Entrance and exit regions are included at each end of the channel in order to ensure that the flow solution is not affected by the inlet and outlet boundary conditions [21-23].

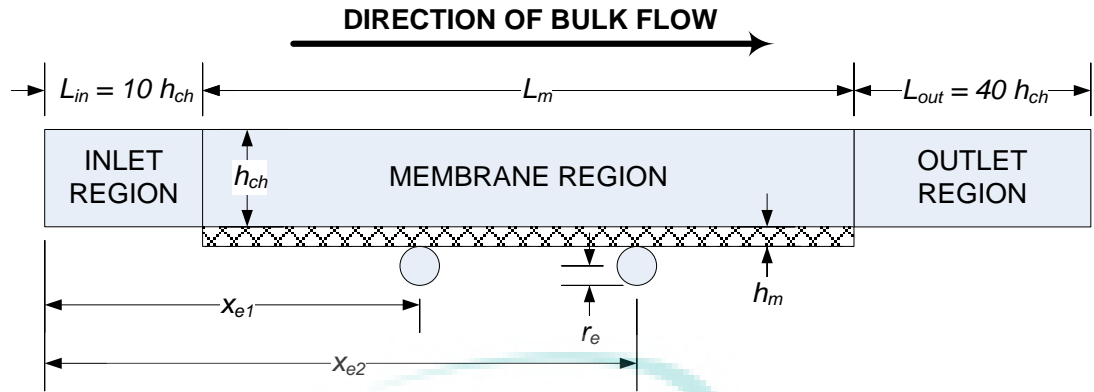


Figure 5.1: Geometry used in ANSYS CFX-13.0 to model 2D empty rectangular channel.

### 5.2.1.1 Boundary conditions

The conditions at the boundaries of the fluid domain are set following the approach in Table 3.3. Variations in permittivity due to membrane properties or the location of the membrane and the electrodes can influence the electric field and, therefore, the slip velocity experienced on the membrane surface. For the case of an RO system, the support layers of the membrane make up most of the membrane thickness. Due to the high porosity of these layers, their permittivity value can be considered similar to that of water [144]. In addition, the selective layer of the membrane is very thin (as thin as  $0.1 \mu\text{m}$  or less) [31], so the effect of the permittivity of this layer can be assumed to be negligible. Thus, for simplicity, this chapter neglects effects associated with the non-uniformity of permittivity. In the general case of non-uniform permittivity and arbitrary electrode geometry and position, the electric field must be obtained numerically.

Figure 5.2 shows a schematic of the uniform and non-uniform electric fields employed in this chapter, as well as their resulting slip velocity profiles along the membrane surface.

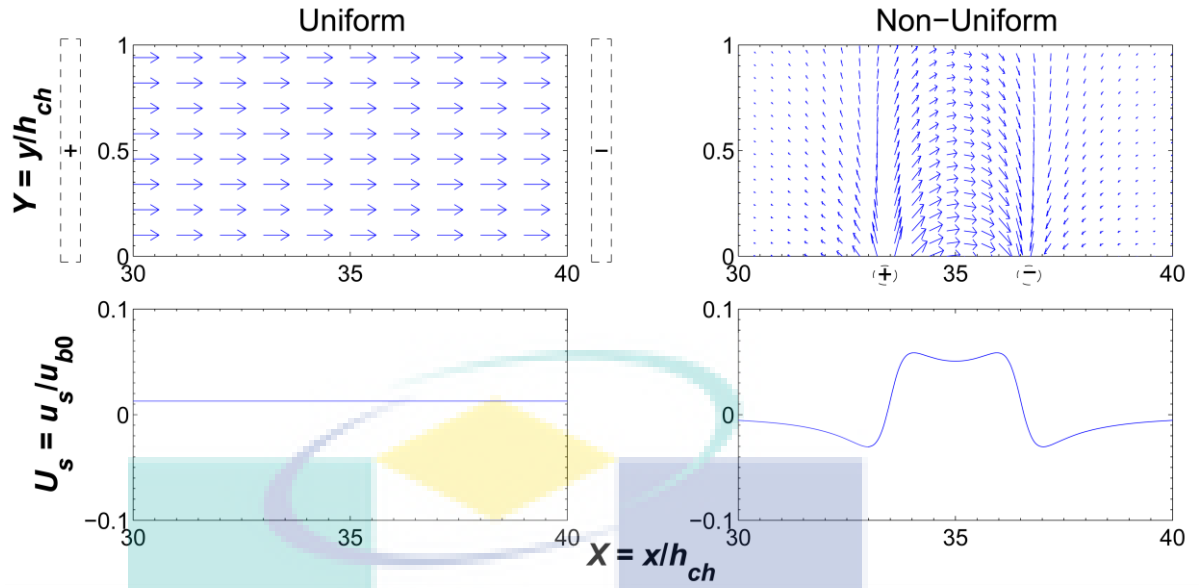


Figure 5.2: Schematic of the uniform and non-uniform electric vector fields showing the resulting forced-slip velocity ( $U_s$ ) at the membrane surface. Note that a positive slip velocity is in the same direction as the bulk cross-flow velocity.

### 5.2.1.2 Assumptions and cases

Table 5.1: Parameters used for non-uniform electric field case study.

Parameter	Value
Feed channel height ( $h_{ch}$ )	1 mm
Membrane thickness ( $h_m$ )	0.25 mm
Entrance length ( $L_{in}$ )	10 mm
Exit length ( $L_{out}$ )	40 mm
Membrane Length ( $L_m$ )	50 mm
Location of first electrode ( $x_{e1}$ )	33.5 mm
Location of second electrode ( $x_{e2}$ )	36.5 mm
Electrode radius ( $r_e$ )	0.25 mm
Potential difference across electrodes ( $V$ )	2 000 V
Reynolds number ( $Re$ )	280
Diffusivity coefficient ( $D$ )	$1.67 \times 10^{-9} \text{ m}^2/\text{s}$
Intrinsic rejection ( $R$ )	99.6 %
Membrane permeability ( $L_p$ )	$3.9 \times 10^{-11} \text{ m s}^{-1} \text{ Pa}^{-1}$
Reflection coefficient ( $\sigma$ )	1
Osmotic pressure coefficient ( $\varphi$ )	80.51 MPa
Inlet Transmembrane Pressure ( $\Delta p_{tm}$ )	2.94 MPa

Mesh independent solutions are obtained using a structured mesh with over 700 000 elements and a Grid Convergence Index (GCI) below 1 % for both mass transfer and permeate flux [23, 35]. The electro-osmotic effects are incorporated into the CFD model for two cases with increasing complexity, in order to identify and separate the different flow components, and to establish confidence that the final simulation model is an accurate reflection of the electro-osmosis phenomenon. The first case considers a uniform forced slip boundary condition at the membrane surface [139]. This boundary condition simulates the effect of an electric field induced by the placement of two flat-plate electrodes at each end of the channel and normal to the direction of the bulk flow. The second case considers a non-uniform slip velocity, taking into account the effect of electric field intensity on the electro-osmotic (slip) velocity [139]. The reference conditions for the non-uniform electric field case are presented in Table 5.1.

The influence of membrane properties ( $L_p$  and  $R$ ) and bulk flow conditions ( $Re$  and  $Sc$ ) on the effectiveness of electro-osmosis is investigated under constant transmembrane pressure. The range of values considered for these properties and operating conditions are based on typical RO operations, and they are summarised in Table 5.2.

Table 5.2: Range of membrane properties and bulk fluid conditions considered.

Parameter	Range
Intrinsic rejection ( $R$ )	0.95 – 1
Intrinsic permeability ( $L_p$ )	$2.21 \times 10^{-12} - 3.95 \times 10^{-10} \text{ m s}^{-1} \text{ Pa}^{-1}$
Reynolds number ( $Re$ )	280 – 2 000
Schmidt number ( $Sc$ )	500 – 1 200

## 5.2.2 Methodology for analysis of results

For the non-uniform electric field case, the level of mixing and its associated variables are averaged over an area that is based on a membrane length equal to twice the distance between the electrodes and centred on the midpoint between the electrodes. This area is used as the reference because it represents the region most affected by a pair of electrodes and where electro-osmosis occurs. Therefore, the area average for any local variable ( $\phi$ ) is:

$$\bar{\phi} = \frac{1}{2L_e} \int_{x_{e1} - \frac{1}{2}L_e}^{x_{e2} + \frac{1}{2}L_e} \phi dx \quad (5.1)$$

where  $x_{e1}$  and  $x_{e2}$  are the locations of the first and second electrodes and  $L_e = x_{e2} - x_{e1}$  is the distance between the electrodes.

## 5.3 Uniform forced-slip results

### 5.3.1 Validation

Validation is a crucial step in any simulation study. However, due to the nature of the phenomena being modelled in this chapter, there is very limited quantitative data available in the literature that can be used. In order to validate our simulation results, we tested our model under similar conditions as those reported by Singh and Laurence [67], that is, permeation from both the top and bottom walls of an unobstructed empty membrane channel. Although our simulations incorporate a variable flux that depends on the concentration at the membrane surface, it was found that the predicted velocity profiles were in excellent agreement with those predicted by Singh and Laurence [67] for the same fraction of fluid extracted. The maximum area-weighted error for both velocity components was below 0.01 %. Given that flow disturbances are the principal driver of mass transfer enhancement for the cases studied in this chapter, this agreement provides significant confidence in the predictions of our model.

### 5.3.2 Hydrodynamics

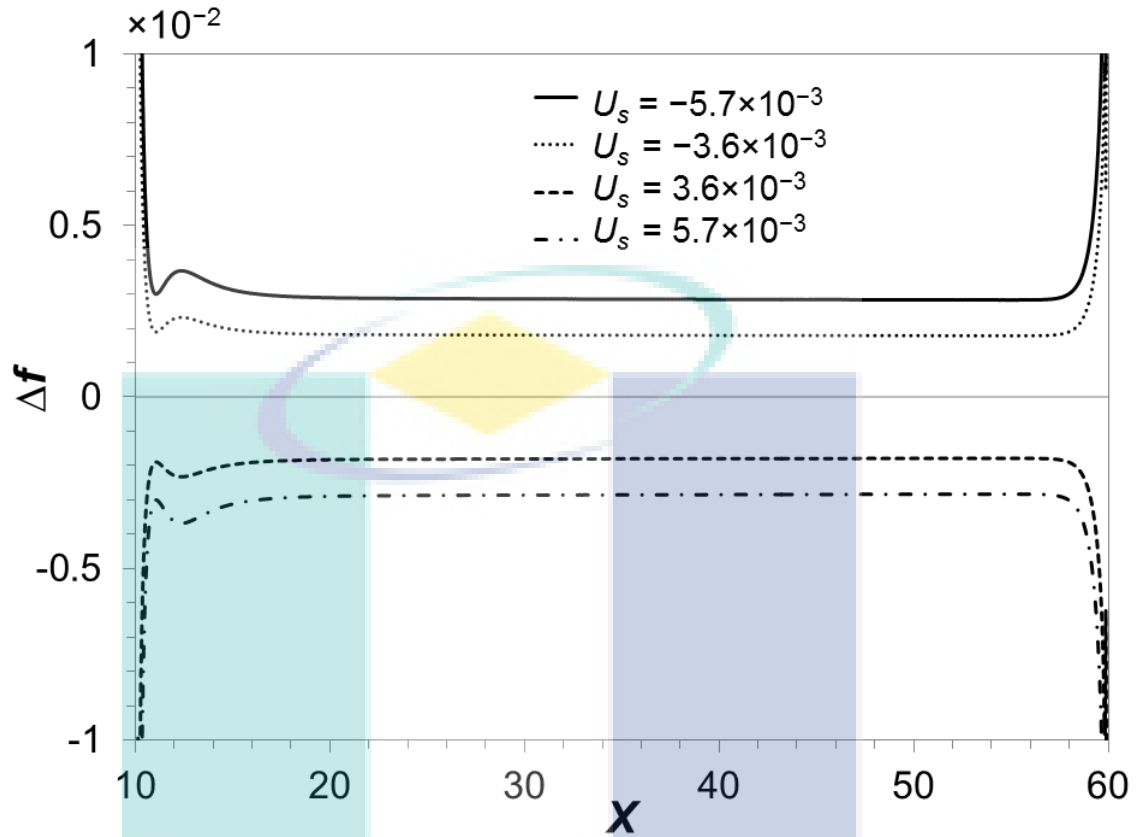


Figure 5.3: Change in local friction factor along the membrane channel under uniform slip velocity.

This section discusses the effect of a uniform slip velocity along the membrane surface, on the hydrodynamics and permeation behaviour within the membrane channel. The results presented in this section are for the base values for the bulk flow conditions ( $Re$  and  $Sc$ ) and membrane properties ( $R$  and  $L_p$ ) summarised in Table 5.1. For this case, the velocity profile becomes fully developed very close to the beginning of the membrane region, as shown in Figure 5.3. Therefore, the friction factor is practically constant along the membrane channel.

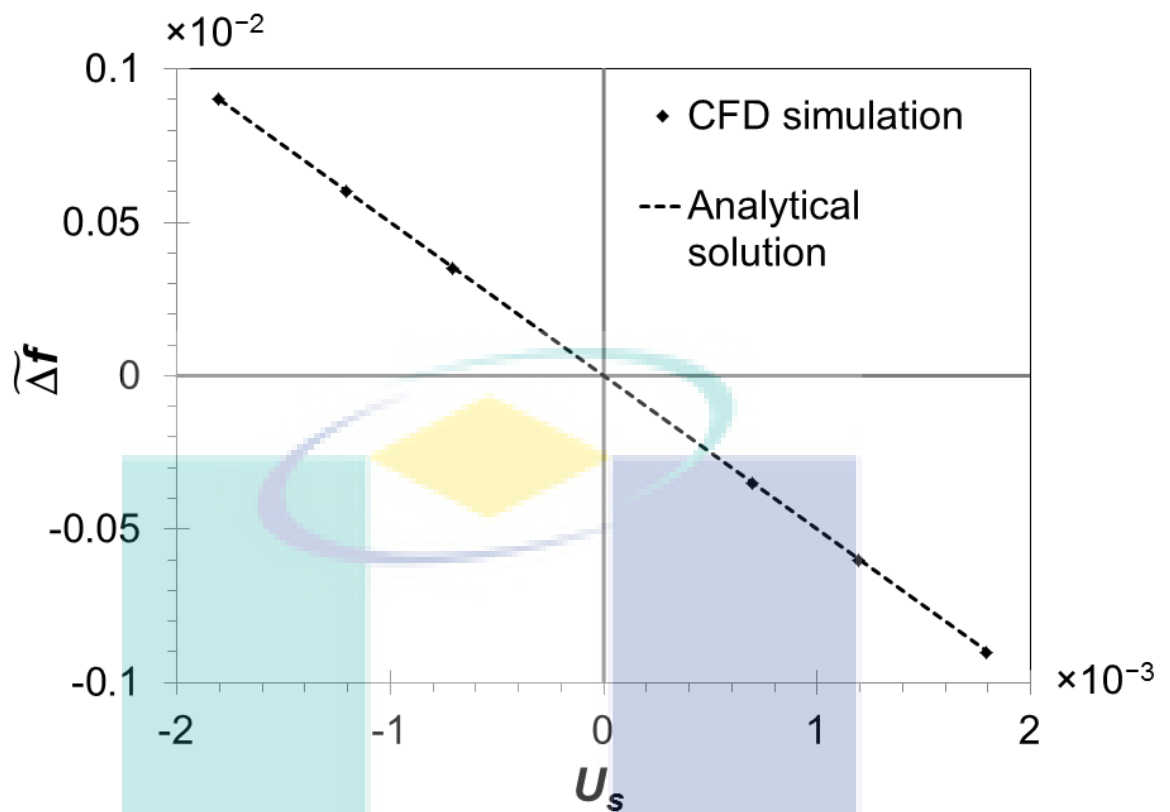


Figure 5.4: Effect of uniform slip velocity on global friction factor.

Figure 5.4 compares global friction factor results against the analytical solution of Beavers et al [137] for slip velocity induced friction factor, which can be expressed as follows:

$$f = \frac{24}{Re} \left( 1 - \frac{U_s}{2} \right) \quad (5.2)$$

Figure 5.4 shows that the simulation results are in excellent agreement with equation (5.2), with the relative error below 0.2 %. It also shows that for a negative slip velocity, the global friction factor is higher. This is expected because a negative slip velocity causes the fluid in the vicinity of the membrane surface to move in the opposite direction to the bulk flow. On the other hand, a positive slip velocity causes the fluid to move in the same direction as the bulk flow, resulting in a decrease in global friction factor.

The effect of slip velocity on friction factor is more evident in Figure 5.5, which depicts the  $u$  velocity profile for different slip velocity conditions in the vicinity of the membrane surface. As shown in this figure, the  $u$  velocity profiles converge as the distance from the membrane surface increases, but diverge near the surface. As a result, negative slip velocities lead to a larger  $u$  velocity gradient normal to the membrane wall and hence a higher friction factor. Conversely, positive slip velocities result in a lower velocity gradient near the surface and, thus, a lower friction factor.

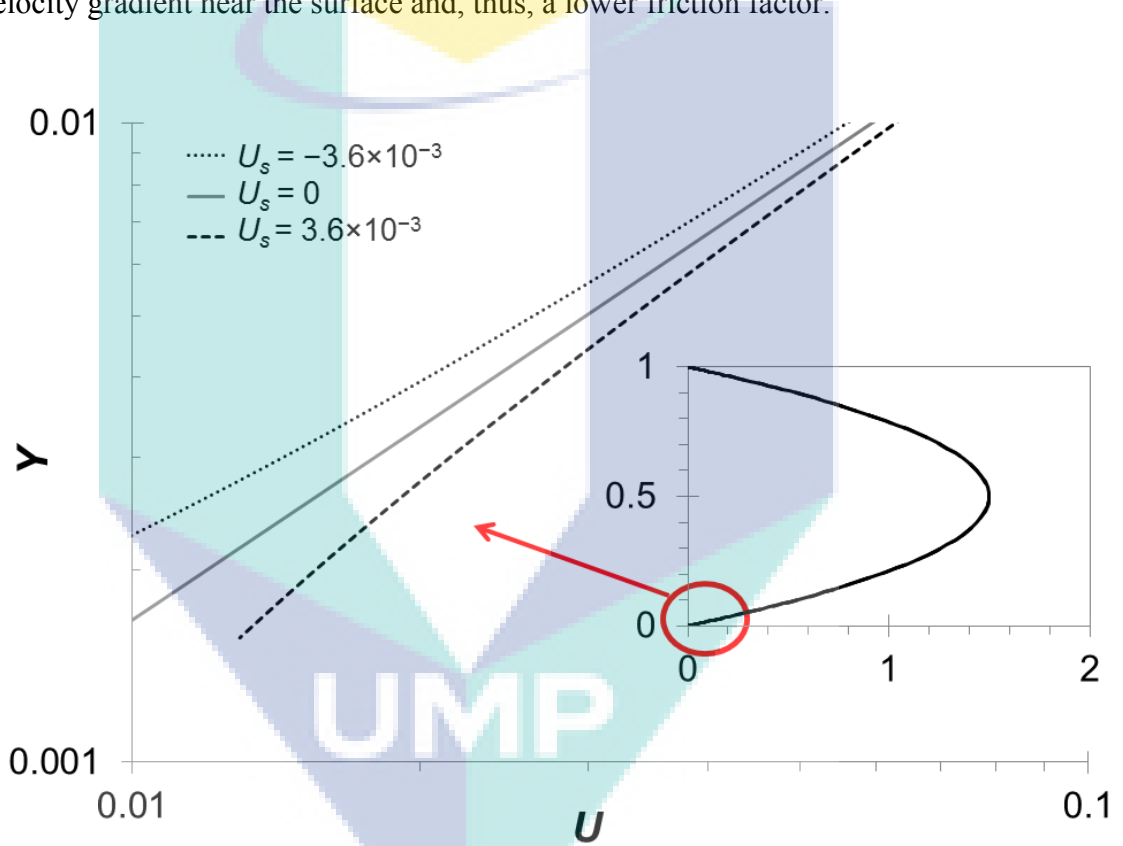


Figure 5.5: Close-up view of  $U$  velocity profiles within the region close to the membrane surface, for several uniform slip velocity values.

### 5.3.3 Concentration polarisation

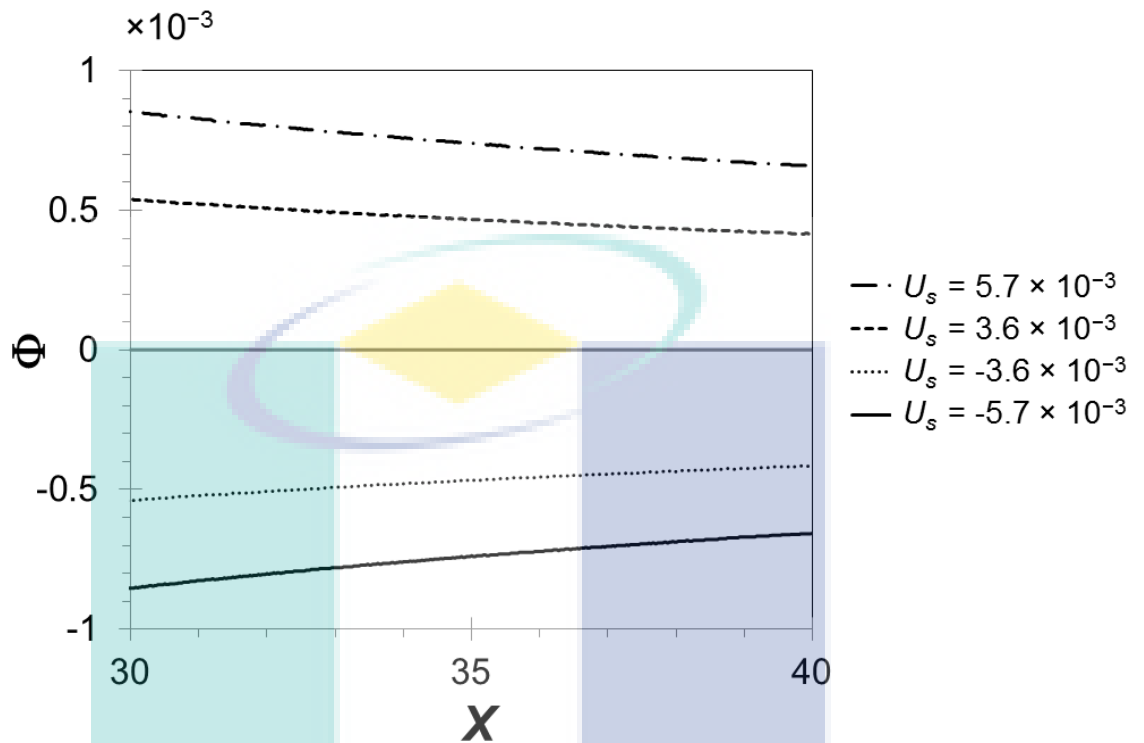


Figure 5.6: Local mass transfer enhancement along the membrane channel at the membrane surface.

Figure 5.6 shows the effect of uniform forced-slip on the  $\Phi$  profile for the membrane channel. It is evident that mass transfer enhancement due to electro-osmosis is not uniform along the channel length. At the channel entrance, where the boundary layer is developing and is therefore thinner, the magnitude of  $\Phi$  is larger than for regions further downstream, where the boundary layer is thicker. This suggests that electro-osmotic disturbances have a stronger effect in the regions where the boundary layer is developing, which is consistent with the observation of Singh and Laurence [67] that slip velocity has a larger effect on reducing concentration polarisation closer to the channel inlet.

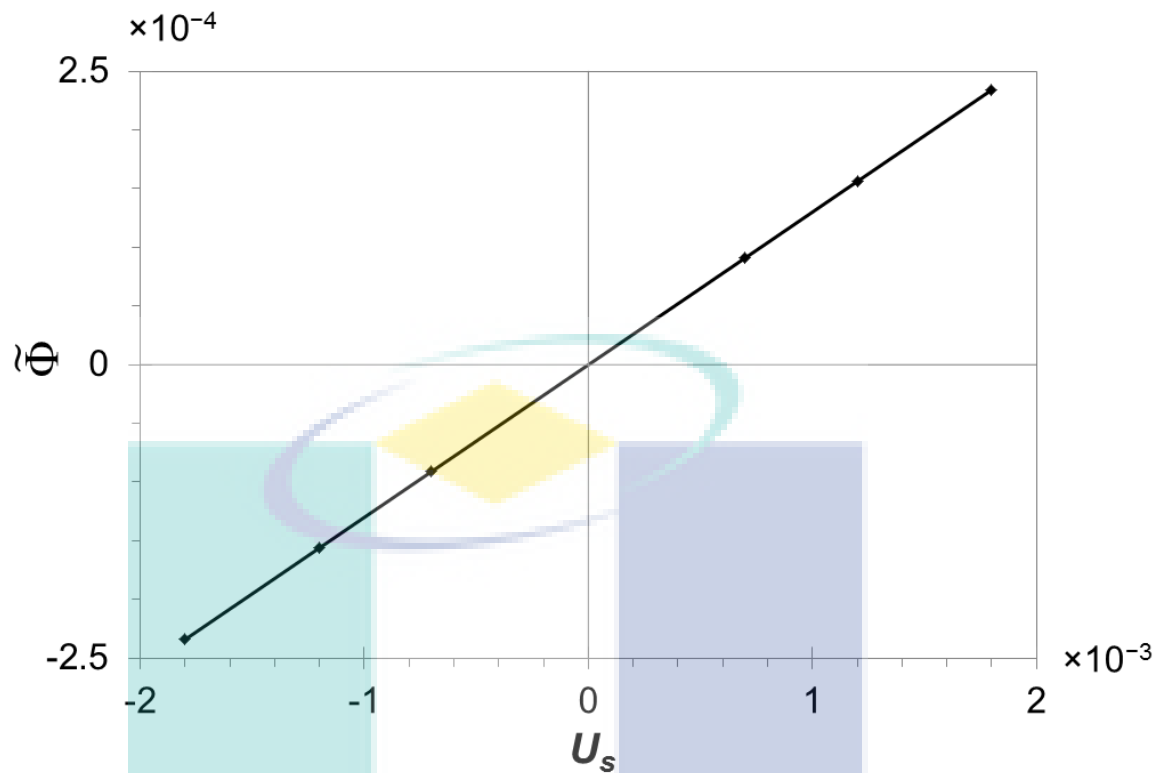


Figure 5.7: Effect of uniform slip velocity on mass transfer enhancement.

Figure 5.6 also shows that a positive slip velocity results in increased electro-osmotic enhancement ( $\Phi$ ) while a negative slip velocity results in negative  $\Phi$ , thus a decline in mass transfer. This trend is observed in Figure 5.7, which shows that  $\tilde{\Phi}$  increases as  $U_s$  increases in the direction of the bulk flow. Therefore, a larger  $U_s$  in the direction of the bulk flow (positive  $U_s$ ) leads to a decrease in friction factor (and hence a decrease in pressure drop (equation 3.34)) and an increase in mass transfer, which means that at every point along the channel the concentration polarisation is lower than for the case without electro-osmosis. These results are consistent with the results reported by Singh and Laurence [67], who found that a larger slip velocity leads to lower concentration polarisation. This increase in mass transfer with a decrease in pressure drop for positive slip velocity is different from the usual trend where it might be expected that a higher mass transfer would lead to a larger pressure drop [35].

The decrease in concentration polarisation with positive  $U_s$  can be explained in terms of the enhanced convective transport at the membrane surface. Because of solute rejection and fluid extraction at the membrane wall, solute mass fraction increases along the membrane surface in the bulk flow direction. A positive slip velocity transports lower concentration fluid downstream, so the solute mass fraction downstream is lower with positive slip velocity than for the no-slip case. Consequently, the concentration polarisation is also lower, resulting in a larger permeate flux relative to the case without electro-osmosis. The opposite behaviour is obtained for the case with a negative slip velocity (higher concentration polarisation and lower permeate flux). These trends are summarised in Table 5.3.

Table 5.3: Summary of changes in permeate flux due to uniform slip velocity.

Negative slip velocity ( $U_s < 0$ )	Positive slip velocity ( $U_s > 0$ )
$(\omega_w)_{U_s < 0} > (\omega_w)_{U_s = 0}$	$(\omega_w)_{U_s > 0} < (\omega_w)_{U_s = 0}$
$\therefore \gamma_{U_s < 0} > \gamma_{U_s = 0}$	$\therefore \gamma_{U_s > 0} < \gamma_{U_s = 0}$
$\therefore J_{U_s < 0} < J_{U_s = 0} < J_{U_s > 0}$	

## 5.4 Non-uniform forced slip results

### 5.4.1 Hydrodynamics and mass transfer

Figure 5.8 shows the effect of non-uniform slip velocity on  $\Phi$  and  $\Delta f$ . The figure shows two sub-cases: in the first sub-case (N) the first electrode has a negative charge, while in the second sub-case (P) the first electrode has a positive charge. It can be seen that locations with positive slip velocity have a lower friction factor and higher  $\Phi$  and vice versa. This agrees with the observations for uniform slip velocity. Figure 5.8 also shows that the magnitudes of  $\Delta f$  and  $\Phi$  just after each electrode are larger than just

before the electrode. This effect is related to the transfer of momentum from upstream of the electrode to downstream of the electrode, and is further discussed in section 5.4.2.

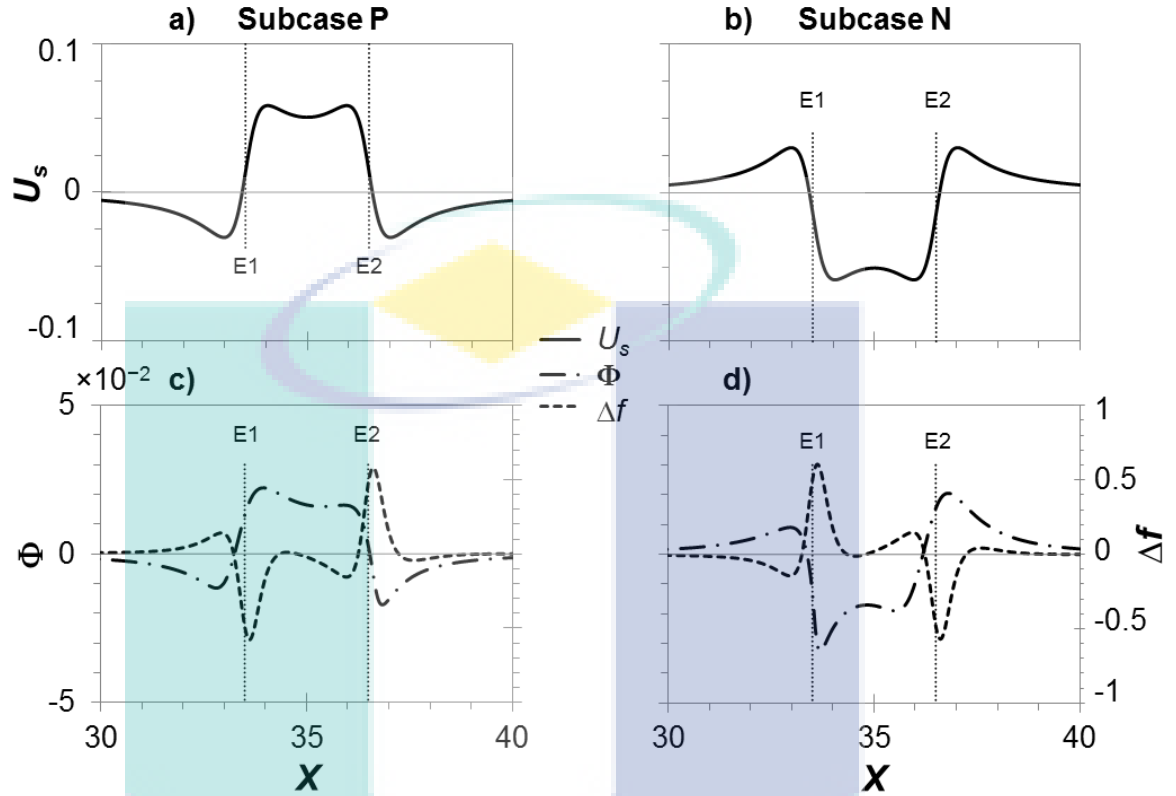


Figure 5.8: Local slip velocity,  $\Phi$  and friction factor change at the membrane surface for non-uniform slip velocity cases where the first electrode is positively (subcase P,  $\bar{U}_s = 1.5 \times 10^{-2}$ ) or negatively charged (subcase N,  $\bar{U}_s = -1.5 \times 10^{-2}$ ). Electrode positions are indicated by E1 and E2.

Figure 5.9 compares the global friction factor under uniform and non-uniform slip velocity. It can be seen that the changes in friction factor with non-uniform slip velocity are similar to those obtained using uniform slip velocity. The friction factor is lower for a net positive slip velocity, i.e., when the charge on the upstream electrode is positive.

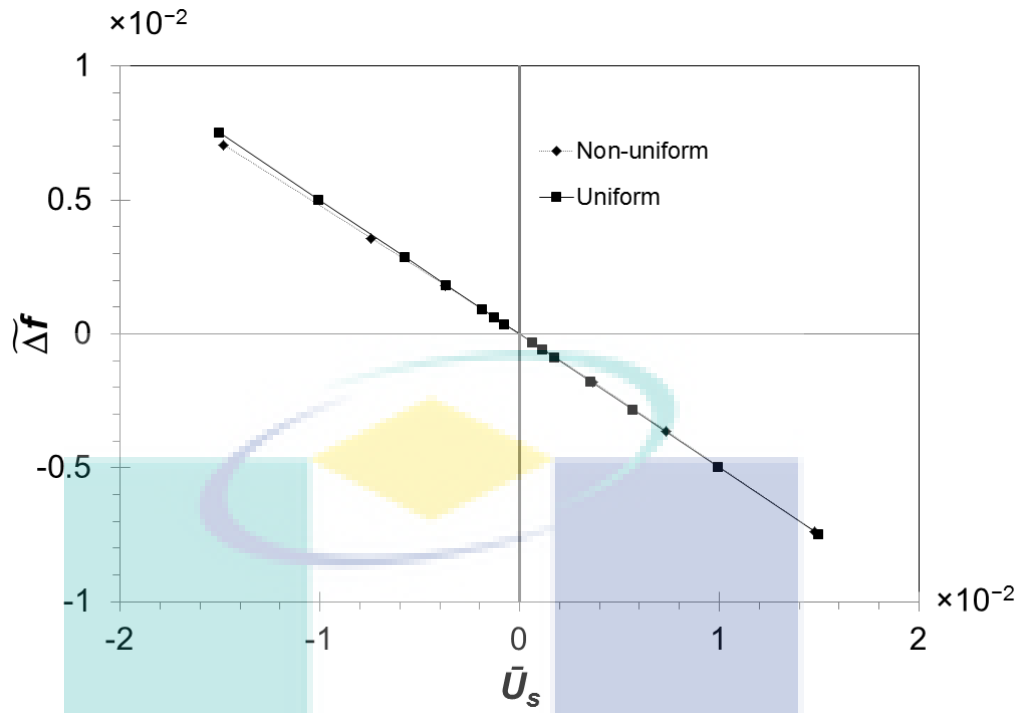


Figure 5.9: Comparison of changes in global friction factor under uniform and non-uniform slip velocity, for the base case conditions in Table 5.1.

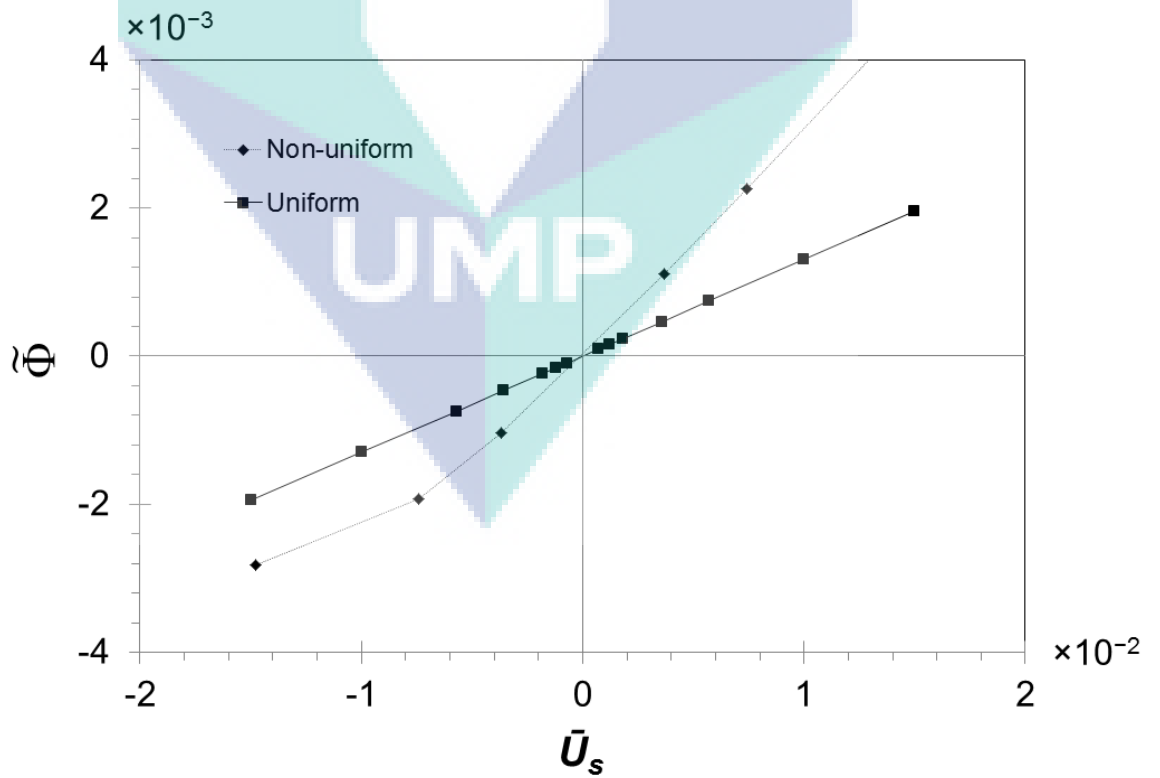


Figure 5.10: Comparison of global electro-osmotic mass transfer enhancement under uniform and non-uniform slip velocity, for the base case conditions in Table 5.1.

Figure 5.10 compares the values of  $\tilde{\Phi}$  for the uniform and non-uniform slip cases. In contrast to global friction factor, the non-uniform slip velocity has a greater effect on mass transfer enhancement. Mass transfer and flux enhancement are larger for a net positive non-uniform slip velocity, i.e., when the charge on the upstream electrode is positive. The reasons for these effects are discussed in the next section.

#### 5.4.2 Concentration polarisation reduction mechanism

The greater effect of a non-uniform than a uniform slip velocity on mass transfer can be explained by the hydrodynamic conditions near the membrane surface, using the 2D continuity equation:

$$\frac{\partial u}{\partial x} = -\frac{\partial v}{\partial y} \quad (5.3)$$

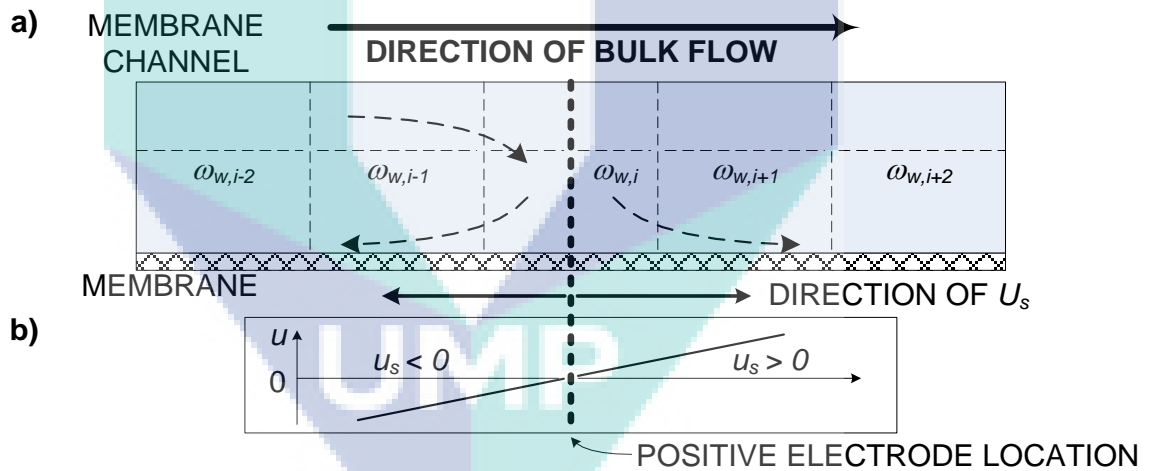


Figure 5.11 : Schematic of the effect of slip velocity on solute mass fraction ( $\omega$ ) at a positively charged electrode. (a) Flow field in the membrane channel; (b)  $u$  velocity profile at membrane surface.

Figure 5.11a shows a schematic of the flow field in the vicinity of the membrane surface for a positively charged electrode. Because the electric field is directed away from the positive electrode, negative and positive slip velocities are produced respectively upstream and downstream of the electrode, as depicted in Figure 5.11b. Figure 5.11b also shows that in the vicinity of the electrode  $\partial u/\partial x > 0$ , so equation (5.3)

requires that  $\partial v/\partial y < 0$ , leading to “suction” of fluid from the bulk. Therefore, low concentration bulk fluid is transported toward the membrane surface, which reduces the solute mass fraction in the region around the positive electrode. Moreover, the solute concentration near the electrode is further reduced because the slip velocity convects the solute away from the electrode. These combined effects result in lower solute concentration ( $\omega_w$ ) and concentration polarisation ( $\gamma$ ) around the positive electrode (see Figure 5.8), which in turn translates to an increase in permeate flux as shown in equation (3.19). In addition, and given the trends summarised in Table 5.3, permeate flux is higher downstream than upstream of the electrode, and thus the permeate flux maximum is located downstream of the electrode.

For the case of a negatively charged electrode the mechanism is reversed, with the slip velocity directed towards the electrode,  $\partial u/\partial x < 0$  and  $\partial v/\partial y > 0$ . Consequently,  $\omega_w$  and  $\gamma$  are higher in the vicinity of electrode and permeate flux is reduced.

## 5.5 Effect of membrane properties and bulk flow conditions

Because permeate flux is affected by membrane properties, this section investigates the effect of these on electro-osmotic permeation enhancement. The analysis focuses on the non-uniform electric field where the positively charged electrode is placed upstream, as this configuration shows a net positive slip velocity, better permeate flux enhancement and lower friction factor.

### 5.5.1 Effect of membrane properties

#### 5.5.1.1 Effect of membrane permeability

Figure 5.12 shows the effect of membrane permeability on pure water flux ( $J_{pure}$ ) and solution permeate flux with and without electro-osmosis ( $J_{EO}$  and  $J_{NS}$ , respectively). It can be seen that  $J_{pure}$  increases linearly with membrane permeability because of the absence of osmotic pressure resistance. On the other hand, the rate of increase in  $J_{NS}$  and

$J_{EO}$  gradually decays as membrane permeability increases. This is because of the increase in the amount of solute transported to the membrane surface, which leads to increased osmotic pressure and lower flux, as is evident from equation (3.12). Figure 5.12 also shows that electro-osmosis leads to an increase in permeate flux between 0.5 to 11 % relative to flux without electro-osmosis.

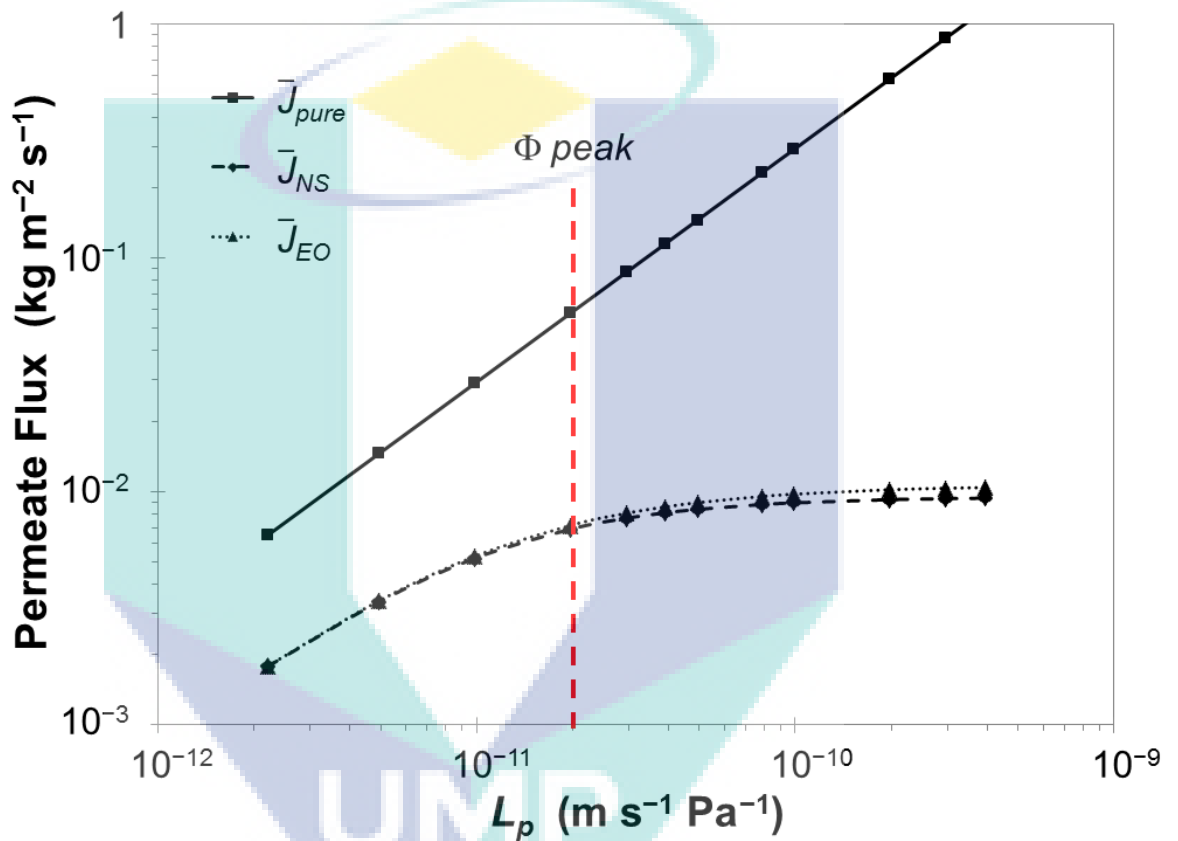


Figure 5.12: Effect of membrane permeability on permeate flux.

Figure 5.13 shows the effect of varying intrinsic membrane permeability on the area-averaged permeate flux ratio ( $\bar{J}/\bar{J}_{pure}$ ), concentration polarisation ( $\bar{\gamma}$ ) and mass transfer coefficient ( $\bar{k}_{mt}$ ), for cases with (EO) and without electro-osmosis (NS). Concentration polarisation increases with increasing permeability because of the increased transport of solute towards the membrane, and asymptotically approaches a constant value. The permeate flux ratio follows the opposite trend, as predicted by equation (3.19). The mass transfer coefficient under electro-osmosis follows the same

trend as the concentration polarisation modulus. However, the mass transfer coefficient without electro-osmosis goes through a maximum.

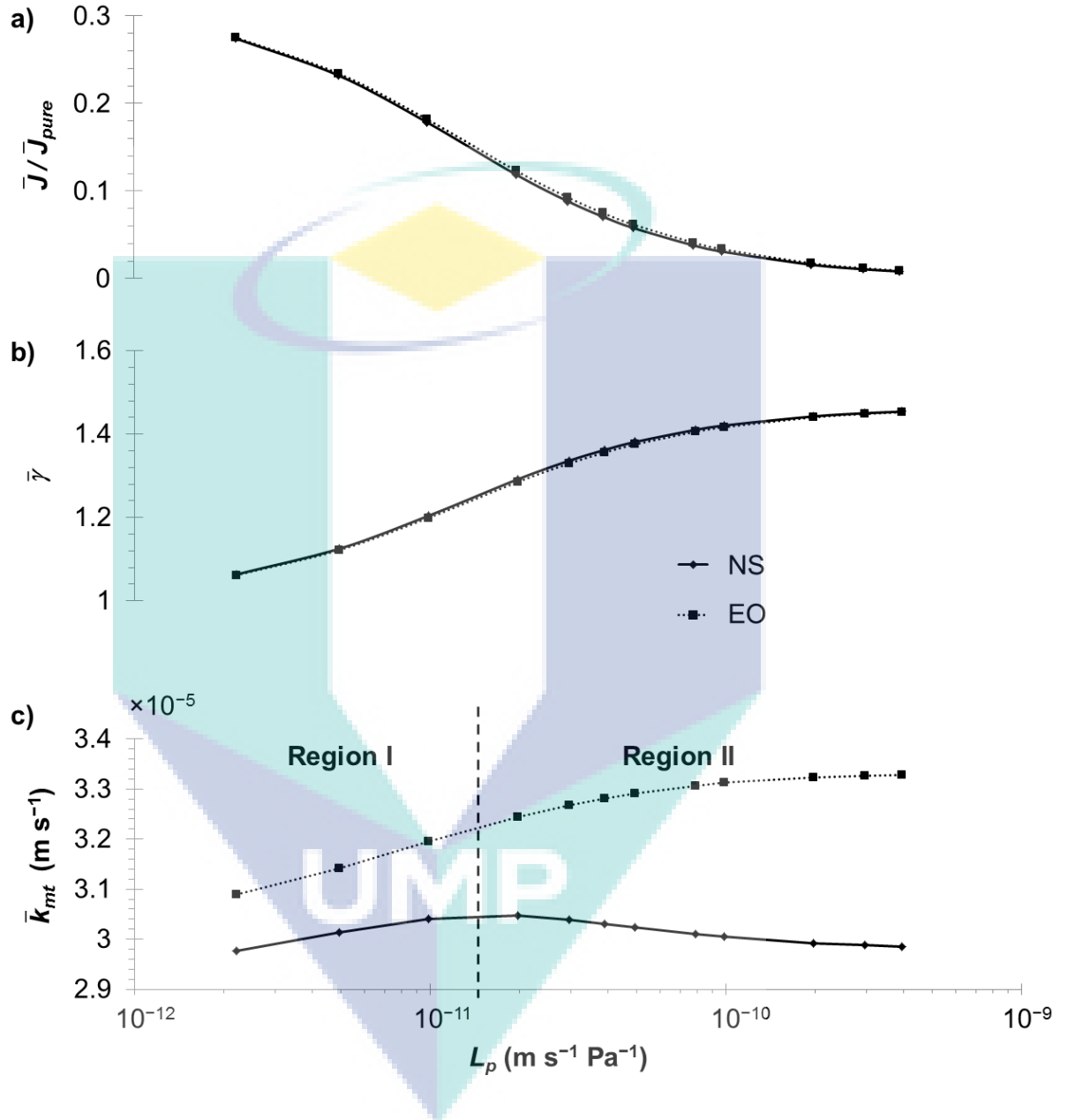


Figure 5.13: Effect of membrane permeability on flux (a), concentration polarisation (b) and mass transfer coefficient (c).

The peak in  $\bar{k}_{mt,NS}$  is related to the competing mechanisms that lead to the decrease of  $\bar{J}/\bar{J}_{pure}$ . At low permeability values (Region I), concentration polarisation is low and the increase in permeate flux dominates, resulting in an increase in mass

transfer coefficient and a thinner boundary layer, as predicted by equation (3.20). However, at high permeability values (Region II) the higher levels of concentration polarisation dominate, leading to a thicker boundary layer and, hence, a decrease in  $\bar{k}_{mt,NS}$ . Because electro-osmosis improves mixing between the bulk and the boundary layer,  $\bar{k}_{mt,EO}$  continues to increase at high permeability values, albeit at a lower rate.

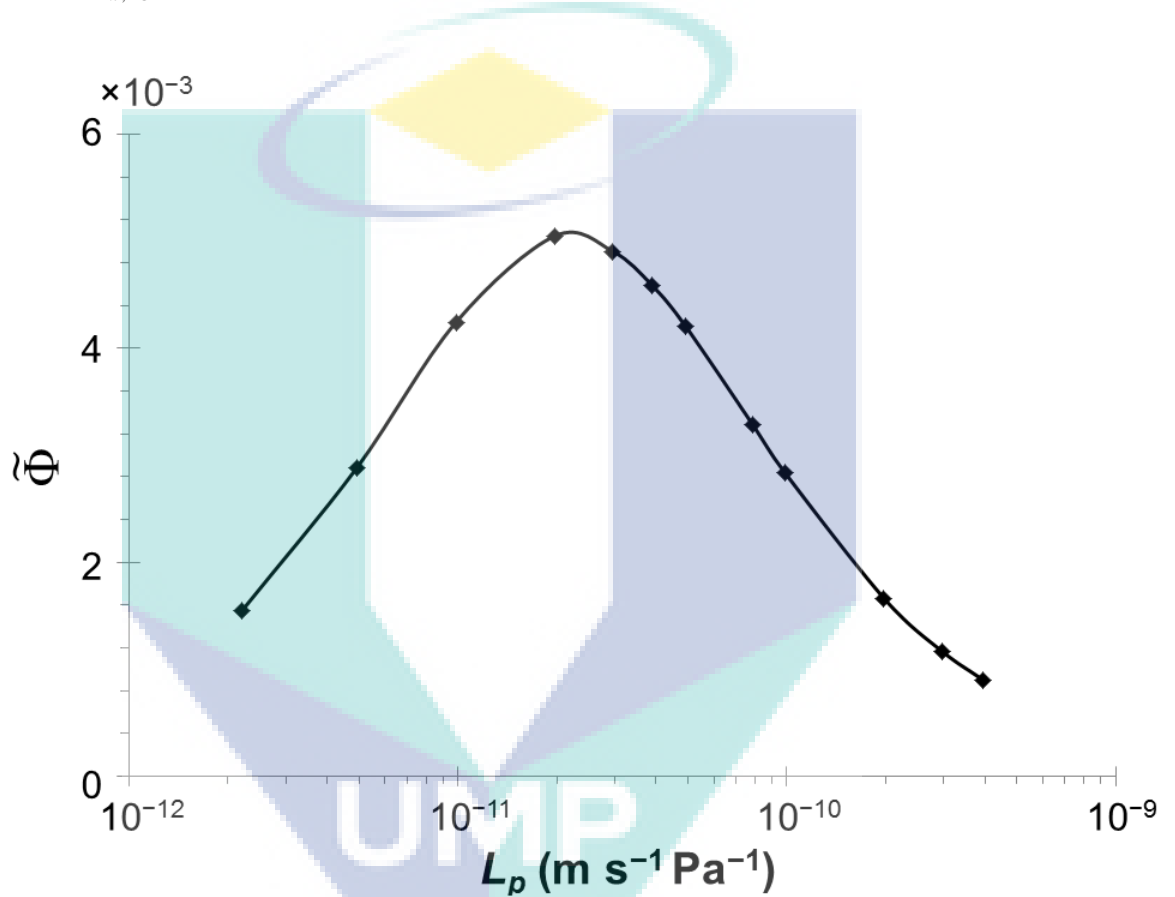


Figure 5.14: Effect of membrane permeability on electro-osmotic mass transfer enhancement.

Figure 5.14 shows the trend of  $\tilde{\Phi}$  as permeability is increased. The peak in  $\tilde{\Phi}$  can be explained through the relationship between the flux ratios ( $\bar{J}_{EO}/\bar{J}_{pure}$  and  $\bar{J}_{NS}/\bar{J}_{pure}$ ) depicted in Figure 5.12 and Figure 5.13a. According to equation (3.29), at lower permeability,  $\tilde{\Phi}$  is dominated by the difference between  $\bar{J}_{EO}$  and  $\bar{J}_{NS}$ , given that the difference between  $\bar{J}_{pure}$  and  $\bar{J}_{NS}$  is smaller. Therefore,  $\tilde{\Phi}$  increases with permeability at lower permeability. On the other hand, at higher permeability  $\bar{J}_{pure}$  is

much larger than  $\bar{J}_{NS}$ , and both  $\bar{J}_{EO}$  and  $\bar{J}_{NS}$  approach a constant value. This therefore leads to a decrease in  $\tilde{\Phi}$  at high permeability. This suggests that electro-osmosis is more effective at mid-range permeabilities for brackish water reverse osmosis. On the other hand, electro-osmosis is more effective for sea water reverse osmosis as permeability increases. For microfiltration and ultrafiltration membranes, electro-osmosis is less effective as permeability increases.

### 5.5.1.2 Effect of intrinsic solute rejection

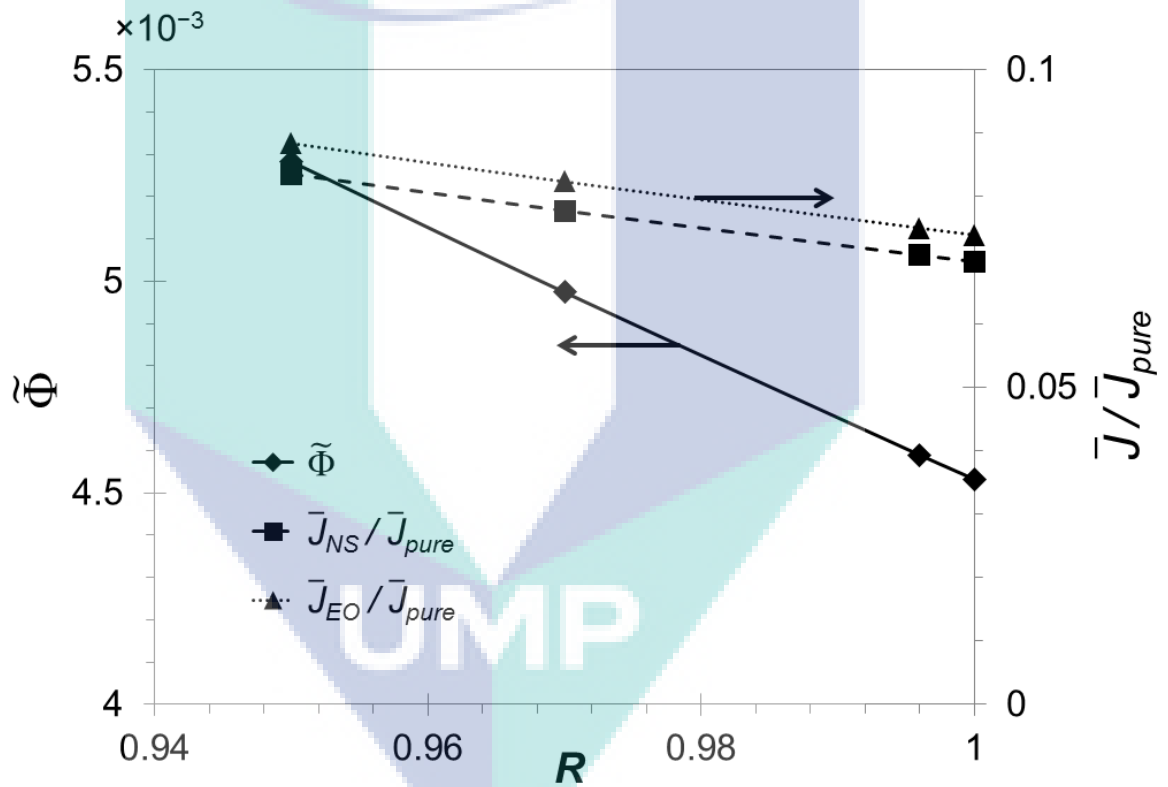


Figure 5.15: Effect of intrinsic rejection ( $R$ ) on dimensionless permeate flux ( $\bar{J}/\bar{J}_{pure}$ ) and electro-osmotic mass transfer enhancement ( $\tilde{\Phi}$ ), under constant transmembrane pressure.

Figure 5.15 shows that  $\tilde{\Phi}$  and  $\bar{J}/\bar{J}_{pure}$  decrease as the intrinsic solute rejection ( $R$ ) increases. Although they are not shown here,  $\bar{\gamma}$  and  $\bar{k}_{mt}$  also decrease as  $R$  increases, both with and without electro-osmosis. This is because, at the constant transmembrane pressure conditions simulated in this chapter, equation (3.19) shows that

the primary effect of a higher rejection is a decrease in flux, which in turn leads to less solute transported to the membrane surface and thus lower  $\gamma$ . These trends are also consistent with equation (3.20). The decrease in  $\gamma$  suggests that there is a lower mixing potential ( $\Phi_{max}$ ), and this leads to lower electro-osmotic enhancement ( $\tilde{\Phi}$ ) at higher values of  $R$ .

## 5.6 Effect of bulk flow conditions

This section analyses the effect of changes in Reynolds and Schmidt number on electro-osmotic mass transfer enhancement. Reynolds and Schmidt numbers are varied by altering the bulk flow velocity and solute diffusivity respectively, while keeping the fluid density and viscosity constant. For laminar and turbulent flow in conduits (pipelines, rectangular channels, etc.), the dependence of Sherwood number on Reynolds and Schmidt numbers is widely documented and quantified [23, 145]. A power law dependence generally shows good agreement with experimental data:

$$Sh = \frac{k_m d_h}{D} = a Re^b Sc^{1/3} \quad (5.4)$$

where the coefficients  $a$  and  $b$  are dependent on channel geometry (i.e. height), whether the flow is laminar steady, unsteady or turbulent, and whether mass transfer enhancement techniques are utilised (e.g. spacers, electro-osmosis, etc.).

Figure 5.16 shows that  $\tilde{\Phi}$  decreases and  $\bar{J}/\bar{J}_{pure}$  increases for an increase in Reynolds number. This is because, according to equation (5.4), an increase in Reynolds number leads to an increase in mass transfer coefficient and therefore more mixing between the bulk and the boundary layer. This results in a lower concentration polarisation index ( $\gamma$ ), as predicted by equation (3.20). As was discussed in section 5.5.1.2, a lower  $\gamma$  leads to lower mixing potential, and therefore less opportunity for electro-osmosis to improve mixing, enhance mass transfer and improve permeate flux.

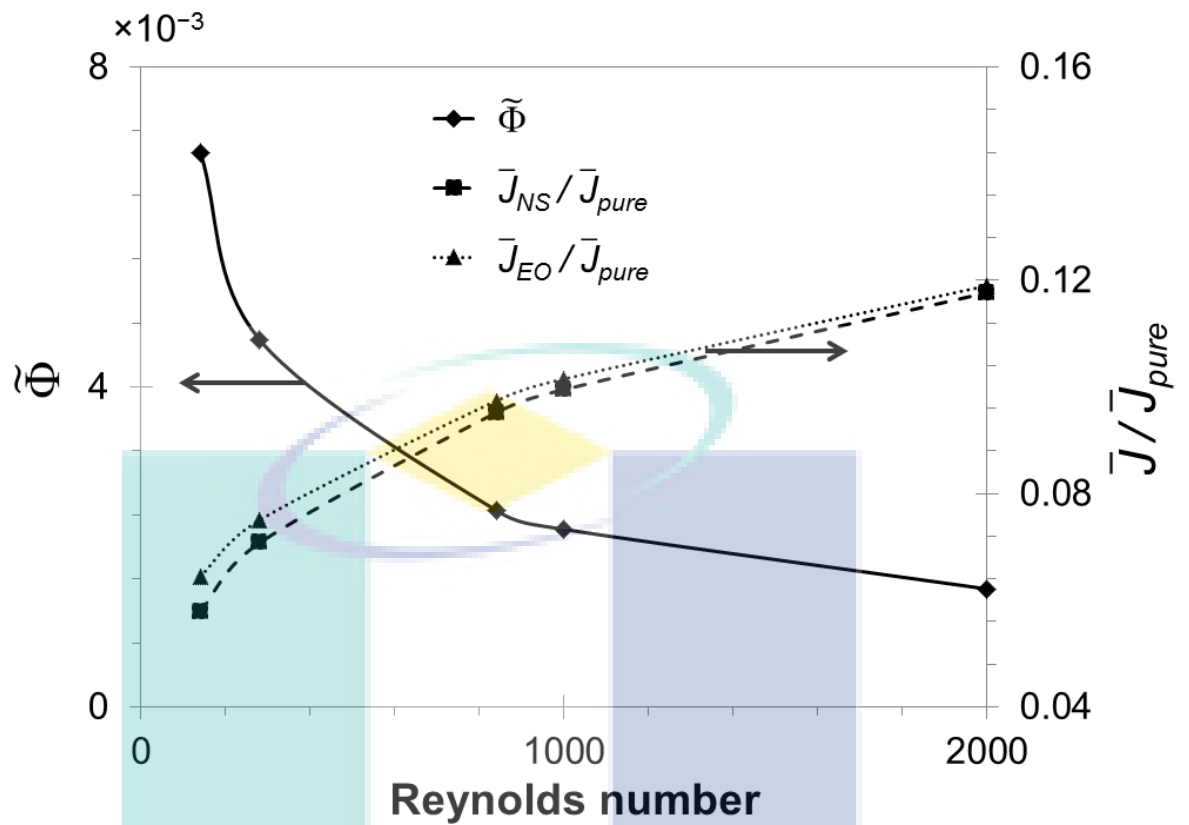


Figure 5.16: Effect of Reynolds number on permeate flux and electro-osmotic mass transfer enhancement, under constant transmembrane pressure.

It should be noted that one of the effects of spacers on mass transfer in the membrane channel is analogous to that of increasing the Reynolds number. This means that the mass transfer enhancement effect of electro-osmosis would be smaller for a channel with spacers than for an empty channel. Nevertheless, further mass transfer enhancement may be possible through interactions between electro-osmotic mixing and the mixing caused by the feed channel spacers, but such investigations are outside the scope of this chapter and are investigated in Chapter 7.

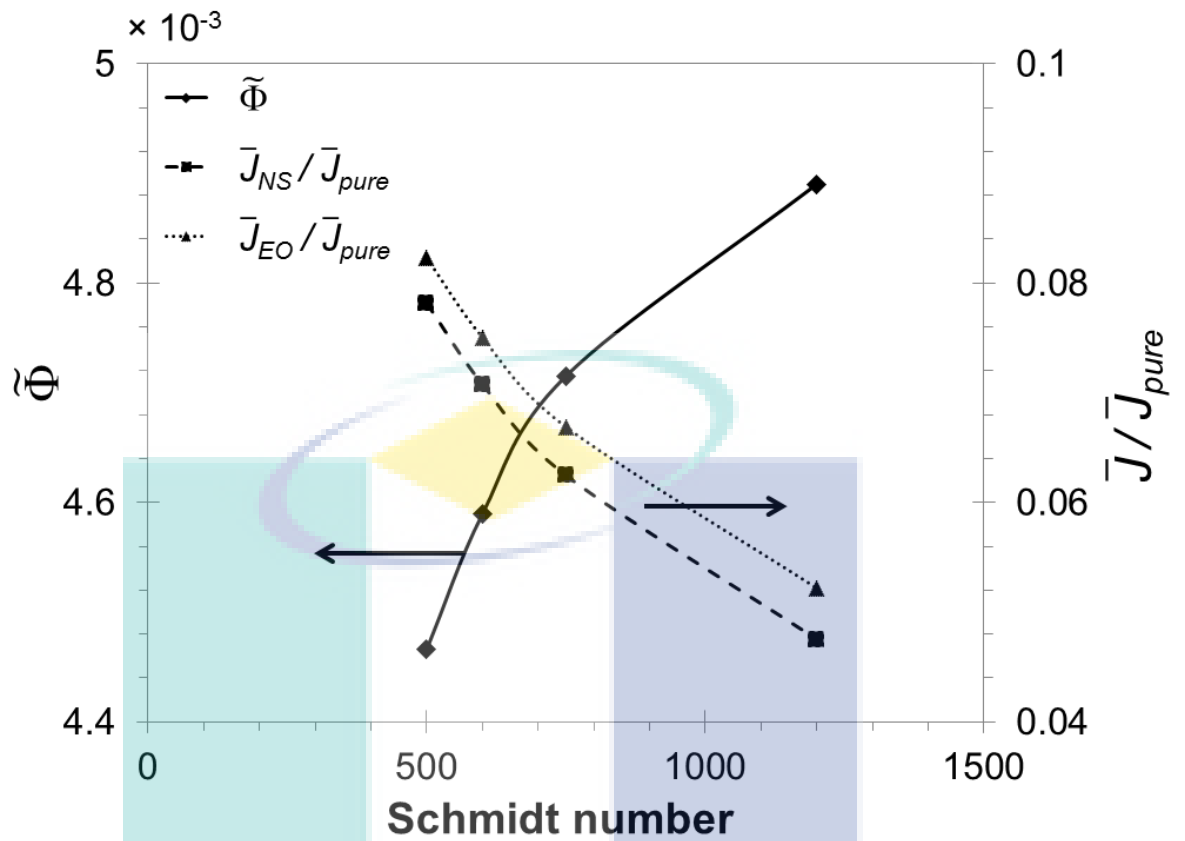


Figure 5.17: Effect of Schmidt number on permeate flux and electro-osmotic mass transfer enhancement, under constant transmembrane pressure.

Figure 5.17 shows that  $\tilde{\Phi}$  increases for an increase in Schmidt number. This trend agrees with the findings of Singh and Laurence [67], who report that a decrease in diffusivity at the same slip velocity leads to an increase in mass transfer enhancement compared to the case without slip. This can also be explained through equations (3.20) and (5.4). A larger Schmidt number (due to a lower solute diffusivity) results in a lower mass transfer coefficient, leading to an increased level of concentration polarisation and, therefore, more mixing potential. For this reason, electro-osmosis is more effective for systems with a larger Schmidt number.

Table 5.4 summarises the relationships of the effect of bulk flow conditions and intrinsic membrane properties on the effectiveness of electro-osmotic mass transfer and flux enhancement.

Table 5.4: Summary of the effect of bulk fluid conditions and membrane properties on concentration polarisation, mass transfer coefficient, flux and electro-osmotic mass transfer enhancement.

		Increase in parameter			
		$L_p$	$R$	$Re$	$Sc$
Effect on parameter	$\gamma$	↑	↓	↓	↑
	$k_{mt}$	↑ (EO)*	↓	↑	↓
	$J/J_{pure}$	↓	↓	↑	↓
	$\tilde{\Phi}$	↓	↓	↓	↑

\* For the no-slip case (NS),  $k_{mt}$  peaks around  $L_p = 2 \times 10^{-11} \text{ m s}^{-1} \text{ Pa}^{-1}$ .

## 5.7 Conclusions

This chapter presents the results of CFD simulations incorporating the effect of electro-osmotic mixing on the hydrodynamics and mass transfer, in an unobstructed empty 2D membrane channel with permeation, under steady state conditions. The cases considered involve a uniform or a non-uniform electro-osmotic forced slip velocity along the membrane surface. For all cases, the simulation results show that a slip velocity in the same direction as the bulk flow decreases the friction factor at the membrane surface, and leads to a decrease in concentration polarisation and an increase in permeate flux. The effect of friction factor agrees with analytical and experimental results, and is related to the changes to the velocity gradient at the membrane surface. The effect on mass transfer is related to the downstream convection of lower concentration fluid. The opposite results are obtained for a slip velocity in the opposite direction, as higher concentration fluid is convected upstream. It was also found that electro-osmosis is more effective in reducing concentration polarisation for a developing boundary layer than for a fully-developed boundary layer.

The results also show that a non-uniform slip velocity leads to a stronger effect due to electro-osmosis. Hence, a non-uniform net slip velocity in the direction of the bulk

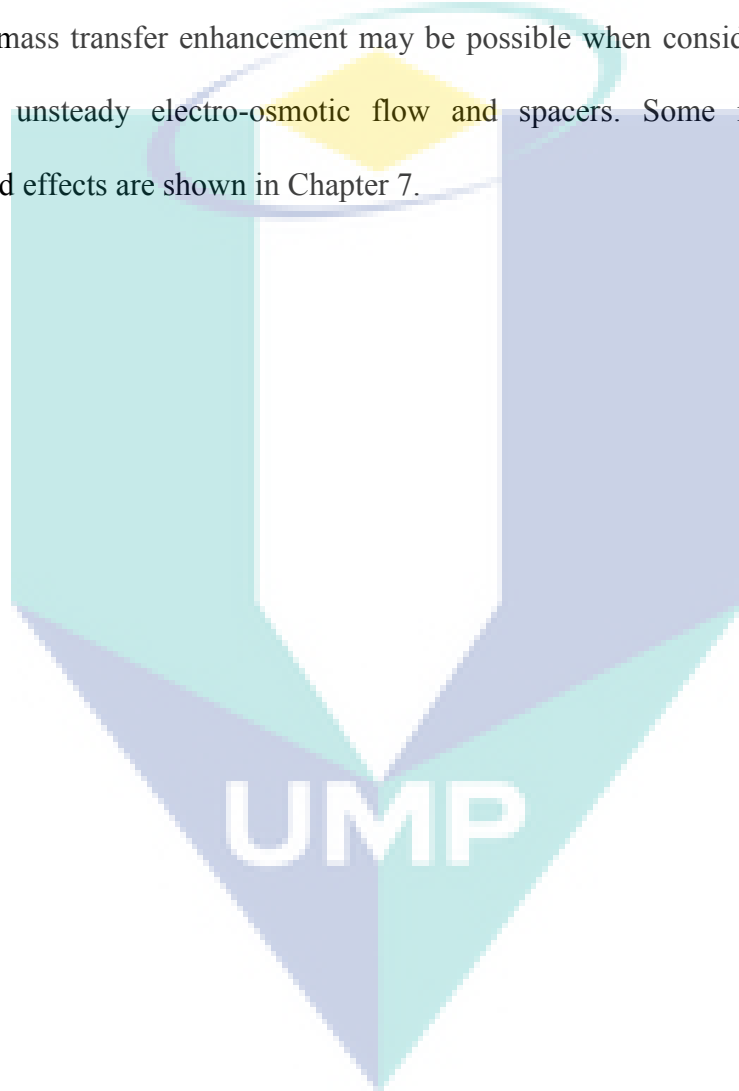
flow results in higher permeate flux enhancement at a similar friction factor, compared to the same case under uniform slip. This difference is caused by the variations in slip velocity, which lead to regions of flow towards and regions of flow away from the membrane surface, resulting in boundary layer renewal and less concentration polarisation. This suggests that the variations in slip velocity are one of the main drivers for mass transfer and permeate flux enhancement. Moreover, a non-uniform electric field configuration would be easier to implement than a uniform electric field, using smaller electrodes and requiring a lower voltage.

The relationships between bulk flow conditions and membrane properties on the effectiveness of electro-osmotic mixing and permeate enhancement under constant transmembrane pressure were also investigated. Effectiveness can be measured through the enhancement factor ( $\Phi$ ), which represents the relative change in concentration polarisation modulus ( $\gamma$ ). In terms of membrane permeability, the results show that electro-osmosis enhancement peaks at permeabilities in the range of brackish water RO membranes for the conditions presented in this chapter. This suggests that, electro-osmosis is more effective for brackish water than for seawater RO membranes, and is less effective for higher permeability membranes such as MF and UF. For the case of seawater RO membranes, electro-osmosis is generally more effective as the permeability is increased.

In terms of intrinsic membrane rejection, the data shows that electro-osmosis enhancement is greater for lower rejection. This suggests that electro-osmosis might be particularly suited for ultra-osmosis, where the membrane rejection characteristics fall between RO and UF. Electro-osmotic enhancement is also greater for solutes with a larger Schmidt number (lower diffusivity), which typically occurs with multivalent ions. Lower Reynolds numbers also lead to greater electro-osmotic enhancement. Therefore,

electro-osmosis might be useful for higher viscosity systems or for cases where lower cross-flow velocity is required to maximise recovery.

In this chapter, it is observed that the electro-osmotic mass transfer enhancement is marginal under the case of intense background mixing and unlikely to be useful in practical applications. Nevertheless, this chapter only considers the steady-state case. Greater mass transfer enhancement may be possible when considering the interactions between unsteady electro-osmotic flow and spacers. Some investigations of the combined effects are shown in Chapter 7.



## Chapter 6

### CFD modelling of unsteady-state electro-osmotic permeate flux enhancement in spiral-wound reverse osmosis membrane systems

#### membrane systems

#### 6.1 Introduction

Given that relatively larger mass transfer enhancement was observed for cases where the EOF was spatially-variant than for their spatially-uniform counterparts [126], a similar increase in mass transfer might be expected for an EOF that is time-variant. This raises interest in investigating temporal variations in slip velocity, especially since pulsatile flow has the potential to enhance wall shear and slow or eliminate the onset of particle fouling [92]. Although a recent study [146] analysed the effect of a time-varying EOF on the concentration boundary layer thickness, the effect on the maximum shear rate and time-averaged permeate flux have not yet been investigated. This chapter therefore focuses on analysing and identifying the mechanisms that lead to uniform unsteady electro-osmotic shear rate. Its effect on local and overall membrane performance is measured in terms of flux and maximum wall shear stress (as a proxy for fouling reduction).

#### 6.2 Problem description, assumptions and methods

##### 6.2.1 Model description

The unsteady-state continuity, momentum and mass transfer equations are solved using CFD ANSYS CFX-15.0. The channel and electrode geometry are shown in Figure 6.1. Entrance and exit regions are included at each end of the membrane channel

to ensure the flow solution is not influenced by the inlet and outlet boundary condition [19-21]. The electrode geometry illustrated in Figure 6.1 consists of the placement of two flat-plate electrodes at each end of the channel and perpendicular to the bulk flow direction, which leads to a spatially uniform slip velocity.

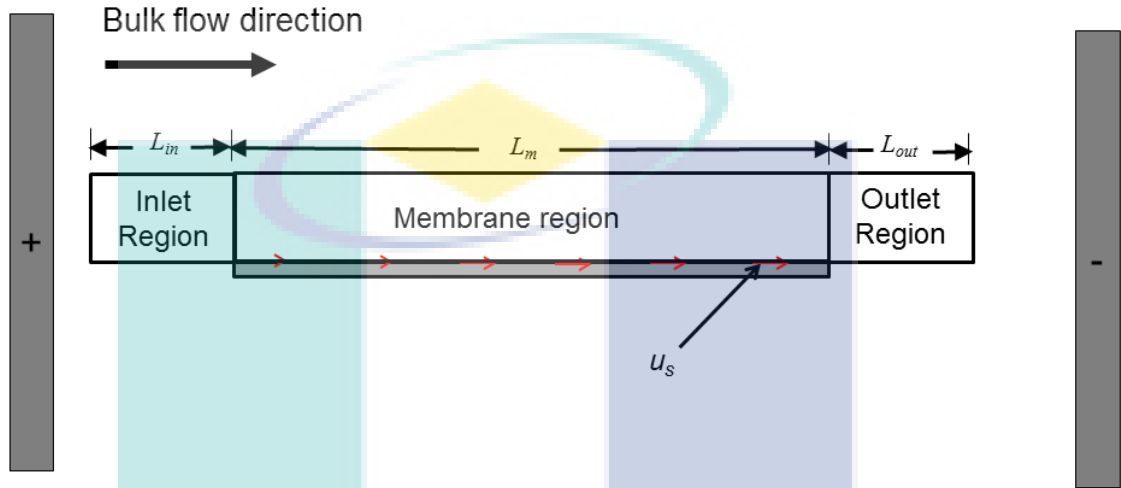


Figure 6.1: Schematic of membrane channel and electrode geometry indicating boundary locations (not to scale).

### 6.2.1.1 Boundary conditions

The conditions at the boundaries of the fluid domain are set following the approach in Table 3.3. A time-varying EOF disturbance is incorporated as a sinusoidal slip velocity, which can be written as follows [135]:

$$u_{s,t} = \bar{u}_s + u_{s,A}[\sin(2\pi f_s t)] \quad (6.1)$$

where  $t$  is time,  $f_s$  and  $u_{s,A}$  are the oscillation frequency and amplitude respectively, and  $\bar{u}_s$  is the time-averaged slip velocity. The slip velocity amplitude and time-averaged values shown in equation 6.1 are chosen so that at any time the slip velocity is positive (in the same direction as the bulk flow), as it was found previously [126] that a positive slip velocity enhances mass transfer and increases permeate flux. The first and second terms on the right hand side of equation 6.1 can be interpreted as the offset and oscillating components of velocity respectively.

### 6.2.1.2 Assumption and cases

An adaptive time step is used throughout the simulations with a minimum time step of  $10^{-10}$  s and a maximum Courant number of 5. The fluid domain is discretised using a mesh with a Grid Convergence Index (GCI) below 1% for both mass transfer and permeate flux. The reference conditions for the simulations are based on typical RO conditions, and are presented in Table 6.1.

Table 6.1: Parameters used for uniform electric field case study.

Parameter	Value
Feed channel height ( $h_{ch}$ )	1 mm
Feed flow rate ( $u_{b0}$ )	0.14 m/s
Entrance length ( $L_{in}$ )	10 mm
Exit length ( $L_{out}$ )	40 mm
Membrane length ( $L_m$ )	50 mm
Reynolds number ( $Re$ )	280
Schmidt number ( $Sc$ )	600
Diffusivity coefficient ( $D$ )	$1.67 \times 10^{-9}$ m <sup>2</sup> /s
Intrinsic rejection ( $R$ )	99.6 %
Membrane permeability ( $L_p$ )	$3.9 \times 10^{-11}$ m s <sup>-1</sup> Pa <sup>-1</sup>
Reflection coefficient ( $\sigma$ )	1
Osmotic pressure coefficient ( $\phi$ )	80.51 MPa
Inlet transmembrane Pressure ( $\Delta p_{im}$ )	2.94 MPa
Time-averaged slip velocity ( $\bar{u}_s$ )	$4 \times 10^{-4}$ m/s
RMS slip velocity ( $u_{s,RMS}$ )	$4.9 \times 10^{-4}$ m/s

The influence of frequency and amplitude of slip velocity on the effectiveness of electro-osmosis is investigated under constant transmembrane pressure, and their value ranges are summarised in Table 6.2. Given common zeta potential values for RO membranes, typical electric field magnitudes employed in microchannels would give rise to EOF velocities of the order of 100  $\mu$ m/s [20, 147], hence these values are

simulated in this chapter. The effect of changes in frequency and amplitude on the slip velocity time series are depicted in Figure 6.2.

Table 6.2: Ranges of frequency and amplitude of slip velocity considered.

Parameter	Range
Frequency ( $f_s$ )	0.25 – 1000 Hz
Oscillation amplitude of slip velocity ( $u_{s,A}$ )	$1 \times 10^{-4}$ – $4 \times 10^{-4}$ m s <sup>-1</sup>

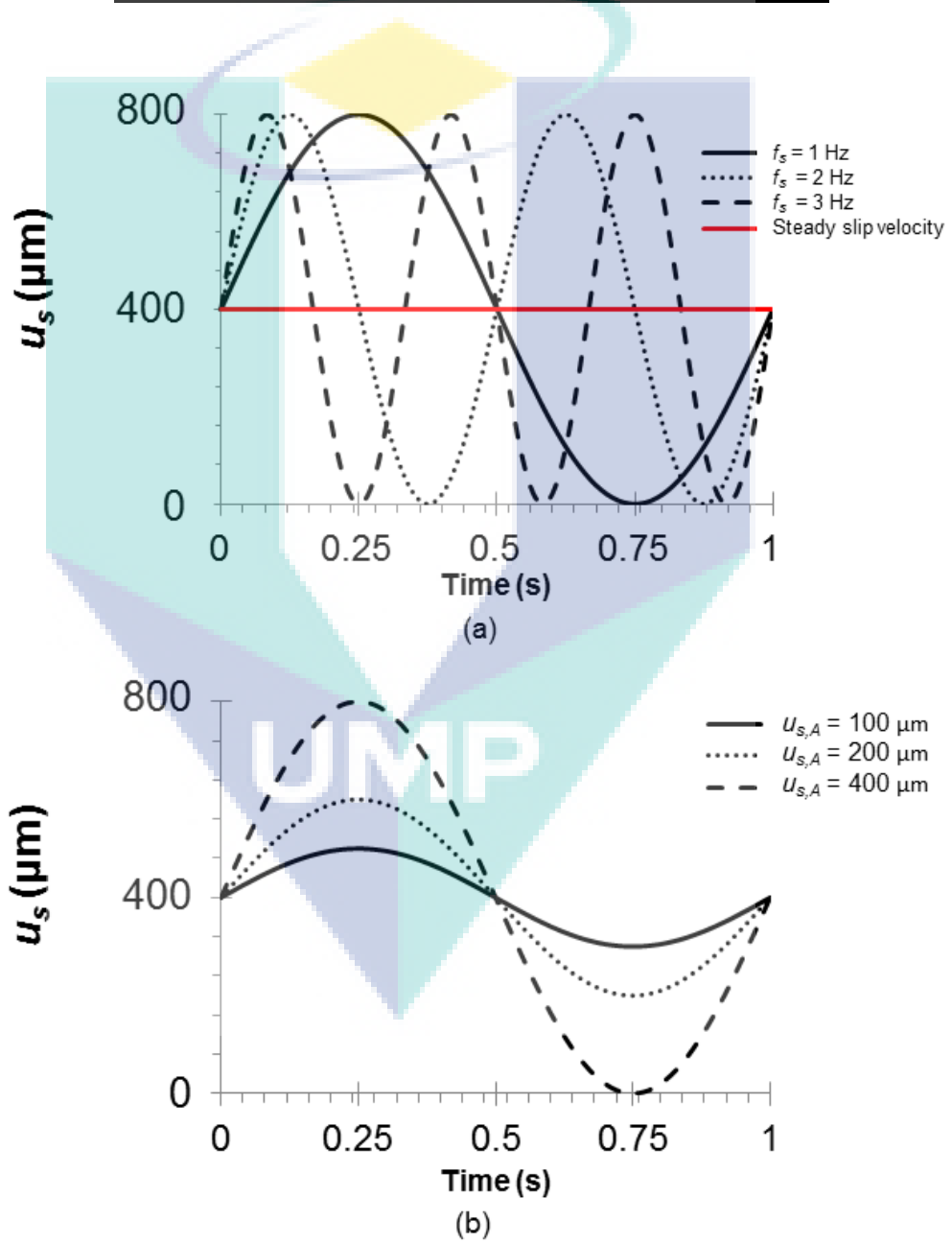


Figure 6.2: Effect on the slip velocity time-series for (a) changes in slip velocity frequency, and (b) changes in slip velocity amplitude.

## 6.2.2 Methodology of analysis of results

The area used for the calculation of global variables is the total membrane area excluding 10 mm from each end of membrane channel. These entrance and exit regions are neglected to remove mathematical entrance and exit effects. Furthermore, membrane lengths for commercial spiral wound modules (SWM) for RO are typically 100 times larger than the simulated case, so the entrance and exit effects will contribute little to the overall membrane performance.

It should be noted that slip velocity does not have an effect on  $J_{pure}$ , because in that case the concentration is zero everywhere in the channel. As there is no mass transfer, slip velocity has no effect on the water flux. The slip velocity affects the velocity boundary condition and, consequently, the velocity gradient at the wall  $\left(\frac{\partial u}{\partial y}\right)_w$  and the wall shear. The effect of a uniform slip velocity on the bulk flow velocity ( $u_b$ ) can be considered small because the membrane area simulated in this chapter is too small for the permeation flux to significantly decrease the feed flow rate.

The maximum  $x$ -component perturbation velocity ( $\hat{u}_p$ ) for a specific location is calculated as the difference between the local velocity in the  $x$  direction ( $\hat{u}$ ) taken at the maximum slip velocity and the constant time-averaged slip velocity ( $\bar{u}_{ss}$ ).

$$\hat{U}_p = \frac{\hat{u}_p}{u_{bo}} = \frac{\hat{u} - \bar{u}_s}{u_{bo}} \quad (6.2)$$

The results for each case with a time-varying slip velocity are compared against two steady-state slip velocity cases, where one has a slip velocity with the same root mean square ( $u_{s,RMS}$ ) as the time-varying slip velocity, and the other one has the same time-averaged slip velocity value ( $\bar{u}_s$ ).

The root means square (RMS) of the slip velocity is a proxy for kinetic energy, which is a measure of the amount of energy input to the system. The RMS slip velocity ( $u_{s,RMS}$ ) is calculated over one sinusoidal cycle:

$$u_{s,RMS} = \sqrt{\frac{1}{t_2-t_1} \int_{t_1}^{t_2} [u_{s,t}]^2 dt} \quad (6.3)$$

The steady-state slip velocity equivalent to the time-averaged value is investigated because it is unclear whether frequency or amplitude of slip velocity (equation 6.1) has an effect on the time-averaged outputs (shear stress, flux and concentration polarisation).

### 6.3 Validation

For any simulation study, model validation is crucial. There are very limited data and correlations available in the literature that can be used to validate the simulation results in this chapter because of the nature of the phenomena being considered. However, Setiawan et al. [148] recently proposed a reduced-order model (ROM) that combines the discretised mass transfer and linearized Navier-Stokes partial differential equations subjected to external and unsteady electro-osmotic flow in a 2D channel. The Navier-Stokes and mass transfer equations are simplified by omitting terms that are second order in the perturbation variables. Their model incorporates mass transfer in the form of a dissolving wall (i.e. no permeation) and was shown to be in excellent agreement with CFD simulation results. Although the model in this chapter directly includes permeation, the permeation velocity is at least 3 orders of magnitude lower than the average fluid velocity, so the effect of fluid extraction on hydrodynamics, mass transfer and the subsequent variation of Reynolds number along the short membrane channel is very small (of the order of 0.01 to 0.1 %) [35]. Therefore, in order to validate the hydrodynamic results, the model used in this chapter was tested under similar conditions as those of Setiawan et al. [148].

Figure 6.3 compares the profiles of perturbation velocity ( $U_p$ ) defined by equation (6.2), along the channel height for different frequencies at  $X = 35$ . At this  $X$  location, the flow can be considered practically fully-developed and the wall shear does not change significantly other than through the effect of permeation. The model comparison presented in Figure 6.3 has a maximum area weighted error below 1 % with the main features of velocity perturbation being closely reproduced with respect to channel height. Because the main mass transfer enhancement mechanism in a membrane channel is through hydrodynamics, this provides confidence in the model predictions.

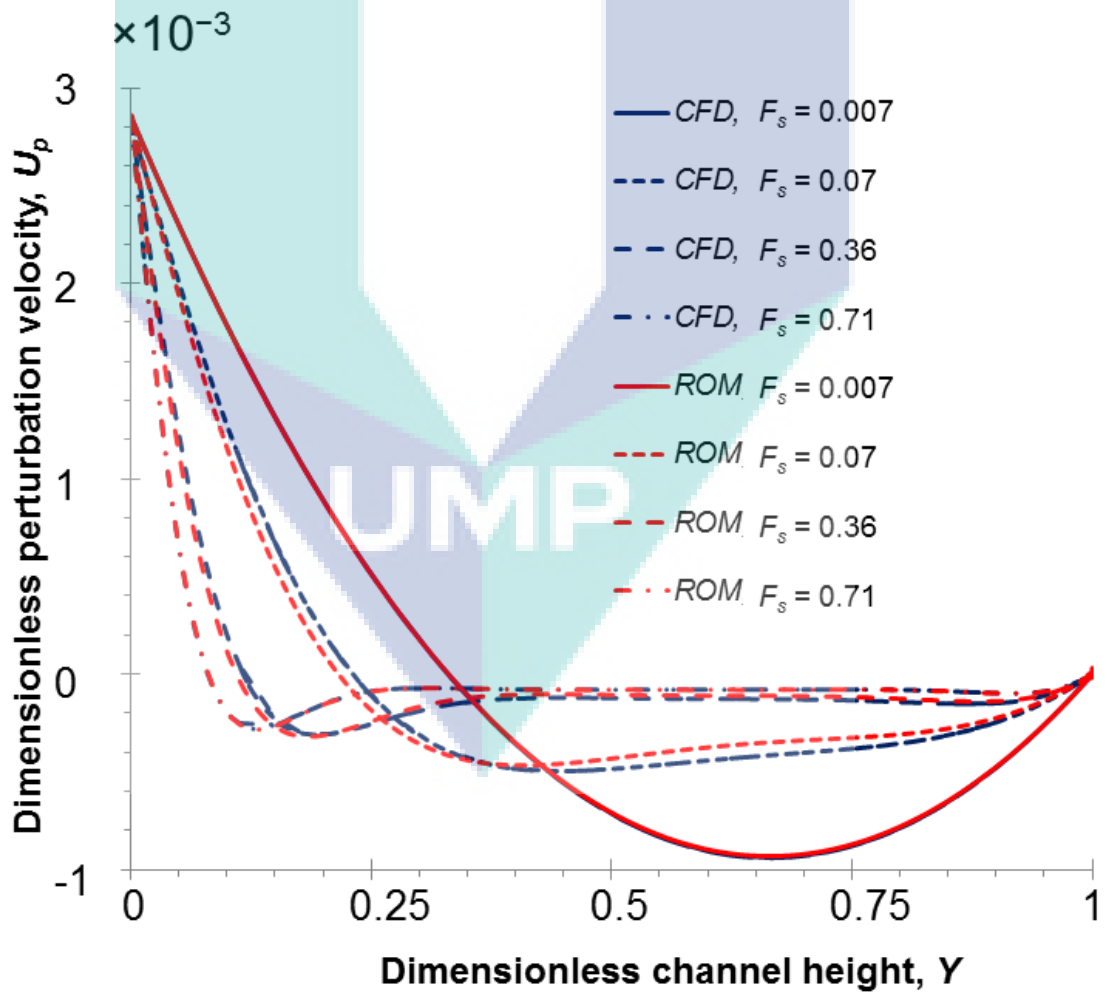


Figure 6.3: Changes in perturbation velocity  $U_p$  along  $Y$  for  $X = 35$  and  $U_s = 0.0029 \pm 0.0029$  at different dimensionless frequencies for the CFD model in this chapter and the reduced order model (ROM) of Setiawan et al. [148].

## 6.4 Results and discussion

### 6.4.1 Unsteady EOF

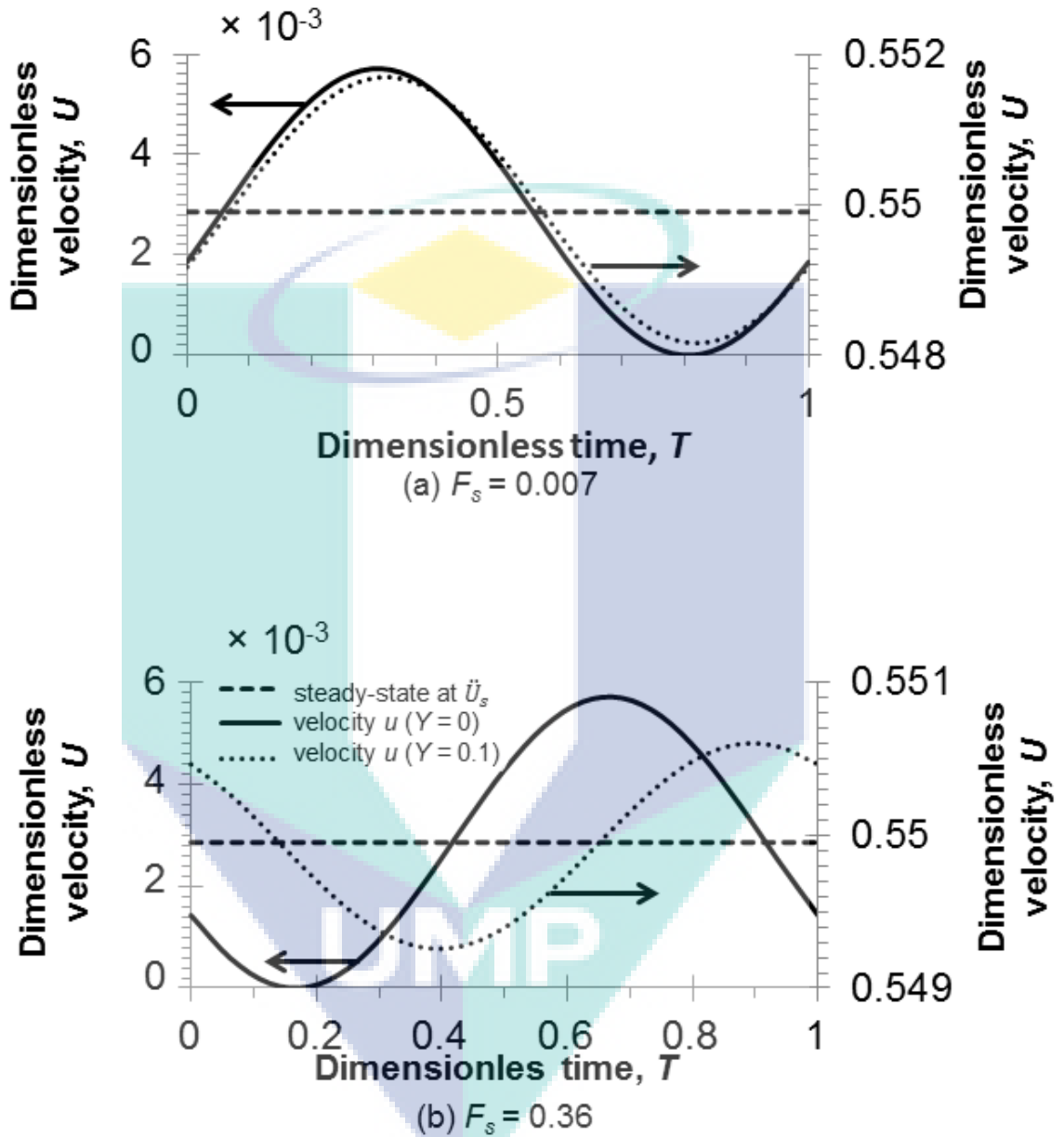


Figure 6.4: Changes in dimensionless velocity,  $U$  along time for (a)  $F = 0.007$  and (b)  $F = 0.36$ .

As shown in Figure 6.4, when the slip velocity oscillation frequency is low (e.g.  $F_s = 0.007$ ), the slip velocity-induced flow perturbations extend through the entire channel height. The changes in slip velocity not only affect the region close to the membrane but also the bulk flow, causing oscillations throughout the channel height. As the slip velocity oscillation frequency increases, the region affected by flow

perturbations becomes smaller, being restricted to less than 25 % of the channel height for  $F_s = 0.71$ . Further, the response of the flow to the slip velocity away from the membrane lags that of the oscillating slip velocity. This is shown in Figure 6.4, where the velocity away from the wall ( $Y = 0.1$ ) lags about  $T = 0.25$  behind the oscillating slip velocity for a higher frequency ( $F_s = 0.36$ ) but there is little lag (around  $T = 0.02$ ) for a lower frequency ( $F_s = 0.007$ ). The reason that the flow in the centre and top half of the channel is not perturbed at higher frequencies is because, as the frequency increases, the slip velocity changes its direction at a faster rate than the fluid above the membrane can respond due to inertial effects.

The effect of slip velocity frequency on penetration depth has been studied in detail by Stokes [104] who developed an analytical solution for the case of an oscillating wall without cross flow or permeation, when the flow is unbounded. He defines the penetration depth induced by an oscillating wall as the location where the perturbation has a value equal to 1% of the maximum slip velocity. The analytical solution shows that the penetration depth can be calculated using equation (6.4).

$$\delta_{st} = 4.6 \sqrt{\frac{\mu}{\pi \rho f_s}} \quad (6.4)$$

As shown in Figure 6.5, the trend of penetration depth for the CFD results agrees well with the Stokes penetration depth prediction, except when the dimensionless frequency is below around 0.1. This discrepancy is mainly because the Stokes penetration depth assumes the flow is unbounded whereas the flow in this chapter is bounded by a top wall and, thus, the penetration depth cannot be larger than the channel height ( $Y = 1$ ).

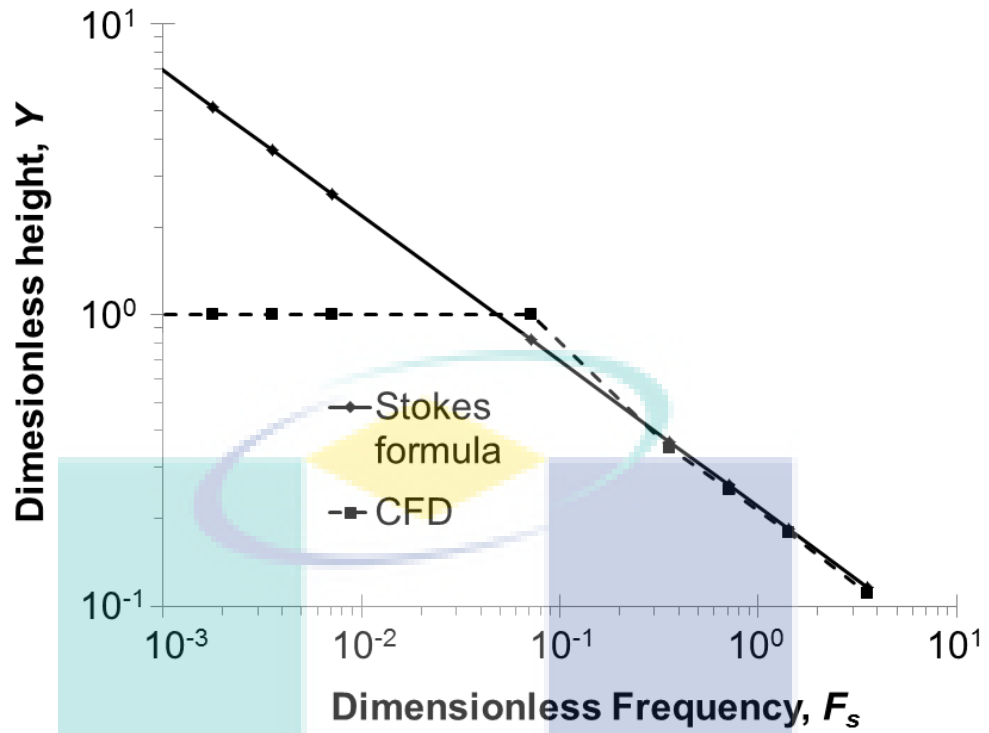


Figure 6.5: Changes in penetration depth for different slip velocity frequencies (Hz)  $U_s = 0.0029 \pm 0.0029$ .

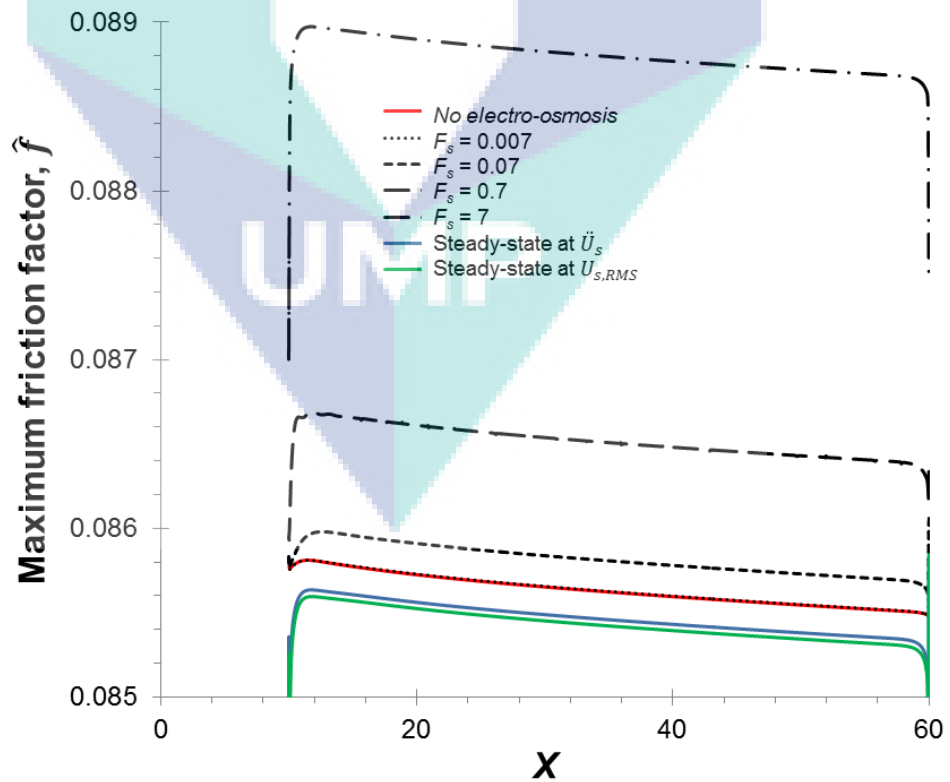


Figure 6.6: Maximum local friction factor profile along the membrane surface for unsteady slip  $U_s = 0.0029 \pm 0.0029$  at different frequencies, and steady slip at  $\dot{U}_s$  and  $U_{s,RMS}$ .

Figure 6.6 shows the effect of an unsteady spatially-uniform electro-osmotic slip along the membrane surface on the hydrodynamics, for different dimensionless frequency values. It shows that the maximum friction factor (and hence, wall shear) decreases slightly along the channel length, by less than 0.5 % of its value at the channel entrance. This decrease is attributed to permeation, which reduces the amount of fluid flowing in the channel (of the order of 0.01 to 0.1 % for the length of channel simulated in this chapter). This change is small because, the amount of fluid removed per unit length through permeation in reverse osmosis is usually significantly less than the bulk flow [35]. Figure 6.6 shows that the friction factor for the cases with steady-state slip velocity (either  $\dot{U}_s$  or  $U_{s,RMS}$ ) are lower than for the case without electro-osmosis. This agrees with our previous finding [126] that an increase in slip velocity results in a decrease in friction factor because of a lower  $u$ -velocity gradient normal to the membrane wall. It can also be seen in Figure 6.6 that the maximum friction factor increases as the frequency is increased. Further, abrupt changes in the maximum friction factor can be noticed at both ends of the membrane channel, which are consistent with our previous findings [149]. These abrupt changes occur because of the step change in zeta potential at both ends of the membrane region. Because there is no slip velocity outside of the membrane region, and thus no oscillations in friction factor, there is no change in friction factor.

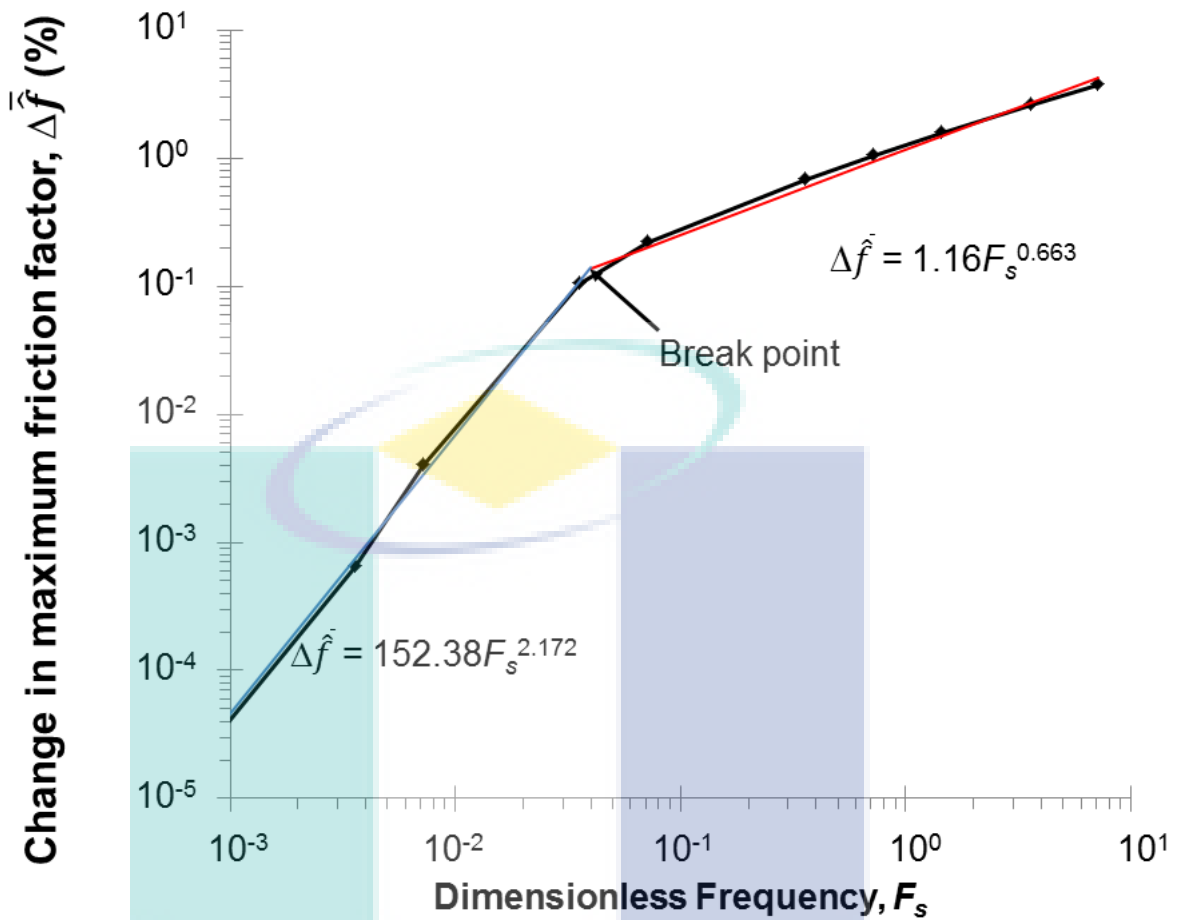


Figure 6.7: Effect of frequency on relative change in maximum friction factor for  $U_s = 0.0029 \pm 0.0029$ .

The increasing trend in maximum friction factor seen in Figure 6.6 as the dimensionless frequency increases is confirmed in Figure 6.7. The effect of frequency on friction factor can be approximately divided into two regions. Below  $F_s$  of about 0.04, the slope of the line is greater, and above that value the slope is smaller. The  $F_s$  at which the transition between the two regions occurs in Figure 6.7 is roughly the same as the  $F_s$  at which the penetration depth reaches the height of the channel ( $\delta_{st}/h_{ch} = 1$ ) in Figure 6.5. This suggests that above this transition frequency ( $F_{s,tr}$ ), the perturbations do not reach the opposite membrane channel wall and any friction related effects are confined to the lower membrane wall, decreasing the rate at which friction factor and shear increase as frequency increases. In terms of Reynolds number and  $F_{s,tr}$  (the

dimensionless transition frequency, at which the penetration depth is equal to the channel height), equation 6.4 can be rearranged to give:

$$F_{s,tr} = \frac{42.32}{\pi Re} \quad (6.5)$$

Equation 6.5 predicts a dimensionless transition frequency of 0.048 for the conditions in Figure 6.7 ( $Re = 280$ ), which roughly agrees with the value shown on that figure. The equation also predicts that the transition frequency is inversely proportional to the Reynolds number. Hence, for systems with a lower Reynolds number (e.g. due to a higher viscosity), the transition would occur at a higher frequency. Conversely,  $F_{s,tr}$  should be lower for systems with a higher Reynolds number.

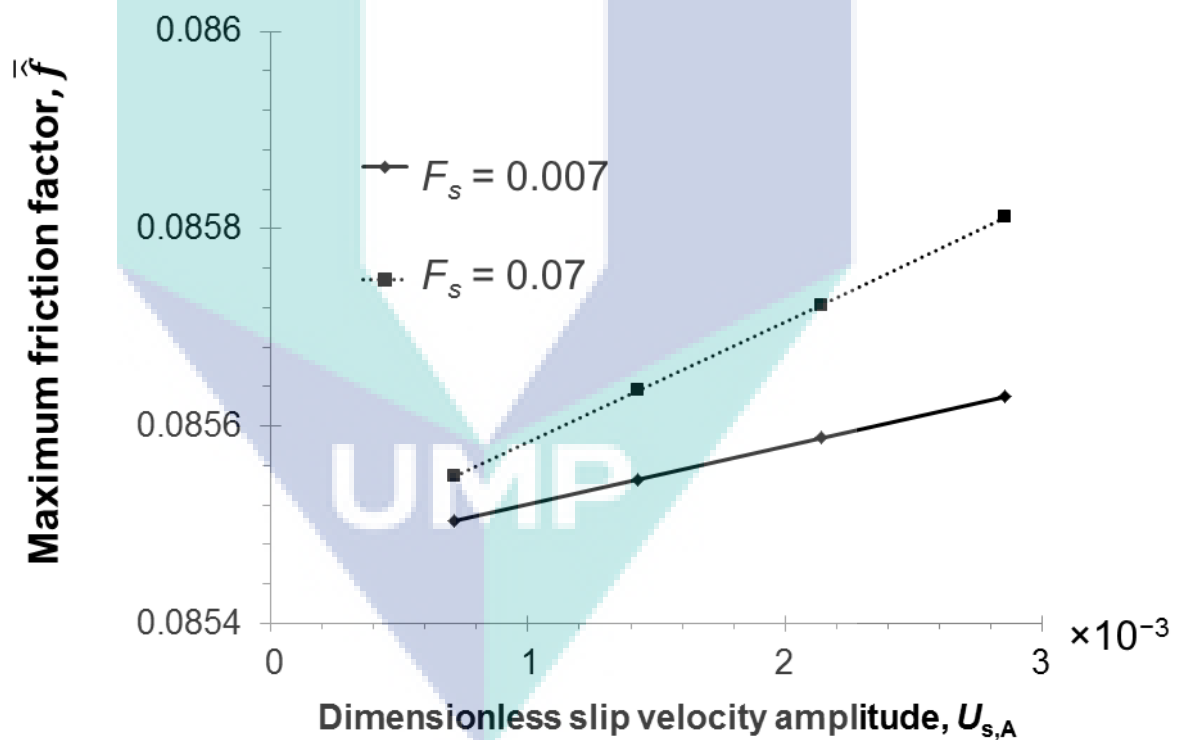


Figure 6.8: Effect of slip velocity amplitude on maximum friction factor.

The slip velocity amplitude ( $U_{s,A}$ ) is another important parameter of the slip velocity input (equation 6.1), as it determines the magnitude of the perturbation. In this analysis,  $U_{s,A}$  is varied while keeping the time-averaged slip velocity ( $\bar{u}_s$ ) constant. Figure 6.8 shows that an increase in  $U_{s,A}$  results in a linear increase in maximum friction factor. As shown in our previous work [126], friction factor decreases linearly as the slip velocity increases in the bulk flow direction. Hence, it is expected that the maximum friction factor occurs at the minimum slip velocity value and vice versa.

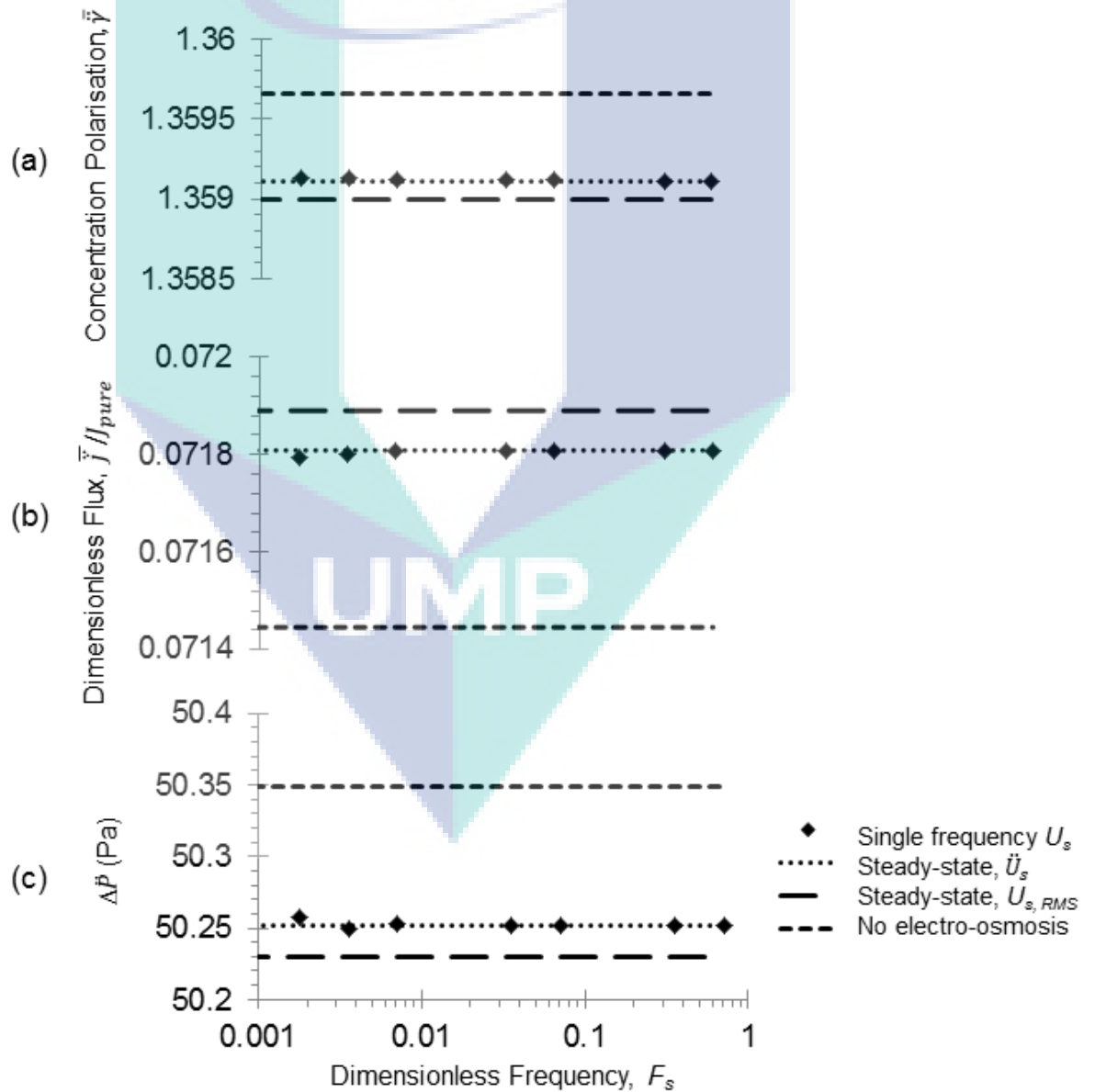


Figure 6.9: Effect of frequency on (a) concentration polarisation, (b) permeate flux and (c) pressure drop for  $U_s = 0.0029 \pm 0.0029$ .

The effect of frequency on time-averaged concentration polarisation ( $\bar{\gamma}$ ), dimensionless permeate flux ( $\bar{j}$ ), and time-averaged pressure drop ( $\Delta\bar{P}$ ) for  $U_s = 0.0029 \pm 0.0029$  is shown in Figure 6.9. As can be seen in this figure, there are only marginal changes in  $\bar{\gamma}$ ,  $\bar{j}$ , and  $\Delta\bar{P}$  as the frequency is varied. The increase in permeate flux relative to the case without electro-osmosis is between 0.48 % and 0.5 % for  $F_s$  values below 0.01 and remains at 0.5 % for frequencies above  $F_s = 0.01$ . This is because, as the slip velocity oscillates around the time-averaged value (as shown in Figure 6.4a), so do the flux and concentration polarisation, as shown in Figure 6.10. The positive and negative effects of slip velocity on permeate flux are of similar magnitude and almost cancel each other. Hence, the time-averaged mass transfer for an unsteady slip velocity is similar to the mass transfer resulting from a steady-state slip velocity equivalent to  $\bar{U}_s$ .

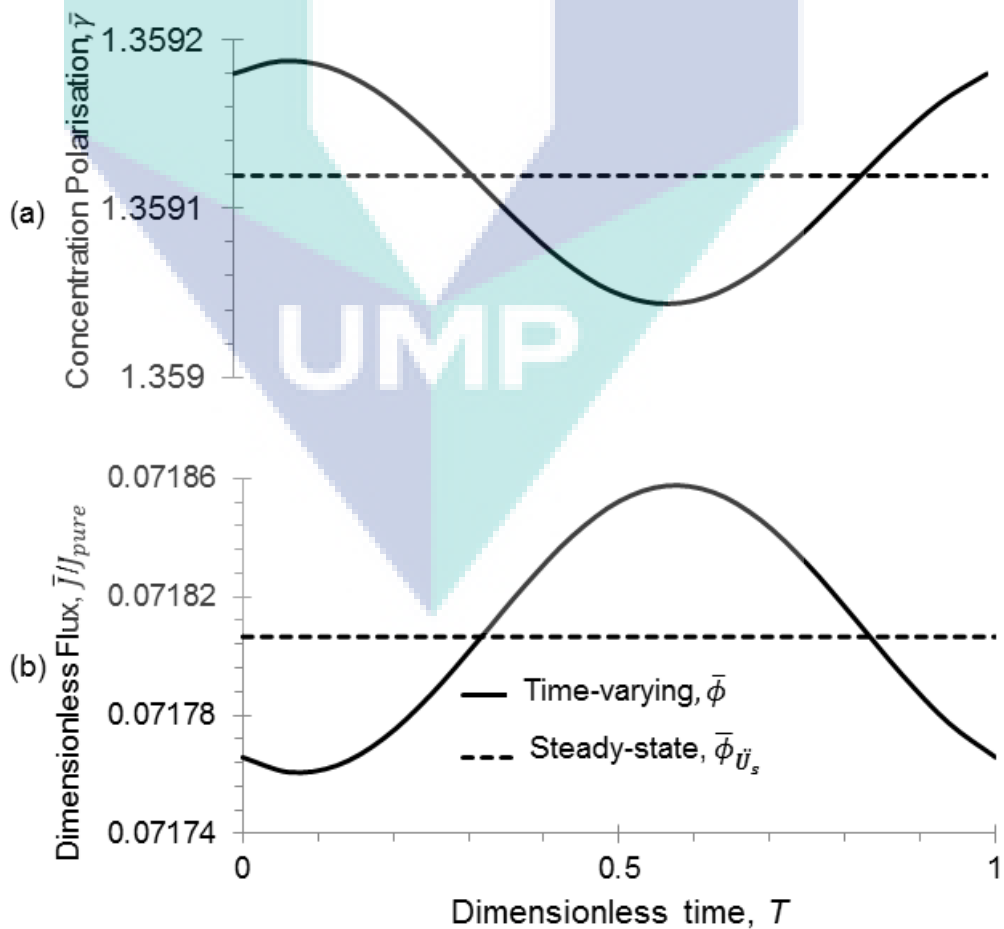


Figure 6.10: Changes in (a) concentration polarisation and (b) dimensionless flux in time for  $F_s=0.007$ .

In Figure 6.8, it is seen that the maximum wall shear (output) has a linear dependence on the amplitude of the slip velocity (input). This suggests that the system investigated in this chapter is linear. Therefore, linear system analysis, a well-developed field [150], could be adopted to gain insights into this system. In order to confirm whether the system is linear, it must obey certain rules. There are two basic tests of linearity, namely homogeneity and additivity.

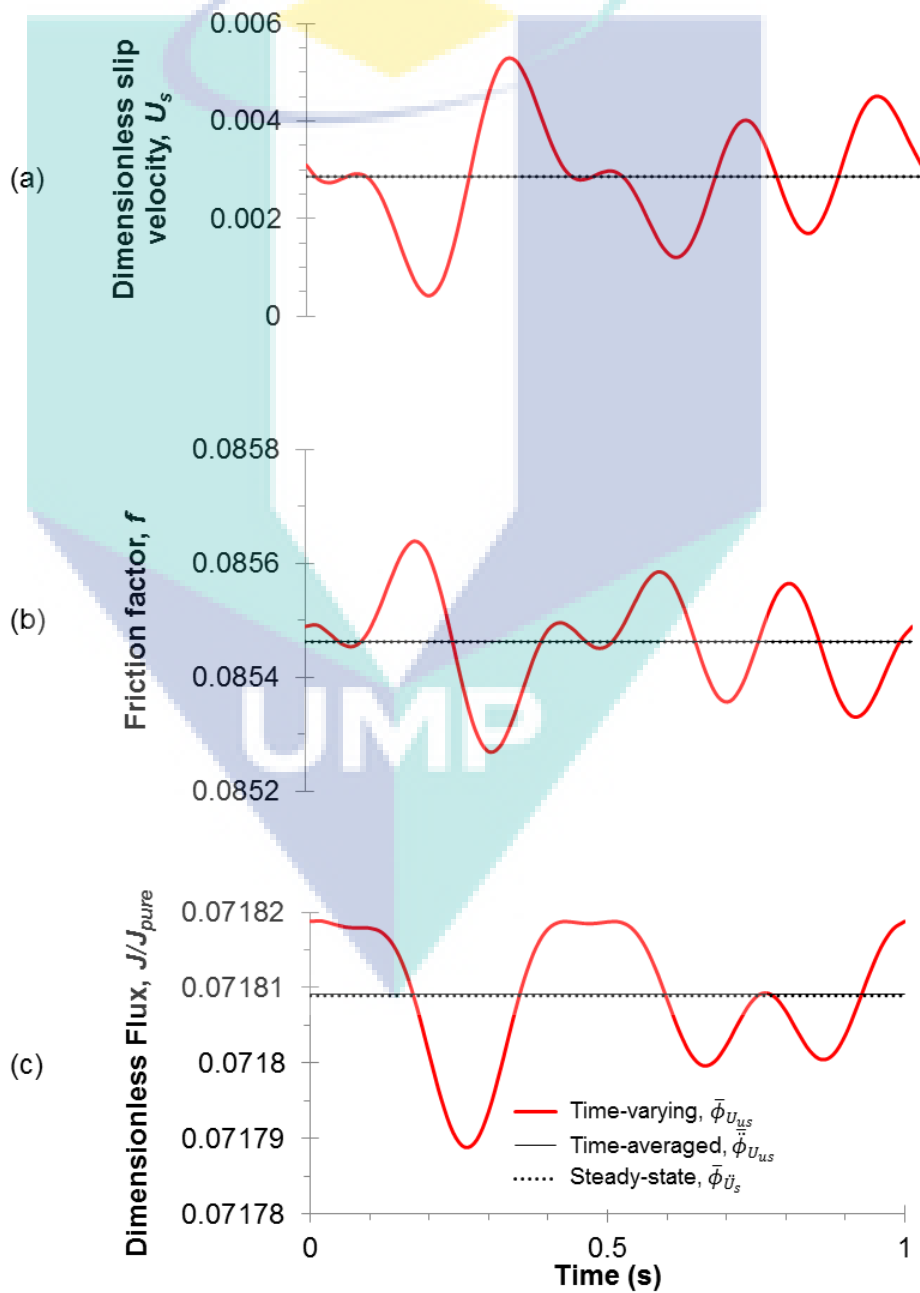


Figure 6.11: Effect of multiple frequency slip velocity,  $U_s$  ( $F_s = 0.014, 0.021, 0.029$ ) on friction factor and flux.

Additivity states that the measured output response must be equal to the sum of the individual responses of all of the components of the input [150]. For hydrodynamics, the time-averaged wall shear should be equivalent to the wall shear resulting from the time-averaged slip velocity, because a constant slip velocity can be defined as the sum of two sinusoidal slip velocity time series of the same frequency and amplitude, each out of phase with the other by  $180^\circ$ . The time-averaged effect should hold, regardless of the waveform of the slip velocity, because the transient effect of slip velocity will always cancel out. Results of a simulation study shown in Figure 6.11 confirm this effect. Figure 6.11a shows an unsteady slip velocity  $u_s$  input composed of oscillations at frequencies of 2, 3 and 5 Hz. The corresponding time-averaged wall shear is equivalent to the wall shear resulting from a steady-state slip velocity  $\bar{u}_s$  as shown in Figure 6.11b.

For mass transfer, the time-averaged concentration polarisation and permeate flux for an unsteady slip velocity  $u_s$  composed of oscillations at different frequencies (shown in Figure 6.11a) is equivalent to the results obtained from a steady-state slip velocity  $\bar{u}_s$  as shown in Figure 6.11c. This analysis therefore confirms that the time-averaged variables are the same, for the range of conditions investigated. Hence, the system passes the additivity test.

Homogeneity states that when the amplitude of the input increases, the amplitude of the output must increase proportionally [150]. This test is shown for slip velocity and maximum wall shear in Figure 6.8. For mass transfer, Figure 6.12 shows that the amplitude of the slip velocity (input) and the amplitude of the solute concentration at the membrane surface (output) form a linear system. Thus, the results of Figure 6.8 and Figure 6.12 confirm that the EOF-friction factor and EOF-wall solute concentration systems are linear for the range of conditions investigated.

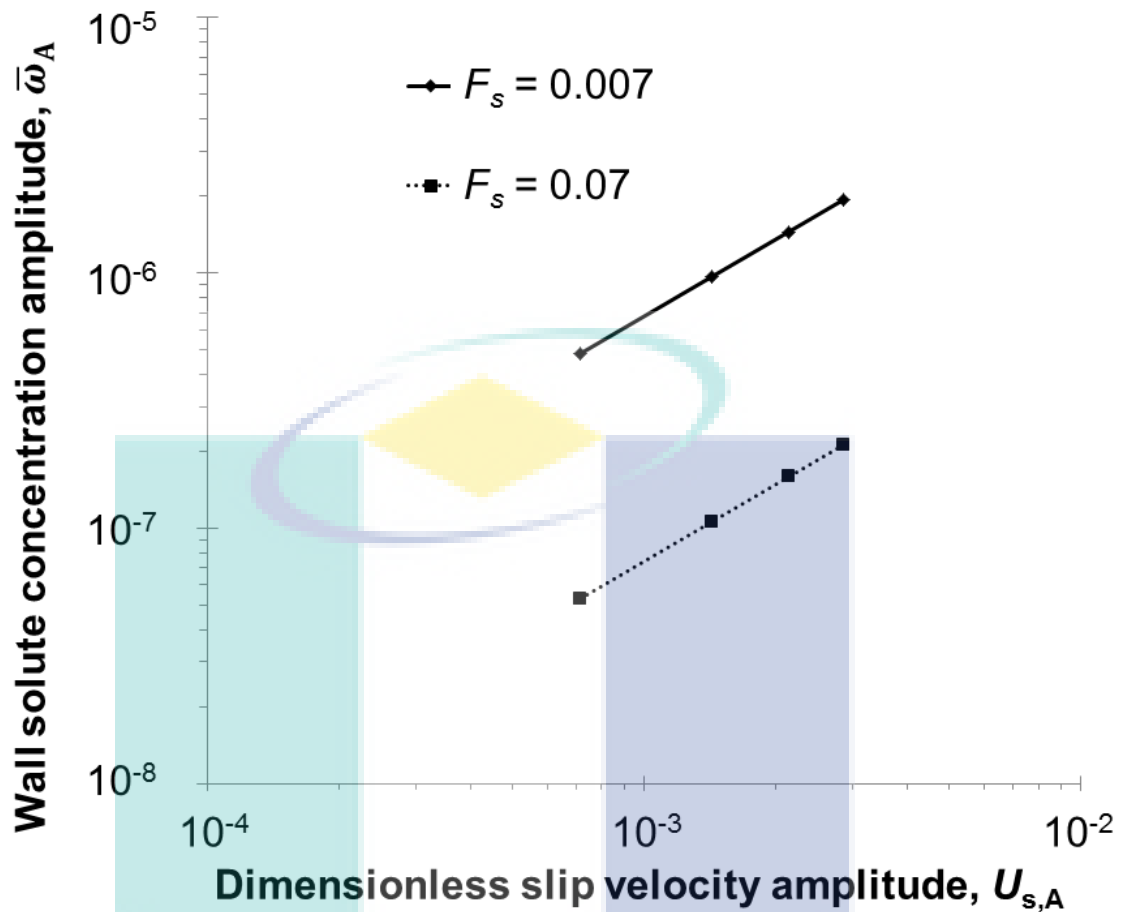


Figure 6.12: Effect of slip velocity amplitude on wall solute concentration.

#### 6.4.2 Comparison of results for different cases

Table 6.3 summarises the comparison between the results for unsteady and either no EOF or steady EOF, in terms of maximum shear/friction factor along with maximum percentage change with time-averaged concentration polarisation, flux and pressure drop for the range of conditions simulated in this chapter. As shown in Figure 6.6, the friction factor for steady-state EOF at  $\dot{U}_s$  and  $U_{s,RMS}$  are lower than for the case without EOF and, thus, a decrease in wall shear ( $-0.192\%$  and  $-0.235\%$  respectively) is observed. In contrast, as shown in Figure 6.7, unsteady EOF results in an increase of maximum friction factor ( $3.71\%$ ) from no EOF. This means that, as shown in Figure 6.6, unsteady EOF results in an even higher maximum wall stress compared to steady-state EOF at  $\dot{U}_s$  or  $U_{s,RMS}$  ( $3.91\%$  or  $3.95\%$  respectively). Given that the maximum

shear stress is proportional to the maximum friction factor (equation 3.21) and a higher shear stress reduces the effect of fouling, this represents an advantage for unsteady EOF over steady EOF in terms of fouling reduction.

For pressure drop, as shown in Figure 6.9, unsteady EOF results in a decrease in pressure drop ( $-0.2\%$ ) compared to no EOF. Figure 6.9 also shows that unsteady slip velocity results in similar time-averaged pressure drop to steady-state EOF at  $\ddot{U}_s$  or a marginally higher time-averaged pressure drop ( $0.05\%$ ) than steady-state EOF at  $U_{s,RMS}$ . For mass transfer, the time-averaged permeate flux for the unsteady slip case is marginally larger ( $0.51\%$ ) than for the no-EOF case. Further, time-averaged permeate flux for the unsteady slip velocity is similar to permeate flux obtained for steady-state EOF at  $\ddot{U}_s$ , or marginally lower ( $-0.13\%$ ) than permeate flux obtained for steady-state EOF at  $U_{s,RMS}$ . Although the time-averaged effects of unsteady uniform EOF on mass transfer are not significant, there are still benefits in terms of fouling reduction/removal as larger frequency and amplitude of slip velocity increase the maximum wall stress with a negligible change in pressure drop.

Table 6.3: Summary of the effect of uniform sinusoidal electro-osmotic flow perturbations and comparison against steady-state with the maximum percentage change for the range of conditions simulated in this chapter.

Variable, $\phi$		Comparison of effect of unsteady ( $U_{us}$ ) against no EOF ( $U_{NS}$ )	Comparison of effect of unsteady ( $U_{us}$ ) against time-averaged ( $\ddot{U}_s$ )	Comparison of effect of unsteady ( $U_{us}$ ) against steady RMS ( $U_{s,RMS}$ )
Effect on parameter	$\tau$ (as $f$ )	$\bar{\phi}_{U_{us}} > \bar{\phi}_{U_{NS}}$ (3.71%)	$\bar{\phi}_{U_{us}} > \bar{\phi}_{\ddot{U}_s}$ (3.91%)	$\bar{\phi}_{U_{us}} > \bar{\phi}_{U_{s,RMS}}$ (3.95%)
	$\gamma$	$\bar{\phi}_{U_{us}} < \bar{\phi}_{U_{NS}}$ ( $-3.97 \times 10^{-4}\%$ )	$\bar{\phi}_{U_{us}} = \bar{\phi}_{\ddot{U}_s}$	$\bar{\phi}_{U_{us}} > \bar{\phi}_{U_{s,RMS}}$ (0.01%)
	$J/J_{pure}$	$\bar{\phi}_{U_{us}} > \bar{\phi}_{U_{NS}}$ (0.51%)	$\bar{\phi}_{U_{us}} = \bar{\phi}_{\ddot{U}_s}$	$\bar{\phi}_{U_{us}} < \bar{\phi}_{U_{s,RMS}}$ ( $-0.13\%$ )
	$\Delta P$	$\bar{\phi}_{U_{us}} < \bar{\phi}_{U_{NS}}$ ( $-0.2\%$ )	$\bar{\phi}_{U_{us}} = \bar{\phi}_{\ddot{U}_s}$	$\bar{\phi}_{U_{us}} > \bar{\phi}_{U_{s,RMS}}$ (0.05%)

## 6.5 Conclusions

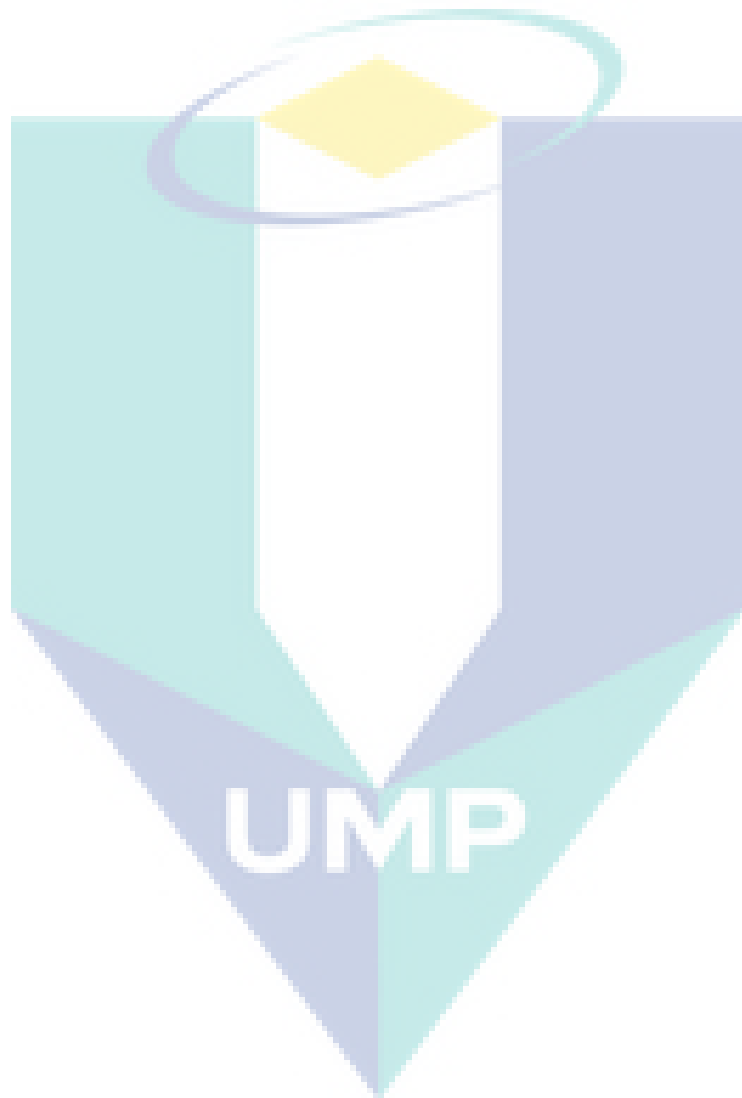
This chapter investigates the mechanisms by which the wall shear and mass transfer are influenced by an oscillating electro-osmotic flow disturbance in an unobstructed empty 2D membrane channel with permeation, under sinusoidal variations of the slip velocity. The cases considered involve a spatially-uniform electro-osmotic forced slip velocity along the membrane surface. The simulated hydrodynamics results are validated against a reduced order model (ROM) and the effect of frequency on the perturbation velocity  $u$  is in excellent agreement.

When comparing the effectiveness of electro-osmosis between steady and unsteady EOF in terms of same perturbation kinetic energy, it was found that the steady slip velocity shows similar or higher time-averaged permeate flux but lower wall stress than the unsteady slip velocity case. Although the friction factor, solute concentration and permeate flux vary as the slip velocity varies in time, the effects are nullified within the oscillation period, leading to a negligible effect when compared to the case with a steady-state slip velocity equivalent to the time-average of the unsteady slip velocity. Therefore, the sinusoidal time oscillation of slip velocity does not lead to any time-averaged mass transfer enhancement.

Nevertheless, there are still advantages in using unsteady EOF in the context of fouling reduction/prevention. This is because as slip velocity frequency and amplitude increase, so does the maximum wall stress. Meanwhile, there is a negligible change in time-averaged pressure drop. This effect is markedly different to the case with steady-state slip velocity.

This chapter is the first study of the effect of unsteady EOF on maximum wall shear stress (a proxy for fouling reduction). Greater maximum wall shear stress and/or mass transfer may be possible due to the interactions between unsteady electro-osmotic

flow perturbations and the perturbations induced by spacers. Some results of such investigation are presented in Chapter 7.



## Chapter 7

### CFD modelling of electro-osmotic permeate flux enhancement in spacer-filled membrane channels

#### 7.1 Introduction

Previous work has shown that the flow inside membrane channels is greatly influenced by spacer geometry [35]. Feed spacers can be oriented such that high cross flow velocities or secondary flow patterns (i.e. recirculation and vortex shedding) form in order to generate stronger scouring forces along the membrane surface and enhance back-mixing from the membrane surface to the bulk of the feed flow [35]. It should be noted that the appearance of recirculation or vortex shedding implies the existence of a non-zero velocity component normal to the membrane surface ( $v$ -velocity). In addition, mass transfer enhancement can occur through the synergy between convection and mass transport if the  $v$ -velocity and the concentration gradient are aligned [151]. This highlights the significance of  $v$ -velocity in terms of vortex shedding and mass transfer enhancement.

At low values of the Reynolds number in the membrane channel, viscous forces are relatively more important than inertial forces, and therefore flow oscillations such as those that lead to vortex shedding are damped by the viscosity. The energy in the oscillations is dissipated and their amplitude is reduced if the viscous action is strong enough. Thus, it is not possible for oscillations to grow and sustain themselves, and hence vortex shedding does not occur at low Reynolds numbers [70]. This is referred to as an overdamped state. On the other hand, at larger values of the Reynolds number

damping of oscillations by viscosity is less effective because inertial forces dominate, so that disturbances can perpetuate and vortex shedding occurs. Oscillations can grow if the input excitation frequency is in the range for which the system can experience resonance [152]. Under such conditions, mass transfer is greatly enhanced because the unsteady effects (particularly vortex shedding) lead to boundary layer renewal [23].

Despite numerous studies into spacer geometry and its effect on mass transfer, only a handful of researchers have investigated the use of spacers combined with other techniques to enhance mixing such as, for example, electrokinetic methods [50]. To the best of our knowledge, there is no study on the integration of the electro-osmotic flow and spacer mixing to enhance mass transfer in membrane systems.

Although EOF has been shown to have the potential to improve mass transfer, further mass transfer enhancement may be possible through the interactions between electro-osmotic mixing and the mixing caused by feed channel spacers. This is because electro-osmotic perturbations have the potential to decrease the Reynolds number at which unsteady flow and vortex shedding occur. Those interactions are the focus of this chapter.

## **7.2 Problem description, assumptions and methods**

### **7.2.1 Model description**

The unsteady-state continuity, momentum and mass transfer equations are solved using commercial CFD software (ANSYS CFX-15.0). The channel and electrode geometry is shown in Figure 7.1. Long entrance and exit regions are included at each end of the membrane channel to ensure the flow solution is not influenced by the inlet and outlet boundary conditions [23]. Preliminary studies show that the channel must be long enough for the flow to become fully developed for multi-spacer channels and this is usually achieved after five to six spacers [70]. For this reason, the simulation is

performed with 10 spacers. The electrode geometry illustrated consists of two flat-plate electrodes placed at each end of the channel and perpendicular to the bulk flow direction. This electrode geometry leads to spatially uniform slip velocity because the electric field magnitude is constant along the length of the membrane wall. Positive slip velocity is obtained when the slip velocity is in the same direction as the bulk flow. Conversely, negative slip velocity is obtained when the slip velocity is in the opposite direction to the bulk flow.

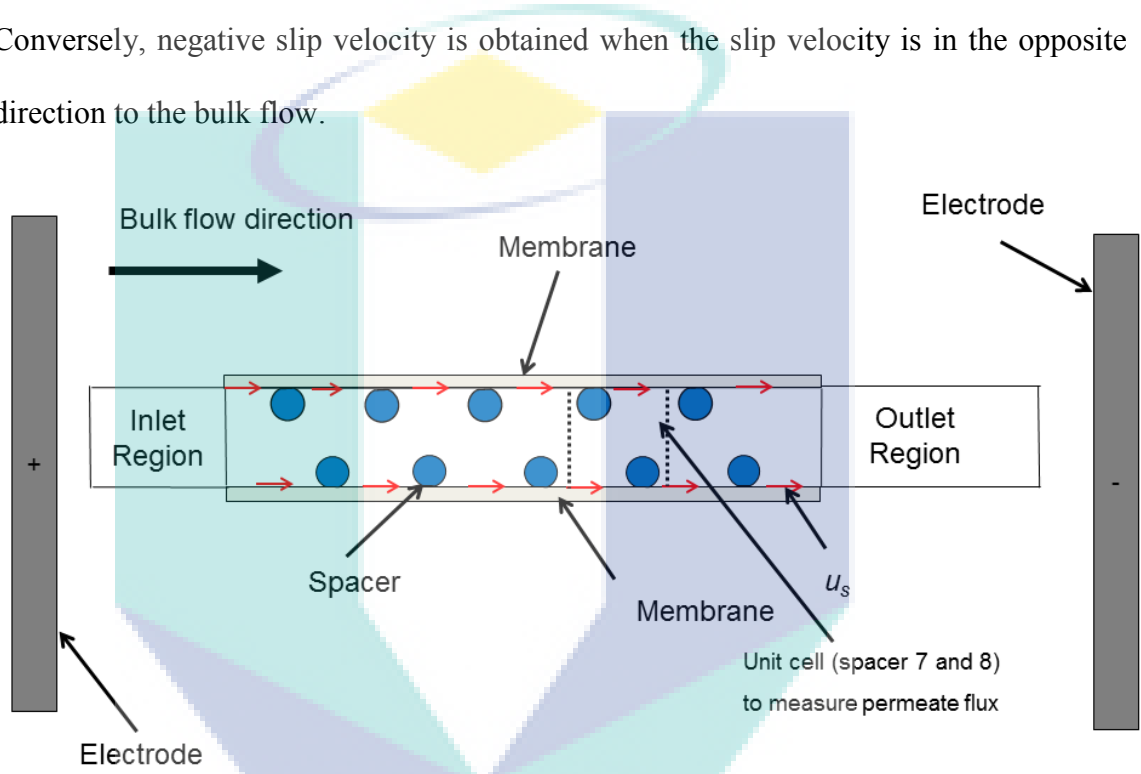


Figure 7.1: Schematic of fluid domain indicating boundary locations.

Each set of two successive spacers comprises a “unit cell”, as depicted in Figure 7.2. This pattern is repeated five times in the computational fluid domain. A basic zigzag spacer arrangement with  $d_f/h_{ch} = 0.6$  and  $l_m/h_{ch} = 4$  is used, as this presents the most similarities to spacers used in real membrane modules, and has been found to perform better than other geometries in terms of mass transfer and pressure loss [22]. The unit cell comprising of 7<sup>th</sup> and 8<sup>th</sup> spacer filaments is chosen for more detailed analysis of concentration, velocity and permeate flux as it is representative of a spatially

periodic channel, where the influence of the channel inlet and outlet on flow is negligible.

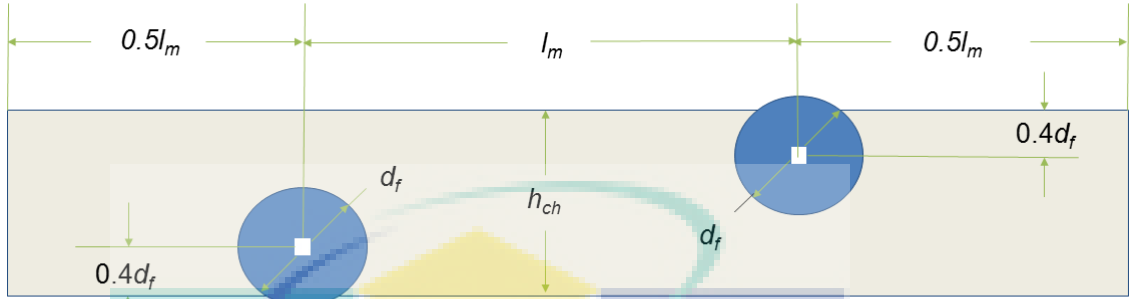


Figure 7.2: Geometry of the spacer unit cell.

### 7.2.1.1 Boundary conditions

The conditions at the boundaries of the fluid domain are set following the approach in Table 3.3. In order to introduce transient perturbations, a time-varying electro-osmotic flow (EOF) disturbance is incorporated as a sinusoidal slip velocity, which can be expressed as follows [135]:

$$u_{s,t} = u_{s,A} \sin(2\pi f_s t) \quad (7.1)$$

where  $t$  is time,  $f_s$  is the oscillation frequency and  $u_{s,A}$  is the slip velocity amplitude.

### 7.2.1.2 Assumptions and cases

An adaptive time step is used throughout the simulations with a minimum time step of  $10^{-10}$  s and a maximum Courant number of 1. The fluid domain is discretised using a mesh with a Grid Convergence Index (GCI) below 5 % for both mass transfer and permeate flux. The reference conditions for the simulations are based on typical RO conditions, and are presented in Table 7.1.

Table 7.1: Parameters used for uniform electric field case study.

Parameter	Value
Feed channel height ( $h_{ch}$ )	3 mm
Entrance length ( $L_m$ )	36 mm
Exit length ( $L_{out}$ )	72 mm
Membrane Length ( $L_m$ )	120 mm
Diffusivity coefficient ( $D$ )	$1.67 \times 10^{-9} \text{ m}^2/\text{s}$
Intrinsic rejection ( $R$ )	99.6 %
Membrane permeability ( $L_p$ )	$3.9 \times 10^{-11} \text{ m s}^{-1} \text{ Pa}^{-1}$
Reflection coefficient ( $\sigma$ )	1
Osmotic pressure coefficient ( $\varphi$ )	80.51 MPa
Inlet Transmembrane Pressure ( $\Delta p_{tm}$ )	2.94 MPa
Electro-osmotic slip velocity amplitude ( $u_{s,A}$ )	$5 \times 10^{-4} \text{ m/s}$

The calculations carried out for this chapter required more than 50,000 time steps in order for the flow and mass transfer to converge. This leads to large computational times (of the order of 100 hours) and memory (just under 14 GB) for each simulation on a HP BL685c G7 computer node comprised of four AMD 6174 12-core processors running at 2.2 GHz.

## 7.2.2 Methodology of analysis of results

Frequency response analysis based on Fourier decomposition is used extensively to analyse the behaviour of systems [153, 154]. This approach uses a pulse test with the slip velocity input,  $u_{s,pulse}$  which is given by:

$$u_{s,pulse} = \left( -\frac{\varepsilon_e \zeta E_x}{\mu} \right) \left[ \frac{1}{2} \left( 1 - \cos \left( \frac{2\pi t}{t_\omega} \right) \right) \right] \quad (7.2)$$

where

$$t_\omega = \frac{4}{\pi \lambda} \quad (7.3)$$

Frequency response is the quantitative measure of the output spectrum of a system in response to a stimulus, and is used to obtain the frequency with the largest gain (peak frequency). The frequency response is obtained by comparing the Fourier

transform of the input and output of the system. In this chapter, the input and output correspond to the slip velocity pulse and the deviation  $v$ -velocity (the difference in  $v$ -velocity between the cases with and without EOF) respectively. The gain obtained from the frequency response analysis is equal to the ratio of the absolute value of the Fourier transform of the output to that of the input. However, frequency response analysis assumes that the system under consideration is linear. Nevertheless, for mildly non-linear systems frequency response can be used as a first approximation to obtain the peak frequency [146].

In this chapter, the peak frequency approximation obtained from frequency response is referred to as  $F_{pl}$ . In addition, a frequency range ( $F_{peak}$  range) around  $F_{pl}$  is studied, with lower and upper limits defined as half  $F_{pl}$  and 1.5 times  $F_{pl}$ . Although the actual peak frequency ( $F_{peak}$ ) value for mass transfer enhancement, maximum wall shear stress and turbulent kinetic energy equivalent may not be the same as  $F_{pl}$  due to the nonlinearity of the system,  $F_{peak}$  is expected to be within the frequency range studied.

### 7.3 Validation

Model validation is one of the most important steps in any simulation study. However, there are no experimental data for electro-osmosis in spacer-filled channel reported in the literature. Although a significant number of experimental studies are available in the literature [131-133, 155, 156] for the case without EOF, the spacer geometry in those papers are very different to the case investigated in this chapter, such that a direct validation against experimental data is not possible. There is, however, numerical data reported in the literature that that can be used for validation in terms of friction factor and mass transfer [38]. It has been shown that permeation has a small effect on wall shear [35], and hence wall shear data for the case without permeation can be used for comparison against the case with permeation. For the Reynolds number

range of 375 to 536, it is found that the Fanning friction under similar spacer geometry and flow conditions as the case without permeation has a maximum relative error below 10 % [38]. The discrepancy is related to the decrease in friction factor due to the permeation effect in this chapter. In addition, at steady-state, the exponent for the Reynolds number dependence of the Sherwood number in our simulation results is 0.62. This agrees with the results of Da Costa [157] and Fimbres-Weihs and Wiley [23], who found values for the exponent in the range of 0.4 to 0.6 for Reynolds numbers below 100 and 0.605 for Reynolds number below 526 respectively. Under unsteady-state conditions, the exponent increased to 0.84, which is similar to the experimental data of Shock and Miquel [40] and Fimbres-Weihs and Wiley [23], who found the value for the Reynolds number exponent of 0.875 and 0.92 respectively.

## **7.4 Results and discussion**

### **7.4.1 Steady-state EOF**

The effect of steady slip velocity on velocity and solute concentration profile is shown in Figure 7.3. A positive slip velocity ( $u_s > 0$ ) transports fluid down the channel, causing more solute to accumulate and the concentration to increase at the upstream corner between the spacer and the membrane, compared to the case without electro-osmosis ( $u_s = 0$ ). On the other hand, at the downstream corner between the spacer and the membrane, there is less solute concentration compared to case without electro-osmosis because of the enhanced convective transport down the channel. The opposite behaviour is observed for the case with negative EOF (lower and higher solute concentrations at the upstream and downstream corners respectively).

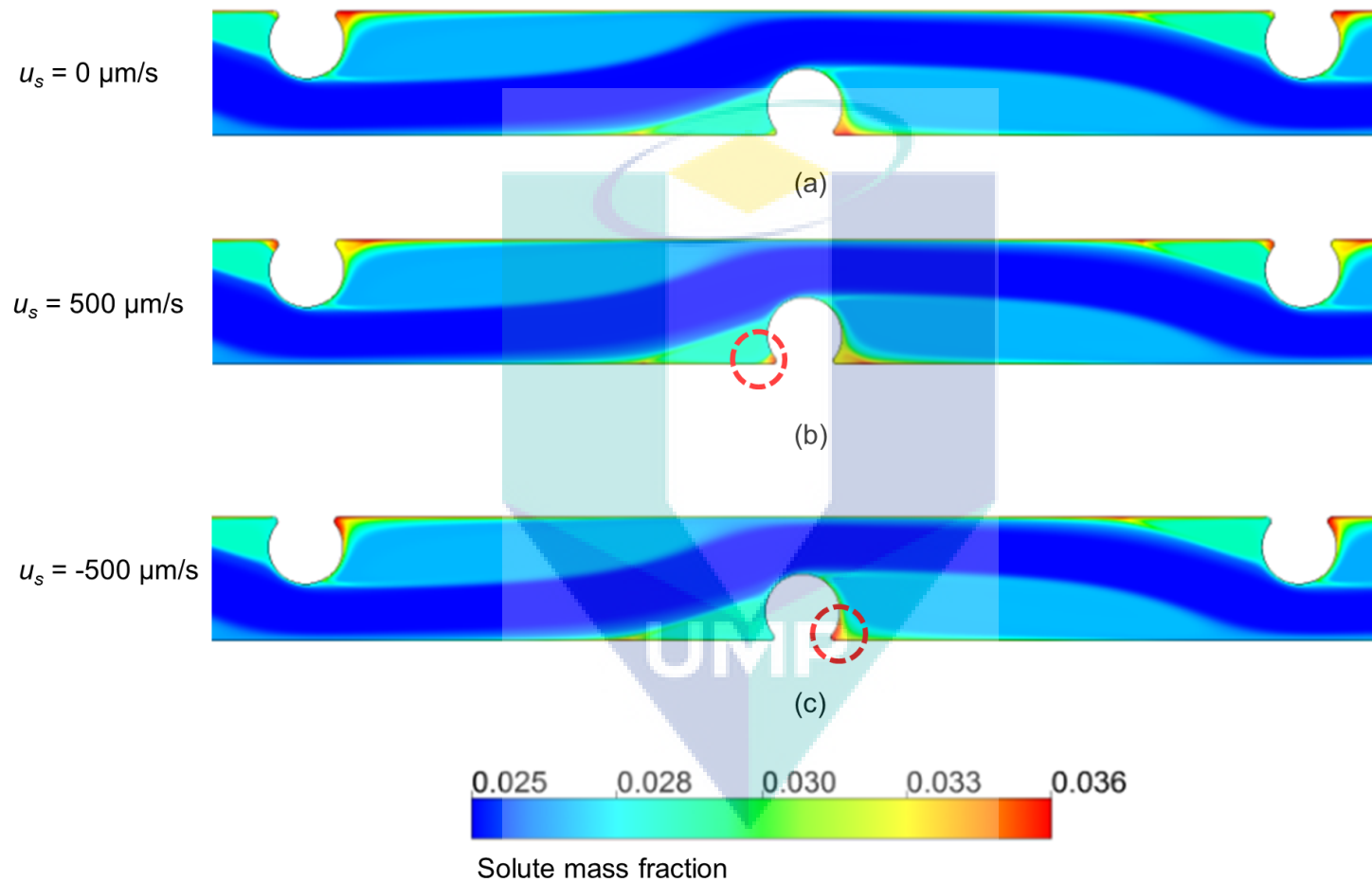


Figure 7.3: Effect of steady slip velocity on solute concentration profile for  $Re = 408$  between the 7<sup>th</sup> and 9<sup>th</sup> spacers; (a)  $u_s = 0 \mu\text{m/s}$  (b)  $u_s = 500 \mu\text{m/s}$  (c)  $u_s = -500 \mu\text{m/s}$ . The red circles identify the regions of accumulated solute concentration between the spacer and the membrane.

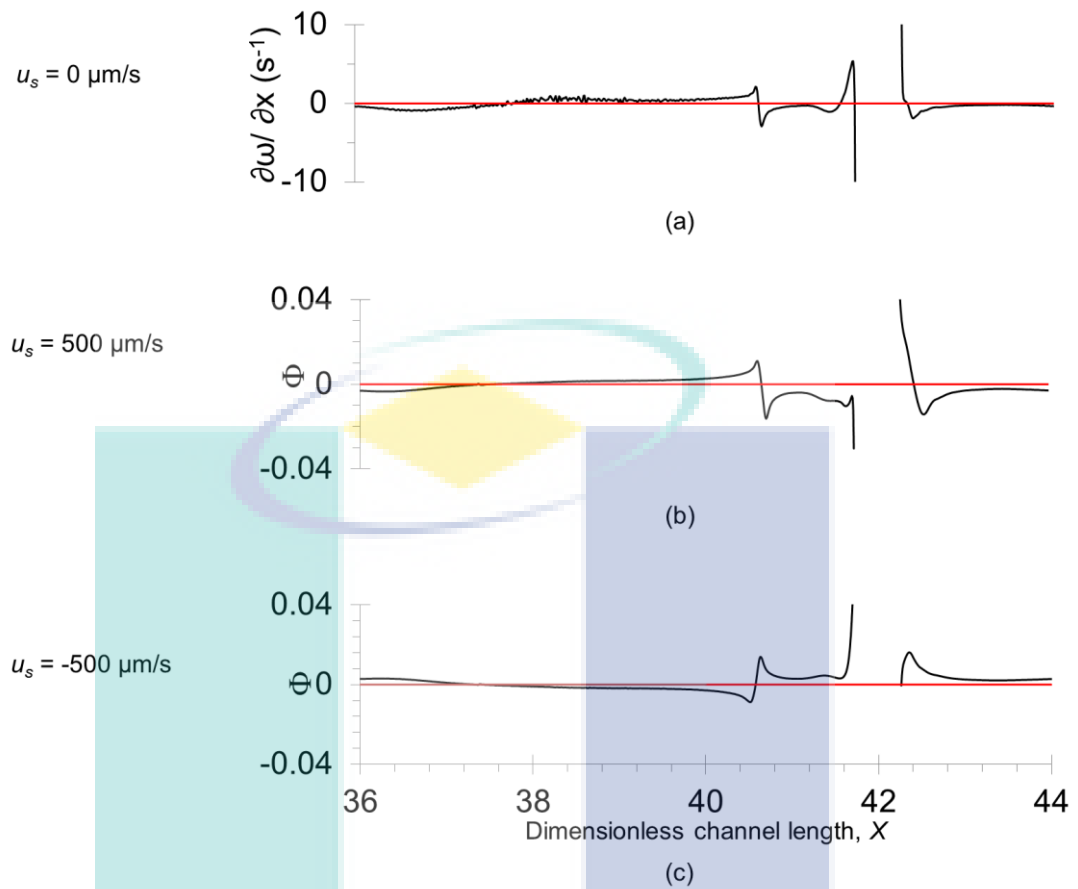


Figure 7.4: (a) Local solute concentration gradient in the  $x$ -direction ( $\partial\omega/\partial x$ ) for unit cell comprised of the 7<sup>th</sup> and 8<sup>th</sup> spacers without electro-osmosis. Mass transfer enhancement factor,  $\Phi$  for (b) steady positive and (c) steady negative slip velocity.

Figure 7.4 shows that for locations where  $\partial\omega/\partial x > 0$ , a positive slip velocity results in increased electro-osmotic enhancement ( $\Phi$ ) while a negative slip velocity results in negative  $\Phi$ , and therefore a decrease in mass transfer. The opposite behaviour is obtained for the locations where  $\partial\omega/\partial x < 0$ . These results are consistent with previous findings [126] in Chapter 5, that a positive slip velocity in the direction of the bulk flow for empty channels (where  $\partial\omega/\partial x$  at all locations) results in an increase in mass transfer.

Figure 7.4 also shows that the change in permeate flux due to uniform and steady negative or positive slip velocity (not changing in time or spatially) relative to the case without electro-osmosis is small, except for locations close to the spacer. The

average values for flux enhancement are 2.3 % and -1.29 % due to negative and positive slip velocity values respectively for this unit cell (7<sup>th</sup> and 8<sup>th</sup> spacer). This is because, for the case without EOF, the area average of  $\partial\omega/\partial x$  for this unit cell is negative. Hence, a negative slip velocity leads to an increased overall permeate flux enhancement.

The effectiveness of mass transfer enhancement in the spacer-filled channel is compared against the case for an empty channel at the same hydraulic Reynolds number and slip velocity magnitude. The flux enhancements due to positive and negative slip velocity for an empty channel are 0.51 % and -0.51 % respectively. These results show that mass transfer enhancement is greater for the spacer-filled channel than for the empty channel.

#### 7.4.2 Unsteady-state EOF

A slip velocity pulse test is performed everywhere within the membrane region for Reynolds numbers 11, 408, 536 and 1,000 and the corresponding  $v$ -velocity is monitored downstream of spacer 8 at location 'A' as shown in Figure 7.5. At  $Re$  11, the response in deviation  $v$ -velocity originates when the input occurs and decays as time progresses. The decay of the response is due to viscous friction at the wall. For  $Re$  408 after a pulse in slip velocity is introduced, the  $v$ -velocity oscillates with a larger amplitude than for  $Re$  11, and then decays with time. Figure 7.5 also shows that the amplitude of  $v$ -velocity for  $Re$  408 is at least 100 times larger than the case for  $Re$  11, because inertial effects for  $Re$  408 are greater.

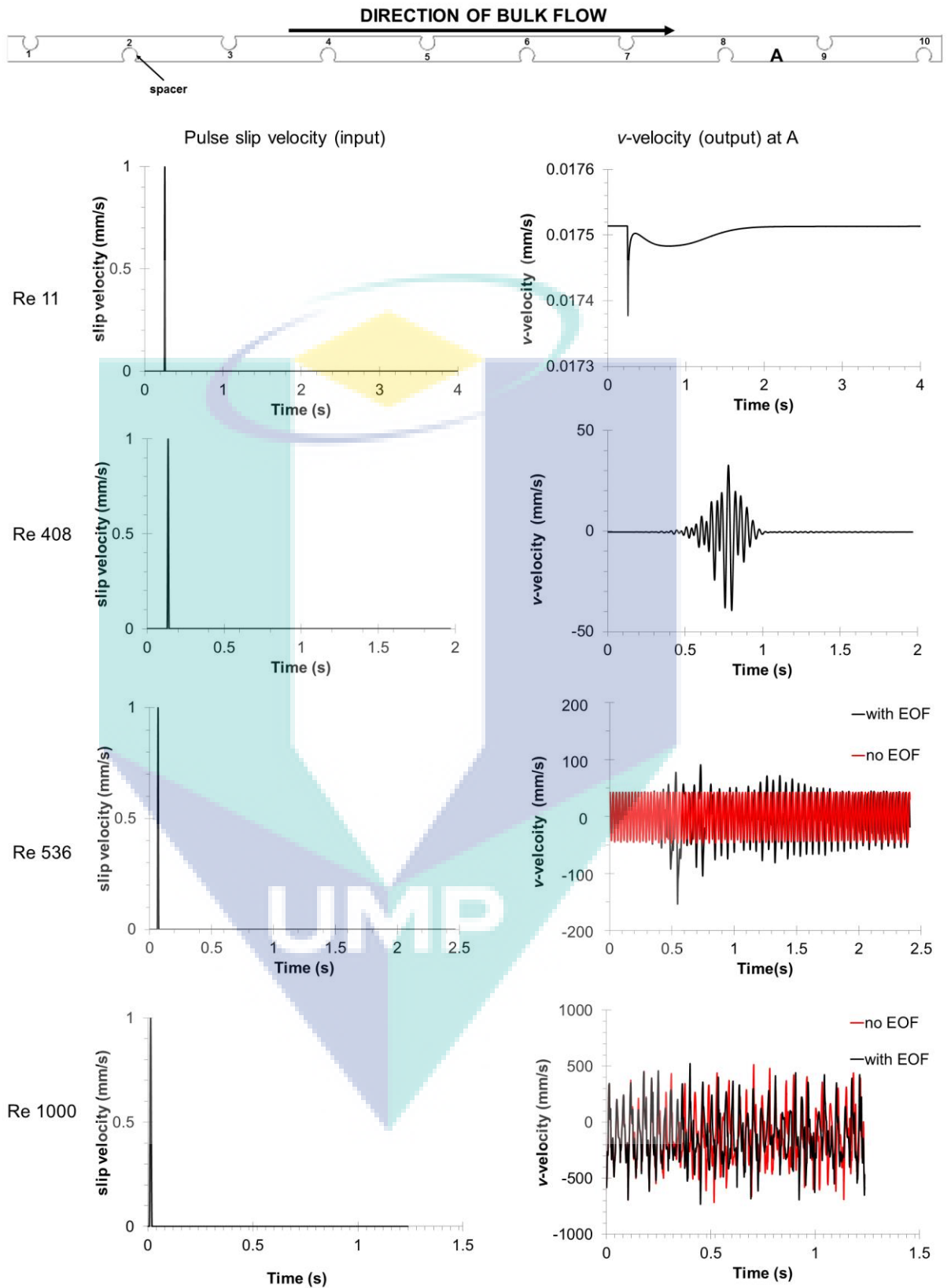


Figure 7.5: Pulse slip velocity and its corresponding v-velocity at location 'A' in the channel for  $Re$  11, 408, 536 and 1000.

For an even higher Reynolds number of  $Re$  536,  $v$ -velocity is oscillating in time prior to the introduction of the pulse. This is because at this Reynolds number, increased inertial effects cause the spacers to perturb the flow and produce a typical vortex shedding pattern. Prior to the pulse in slip velocity for  $Re$  536, the amplitude of  $v$ -velocity is about twice as large as for  $Re$  408 with a pulse in slip velocity. After the pulse is introduced, the maximum value of  $v$ -velocity for  $Re$  536 is at least twice as large as for  $Re$  408. For  $Re$  1,000, as was the case for  $Re$  536, the  $v$ -velocity oscillates before the EOF pulse, but with an amplitude approximately 10 times larger than for  $Re$  408. After the pulse in slip velocity at  $Re$  1,000, however, there appears to be no significant change in the amplitude of  $v$ -velocity. This data shows that the slip velocity can amplify the  $v$ -velocity but only within a certain Reynolds number range.

Figure 7.6 shows the frequency response results from the pulse tests. For  $Re$  11, larger gains are found as the slip velocity frequency is decreased and no maximum is observed, hence suggesting that the system behaves as an overdamped system. For  $Re$  408, 536 and 1,000, on the other hand, there is a peak frequency ( $F_{pl}$ ) centred around 0.87, 1 and 0.41 respectively as indicated in Figure 7.6. The frequency ranges ( $F_{peak}$  ranges) around the  $F_{pl}$  that are used to investigate the effect of forced slip velocity frequency on velocity and solute concentration profile are summarised in Table 7.2. Further, Table 7.2 also shows that the peak frequencies ( $F_{peak}$ ) for mass transfer enhancement, maximum wall shear stress and turbulent kinetic energy equivalent (see Figure 7.7) are within the  $F_{peak}$  ranges investigated, hence validating the use of frequency response analysis as a tool to determine the approximate range of  $F_{peak}$ .

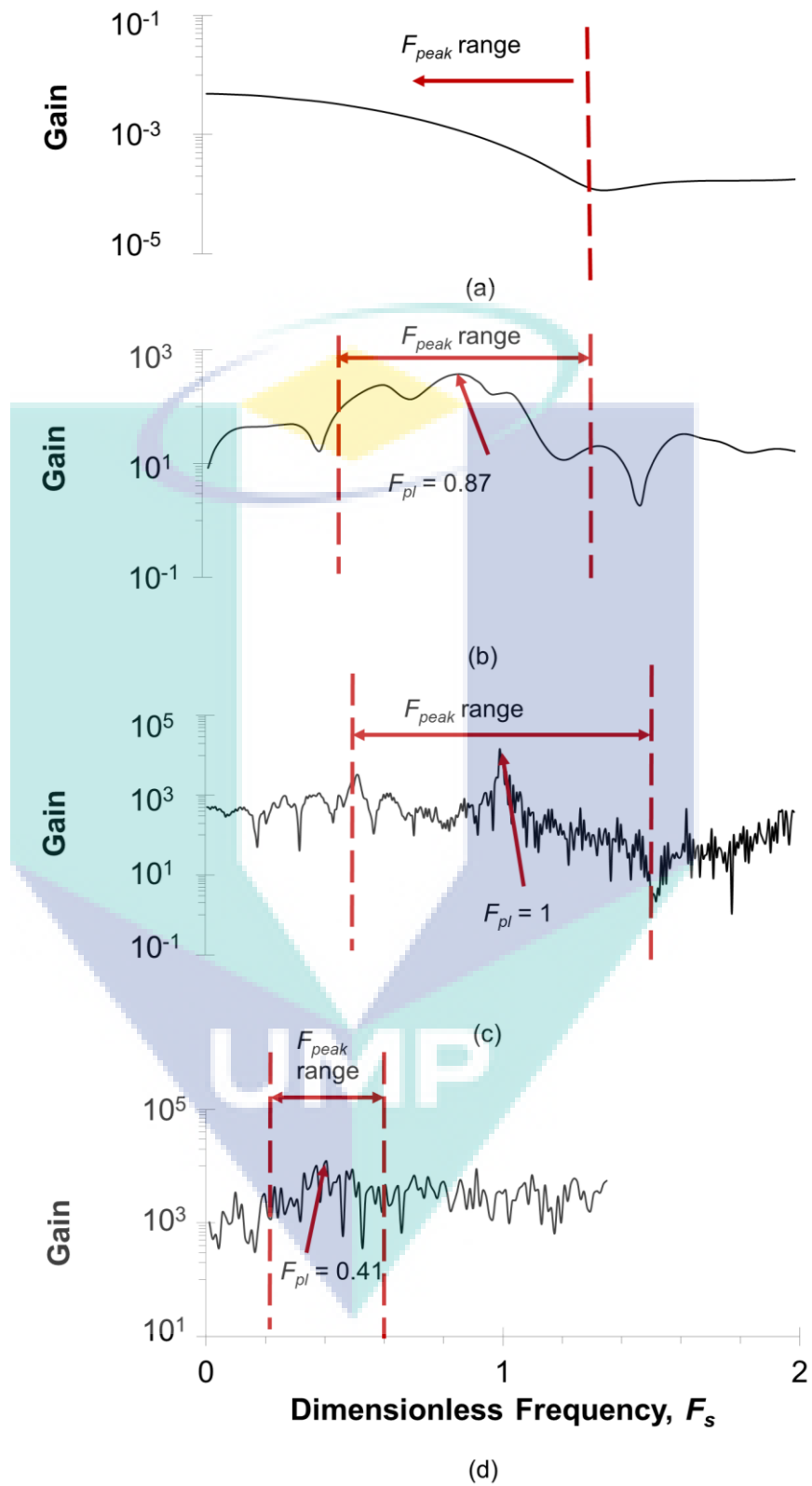


Figure 7.6: Frequency response of  $v$ -velocity at location 'A' to a pulse in slip velocity for (a)  $Re = 11$  (b)  $Re = 408$  (c)  $Re = 536$  (d)  $Re = 1000$ .

Table 7.2: Results of peak frequency and ranges for different Reynolds numbers.

Reynolds number	Peak frequency ( $F_{pl}$ )	$F_{peak}$ range	$F_{peak}$
11	N/A	< 1.36	N/A
408	0.87	0.44 – 1.31	0.67
536	1	0.5 – 1.5	0.76
1,000	0.41	0.21 – 0.62	N/A

As shown in Figure 7.7, the electro-osmotic mass transfer enhancement ( $\widetilde{\Phi}$ ) is greater for  $Re$  408 and 536 (at  $F_{peak}$  of 0.67 and 0.76) than for the cases at  $Re$  11 and 1,000. Given that without EOF the flow transitions from steady to unsteady at a  $Re$  between 408 and 536 (as evidenced by Figure 7.5 prior to the slip velocity pulse), this indicates that EOF is most effective for Reynolds numbers near this transition. The  $F_{peak}$  values for  $\widetilde{\Phi}$  match the  $F_{peak}$  values for flux and maximum wall stress. These  $F_{peak}$  values correspond to the resonant frequency because maximum values in turbulent kinetic energy equivalent (and hence, amplitude of  $v$ -velocity) are also observed at those frequencies. The corresponding increases in flux and recovery rate due to EOF at the  $F_{peak}$  value for  $Re$  408 and 536 are 17 % and 21 % respectively. In terms of fouling reduction/removal, the corresponding increases in maximum wall stress due to EOF for  $Re$  408 and 536 are 137 % and 116 % respectively, which indicates the potential of EOF to minimise the onset of fouling. At  $F_{peak}$ , it can be seen that EOF can induce vortex shedding for a flow regime without vortex shedding (Figure 7.8), or it can induce stronger vortex shedding for a flow regime that already presented vortex shedding (Figure 7.9). Figure 7.8 shows that when there is vortex shedding, the solute concentration is better mixed. Further, Figure 7.8 and Figure 7.9 show that above or below frequencies, vortex shedding is not enhanced. The reader is referred to the video

provided with this thesis which shows the animated flow and solute concentration patterns.

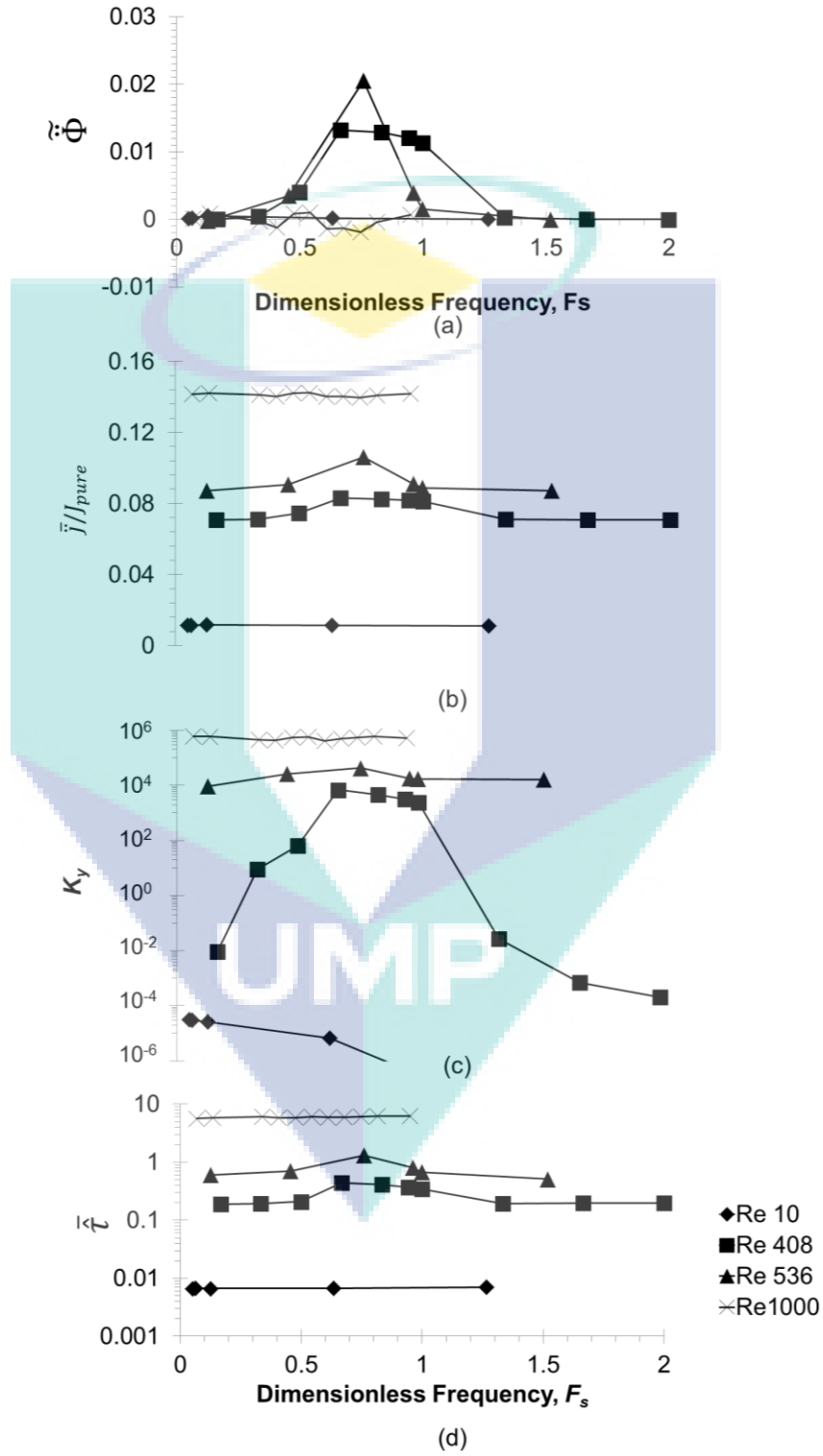


Figure 7.7: Effect of dimensionless frequency on (a) EOF mass transfer enhancement, (b) permeate flux, (c) turbulent kinetic energy equivalent measured at location 'A' and (d) maximum shear stress for Reynolds number of 11, 408, 536 and 1000.

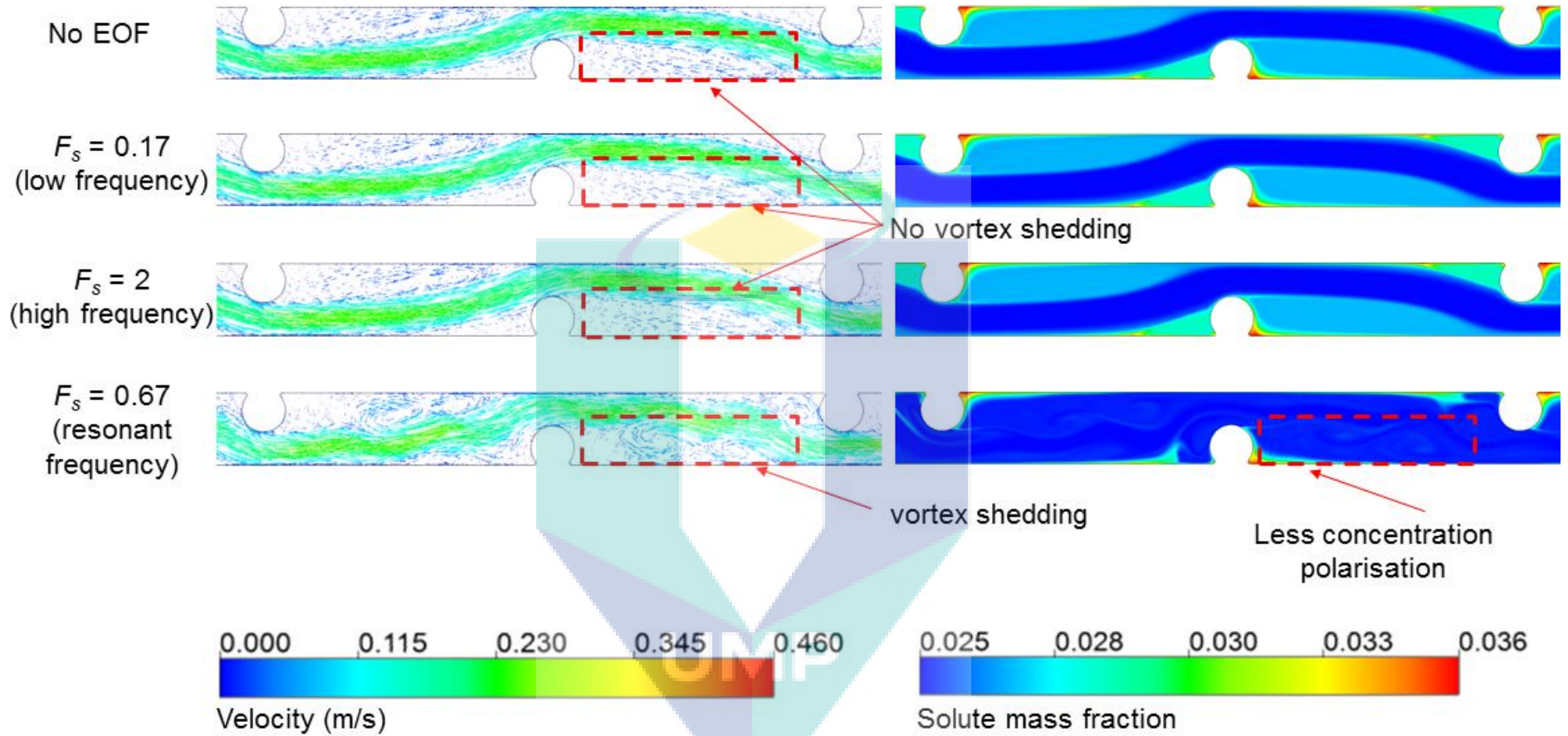


Figure 7.8: Effect of slip velocity frequency on velocity and solute concentration from spacer 7 to 9 for  $Re$  408.

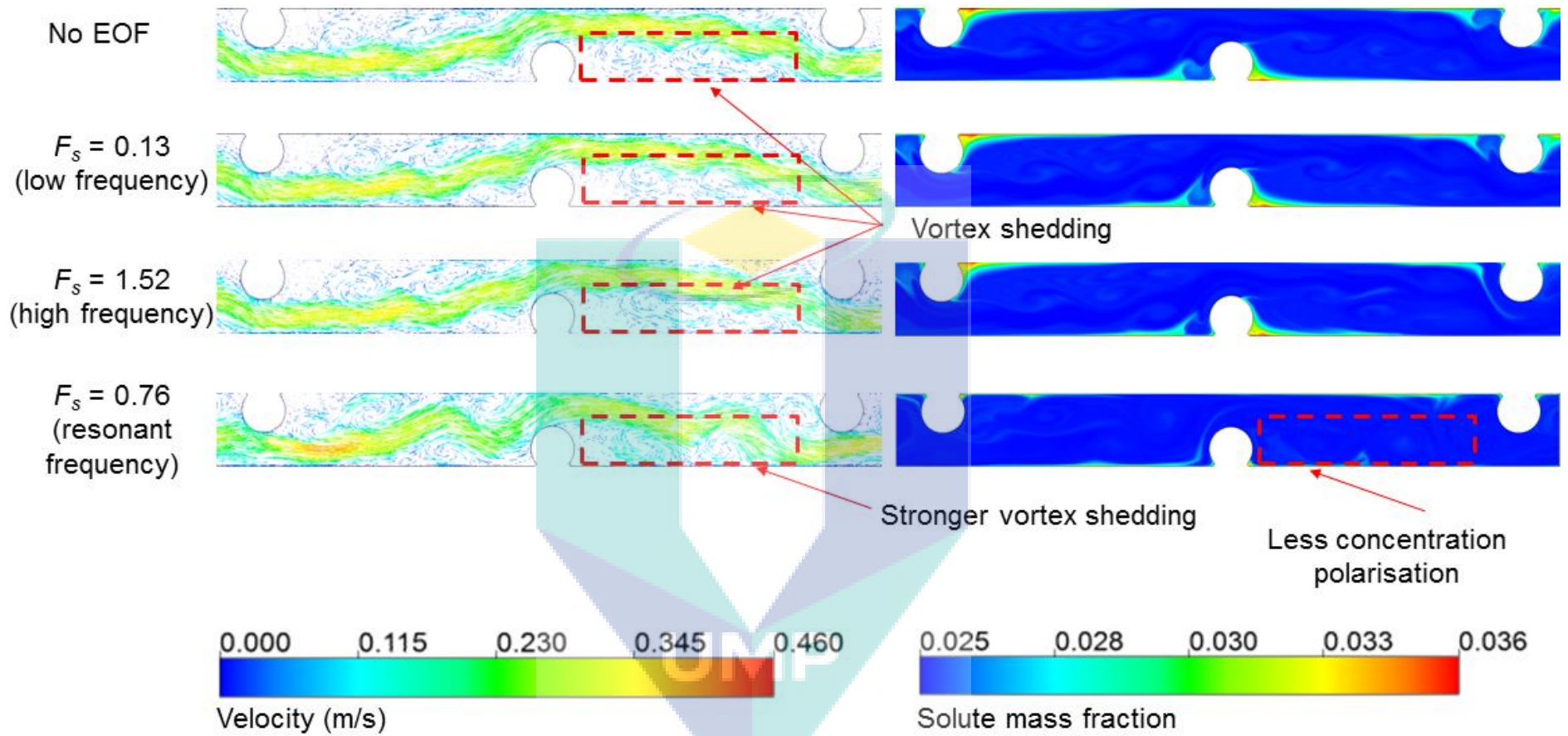


Figure 7.9: Effect of slip velocity frequency on velocity and solute concentration from spacer 7 to 9 for  $Re$  536.

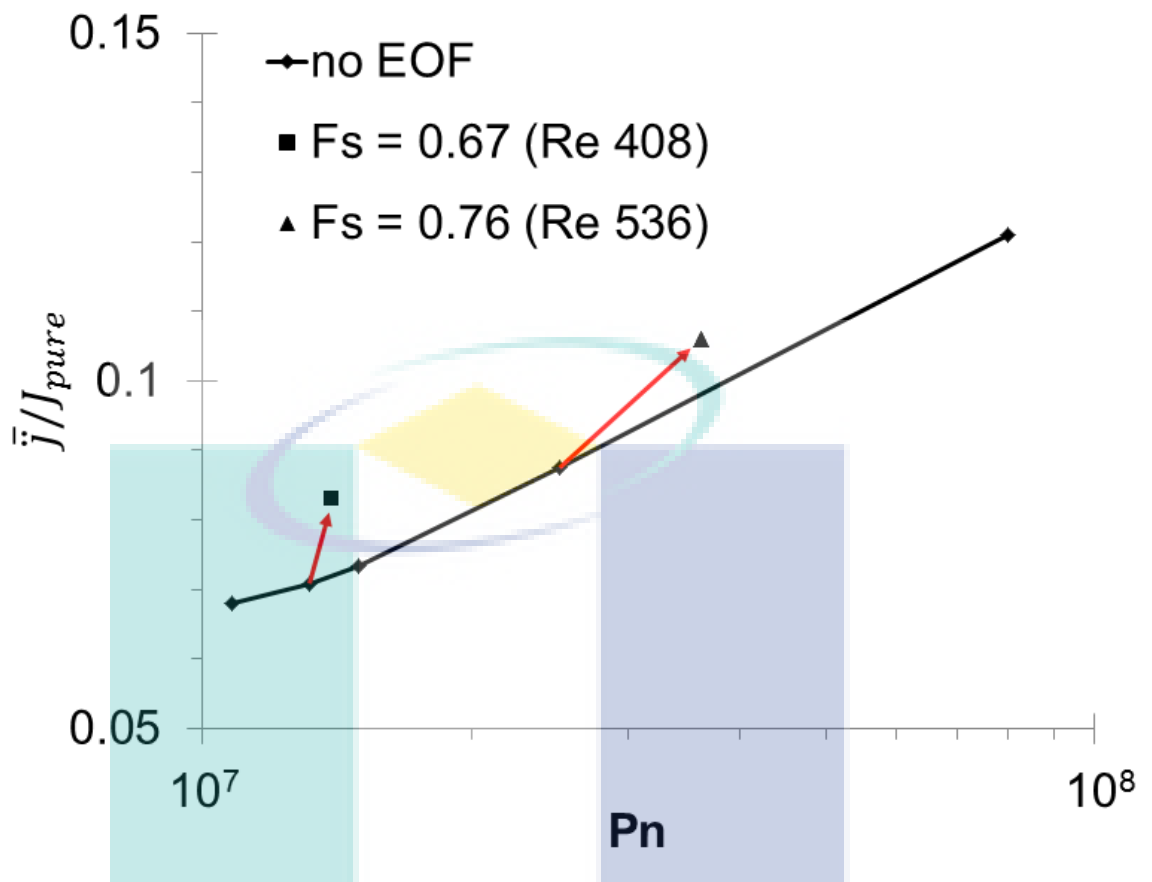


Figure 7.10: Effect of  $P_n$  with and without EOF on dimensionless permeate flux.

As seen in Figure 7.10, at the same permeate flux, EOF results in a significantly lower Power number (a proxy for pumping energy) of about 35.7 % and 36 % than the case without EOF. At the same Reynolds number, the increase in flux due to EOF is accompanied by an increase in Power number of about 5.9 % ( $Re$  408) and 44.4 % ( $Re$  536). This is expected, as the occurrence of vortex shedding or stronger vortex shedding can lead to an increase in Fanning friction factor, hence resulting in an increase in Power number. Figure 10 also reveals that at the same pumping power ( $P_n = 1.4 \times 10^7$  and  $3.6 \times 10^7$ ), the flux with EOF is larger (15.6 % and 12.5 % respectively) than without EOF.

## 7.5 Conclusion

The results presented in this chapter show that electro-osmotic flow (EOF) next to the membrane wall produces a larger mass transfer enhancement in spacer-filled channel than in empty channels. For the steady state, it is shown that uniform slip velocity reduces the development of stagnant and high concentration regions near spacer filaments when the slip velocity direction is away from the spacer. For the unsteady state, the results show that a spatially uniform and time-varying EOF has significant potential to improve mass transfer by up to 21 %, even at low slip velocity value. In addition, EOF induced vortex shedding increases wall shear stress by about 137 % along the membrane, thus potentially slowing the onset of fouling. The simulation results also shows that at the same permeate flux, EOF results in a significantly lower Power number (a proxy for pumping energy) by about 36 %, than the case without EOF.

The electrode configuration considered in this chapter is two flat-plate electrodes at each end of the channel and perpendicular to the bulk flow direction. This means that the external electric field can be applied outside the membrane channel, thus not requiring any modification to the spiral wound membrane module. The data presented in this chapter shows that EOF mass transfer enhancement is significant when a resonant frequency of EOF is applied. Nevertheless, the conditions simulated in this study and the resulting mass transfer enhancement observed may not be optimal, since this chapter is the first study of EOF mass transfer enhancement in spacer-filled channels. Because of the non-linear nature of the mass transfer system, greater mass transfer enhancement may be possible with other input signal waveforms than the case considered in this chapter.

## Chapter 8

### Conclusions

While the permeability of RO membranes has been continuously increasing over the past decades, within the next 10 years they will probably reach the limit at which the constraints of fluid mechanics and membrane module engineering prevent further flux increases [158]. This underlines the need for new strategies to increase permeate flux rather than continuing to improve permeability. Boundary layer renewal could be one focus, because it can promote mixing that can help reduce CP, which ultimately increases flux.

EOF is proposed in this thesis as a boundary layer renewal technique because it can result in a disruption of the concentration boundary layer through the movement of a thin layer of fluid in the vicinity of the membrane surface. Thus, the work presented in this thesis studies the hydrodynamics and mass transfer behaviour of unobstructed and obstructed membrane channels under the influence of EOF. The understanding of flow patterns, mass transfer and pressure drop due to EOF in unobstructed and obstructed membrane channels developed in this thesis may lead to the development of improved operation modes for SWM modules.

Computational Fluid Dynamics (CFD), a proven tool for the systematic study of hydrodynamic and mass transport phenomena, is used in this thesis to gain insights into the effects of EOF on mass transfer at the local level, something that cannot be achieved using current experimental approaches. CFD offers the flexibility to parametrically vary operating conditions, fluid and membrane properties. For instance, the fluid velocity,

solute diffusivity and inlet solute concentration can be set to constant values for the simulation, thus not requiring any control of these variables.

As the first step for investigating the effects of EOF in membrane systems (Chapter 4), a mathematical simplification for a more rigorous EOF model was developed. This simplification reduces the computational time and resources required, while retaining the accuracy and physical meaning of the rigorous model. One of the key issues associated with numerical simulation of EOF is the high computational effort required to solve the Poisson and Navier-Stokes equations at the scale of the electrical double layer ( $10^{-9}$  m) when considering the dimensions of a typical membrane channel ( $10^{-3}$  m). This requires very fine spatial discretisation near the wall in order to capture the velocity profile caused by EOF. The simplification used for the numerical simulation of EOF involves adopting the Helmholtz-Smoluchowski (HS) slip velocity. The HS slip velocity only takes into account the electric field in the  $x$ -direction ( $E_x$ ), and not the normal component. Comparison of the effect of the normal component of the electric field ( $E_y$ ) on the flow field from the more rigorous charge density (CD) solution against the solution using the HS approximation showed that the effect of  $E_y$  is minimal. Greater agreement between the CD solution and the HS approximation was found at higher bulk solute mass fractions, such as those typically found on the membrane surface in RO systems. This therefore demonstrates the suitability of using the HS slip velocity as an approximation in a RO desalination system, and is used in the rest of the thesis.

The dynamic components describing membrane fouling form a very complex system due to the interactions between membrane properties, solution composition and operating conditions. Although fouling was not modelled in this thesis, several indicators for mass transfer enhancement and fouling reduction due to EOF are

proposed. It has been shown elsewhere that during pulsatile flow [122-124], a high-amplitude shear may lead to a reduced fouling layer. Maximum wall shear was therefore used as proxy measure for long term fouling reduction.

Further, Chapter 5 proposes the use of a mass transfer enhancement factor ( $\Phi$ ) to quantify how far the system is from the “fully mixed” state using the electro-osmotic mass transfer enhancement (EOMTE) approach. This indicator is a simple and meaningful measure of membrane system performance that can also be used for assessing other mass transfer enhancement strategies, e.g. different spacer approaches. A positive value of  $\Phi$  represents the case where electro-osmosis causes an increase in mass transfer and hence an increase in flux. Conversely, a negative value of  $\Phi$  means that there is less mass transfer with EOF than without it, such that there is a decrease in flux.

In order to more completely analyse the effect of EOF on membrane system performance, changes in other key variables are also quantified. Fluid mixing is thus used as a first-pass indicator for a reduction in concentration polarisation, which should ultimately increase permeate flux. In Chapter 7, turbulent kinetic energy equivalent is proposed as a mixing measure for flows with time-varying eddies and recirculation regions in spacer-filled channels. The turbulent kinetic energy equivalent in the  $y$ -direction ( $k_y$ ) is used due to the significance of  $v$ -velocity in promoting vortex shedding and mass transfer enhancement. Chapter 7 found that the slip velocity frequency with highest  $k_y$  presents the maximum permeate flux for a Reynolds number near the transition from steady to unsteady flow. Thus,  $k_y$  may be used to predict optimal mixing in spacer-filled channels. The main advantage of using  $k_y$  is that it is purely based on hydrodynamics, and does not require the time-consuming calculation of mass transfer in CFD models.

Apart from establishing measures for mass transfer enhancement and fouling reduction, this thesis also uses these measures to analyse different aspects of EOF and its potential effect on these two factors. Chapter 5 investigated the effect of steady electro-osmosis on permeate flux enhancement in an unobstructed membrane channel. Two types of electrode configurations were considered: (1) parallel and perpendicular to the bulk flow, and (2) adjacent to the membrane surface. The first electrode configuration results in uniform slip velocity because the electric field magnitude is the same everywhere within the membrane channel. For this configuration, it was found that a slip velocity in the direction of the bulk flow results in a flux increase, while a slip velocity in the opposite direction results in flux decline. The second electrode configuration results in a spatially varying slip velocity (non-uniform slip velocity) which causes greater flux enhancement than the case with the first electrode configuration. The mass transfer enhancement indicator ( $\Phi$ ) showed that under steady-state, electro-osmosis is more effective in enhancing flux for systems that originally present a higher level of concentration polarisation; i.e. systems at low Reynolds number and/or high Schmidt number. The data suggested that for seawater RO, EOMTE is more effective as the permeability of the membrane is increased, and reaches a peak in the permeability range of brackish water RO membranes. The data also revealed better electro-osmotic enhancement for membranes with lower intrinsic rejection, which might be particularly suited for ultra-osmosis.

Chapter 6 extends the preceding chapter and focuses on analysing and identifying the mechanisms that lead to changes in shear rate under uniform unsteady EOF in an unobstructed channel. The effect of such changes in shear rate on local and overall membrane performance was measured in terms of flux and maximum wall shear stress (as a proxy for fouling reduction). It was found that the dependencies of solute

concentration amplitude and maximum wall stress on slip velocity amplitude are linear, both in terms of homogeneity and additivity. This implies that time-averaged hydrodynamics and mass transfer do not vary significantly regardless of changes in the frequency and amplitude of the slip velocity, because the effect is cancelled within the time oscillation period. Nevertheless, there are clear advantages for this type of perturbation, as larger slip velocity frequency and amplitude increase the maximum wall stress while having only a marginal effect on pressure drop.

Spacers are another way of enhancing mixing in membrane channels. One of the negative effects associated with the presence of spacers is the stagnant flow in the region near the spacer filament, which leads to an accumulation of solute concentration between the spacer and the membrane. In Chapter 7, it was shown that uniform steady slip velocity in the direction away from the spacer can assist the bulk flow in reaching the stagnant flow region and, hence, reduce the development of high-concentration regions near the spacer filaments. This reveals the importance of electrode location, because it can affect the magnitude and direction of the slip velocity and, hence, affect mass transfer enhancement. The work presented in this thesis has not studied the interaction between electrode location (and hence slip velocity location), hydrodynamics and mass transfer enhancement in spacer-filled channels. Those interactions should be investigated in the future.

It is generally agreed that the interactions between hydrodynamics, mass transfer and pressure drop are complex. However, to the author's knowledge, this thesis is a first study into the synergies of EOF and spacer filaments. A uniform unsteady slip velocity in Chapter 7 is shown to induce vortex shedding for Reynolds numbers near the transition from steady to unsteady flow, especially when a resonant frequency is employed. EOF induced vortex shedding increases wall shear stress up by about 137 %

along the membrane, thus hindering the onset of fouling. Further, EOF results in an increase of permeate flux of up to 21 %. The data also revealed that, at the same permeate flux, EOF requires significantly lower pumping power (about 36 %) than the case without EOF. As might be expected, these performance increases were only observed at or near the resonant frequency of the spacer filled channel, and lower or no performance increase was observed for EOF frequencies outside an “optimal” range. This result is significant, given that current membrane research focuses on increased productivity and reduced energy consumption, as current desalination technologies still require large capital investments and incur high energy costs [10]. Chapter 7 only focuses on the effect of uniform steady and unsteady slip velocity on membrane overall performance. It does not investigate the use of a non-uniform unsteady slip velocity. This could be the focus of a future study because a mass transfer enhancement up to 10 % is observed for the case of non-uniform EOF without spacers. Therefore, the synergy between non-uniform EOF and spacers may result in greater mass transfer enhancement than was observed for uniform unsteady EOF and spacers.

The combined results of this thesis cover the effects of spatial and temporal variations in slip velocity on membrane system performance. For spatially uniform steady slip velocity in an empty channel, the effect on mass transfer enhancement is relatively small. A larger effect on mass transfer is observed with a spatially non-uniform steady slip velocity, due to boundary layer renewal with low concentration bulk fluid. This renewal is caused by the spatial variation of slip velocity, which leads to flow perpendicular to the membrane surface. In terms of pressure losses, the change in friction factor relative to the case without electro-osmosis is quite similar whether the slip velocity is uniform or non-uniform, as long as the area-averaged slip velocity is the same.

For spatially uniform unsteady slip velocity in an empty channel, the time-averaged mass transfer enhancement does not vary significantly with frequency and amplitude but there are still benefits in terms of fouling reduction. However, if there are flow obstructions in the channel, there is a resonant frequency that can induce vortex shedding, which significantly increases mass transfer. The main feature distinguishing the empty and the spacer-filled channel cases without EOF is the presence of a  $v$ -velocity in the latter case due to the continuity. Given the importance of  $v$ -velocity for mass transfer enhancement, this means there is significant potential to increase mass transfer using EOF, especially when vortex shedding is induced or strengthened.

To gain further insights into the dynamic behaviour of the system, it is useful to understand whether a time-varying system is linear or nonlinear. This is because, if the system is linear, the time-averaged behaviour of a dynamically perturbed system will be the same as the behaviour resulting from a steady perturbation equivalent to the time-average of the unsteady perturbation. A linear system also implies that any design of input waveform consisting of several frequency components (i.e. square, triangle, sawtooth) is unnecessary because only the time-averaged value has an impact, and not the waveform. In Chapter 6, it was found that the system without obstruction is linear. However, a system with obstructions (spacers) is not completely linear due to the wall-normal convection term caused by the interactions between the flow and the spacers. Given the non-linear nature of the mass transfer system, there is still a knowledge gap in understanding the effect of an input that consists of several frequency components for spacer-filled channels with EOF. Those effects could result in greater mass transfer enhancement and, thus, should be studied in the future.

Given that the permeability of currently available membranes is several times larger than those reported half a century ago, the effect of concentration polarisation on

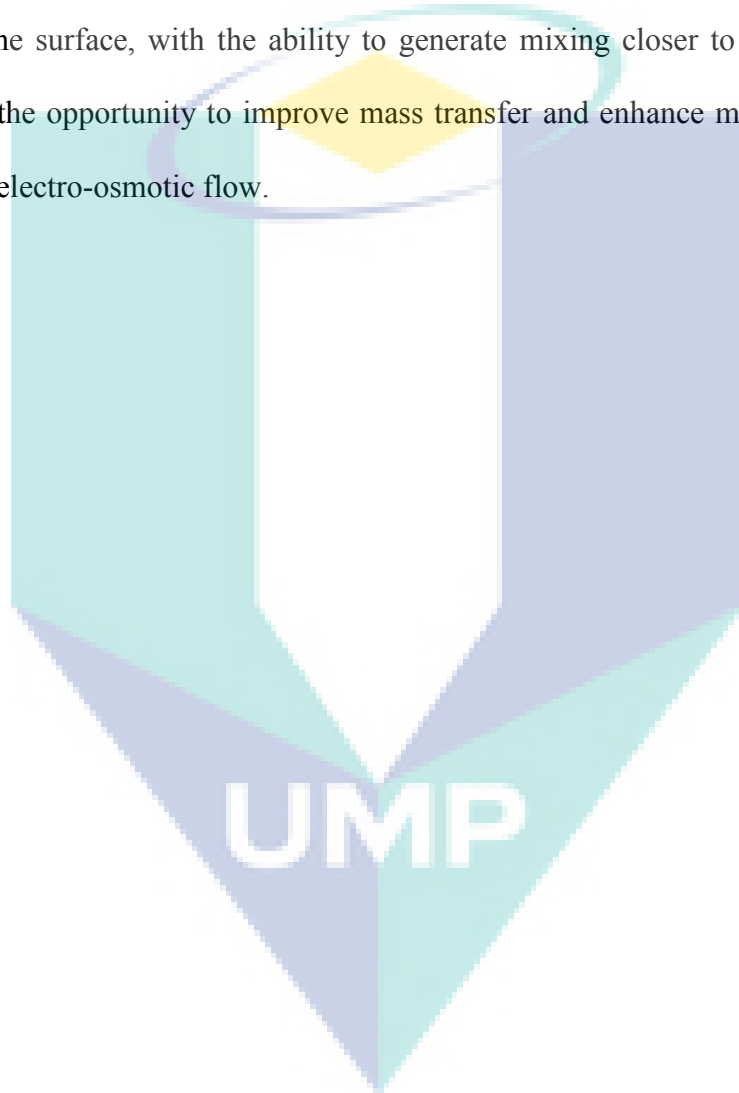
system performance has also become more significant than in the past. Although it was found in Chapter 5 that EOF is most effective in the permeability range of brackish water RO membranes, those results are based on steady-state conditions. The effect of unsteady-state slip velocity on permeate flux enhancement for large permeability membranes in spacer-filled channels has not yet explored. This is vital for future studies because large membrane permeability may affect the  $v$ -velocity at the membrane surface and hence affect the resonant frequency.

Future work should consider extending the results of this thesis to 3D geometries, which are more representative of real-world membrane systems [35]. Three-dimensional (3D) calculations would require a fine grid for the third dimension, further increasing the computational load requirement, above those of the 2D simulations completed in this thesis. Such studies should analyse the mechanisms that give rise to mass transfer enhancement in 3D flow. The insights into the effect of those flow conditions due to slip velocity are crucial for membrane unit design and optimisation.

Despite the good agreement between the CFD model and available published data, it was not possible to validate all of the simulation results. Recent improvements in Micro Particle Image Velocimetry (microPIV) mean that it might be useful for evaluating the resonant frequency for EOF that clearly induces vortex shedding and hence increases flux. MicroPIV is a suitable technology, as it can be used to measure spatial velocity profiles at sub-micron resolutions that could be compared to data obtained from CFD simulations [159]. The availability of new confocal microscopes that can measure at the nanometre scale [160], may provide another means of obtaining data for comparison with CFD simulations.

In conclusion, the CFD simulations in this thesis have provided key insights into the mechanisms of steady and unsteady electro-osmotic mass transfer enhancement in

obstructed and unobstructed membrane channels. The results presented have demonstrated the significance of vortex shedding induced by the synergy between electro-osmotic disturbances and spacer design for enhancing mixing and mass transfer. With the ongoing development of corrosion resistant yet inexpensive electrodes, the design of the next generation of membranes could have electrodes built-in near the membrane surface, with the ability to generate mixing closer to the wall. This would provide the opportunity to improve mass transfer and enhance membrane performance through electro-osmotic flow.



## References

1. Strathmann, H., *Membrane separation processes, 1. Principles*, in *Ullmann's Encyclopedia of Industrial Chemistry*. 2000, Wiley-VCH Verlag GmbH & Co. KGaA.
2. Schwinge, J., et al., *Spiral wound modules and spacers: review and analysis*. *Journal of Membrane Science*, 2004. **242**(1–2): p. 129-153.
3. Cummings, S. *Global markets for reverse osmosis membranes and components to reach \$8.1 billion by 2018: BCC research*. 2014; Available from: <http://www.prweb.com/pdfdownload/10959343.pdf>.
4. Zamani, F., et al., *Unsteady-state shear strategies to enhance mass-transfer for the implementation of ultrapermeable membranes in reverse osmosis: A review*. *Desalination*, 2015. **356**(0): p. 328-348.
5. Das, R., et al., *Carbon nanotube membranes for water purification: a bright future in water desalination*. *Desalination*, 2014. **336**(0): p. 97-109.
6. Holt, J.K., et al., *Fast mass transport through sub-2-nanometer carbon nanotubes*. *Science*, 2006. **312**(5776): p. 1034-1037.
7. Lee, K.P., T.C. Arnot, and D. Mattia, *A review of reverse osmosis membrane materials for desalination—development to date and future potential*. *Journal of Membrane Science*, 2011. **370**(1–2): p. 1-22.
8. Shen, Y.-x., et al., *Biomimetic membranes: a review*. *Journal of Membrane Science*, 2014. **454**(0): p. 359-381.
9. UNESCO, *The United Nations World Water Development Report 2014*. UNESCO, Paris, 2014.
10. Cohen-Tanugi, D., et al., *Quantifying the potential of ultra-permeable membranes for water desalination*. *Energy & Environmental Science*, 2014. **7**(3): p. 1134-1141.
11. Côté P., S. Siverns, and S. Monti, *Comparison of membrane-based solutions for water reclamation and desalination*. *Desalination*, 2005. **182**(1–3): p. 251-257.
12. Karagiannis, I.C. and P.G. Soldatos, *Water desalination cost literature: Review and assessment*. *Desalination*, 2008. **223**(1–3): p. 448-456.
13. Shaw, R.A., R. Deluca, and W.N. Gill, *Reverse osmosis: increased productivity by reduction of concentration polarization in laminar flow reverse osmosis using intermediate non-rejecting membrane sections*. *Desalination*, 1972. **11**(2): p. 189-205.
14. Sherwood, T.K., et al., *Salt concentration at phase boundaries in desalination by reverse osmosis*. *Industrial & Engineering Chemistry Fundamentals*, 1965. **4**(2): p. 113-118.
15. Brian, P.L.T., *Concentration polarization in reverse osmosis desalination with variable flux and incomplete salt rejection*. *Industrial & Engineering Chemistry Fundamentals*, 1965. **4**(4): p. 439-445.
16. Matthiasson, E. and B. Sivik, *Concentration polarization and fouling*. *Desalination*, 1980. **35**(0): p. 59-103.
17. Jagannadh, S.N. and H.S. Muralidhara, *Electrokinetics methods to control membrane fouling*. *Industrial & Engineering Chemistry Research*, 1996. **35**(4): p. 1133-1140.

18. Hunter, R.J., *Zeta potential in colloid science: Principles and applications*. 1981: Academic Press.
19. Probstein, R.F., *Physicochemical hydrodynamics: an introduction*. 1989: Butterworths.
20. Rawool, A. and S. Mitra, *Numerical simulation of electroosmotic effect in serpentine channels*. *Microfluidics and Nanofluidics*, 2006. **2**(3): p. 261-269.
21. Schwinge, J., D.E. Wiley, and D.F. Fletcher, *Simulation of the flow around spacer filaments between narrow channel walls. 1. Hydrodynamics*. *Industrial & Engineering Chemistry Research*, 2002. **41**(12): p. 2977-2987.
22. Schwinge, J., D.E. Wiley, and D.F. Fletcher, *Simulation of the flow around spacer filaments between channel walls. 2. Mass-transfer enhancement*. *Industrial & Engineering Chemistry Research*, 2002. **41**(19): p. 4879-4888.
23. Fimbres-Weihs, G.A., D.E. Wiley, and D.F. Fletcher, *Unsteady Flows with mass transfer in narrow zigzag spacer-filled channels: a numerical study*. *Industrial & Engineering Chemistry Research*, 2006. **45**(19): p. 6594-6603.
24. Fimbres-Weihs, G.A. and D.E. Wiley, *Numerical study of mass transfer in three-dimensional spacer-filled narrow channels with steady flow*. *Journal of Membrane Science*, 2007. **306**(1-2): p. 228-243.
25. Vrouwenvelder, J.S., et al., *Biofouling in spiral wound membrane systems: Three-dimensional CFD model based evaluation of experimental data*. *Journal of Membrane Science*, 2010. **346**(1): p. 71-85.
26. Parvareh, A., et al., *Experimental and CFD Study on the role of fluid flow pattern on membrane permeate flux*. *Chinese Journal of Chemical Engineering*, 2011. **19**(1): p. 18-25.
27. Yu, H., et al., *Analysis of heat and mass transfer by CFD for performance enhancement in direct contact membrane distillation*. *Journal of Membrane Science*, 2012. **405-406**(0): p. 38-47.
28. Shakaib, M., et al., *A CFD study on the effect of spacer orientation on temperature polarization in membrane distillation modules*. *Desalination*, 2012. **284**(0): p. 332-340.
29. Li, Y.-L., et al., *CFD analysis of the initial stages of particle deposition in spiral-wound membrane modules*. *Desalination*, 2012. **287**(0): p. 200-208.
30. Kostoglou, M. and A.J. Karabelas, *A mathematical study of the evolution of fouling and operating parameters throughout membrane sheets comprising spiral wound modules*. *Chemical Engineering Journal*, 2012. **187**: p. 222-231.
31. Baker, R., *Membrane technology and applications*. 2004: Wiley.
32. Bian, R., K. Yamamoto, and Y. Watanabe, *The effect of shear rate on controlling the concentration polarization and membrane fouling*. *Desalination*, 2000. **131**(1-3): p. 225-236.
33. Blasius, H., *Grenzschichten in flüssigkeiten mit kleiner reibung*.
34. Rana, D. and T. Matsuura, *Surface modifications for antifouling membranes*. *Chemical Reviews*, 2010. **110**(4): p. 2448-2471.
35. Fimbres-Weihs, G.A. and D.E. Wiley, *Review of 3D CFD modeling of flow and mass transfer in narrow spacer-filled channels in membrane modules*. *Chemical Engineering and Processing: Process Intensification*, 2010. **49**(7): p. 759-781.
36. AG, F., B. P, and L. H, *Membrane fouling and its control in environmental applications*. *Water Science Technology*, 2000: p. 303-308.
37. Schwinge, J., et al., *Characterization of a zigzag spacer for ultrafiltration*. *Journal of Membrane Science*, 2000. **172**(1-2): p. 19-31.

38. Fimbres-Weihs, G.A. and D.E. Wiley, *Numerical study of two-dimensional multi-layer spacer designs for minimum drag and maximum mass transfer*. Journal of Membrane Science, 2008. **325**(2): p. 809-822.
39. Li, F., et al., *Optimization of commercial net spacers in spiral wound membrane modules*. Journal of Membrane Science, 2002. **208**(1-2): p. 289-302.
40. Schock, G. and A. Miquel, *Mass transfer and pressure loss in spiral wound modules*. Desalination, 1987. **64**(0): p. 339-352.
41. Fákov á J., *The pressure drop in membrane module with spacers*. Journal of Membrane Science, 1991. **64**(1-2): p. 103-111.
42. Suwarno, S.R., et al., *The impact of flux and spacers on biofilm development on reverse osmosis membranes*. Journal of Membrane Science, 2012. **405-406**(0): p. 219-232.
43. Xie, P., L.C. Murdoch, and D.A. Ladner, *Hydrodynamics of sinusoidal spacers for improved reverse osmosis performance*. Journal of Membrane Science, 2014. **453**: p. 92-99.
44. Bechhold, H., *Ultrafiltration and electro-ultrafiltration*. In: J. Alexander (Ed.), *Colloid Chemistry, I, Chemical Catalogue Company*. New York, 1926: p. 820-837.
45. Weigert, T., J. Altmann, and S. Ripperger, *Crossflow electrofiltration in pilot scale*. Journal of Membrane Science, 1999. **159**(1-2): p. 253-262.
46. Schoch, R.B., J. Han, and P. Renaud, *Transport phenomena in nanofluidics*. Reviews of Modern Physics, 2008. **80**(3): p. 839-883.
47. Mohammad, A., et al., *Ultrafiltration in food processing industry: review on application, membrane fouling, and fouling control*. Food and Bioprocess Technology, 2012. **5**(4): p. 1143-1156.
48. Huotari, H.M., G. Tr äg ärdh, and I.H. Huisman, *Crossflow membrane filtration enhanced by an external DC electric field: a review*. Chemical Engineering Research and Design, 1999. **77**(5): p. 461-468.
49. Wakeman, R.J. and M.N. Sabri, *Utilizing pulsed electric fields in crossflow microfiltration of titania suspensions*. Vol. 73. 1995, Trans IChemE.
50. Jurado, J. and B.J. Bellhouse, *Application of electric fields and vortex mixing for enhanced ultrafiltration*. Filtration & Separation, 1994. **31**(3): p. 273-268.
51. Raats, M.H.M., et al., *Full scale electrokinetic dewatering of waste sludge*. Colloids and Surfaces A: Physicochemical and Engineering Aspects, 2002. **210**(2-3): p. 231-241.
52. Kondoh, S.a.H., M. , *Commercialization of pressurized electroosmotic dehydrator (PED)*. Water Science and Technology, 1990. **22**(12): p. 259-268.
53. Ho, W.S.W. and K.K. Sirkar, *Membrane handbook*. 1992: Van Nostrand Reinhold.
54. Hu, G. and D. Li, *Multiscale phenomena in microfluidics and nanofluidics*. Chemical Engineering Science, 2007. **62**(13): p. 3443-3454.
55. Rubinstein, S.M., et al., *Direct observation of a nonequilibrium electro-osmotic instability*. Physical Review Letters, 2008. **101**(23): p. 236101.
56. Rubinstein, I. and B. Zaltzman, *Electro-osmotic slip of the second kind and instability in concentration polarization at electrodialysis membranes*. Mathematical Models and Methods in Applied Sciences, 2001. **11**(2): p. 263-300.
57. Rubinstein, I. and B. Zaltzman, *Electro-osmotically induced convection at a permselective membrane*. Physical Review E, 2000. **62**(2): p. 2238-2251.

58. Rubinstein, I. and B. Zaltzman, *Electro-convective versus electroosmotic instability in concentration polarization*. Advances in Colloid and Interface Science, 2007. **134–135**(0): p. 190-200.
59. Rubinshtein, I., et al., *Experimental verification of the electroosmotic mechanism of overlimiting conductance through a cation exchange electro dialysis membrane*. Russian Journal of Electrochemistry, 2002. **38**(8): p. 853-863.
60. Fang, Y., Q. Li, and M.E. Green, *Noise spectra of transport at an anion membrane-solution interface*. Journal of Colloid and Interface Science, 1982. **86**(1): p. 185-190.
61. Rubinstein, I., et al., *Elimination of acid-base generation ('water-splitting') in electro dialysis*. Desalination, 1984. **51**(1): p. 55-60.
62. Russel, W.B., D.A. Saville, and W.R. Schowalter, *Colloidal dispersions*. 1992: Cambridge University Press.
63. Patankar, N.A. and H.H. Hu, *Numerical simulation of electroosmotic flow*. Analytical Chemistry, 1998. **70**(9): p. 1870-1881.
64. Cummings, E.B., et al., *Conditions for similitude between the fluid velocity and electric field in electroosmotic flow*. Analytical Chemistry, 2000. **72**(11): p. 2526-2532.
65. Ghidossi, R., D. Veyret, and P. Moulin, *Computational fluid dynamics applied to membranes: state of the art and opportunities*. Chemical Engineering and Processing: Process Intensification, 2006. **45**(6): p. 437-454.
66. Gill, W.N., C. Tien, and D.W. Zeh, *Concentration polarization effects in a reverse osmosis system*. Industrial & Engineering Chemistry Fundamentals, 1965. **4**(4): p. 433-439.
67. Singh, R. and R.L. Laurence, *Influence of slip velocity at a membrane surface on ultrafiltration performance—II. Tube flow system*. International Journal of Heat and Mass Transfer, 1979. **22**(5): p. 731-737.
68. Youm, K.H., A.G. Fane, and D.E. Wiley, *Effects of natural convection instability on membrane performance in dead-end and cross-flow ultrafiltration*. Journal of Membrane Science, 1996. **116**(2): p. 229-241.
69. Pellerin, E., et al., *Turbulent transport in membrane modules by CFD simulation in two dimensions*. Journal of Membrane Science, 1995. **100**(2): p. 139-153.
70. Alexiadis, A., et al., *Laminar flow transitions in a 2D channel with circular spacers*. Industrial & Engineering Chemistry Research, 2007. **46**(16): p. 5387-5396.
71. Monfared, M.A., et al., *CFD simulation of baffles arrangement for gelatin-water ultrafiltration in rectangular channel*. Desalination, 2012. **284**(0): p. 288-296.
72. Al-Sharif, S., et al., *Modelling flow and heat transfer in spacer-filled membrane distillation channels using open source CFD code*. Desalination, 2013. **311**(0): p. 103-112.
73. Saeed, A., R. Vuthaluru, and H.B. Vuthaluru, *Impact of feed spacer filament spacing on mass transport and fouling propensities of RO membrane surfaces*. Chemical Engineering Communications, 2014: p. null-null.
74. Sousa, P., et al., *A CFD study of the hydrodynamics in a desalination membrane filled with spacers*. Desalination, 2014. **349**(0): p. 22-30.
75. Li, Y.-L., P.-J. Lin, and K.-L. Tung, *CFD analysis of fluid flow through a spacer-filled disk-type membrane module*. Desalination, 2011. **283**(0): p. 140-147.

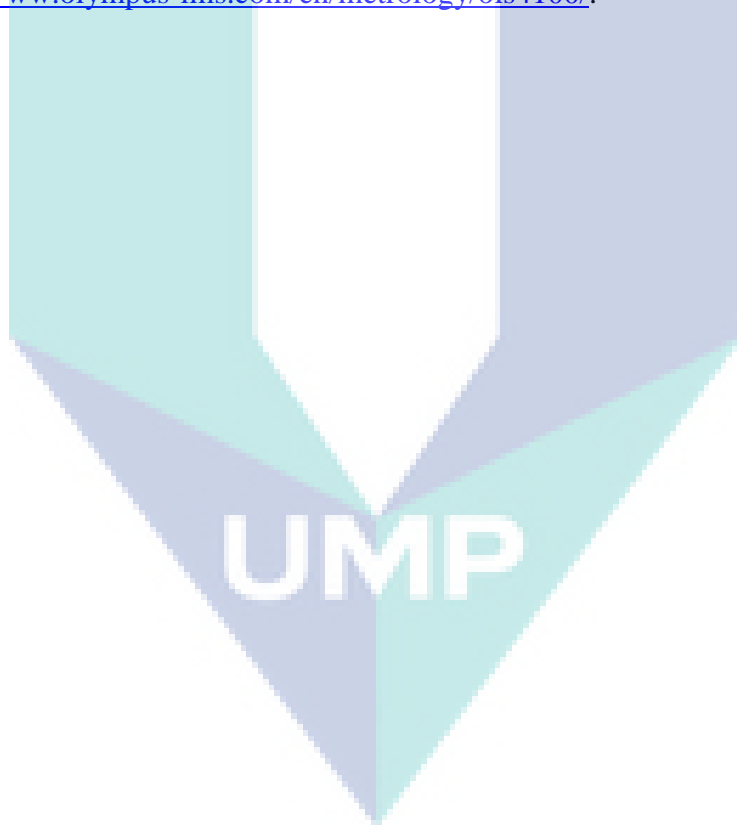
76. Willems, P., et al., *Use of particle imaging velocimetry to measure liquid velocity profiles in liquid and liquid/gas flows through spacer filled channels*. Journal of Membrane Science, 2010. **362**(1–2): p. 143-153.
77. Petty, M.C., *Molecular electronics: From principles to practice*. 2007: Wiley.
78. Huang, H.T., H.E. Fiedler, and J.J. Wang, *Limitation and improvement of PIV*. Experiments in Fluids, 1993. **15**(3): p. 168-174.
79. Cao, Z., D.E. Wiley, and A.G. Fane, *CFD simulations of net-type turbulence promoters in a narrow channel*. Journal of Membrane Science, 2001. **185**(2): p. 157-176.
80. Wiley, D.E. and D.F. Fletcher, *Computational fluid dynamics modelling of flow and permeation for pressure-driven membrane processes*. Desalination, 2002. **145**(1–3): p. 183-186.
81. Schwinge, J., D.E. Wiley, and D.F. Fletcher, *Simulation of unsteady flow and vortex shedding for narrow spacer-filled channels*. Industrial & Engineering Chemistry Research, 2003. **42**(20): p. 4962-4977.
82. Picioreanu, C., J.S. Vrouwenvelder, and M.C.M. van Loosdrecht, *Three-dimensional modeling of biofouling and fluid dynamics in feed spacer channels of membrane devices*. J. Membr. Sci., 2009. **345**(1–2): p. 340-354.
83. Bucs, S.S., et al., *Effect of different commercial feed spacers on biofouling of reverse osmosis membrane systems: A numerical study*. Desalination, 2014. **343**(0): p. 26-37.
84. von der Schulenburg, D.A.G., et al., *Three-dimensional simulations of biofilm growth in porous media*. AIChE Journal, 2009. **55**(2): p. 494-504.
85. Radu, A.I., et al., *Modeling the effect of biofilm formation on reverse osmosis performance: flux, feed channel pressure drop and solute passage*. Journal of Membrane Science, 2010. **365**(1–2): p. 1-15.
86. Pintelon, T.R.R., et al. *Validation of 3D simulations of reverse osmosis membrane biofouling*. Biotechnology and Bioengineering 2010 [cited 106 4]; 677-689]. Available from: <http://dx.doi.org/10.1002/bit.22717>.
87. Karabelas, A.J., M. Kostoglou, and S.T. Mitrouli, *Incipient crystallization of sparingly soluble salts on membrane surfaces: the case of dead-end filtration with no agitation*. Desalination, 2011. **273**(1): p. 105-117.
88. Radu, A.I., et al., *Combined biofouling and scaling in membrane feed channels: a new modeling approach*. Biofouling, 2015. **31**(1): p. 83-100.
89. Radu, A.I., et al., *A two-dimensional mechanistic model for scaling in spiral wound membrane systems*. Chemical Engineering Journal, 2014. **241**(0): p. 77-91.
90. Kostoglou, M. and A.J. Karabelas, *On modeling incipient crystallization of sparingly soluble salts in frontal membrane filtration*. Journal of Colloid and Interface Science, 2011. **362**(1): p. 202-214.
91. Davis, R.H. and D.T. Leighton, *Shear-induced transport of a particle layer along a porous wall*. Chemical Engineering Science, 1987. **42**(2): p. 275-281.
92. Flemming, H.-C., *Reverse osmosis membrane biofouling*. Experimental Thermal and Fluid Science, 1997. **14**(4): p. 382-391.
93. Khan, S.J. and C. Visvanathan, *Influence of mechanical mixing intensity on a biofilm structure and permeability in a membrane bioreactor*. Desalination, 2008. **231**(1–3): p. 253-267.
94. Sui, P., X. Wen, and X. Huang, *Feasibility of employing ultrasound for on-line membrane fouling control in an anaerobic membrane bioreactor*. Desalination, 2008. **219**(1–3): p. 203-213.

95. Jaffrin, M.Y., *Dynamic shear-enhanced membrane filtration: a review of rotating disks, rotating membranes and vibrating systems*. Journal of Membrane Science, 2008. **324**(1–2): p. 7-25.
96. Suh, Y.K., *Numerical study on transient induced-charge electro-osmotic flow in a cavity*. Colloids and Surfaces A: Physicochemical and Engineering Aspects, 2011. **376**(1–3): p. 111-121.
97. Song, H., et al., *Chaotic mixing in microchannels via low frequency switching transverse electroosmotic flow generated on integrated microelectrodes*. Lab on a Chip, 2010. **10**(6): p. 734-740.
98. Tang, G.Y., et al., *Numerical analysis of the thermal effect on electroosmotic flow and electrokinetic mass transport in microchannels*. Analytica Chimica Acta, 2004. **507**(1): p. 27-37.
99. Zeng, Y., et al., *Numerical simulation on mass transport in a microchannel bioreactor for co-culture applications*. Journal of Biomechanical Engineering, 2006. **129**(3): p. 365-373.
100. Marcos, et al., *Frequency-dependent laminar electroosmotic flow in a closed-end rectangular microchannel*. Journal of Colloid and Interface Science, 2004. **275**(2): p. 679-698.
101. Marcos, et al., *Frequency-dependent velocity and vorticity fields of electro-osmotic flow in a closed-end cylindrical microchannel*. Journal of Micromechanics and Microengineering, 2005. **15**(2): p. 301.
102. Yan, D., et al., *Enhancement of electrokinetically driven microfluidic T-mixer using frequency modulated electric field and channel geometry effects*. ELECTROPHORESIS, 2009. **30**(18): p. 3144-3152.
103. Reynolds, O., *An experimental investigation of the circumstances which determine whether the motion of water shall be direct or sinuous, and of the law of resistance in parallel channels*. Proceedings of the Royal Society of London, 1883. **35**(224-226): p. 84-99.
104. Schlichting, H., K. Gersten, and K. Gersten, *Boundary-layer theory*. 2000: Springer.
105. Bird, R.B., W.E. Stewart, and E.N. Lightfoot, *Transport phenomena*. 2007: J. Wiley.
106. Winzeler, H.B. and G. Belfort, *Enhanced performance for pressure-driven membrane processes: the argument for fluid instabilities*. Journal of Membrane Science, 1993. **80**(1): p. 35-47.
107. Ahmad, A.L. and K.K. Lau, *Impact of different spacer filaments geometries on 2D unsteady hydrodynamics and concentration polarization in spiral wound membrane channel*. Journal of Membrane Science, 2006. **286**(1–2): p. 77-92.
108. Arnal, M.P., D.J. Goering, and J.A.C. Humphrey, *Vortex shedding from a bluff body adjacent to a plane sliding wall*. Journal of Fluids Engineering, 1991. **113**(3): p. 384-398.
109. Kumarasamy, S. and J.B. Barlow, *Computation of unsteady flow over a half-cylinder close to a moving wall*. Journal of Wind Engineering and Industrial Aerodynamics, 1997. **69–71**(0): p. 239-248.
110. Bhattacharyya, S. and D.K. Maiti, *Vortex shedding from a square cylinder in presence of a moving wall*. International Journal for Numerical Methods in Fluids, 2005. **48**(9): p. 985-1000.
111. Huang, W.-X. and H.J. Sung, *Vortex shedding from a circular cylinder near a moving wall*. Journal of Fluids and Structures, 2007. **23**(7): p. 1064-1076.
112. Chung, T.J., *Computational fluid dynamics*. 2002: Cambridge University Press.

113. Versteeg, H.K. and W. Malalasekera, *An introduction to computational fluid dynamics: The finite volume method*. 2007: Pearson Education Limited.
114. Fletcher, D.F. and D. Wiley, *A computational fluids dynamics study of buoyancy effects in reverse osmosis*. J. Membr. Sci., 2004. **245**(1-2): p. 175-181.
115. Halliday, D., R. Resnick, and J. Walker, *Fundamentals of physics*. 2010: John Wiley & Sons.
116. Hoffmann, J.N. and P. Pulino, *New developments on the combined application of charge simulation and numerical methods for the computation of electric fields*. IEEE Transactions on Power Delivery, 1995. **10**(2): p. 1105-1111.
117. Song, L. and S. Yu, *Concentration polarization in cross-flow reverse osmosis*. AIChE Journal, 1999. **45**(5): p. 921-928.
118. Kedem, O. and A. Katchalsky, *Thermodynamic analysis of the permeability of biological membranes to non-electrolytes*. Biochimica et Biophysica Acta, 1958. **27**(0): p. 229-246.
119. Sourirajan, S., *Reverse osmosis*. 1970: Academic Press.
120. Geraldes, V. and M.D. Afonso, *Generalized mass-transfer correction factor for nanofiltration and reverse osmosis*. AIChE Journal, 2006. **52**(10): p. 3353-3362.
121. McCabe, W.L., J. Smith, and P. Harriott, *Unit operations of chemical engineering*. 2005: McGraw-Hill Education.
122. Rodgers, V.G.J. and R.E. Sparks, *Effect of transmembrane pressure pulsing on concentration polarization*. Journal of Membrane Science, 1992. **68**(1-2): p. 149-168.
123. Li, H.-y., C.D. Bertram, and D.E. Wiley, *Mechanisms by which pulsatile flow affects cross-flow microfiltration*. AIChE Journal, 1998. **44**(9): p. 1950-1961.
124. Alexiadis, A., et al., *Analysis of the dynamic response of a reverse osmosis membrane to time-dependent transmembrane pressure variation*. Industrial & Engineering Chemistry Research, 2005. **44**(20): p. 7823-7834.
125. Kraume, M. and A. Drews, *Membrane bioreactors in waste water treatment – status and trends*. Chemical Engineering & Technology, 2010. **33**(8): p. 1251-1259.
126. Liang, Y.Y., et al., *CFD modelling of electro-osmotic permeate flux enhancement on the feed side of a membrane module*. Journal of Membrane Science, 2014. **470**: p. 378-388.
127. Oberkampf, W.L. and T.G. Trucano, *Verification and validation in computational fluid dynamics*. Progress in Aerospace Sciences, 2002. **38**(3): p. 209-272.
128. Roache, P.J., *Quantification of uncertainty in computational fluid dynamics*. Annual Review of Fluid Mechanics, 1997. **29**(1): p. 123-160.
129. Dahl, E., *Ecological salinity boundaries in poikilohaline waters*. Oikos, 1956. **7**(1): p. 1-21.
130. Saville, D.A., *Electrokinetic effects with small particles*. Annual Review of Fluid Mechanics, 1977. **9**(1): p. 321-337.
131. Focke, W.W., *On the mechanism of transfer enhancement by eddy promoters*. Electrochimica Acta, 1983. **28**(8): p. 1137-1146.
132. Kim, D.H., I.H. Kim, and H.N. Chang, *Experimental study of mass transfer around a turbulence promoter by the limiting current method*. International Journal of Heat and Mass Transfer, 1983. **26**(7): p. 1007-1016.
133. Kim, W.S., J.K. Park, and H.N. Chang, *Mass transfer in a three-dimensional net-type turbulence promoter*. International Journal of Heat and Mass Transfer, 1987. **30**(6): p. 1183-1192.

134. Ouyang, H., et al., *Optimal feedback design for mixing enhancement in boundary layers of membrane systems*. Australian Control Conference, 2012.
135. Ouyang, H., et al., *Control study on mixing enhancement in boundary layers of membrane systems*. Journal of Process Control, 2013. **23**(8): p. 1197-1204.
136. Beavers, G.S. and D.D. Joseph, *Boundary conditions at a naturally permeable wall*. Journal of Fluid Mechanics, 1967. **30**(01): p. 197-207.
137. Beavers, G.S., E.M. Sparrow, and R.A. Magnuson, *Experiments on coupled parallel flows in a channel and a bounding porous medium*. Journal of Basic Engineering, 1970. **92**(4): p. 843-848.
138. Qian, S. and H.H. Bau, *Theoretical investigation of electro-osmotic flows and chaotic stirring in rectangular cavities*. Applied Mathematical Modelling, 2005. **29**(8): p. 726-753.
139. Liang, Y.Y., G.A. Fimbres Weihs, and D.E. Wiley, *Approximation for modelling electro-osmotic mixing in the boundary layer of membrane systems*. Journal of Membrane Science, 2014. **450**: p. 18-27.
140. Karabelas, A.J., *Key issues for improving the design and operation of spiral-wound membrane modules in desalination plants*. Desalination and Water Treatment, 2013. **52**(10-12): p. 1820-1832.
141. Keir, G. and V. Jegatheesan, *A review of computational fluid dynamics applications in pressure-driven membrane filtration*. Reviews in Environmental Science and Bio/Technology, 2014. **13**(2): p. 183-201.
142. Alexiadis, A., et al., *Dynamic response of a high-pressure reverse osmosis membrane simulation to time dependent disturbances*. Desalination, 2006. **191**: p. 397-403.
143. Jalilvand, Z., et al., *Computational fluid dynamics modeling and experimental study of continuous and pulsatile flow in flat sheet microfiltration membranes*. Journal of Membrane Science, 2014. **450**: p. 207-214.
144. Antony, A., et al., *In situ structural and functional characterization of reverse osmosis membranes using electrical impedance spectroscopy*. Journal of Membrane Science, 2013. **425-426**(0): p. 89-97.
145. Schock, G. and A. Miquel, *Mass transfer and pressure loss in spiral wound modules*. Desalination, 1987. **64**: p. 339-352.
146. Ratnayake, P., et al., *Spatio-temporal frequency response analysis of forced slip velocity effect on solute concentration oscillations in a reverse osmosis membrane channel*. Computers & Chemical Engineering, 2016. **84**: p. 151-161.
147. Sinton, D. and D. Li, *Electroosmotic velocity profiles in microchannels*. Colloids and Surfaces A: Physicochemical and Engineering Aspects, 2003. **222**(1-3): p. 273-283.
148. Setiawan, R., et al., *Reduced-order model for the analysis of mass transfer enhancement in membrane channel using electro-osmosis*. Chemical Engineering Science, 2015. **122**(0): p. 86-96.
149. Fu, L.M., J.Y. Lin, and R.J. Yang, *Analysis of electroosmotic flow with step change in zeta potential*. Journal of Colloid and Interface Science, 2003. **258**(2): p. 266-275.
150. *Discrete-time signal processing*. 1999: Pearson Education.
151. Tao, W.-Q., Z.-Y. Guo, and B.-X. Wang, *Field synergy principle for enhancing convective heat transfer - its extension and numerical verifications*. Int. J. Heat Mass Tran., 2002. **45**: p. 3849-3856.
152. Seborg, D.E., et al., *Process dynamics and control*. 2010: John Wiley & Sons.

153. Law, V.J. and R.V. Bailey, *A method for the determination of approximate system transfer functions*. Chemical Engineering Science, 1963. **18**(3): p. 189-202.
154. Doebelin, E.O., *System modeling and response: theoretical and experimental approaches*. 1980: Wiley.
155. Da Costa, A.R., et al., *Optimal channel spacer design for ultrafiltration*. Journal of Membrane Science, 1991. **62**(3): p. 275-291.
156. Winograd, Y., A. Solan, and M. Toren, *Mass transfer in narrow channels in the presence of turbulence promoters*. Desalination, 1973. **13**(2): p. 171-186.
157. Da Costa, A.R., *Fluid flow and mass transfer in spacer-filled channels for ultrafiltration*. 1993: University of New South Wales.
158. Fane, A.G., R. Wang, and M.X. Hu, *Synthetic membranes for water purification: status and future*. Angew Chem Int Ed Engl, 2015. **54**(11): p. 3368-86.
159. FlowMaster Micro-PIV [cited 9 September 2015]; Available from: [www.lavision.de/en/products/flowmaster/micro-piv.php](http://www.lavision.de/en/products/flowmaster/micro-piv.php).
160. Microscope Solutions OLS4100 [cited 9 September 2015]; Available from: [www.olympus-ims.com/en/metrology/ols4100/](http://www.olympus-ims.com/en/metrology/ols4100/).



## Appendix

- File name: YYLiang\_Thesis.pdf

Content: pdf version of the thesis

Instructions: Open in Adobe Reader version

- File name: YYLiang\_Chapter7.pptx

Content: power point presentation with embedded video of vortex shedding related to Figure 7.8 and Figure 7.9.

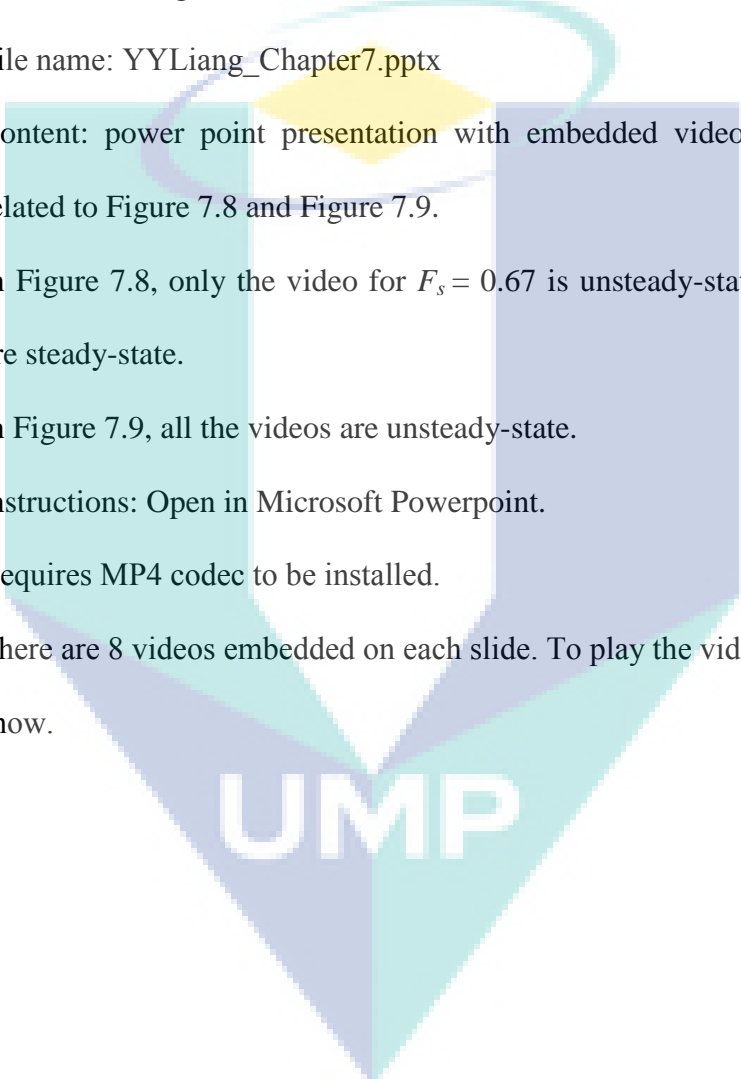
In Figure 7.8, only the video for  $F_s = 0.67$  is unsteady-state whereas the others are steady-state.

In Figure 7.9, all the videos are unsteady-state.

Instructions: Open in Microsoft Powerpoint.

Requires MP4 codec to be installed.

There are 8 videos embedded on each slide. To play the videos, start the slide show.

The logo for UMP (Universiti Malaysia Perlis) is a large, downward-pointing arrow shape. It is composed of four triangular sections meeting at a central point. The top-left and bottom-right sections are light blue, while the top-right and bottom-left sections are a slightly darker blue. The letters 'UMP' are written in a bold, white, sans-serif font across the center of the arrow.

UMP